

# The topology of structural brain connectivity in diseases and spatio-temporal connectomics

THÈSE N° 6586 (2015)

PRÉSENTÉE LE 22 MAI 2015

À LA FACULTÉ DES SCIENCES ET TECHNIQUES DE L'INGÉNIEUR  
LABORATOIRE DE TRAITEMENT DES SIGNAUX 5  
PROGRAMME DOCTORAL EN GÉNIE ÉLECTRIQUE

ÉCOLE POLYTECHNIQUE FÉDÉRALE DE LAUSANNE

POUR L'OBTENTION DU GRADE DE DOCTEUR ÈS SCIENCES

PAR

**Alessandra GRIFFA**

acceptée sur proposition du jury:

Prof. A. Skrivervik, présidente du jury  
Prof. J.-Ph. Thiran, Dr P. Hagmann, directeurs de thèse  
Prof. O. Sporns, rapporteur  
Prof. G. Deco, rapporteur  
Prof. D. Van De Ville, rapporteur



ÉCOLE POLYTECHNIQUE  
FÉDÉRALE DE LAUSANNE

Suisse  
2015



*“Any man could, if he were so inclined,  
be the sculptor of his own brain.”*

S. Ramón y Cajal



# Abstract

---

The brain is a complex system, composed of multiple neural units interconnected at different spatial and temporal scales. Diffusion MRI allows probing *in vivo* the anatomical connectivity between different cortical areas through white matter tracts. In parallel, functional MRI records neural-related signals of brain activity. Particularly, during rest (in absence of specific external task) reproducible dynamical patterns of functional synchronization have been shown across different brain areas. This rich information can be conveniently represented in the form of a graph, a mathematical object where nodes correspond to cortical regions and are connected by edges representing anatomical connections. On the top of this structural network, or brain connectome, individual nodes are associated to functional signals representing neural activity over observation periods.

Network science has fundamentally contributed to the characterization of the human connectome. The brain is a small-world network, able to combine segregation and integration aspects. These properties allow functional specialization on the one side, and efficient communication between distant brain areas on the other side, supporting complex cognitive and executive functions. Graph theoretical methods quantify brain topological properties, and allow their comparison between different populations and conditions. In fact, brain connectivity patterns and interdependences between anatomical substrate and functional synchronization have been proved to be impaired in a variety of brain disorders, and to change across human development and aging.

Despite these important advancements in the understanding of the brain structure and functioning, many questions are currently unanswered. It is not clear for instance how structural connectivity features are related to individual cognitive capabilities and deficits, and if they have the concrete potential to distinguish pathological subgroups for early diagnosis of brain diseases. Most importantly, it is not yet understood how the connectome topology relates to specific brain functions, and how the transmission of information happens on the top of the structural connectivity infrastructure in order to generate observed functional dynamics.

This thesis was motivated by these interdisciplinary inputs, and is the result of a strong interaction between biological and clinical questions on the one hand, and methodological development needs on the other hand.

First, we have contributed to the characterization of the human connectome in health and pathologies by adapting and developing network measures for the description of the brain architecture at different scales. Particularly, we have focused on the topological characterization of subnetworks role within the overall brain network. Importantly, we have shown that the topological alteration of distinct brain subsystems may be a biomarker for different brain disorders.

Second, we have proposed an original multi-layer network model for the joint representation of brain structural and functional connectivity properties, named spatio-temporal connectome. This flexible framework allows the investigation of functional dynamics at multiple temporal scales. Importantly, the analysis of spatio-temporal graphs in healthy subjects has disclosed temporal relationships between transient brain activations in resting state recordings, and highlighted functional communication principles on the top of the brain structural network.

Finally, we have applied developed measures and frameworks to the investigation of dysconnectivity traits in schizophrenia, 22q11 deletion syndrome and extremely preterm birth condition.

**Keywords:** *brain imaging, brain connectivity, brain dynamics, connectome, graph theory, diffusion MRI, functional MRI, resting state, schizophrenia, psychosis*

# Résumé

---

Le cerveau est un système complexe, composé de multiples unités neuronales interconnectées à différentes échelles d'espace et de temps. L'IRM de diffusion permet de sonder *in vivo* la connectivité anatomique entre différentes aires corticales à partir des fibres de la matière blanche. En parallèle, l'IRM fonctionnelle enregistre les signaux neuronaux liés à l'activité cérébrale. En particulier, pendant l'état de repos (en absence de tâche externe spécifique) des schémas dynamiques reproductibles de synchronisation fonctionnelle ont été décelés à travers différentes aires cérébrales. Cette information riche peut être représentée sous la forme d'un graphe, un objet mathématique où les noeuds correspondent aux régions corticales et sont connectés par des arêtes représentant les connections anatomiques. Par dessus ce réseau structurel, encore appelé connectome du cerveau, les noeuds individuels sont associés aux signaux fonctionnels représentant l'activité neuronale pendant les périodes d'observation.

La science des réseaux a contribué de manière fondamentale à la caractérisation du connectome humain. Le cerveau est un réseau petit-monde capable de combiner des aspects de segregation et d'intégration. Ces propriétés permettent d'un coté des fonctions de spécialisation et de l'autre une communication efficace entre des aires cérébrales distantes. Les méthodes issues de la théorie des graphes permettent de quantifier les propriétés topologiques du cerveau ainsi que leur comparaison entre différentes populations et conditions. Dans les faits, les schémas de connection du cerveau et les interdépendances entre substrat anatomique et synchronisation fonctionnelle sont altérées dans beaucoup de désordres psychiques et évoluent pendant le développement humain et le vieillissement.

Malgré des avancées importantes dans la compréhension de la structure cérébrale et de ses fonctions, beaucoup de questions restent encore sans réponse. Par exemple, le lien n'est pas clair entre la connectivité structurelle et les capacités et déficiences cognitives d'un individu, et si cette connectivité permet de distinguer des sous-groupes pathologiques pour la détection précoce de maladies du cerveau. Plus important encore, le lien entre la topologie du connectome et les fonctions cérébrales spécifiques ainsi que la transmission d'information dans cette infrastructure et la génération de la dynamique fonctionnelle observée, tout ceci n'est pas encore compris.

Cette thèse a été motivée par ces questions interdisciplinaires et est le résultat de la forte interaction entre biologie et questions cliniques d'une part et les besoins de développement méthodologique d'autre part.

D'abord, nous avons contribué à la caractérisation du connectome humain sain et pathologique en adaptant et développant des mesures issues de la théorie des réseaux, décrivant l'architecture cérébrale à différentes échelles. En particulier, nous nous sommes concentrés sur la caractérisation topologique du rôle des sous-réseaux à l'intérieur du réseau cérébral global. Fait d'importance, nous avons montré que l'altération topologique de certains sous-systèmes du cerveau est un bio-marqueur pour différents désordres psychiques.

Ensuite, nous avons proposé un modèle de réseau original pour la représentation conjointe des propriétés de la connectivité structurelle et fonctionnelle. Ce cadre spatio-temporel flexible permet l'investigation de la dynamique fonctionnelle à de multiples échelles de temps. L'analyse des graphes spatio-temporels de sujets sains a permis de mettre en lumière des relations temporelles entre activations cérébrales locales dans les enregistrements d'états de repos ainsi que certains

principes de communication fonctionnelle à travers le réseau structurel cérébral.  
Finalement, nous avons développé des mesures et un cadre de travail pour l'investigation de la dysconnectivité dans la schizophrénie, dans le syndrome « deletion 22q11 » et pour les bébés prématurés.

**Mots clefs :** *imagerie cérébrale, connectivité cérébrale, dynamiques cérébrales, connectome, théorie des graphes, IRM de diffusion, IRM fonctionnelle, fonctionnement cérébral à l'état de repos, schizophrénie, psychose*



# Acknowledgements

---

This thesis marks the end of an intense period of learning and work, whose completion would not have been possible without the help and support of many great people around me.

First and foremost, I would like to thank my supervisors, Prof. Jean-Philippe Thiran and Dr. Patric Hagmann. I am very grateful to you for giving me the chance to work on such an interesting research topic, within a privileged and lively scientific environment.

Jean-Philippe, thank you for your constant support and essential help in all the crucial moments of my PhD. At any obstacle or doubt, a discussion with you has always given me courage, positiveness and a new perspective to look at things. Thank you as well for making the LTS5 such a fertile and friendly working environment with your multifaceted scientific vision and sensibility: I could not have imagined a better milieu to learn and develop my skills.

Patric, thank you for the uncountable passionate and prolific discussions: I feel that my work would have never advanced without them. Thank you for the brilliant ideas you shared with me, for your trust, and for always pushing me toward new research questions and interesting collaborations. I am conscious and very grateful for all the opportunities you offered me.

I would like to acknowledge all the exchange of ideas and interactions with collaborators and advisors, fundamental to complete this thesis work.

Thank you to Prof. Kim Do for creating such a unique interdisciplinary network, for your passion, for the helpful discussions, and importantly for always trying to bridge the gap between complementary fields of research. A sincere thanks goes to Dr. Philipp Baumann, with whom I have profitably collaborated since the beginning of my PhD. Over these years you fed my interest and curiosity for psychiatric sciences, and you generously shared your knowledge with me: thank you! I also would like to express my gratitude to Prof. Philippe Conus and Prof. Michel Cuénod for all their insightful comments and discussions, and to all the members of the Unit for Research in Schizophrenia of the *Centre Hospitalier Universitaire Vaudois*: many thanks to Carina (always answering my annoying questions), Aline (always smiling), Pascal, Margot, Raoul, Luis and to all the others.

Moreover, I would like to express my gratitude to the Signal Processing Laboratory LTS2, headed by Prof. Pierre Vandergheynst. In particular, many thanks to Dr. Benjamin Ricaud for countless and fruitful discussions, precious help in understanding data and open ideas sharing. I appreciated your ethics and lively interest for neuroscience questions. Many thanks to Dr. Xavier Bresson, always available for insightful discussions around brain mechanisms on the one hand, and mathematical instruments on the other hand. Thank you for your sharp comments and ideas.

I would also like to sincerely thank all the scientists, doctors, technicians and students of the *Centre Hospitalier Universitaire Vaudois* with whom I had the chance to collaborate and discuss. I could learn a lot from all these interactions! In particular, many thanks to Lijing Xin, František Váša, Cecilia Maeder, Elena Najdenovska, Nicolas Chevrey, Sebastien Urben, Constantin

Tuleasca, Eleonora Fornari among the others.

I would like to thank the members of the jury, who read through my manuscript and led a fruitful discussion during my PhD exam. I thank Prof. Anja Skrivervik, president of the jury; Prof. Dimitri Van De Ville and Prof. Gustavo Deco for their insightful questions and comments. I would like to express my sincere gratitude to Prof. Olaf Sporns, that I also had the chance to visit in Bloomington during my PhD. Thank you for having hosted me in your group in such a nice way, giving me the possibility of taking part into exciting scientific discussions and projects. This experience was extremely valuable for me. In this connection, I take the occasion to thank the members of the Computational Cognitive Neuroscience Laboratory, and particularly Joaquín Goñi for the excellent discussions, Andrea Avena Koenigsberger (and the flocks patterns inspiration), and Richard Betzel.

Certainly many thanks go to all the present and past members of the LTS5, LTSs, MMSPG, ASPG and LIONS groups.

First of all I would like to thank my office mates, Meri and Elda, for enriching every working day with a friendly chat, a scientific idea, or simply a little break. Elda, I truly think I would have not manage to go through the writing period without your precious and not foregone help. Thank you for having read every single word of my thesis, for your patience, listening and friendship.

A huge thank you goes to Eleni, Anna and Anil, for your daily presence, for all the cheerful breaks and funny moments, for always helping me in many senses, for your friendship. I feel very lucky for having shared these last years with you!

Thank you to Andrea (always there to share a laugh, a beer and even a Latex template), Francesca (taking care of me during the writing period!), Alia (sharing very nice moments in the mountain), Alessandro (teaching me everything I know about tractography, and always there to answer the more diverse questions), Laura (always bringing a smile of optimism), Leila, Ashkan, Martin, Frank, Ana, Dorina, Sophia and all the others in the labs!

A special thanks goes to Rosie, for her extremely good organization, administrative help and little moments around a coffee.

Thanks to my friends, who have made my life outside EPFL whole and joyous. Thanks to who stayed with me late at night in the office when I needed energy to work, to who listened to my presentation even on Sunday evening, to who shared with me his ideas, smiles and time. Thank you to Cris for listening to my doubts even before starting this PhD, and for making me feel home. Thank you to Nadia, Elena and all my friends *di sempre* from Torino, Aosta, Milano.

Last but not least, my greatest gratitude goes to my family. Thank you to my mum and dad, who always supported me. Thank you for granting me freedom in all my choices, and for always being there with priceless understanding, advices and love. Thank you also to my uncle and aunt Giorgio and Simona with little Luca, for bringing life and adventures. Thank you!

*Alessandra*

# Contents

---

<b>Abstract</b>	<b>v</b>
<b>1 Preface</b>	<b>1</b>
1.1 Context . . . . .	1
1.2 Motivations . . . . .	1
1.3 Contributions of the thesis and organization of the manuscript . . . . .	3
<b>2 Introduction</b>	<b>5</b>
2.1 Brain anatomy . . . . .	5
2.2 Probing brain architecture and activity with diffusion and functional MRI . . . . .	6
2.3 Estimating brain connectivity networks . . . . .	7
2.4 Brain networks characterization . . . . .	8
<b>I Part 1</b>	<b>11</b>
<b>Overview</b>	<b>13</b>
<b>3 Topological characterization of brain subnetworks: background and methods</b>	<b>15</b>
3.1 <i>Background</i>	
Scales and statistics for group-comparison of network topologies . . . . .	15
3.2 <i>Background</i>	
Network attack for resilience and centrality assessment . . . . .	18
3.2.1 Network resilience . . . . .	18
3.2.2 Brain network attack . . . . .	20
3.3 <i>Methods</i>	
Subnetwork topological centrality . . . . .	21
3.3.1 Definition . . . . .	22
3.3.2 Characterization . . . . .	24
3.3.3 Centrality of brain circuits . . . . .	35
3.4 Conclusions . . . . .	40
<b>4 Topological characterization of brain subnetworks in diseases</b>	<b>41</b>
4.1 <i>Applications</i>	
Tracking brain connectivity alterations across psychosis stages . . . . .	41
4.1.1 Purposes . . . . .	41
4.1.2 Introduction . . . . .	42
4.1.3 Methods and Materials . . . . .	44
4.1.3.1 Subject cohorts . . . . .	44
4.1.3.2 Diffusion MRI . . . . .	45

4.1.3.3	A graph-theory based pipeline for diffusion data analysis . . . .	46
4.1.4	Results . . . . .	51
4.1.5	Discussion . . . . .	59
4.2	<i>Applications</i>	
	Identifying the affected core of 22q11 deletion syndrome . . . . .	62
4.2.1	Purposes . . . . .	62
4.2.2	Introduction . . . . .	62
4.2.3	Methods and Materials . . . . .	63
4.2.4	Results . . . . .	64
4.2.5	Discussion . . . . .	66
4.3	Conclusions . . . . .	67
<b>II</b>	<b>Part 2</b>	<b>69</b>
	<b>Overview</b>	<b>71</b>
<b>5</b>	<b>Group-comparison of brain network community structure</b>	<b>73</b>
5.1	<i>Background</i>	
	Estimation and comparison of clustering structures . . . . .	73
5.1.1	Algorithms for community detection . . . . .	73
5.1.2	Information theory metrics for clustering comparison . . . . .	75
5.2	<i>Methods</i>	
	Strategies for group-comparison and representative partitions . . . . .	76
5.2.1	Methods and Materials . . . . .	78
5.2.2	Results and Discussion . . . . .	79
5.3	<i>Applications</i>	
	Brain network modular fingerprint of high-risk preterm born children . . . . .	82
5.3.1	Introduction . . . . .	82
5.3.2	Methods and Materials . . . . .	83
5.3.3	Results . . . . .	84
5.3.4	Discussion . . . . .	85
5.4	Conclusions . . . . .	86
<b>III</b>	<b>Part 3</b>	<b>87</b>
	<b>Overview</b>	<b>89</b>
<b>6</b>	<b>Mapping resting-state dynamics on spatio-temporal connectomes</b>	<b>91</b>
6.1	<i>Background</i>	
	Relationship between brain structure and function . . . . .	91
6.2	<i>Background</i>	
	Dynamic resting-state connectivity . . . . .	92
6.3	<i>Methods</i>	
	Definition of a spatio-temporal framework . . . . .	94
6.3.1	Underlying hypotheses . . . . .	94
6.3.2	fMRI data reduction . . . . .	95
6.3.3	The spatio-temporal connectome model . . . . .	96
6.4	<i>Methods</i>	
	Identification of representative spatio-temporal patterns of brain activity . . . . .	99
6.5	Conclusions . . . . .	102

<b>7</b>	<b><i>Applications</i></b>	
	<b>Functional dynamics and anatomical substrate in the human brain</b>	<b>103</b>
7.1	Methods and materials . . . . .	104
7.1.1	Human brain datasets and MRI data processing . . . . .	104
7.1.2	Spatio-temporal graph construction and components clustering . . . . .	105
7.2	Results and Discussion . . . . .	107
7.2.1	Individual spatio-temporal activation components . . . . .	107
7.2.2	Representative dynamical patterns of resting state activity . . . . .	107
7.2.3	Structure-function relationship . . . . .	111
7.2.4	Mapping the functional usage of anatomical networks . . . . .	113
7.3	Conclusions . . . . .	116
<b>8</b>	<b>Discussion and Conclusions</b>	<b>119</b>
8.1	Summary and contributions . . . . .	119
8.2	Perspectives . . . . .	120
	<b>Bibliography</b>	<b>123</b>
	<b>Curriculum Vitæ</b>	<b>141</b>
	<b>Publications</b>	<b>143</b>



# List of Acronyms

---

$\tilde{G}$	spatio-temporal connectome
ADC	apparent diffusion coefficient
BOLD	blood-oxygen-level dependent
CC	connected component of $\tilde{G}$
CPZ	chlorpromazine equivalent dose
CSF	cerebrospinal fluid
CTRL	healthy subjects control group
DMN	default mode network
dMRI	diffusion magnetic resonance imaging
DSI	diffusion spectrum imaging
DTI	diffusion tensor imaging
DWI	diffusion weighted imaging
EP	early psychosis patients group (ch. 4) or extreme premature children group (ch. 5)
FA	fractional anisotropy
FC	functional connectivity
FDR	false discovery rate
fMRI	functional magnetic resonance imaging
gFA	generalized fractional anisotropy
GLM	generalized linear model
GM	grey matter
ICA	independent component analysis
ICN	intrinsic connectivity network
IUGR	intrauterine growth restriction
MI	mutual information index

$MI_n$	normalized mutual information index
MPRAGE	magnetization prepared rapid acquisition gradient echo
MRI	magnetic resonance imaging
ODF	orientation distribution function
PCA	principal component analysis
PP	point process
ROI	region of interest
rs-fMRI	resting state functional magnetic resonance imaging
SC	structural connectivity
SCHZ	schizophrenia patients group
TA	acquisition time
TE	echo time
TI	inversion time
TPM	transition probability matrix
TR	repetition time
VI	variation of information index
$VI_n$	normalized variation of information index
VOI	volume of interest
WM	white matter
WRS	Wilcoxon rank-sum statistical test
WSR	Wilcoxon signed-rank statistical test



# List of Tables

---

3.1	Benchmark networks topological properties . . . . .	27
4.1	Network characteristics for schizophrenia and early psychosis patients . . . . .	48
4.2	Affected core closeness centrality and local efficiency for schizophrenia patients .	53
4.3	Affected cores overlap between schizophrenia and 22q11 deletion syndrome . . .	67
5.1	Intra-subject and inter-subject variability of structural brain networks modular decomposition . . . . .	81
5.2	Number of clusters and modularity $Q$ for high-risk children cohorts . . . . .	84
5.3	$Min$ and $VIn$ clustering similarity for high-risk children cohorts . . . . .	85
7.1	Statistics for representative resting-state patterns . . . . .	109



# List of Figures

---

2.1	Coronal views of the brain . . . . .	6
2.2	Whole-brain tractography and brain connectivity matrices . . . . .	8
3.1	Scales for brain networks comparison . . . . .	16
3.2	Erdős–Rényi and scale-free networks resilience . . . . .	20
3.3	White matter edge centrality from selective network lesioning . . . . .	22
3.4	Subnetwork topological centrality computation . . . . .	23
3.5	Structural brain network . . . . .	25
3.6	Randomized structural brain network . . . . .	26
3.7	Erdős–Rényi network . . . . .	26
3.8	Scale-free network . . . . .	26
3.9	Average degree for hybrid attack . . . . .	28
3.10	Network resilience to hybrid attack: efficiency . . . . .	30
3.11	Network resilience to hybrid attack: size of largest connected component . . . . .	31
3.12	Network resilience to hybrid attack: average size of connected components . . . . .	32
3.13	Degree mixing rate - efficiency curves . . . . .	33
3.14	Subnetwork topological centrality for benchmark networks . . . . .	36
3.15	Structural brain network, 1014 nodes . . . . .	37
3.16	1014-node brain network communities . . . . .	39
3.17	Topological centrality of connector and peripheral hub subnetworks . . . . .	39
4.1	Outline of clinical staging in psychotic disorders . . . . .	43
4.2	Histograms of connectivity strength as a function of streamline length . . . . .	47
4.3	Connectivity matrices for healthy and schizophrenia subjects . . . . .	47
4.4	Global network properties in schizophrenia and early psychosis patients . . . . .	51
4.5	Schizophrenia affected core . . . . .	52
4.6	Nodes centrality ranking in schizophrenia and early psychosis patients . . . . .	54
4.7	Affected core topological centrality $\zeta^w$ in schizophrenia and early psychosis patients . . . . .	55
4.8	Shortest paths layout and schizophrenia affected core . . . . .	56
4.9	Quantitative characterization ( $wgFA$ and $wiADC$ values) of the affected core in schizophrenia and early psychosis patients . . . . .	57
4.10	Affected core topological centrality for schizophrenia and early psychosis patients . . . . .	58
4.11	Global network properties in 22q11.2 deletion syndrome patients . . . . .	64
4.12	22q11.2 deletion syndrome affected core . . . . .	65
4.13	Affected core topological centrality $\zeta^2$ in 22q11.2 deletion syndrome patients . . . . .	65
5.1	Schematic representation of Louvain algorithm . . . . .	74
5.2	Mutual and variation of information logical representation . . . . .	77
5.3	Single subject structural connectivity matrix and modular decomposition . . . . .	80

5.4	Consensus matrix from brain network modular decomposition of 40 healthy subjects . . . . .	81
5.5	Structural brain network representative partitions for a group of 40 healthy subjects	82
5.6	<i>Min</i> and <i>VIn</i> clustering similarity for high-risk children cohorts . . . . .	85
5.7	Network communities consensus clustering for high-risk children cohorts . . . . .	86
6.1	Prediction of functional connectivity with measures of shortest path embedding . . . . .	93
6.2	Point process analysis . . . . .	96
6.3	Schematic representation of a spatio-temporal graph construction . . . . .	98
6.4	Activation component of a spatio-temporal graph . . . . .	99
6.5	Schematic representation of feature matrix construction . . . . .	101
7.1	Practical implementation of $\tilde{G}$ construction . . . . .	106
7.2	Examples of individual connected components . . . . .	108
7.3	Representative dynamical patterns of resting state activity . . . . .	110
7.4	Overlap between resting-state dynamical patterns and ICNs . . . . .	111
7.5	Cluster centroids of reference spatio-temporal graphs . . . . .	112
7.6	Edge reproducibility analysis on spatio-temporal graphs . . . . .	113
7.7	Comparison of spatio-temporal graphs with and without anatomical prior . . . . .	113
7.8	Brain transition probability matrix . . . . .	114
7.9	Structural and functional brain connectivity matrices . . . . .	115
7.10	Correlations between structural connectivity, functional connectivity and transition probabilities . . . . .	116

# 1

## Preface

---

### 1.1 Context

The brain is probably the most complex organ of the human body, counting a trillion of interconnected nervous cells highly organized over multiple spatial scales. Such highly structured architecture supports the huge variety of possible mental processes, from basic sensorimotor processing to high-level cognitive and executive functions.

Recent advanced in diffusion magnetic resonance imaging (MRI) have allowed for the first time to imaging *in vivo* white matter brain connectivity patterns between cortical areas. On top, functional MRI indirectly probes local dynamics of cortical activity, during mental tasks or rest conditions. Together, these two techniques map the macroscopic set of anatomical and functional relationships between different brain regions, namely the human connectome.

### 1.2 Motivations

The characterization of overall brain connectivity patterns is of great current interest. Formally, the pairwise connectivity information (structural or functional) can be mathematically described as a graph. This new paradigm that considers the brain as an integrative complex system enables the characterization of overall brain connectivity patterns. The so-called connectome borrows the solid theoretical instruments of graph theory to study brain structure and function.

The structural (or anatomical) connectome describes the ensemble of white matter connections between the different cortical and subcortical regions and allows to gain new insights into fundamental brain organizational principles. Structurally, the human brain has been characterized as being a small-world, assortative, hierarchical network where a set of central rich-club nodes integrate distinct functional modules. Such highly organized architecture, that combines integration and segregation properties, supports the large variety of functional processes giving rise to complex cognitive, executive and behavioural tasks.

Functional connectomes are networks representing statistical pair-wise relationships between local brain dynamics, estimated *via* functional MRI. Functional connectomes share common topological features with their structural counterpart, and show reproducible spatial communities of co-activation consistent with corresponding structural modules. In fact, different network measures of structural connectivity, such as shortest paths or path topological embedding, have been shown to (partially) predict functional patterns of correlation. Following this line, it has been shown that complex computational neural models that use the information embedded in the

structural connectome are able to reproduce observed functional connectivity characteristics.

The uncovering of the inter-dependence between functional synchronization patterns across distributed brain regions and their anatomical substrate is certainly of primary interest in cognitive neuroscience. Nevertheless, the structural and the functional connectomes refer to two substantially divergent dimensions. On the one hand, at the spatial resolution achievable by means of diffusion MRI (dMRI), the structural connectivity network is essentially static, at least at a short-term temporal scale. On the other hand, the functional dimension is intrinsically dynamic and condition-dependent. Indeed, a relatively high variability of the within-subject functional connectivity has been shown even during resting-state recordings. Recent exploratory works on brain resting-state activity have highlighted non-stationary aspects of brain dynamics and transient patterns of synchronization, shifting the attention from time-average resting state networks, to a more complex space of connectivity states that the resting brain would dynamically visit. Under this perspective, the brain structure-function information is highly complex and multi-dimensional. One might say that while a static structural network describes the anatomical relationships between the different brain nodes, an evolving signal can be associated to each node, representing the functional patterns of it.

Although the characterization of signal on graphs have been extensively studied in graph theory, and time-dependent networks have been formalized, it is not clear yet how to better represent the complex multidimensional and multi-modal information extracted from diffusion and functional MRI using an appropriate network model. The development of a suitable framework for the structure-function representation of brain interregional relations would clearly help addressing fundamental biological questions. In this connection, several challenges and concerns need to be addressed: Is there a finite set of (resting-state) dynamic functional configurations, and in which form do they relate to the underlying structural network topology? How does communication take place on the top of the anatomical substrate, and how is information distributed across the brain network? Most importantly, what is the impact of anatomical connectivity alterations on brain activity dynamics, and ultimately on brain functionalities? And furthermore, how structural brain alterations may relate to cognitive deficits and symptoms observed in brain disorders? Answering these questions certainly need future methodological development within the related fields of connectomics analysis and network science.

Since it has become clearer that nervous systems generally have non-random topological properties of the same kind as seen in many other complex systems, connectomics analyses have been widely used in a broad spectrum of brain disorders. The application of network models and theoretical graph analysis to clinical investigations mainly aims to uncover pathological mechanism, and possibly identify quantitative biomarkers suitable for early diagnosis and monitoring of pathology progression. Connectomics studies based on MRI data showed that substantially different brain disorders share common alterations of the structural network topology, such as diminished overall communication efficiency and preferential vulnerability of central hub nodes. Finer-grain analyses at the nodal level have allowed to identify different sets of brain regions and connections, typically broadly distributed across the brain network, involved in distinct pathologies. It is still unclear however if the connectivity alteration of specific brain subnetworks might be directly associated with specific symptoms and cognitive impairments, or if such alterations may discriminate diagnostic sub-groups. In other words, is it actually possible to identify connectomics biomarkers of disease severity? Can specific brain subnetworks be unequivocally associated with particular symptoms or pathological populations? How localized dysconnectivity alterations impact the way brain communication takes place on the top of the underlying anatomical networks, and ultimately influence or determine brain (dys)functions? The answers to these open questions are probably not unique, might depend on the particular disorder under investigation, but certainly require a convergence of multiple inputs. The accumulation of neuroimaging

evidences together with the formulation of plausible clinical and biological hypotheses need to be combined with the development and refinement of dedicated network analysis tools.

This thesis emerges from these needs and from an iterative mutual interaction between biological questions on the one side, and network analysis methodological needs on the other side. A primary trigger of this dissertation certainly appeared from a set of clinical questions around psychosis development and schizophrenia, and the hypothesis that these neurological dysfunctions were rooted in brain dysconnectivity patterns. The extremely subtle brain alterations underlying the earlier stages of psychosis pushed us to refine network analysis methods, and to define a theoretical measure of subnetwork topological centrality for the characterization of observed alteration across populations. On top of that, the key point of this dissertation is the study of the brain structure and function relationship, using an original network model that encompass multi-modal data integration. The proposed spatio-temporal graph framework integrates brain anatomical networks and, importantly, dynamical aspects of functional connectivity.

### 1.3 Contributions of the thesis and organization of the manuscript

The core of this dissertation is organized into three main parts encompassing, in this order, brain network topological characterization, group representation and group-comparison analysis and structure-function integration. Each of these parts comprises a (i) *Background* section where relevant state-of-the-art findings are reviewed, a (ii) *Methods* section defining the original methodological contribution and an (iii) *Applications* part where developed methods are directly applied to clinical data. As an introductory chapter, Chapter 2 of this thesis contains a general introduction on structural and functional brain connectomics.

Part I, mainly centred on brain network topological characterization, includes two chapters: Chapter 3 and 4. In Chapter 3, a new theoretical measure  $\zeta$  is presented. This network measure quantifies the topological centrality of a certain subnetwork within a given overall brain network architecture. This measure becomes interesting in clinical connectomics, as several brain disorders such as schizophrenia can be associated not to the global network architecture but to localized connectivity disruption within a specific subnetwork. For a better understanding of pathological mechanisms it is certainly of interest to characterize the topological role of such specific brain cores, and evaluate how their impairment may impact the overall brain communication system. The topological centrality measure here proposed is conceptually based on the use of network attacks for the characterization of elements' topological roles. While classic attack analysis deals with random or targeted (centrality-ranked) deletion of network elements, here we are interested in the damage of specific subnetworks of variable size and mixing rate (where mixing rate stands for the ratio of higher and lower centrality nodes included in the subnetwork of interest). In order to characterize the subnetwork topological measure  $\zeta$  for a set of benchmark networks, we define a hybrid network attack strategy where dedicated parameters control the size and the mixing rate of the damaged subnetwork.

Chapter 4 is entirely devoted to the characterization of structural brain dysconnectivity across psychosis stages, schizophrenia and 22q11 deletion syndrome. For the different pathological conditions we could identify specific affected subnetworks, or affected cores, mainly responsible for the observed loss of global network integration properties. We used the subnetwork topological centrality  $\zeta$  to quantitatively characterize such affected cores in healthy and disease.

The work described in this chapter was published in (Griffa *et al.*, 2015a, 2014, 2015c; Vasa *et al.*, 2015). Moreover, structural brain connectivity alterations occurring in neurological and psychiatric disorders have been reviewed in (Griffa *et al.*, 2013b).

Part II is dedicated to the modular aspects and community decomposability of the human brain structural network. In particular, we advocate the use of partition distance measures for the characterization of community architectures across populations, and we test different strategies (including the consensus clustering algorithm) for the identification of group-representative network partitions. Applying these instruments, in chapter 5 we investigate the brain community structure of particularly sensitive populations of high-risk preterm born children.

Part of the work discussed in chapter 5 was published in (Fischi-Gomez *et al.*, 2015; Griffa *et al.*, 2013a).

Part III of this dissertation is entirely dedicated to the formalization and investigation of the brain structure-function relationship. In chapter 6 we propose an original network model for the joint representation of brain structural connectivity and functional dynamics as estimated by means of diffusion and resting-state MRI. Our model relies on the arrangement of the structural and functional information on a spatio-temporal graph. The edges of the spatio-temporal graph represent brain regions closeness in both space (the space of the brain anatomical static graph) and time.

In chapter 7 we use the formalism introduced in the previous chapter 6 to investigate brain structure-function dynamics in a set of healthy individuals. The spatio-temporal graph model allows us to identify connected subnetworks of regions anatomically linked and transiently synchronized in time, and to investigate their dynamics. By clustering the detected components, we could identify transient but reproducible patterns of brain spatio-temporal synchronization closely resembling task-based activation circuits. Moreover, we show that the role of the anatomical graph is fundamental to increase the robustness of the functional components detection, and to separate potentially independent functional phenomena.

Elements of the work discussed in this Part III were published in (Griffa *et al.*, 2015b).

Finally, the main results of these thesis and, importantly, suggestions for future research are summarized and discussed in chapter 8.



# Introduction

---

# 2

The brain is a fascinating complex system, composed by 100 billions of neurons distributed across multiple layers in the cortical volume. Each neuron may be connected to up to 10'000 other neurons, passing signals to each other via as many as 1'000 trillion synaptic connections. Long axonal projections compose the bulk of the white matter volume, and connect distant neuronal populations.

This intricate set of electrically excitable and signaling cells, together with their multi-scale interconnections, integrates sensory information coming from our sensory organs, coordinates our body movements, and governs our behaviours, decisions and thinking.

At a macroscopic scale, Magnetic Resonance Imaging (*MRI*) allows to characterize the brain architecture under different perspectives. Diffusion-weighted imaging (*dmRI*) maps the whole-brain set of white matter bundles connecting the different cortical and subcortical regions. Functional magnetic resonance imaging (*fMRI*) records blood flow variations related to local brain activity and neural processes.

The overall patterns of brain connections and functional interactions can be modelled in the form of networks, with nodes (cortical and subcortical areas) interconnected by edges representing white matter fiber bundles, or functional synchronization between local neural activities. The term *connectome* refers in fact to these macroscopic, comprehensive maps of neural connections. The representation of the brain connectivity in the form of a network is convenient for the characterization of brain organizational and communication principles, and of their possible alteration in neurological and psychiatric disorders.

In this chapter we briefly summarize notions of brain anatomy and magnetic resonance imaging. Next, we introduce in some more details the network representation of the whole-brain connectivity patterns, and we discuss fundamental characteristics of such brain networks.

## 2.1 Brain anatomy

The human brain forms the central nervous system together with the spinal cord, and consists of several structures. The brain is divided into the following elements: (i) the brainstem, including the medulla oblongata, the pons and the midbrain, which controls basic functions and integrates sensorimotor connections from and toward the rest of the body; (ii) the cerebellum, responsible for the motor control; (iii) the thalamus and hypothalamus, regulating the autonomic nervous system; (iv) the cerebrum, consisting in the cortex, the deep grey nuclei, and a mass of nervous fibers interconnecting cortical and subcortical structures.

The cerebrum occupies the largest part of the brain. It receives and elaborates sensitive information for the control of movements and sensations, language, memory, emotions. The unit performing all these tasks is the cerebral cortex, a 3 mm-thick grey matter layer constituting the most external part of the cerebrum, together with the subcortical structures. The grey matter is made up of neuronal somas, highly interconnected between them and organized in multiple cortical layers. Due to the large surface occupied (from  $1500\text{ cm}^2$  to  $2000\text{ cm}^2$ ), the cortex is folded in sulci and giri.

The brain cortex can be subdivided into four lobes with different functions: the temporal lobe, the frontal lobe, the occipital lobe and the parietal lobe. They cover the two hemispheres of the brain, the right and the left one. The two hemispheres are separated by the interhemispheric fissure, but they communicate through the corpus callosum, and the anterior and posterior commissures.

The white matter is mainly composed of axons, i.e. nervous fibers interconnecting the different cortical and subcortical structures. The typical white color is given by the myelin, an insulating material enhancing the velocity of conduction of electrical signals.

Figure 2.1 pictures two coronal views of the brain, showing the location of its main structures.

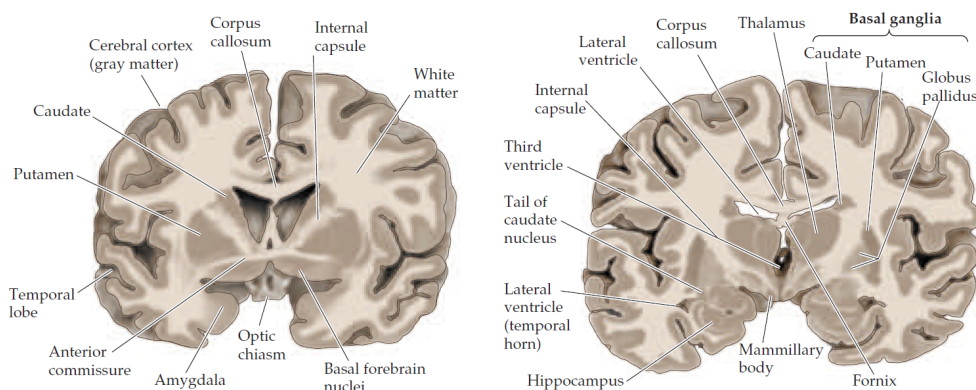


Figure 2.1 – Coronal views of the brain, showing its principal cortical, subcortical and white matter structures. From Purves et al.: Neuroscience, Third Edition, Sinauer Associates, Inc., Sunderland, MA, 2004 (Purves *et al.*, 2004). Used with permission.

## 2.2 Probing brain architecture and activity with diffusion and functional MRI

Over the last decades, a fast development of non-invasive neuroimaging techniques has made possible to probe *in vivo* different aspects of the human brain architecture.

Magnetic resonance imaging (*MRI*) techniques exploit a strong magnetic field and radio waves to image brain anatomy and physiology, including tissues contrast, white and grey matter (micro)structural characteristics, local metabolites' concentration, cerebral perfusion and blood flow dynamics.

Among the different *MRI* techniques, **diffusion MRI** (*dMRI*) allows to characterize local profiles of water molecules displacement in brain tissues.

In the *MRI* pulsed gradient spin-echo sequence (SE) used in diffusion weighted imaging, two pulsed field gradients are applied sequentially in time. The first gradient pulse magnetically labels water molecules according to their spatial location, by introducing a spin phase shift that

is dependent on the strength of the gradient at the position of the spin. A second gradient pulse of the same intensity as the first one, but with opposite direction, is applied after a temporal interval  $t = \Delta$ . The second gradient pulse induces a phase shift dependent on the spin position at  $t = \Delta$ . Spins which keep the same position along the gradients axis over the time interval  $\Delta$  return to their initial state, while spins which move feel a different field strength during the second pulse. The net phase shift produces a decrease of the detected *MRI* signal intensity: higher phase shifts correspond to larger displacements and to greater decreases of the signal.

By applying gradient pulses along different spatial directions, it is possible to reconstruct voxel-wise profiles of water molecules diffusion.

In brain tissues, water molecules spontaneously move (or equivalently, diffuse) agitated by thermal energy. Water molecules in the cerebrospinal fluid are free to randomly move in any spatial direction (free diffusion). On the contrary, diffusion in grey and white matter tissues is not free, but reflects interactions with many obstacles, such as macromolecules and membranes. The white matter is mostly composed by glial cells and myelinated nervous fibers. The myelin is a lipidic material and is partially impermeable. In the white matter, water molecules diffusion is therefore constrained and follows the nervous fiber directions. Consequently, the voxel-wise diffusion profiles reconstructed *via dMRI* map at a macroscopic (mm) scale the local nervous fiber directions.

This information allows reconstructing whole-brain tractograms of white matter fiber bundles.

**Functional MRI (*fMRI*)** provides an indirect measurement of brain neural activity, by detecting the related changes in blood flow and blood oxygenation (BOLD, blood-oxygen-level dependent contrast).

Neuronal activity is associated with glucose and oxygen consumption. In order to compensate for the increased oxygen demand during neurons firing, the local blood flow is increased. This phenomenon is known as neurovascular coupling. Because of an over-compensation mechanism, during neural activity it is possible to observe a local increase of oxygenated hemoglobin (oxyhemoglobin) relative to its deoxygenated form (deoxyhemoglobin).

Thanks to the different magnetic susceptibility of the two molecules, the  $T2^*$  MRI contrast used in *fMRI* is sensitive to the local oxy-to-deoxyhemoglobin ratio and therefore, indirectly, to the local neural activity.

## 2.3 Estimating brain connectivity networks

The whole-brain ensemble of white matter connections, and the inter-regional patterns of functional activity synchronizations can be represented in the form of brain networks.

A network is a mathematical object composed by a set of nodes interconnected by a set of edges, and can be described by means of an adjacency matrix. The single elements of an adjacency matrix represent the existence and, eventually, the strength of a connection between pairs of nodes.

In the brain network, nodes correspond to cortical and subcortical regions, typically estimated from an anatomical atlas, but also from functional atlases or data-driven approaches.

Structural brain networks describe the overall set of brain anatomical connections as estimated by means of *dMRI*. The voxel-wise profiles quantifying local water molecules diffusion processes can be fed to a tractography algorithm for the reconstruction of a whole-brain tractogram (an example is shown in figure 2.2a). Even though a large variety of tractography algorithms is available, many studies employ simple deterministic approaches, where a set of

streamlines is initiated within the white matter, and propagated by following the most coherent direction of diffusion in neighbouring voxels.

In a brain structural network, an edge will connect two nodes if a minimal number of streamlines links the two corresponding brain regions. Network edges can be weighted by the number of connecting streamlines (an example is given in figure 2.2b), or by some other white matter index averaged along the connecting streamlines pathways.

Functional brain networks represent the pair-wise statistical dependencies between the functional signals associated to cortical and subcortical nodes. Voxel-wise functional signals are recorded *via* functional MRI. Next, node-wise representative signals are computed, for example by averaging the voxel-wise time series over the voxels belonging to the single nodes.

A widely used measure of signals statistical dependency is the Pearson's correlation coefficient. In this case the estimated functional networks are complete graph, i.e. a connection exists between each pair of network nodes. An example of Pearson's correlations adjacency matrix is shown in figure 2.2c.

The characterization of a complete graph is not straightforward. Therefore, Pearson's correlation adjacency matrices are typically thresholded before further investigations. Otherwise, other statistical dependency measures can be used, such as the signals inverse covariance matrix that estimates conditional relationships and results in a sparser connectivity matrix.

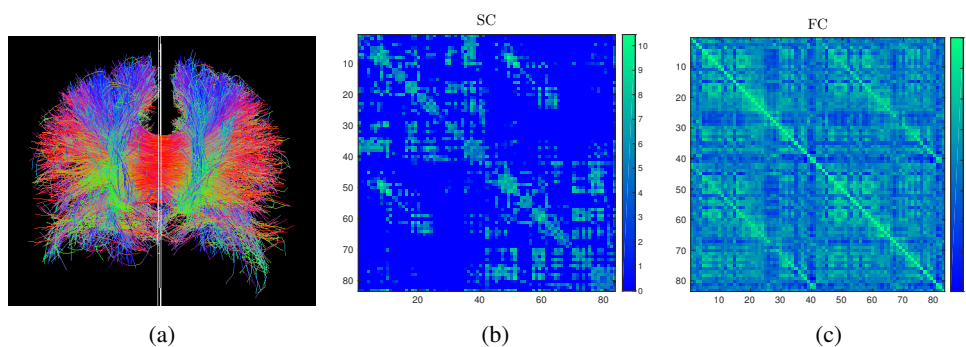


Figure 2.2 – Examples of (a) whole-brain tractography (the color-coding represents the fiber directions), (b) structural connectivity adjacency matrix (color-coding: scaled number of connecting streamlines), and (c) functional connectivity adjacency matrix (color-coding: Pearson's correlation coefficients).

## 2.4 Brain networks characterization

The human connectome is conceptually and mathematically a complex object. Measures derived from graph theory allow to quantitatively describe the architecture of both structural and functional brain networks, at different scales of investigation. Maybe non surprisingly, structural and functional brain graphs have been shown to possess similar network topological characteristics.

The nodal degree distribution is a first simple but very informative characteristic of brain networks. The degree is defined as the number of edges attached to a considered node. In a weighted network, the equivalent nodal strength is the sum of the weights assigned to the edges attached to a considered node. The structural and functional human brain networks demonstrate

an exponential or exponentially-truncated power law degree distribution, indicating the presence of a major population of low-degree nodes, and of few high-degree nodes.

Nodes with higher degree act as hubs of communication between more specialized and spatially segregated brain areas. Indeed, the distribution of high-degree nodes is spatially organized. Higher degree nodes concentrate along the brain midline (superior frontal, precuneus and posterior cingulate cortices), and include the superior parietal cortices and subcortical structures. Hub nodes are highly interconnected between them, at a level that exceeds what would be expected by their degree only, therefore forming a rich-club organization which is central for integration of information across the brain network.

The brain network topology balances integration and segregation properties. Conceptually, segregation and integration aspects underlie on the one hand functional specialization (e.g. sensory and motor circuits), and on the other hand higher order functions (such as multisensory integration, cognition and executive functions) that require large scale integration and communication between distant brain areas.

Segregation relates to the presence in the network of cliques and communities of nodes highly interconnected between them, but poorly connected with the rest of the network. Integration refers to a short average distance between each pair of network nodes. In an integrated network it is therefore easy, on average, to reach a particular node from any other node.

Formally, segregation topological properties can be quantified by means of the clustering coefficient, the transitivity, the local efficiency, the motif distribution, the modularity index among other measures. Integration is typically quantified in terms of characteristic path length or global efficiency.

Networks that preserve a certain level of segregation, while holding a considerable level of integration (high global efficiency of communication) are referred to as small world networks. A measure of balance between integration and segregation is the small world index, defined as the ratio between the clustering coefficient and the characteristic path length, normalized with respect to an equivalent randomized network. A small world network has characteristic path length similar to the one of a random network, but higher clustering coefficient.

The human structural and functional connectomes have been characterized as small-world, modular, hierarchical networks.

For a comprehensive discussion of graph theory elements and application to brain networks characterization we refer to (Alstott *et al.*, 2014; Newman, 2010; Rubinov & Sporns, 2010, 2011; van den Heuvel & Sporns, 2011).



Part I

---

**Topological characterization of  
brain structural subnetworks**





# Overview

---

The human brain is a multi-scale system. From a structural point of view the brain cortex can be subdivided into lobes, areas, sub-areas, down to nervous columns, neuronal layers and single cells. These subunits are interconnected in a complex manner. The characterization of the brain architecture in health and diseases can therefore take place at different scales of investigation. Graph theoretical measures quantify brain network characteristics at system scale (e.g. network efficiency, transitivity), subsystem scale (e.g. communities, rich-club, motif) and local scale (e.g. nodal clustering coefficient, closeness centrality) (Rubinov & Sporns, 2010). Dedicated statistical instruments allow to robustly compare brain connectivity features across populations, facing multivariate analysis and multiple comparison correction issues (Meskaldji *et al.*, 2013). Importantly, brain network measures are altered in almost all neurological and psychiatric disorders (Castellanos *et al.*, 2013; Fornito & Bullmore, 2014; Griffa *et al.*, 2013b). The impairment of system-scale features as network efficiency is probably an hallmark for the majority of brain diseases, and can reflect local insults or spatially distributed connectivity alterations. Particularly, brain network hubs (or rich-club) prove to be preferentially affected in many pathologies (Crossley *et al.*, 2014). The peculiar vulnerability of rich-club nodes may relate to the decrease of network efficiency observed in many brain diseases.

Nevertheless, an abundant literature of clinical studies based on neuroimaging techniques, suggests that different brain disorders can be associated with the impairment of different and specific brain subnetworks that include, but do not limit to, hub nodes. For example, the hypo-connectivity of a brain subnetwork comprising fronto-parietal and occipital cortices has been associated with schizophrenia (Zalesky *et al.*, 2011); the hyper-connectivity of a distributed circuit comprising parietal areas, precuneus, angular and supramarginal gyri has been associated with autism spectrum disorders (Li *et al.*). Specifically affected brain subsystems may have variable size, and include variable proportions of central hubs and peripheral nodes. The disruption of peculiar brain subnetworks can have different impacts on the overall brain network communication properties, leading to specific functional alterations and symptoms.

In Part I of this thesis we questioned how to better characterize the topological role of subsystems within the overall brain network, and whether the topological characterization of affected subsystems can provide valuable biomarkers for brain diseases. To this end, we introduced a theoretical measure  $\zeta$  of subnetwork topological centrality. The computation of  $\zeta$  is based on the comparison of targeted and random attack procedures. Thereafter, within a graph theoretical framework, we investigated brain connectivity alterations in schizophrenia, early psychosis and 22q11 deletion syndrome patients. For the different clinical groups we identified impaired subnetworks, or affected cores, and quantified their topological centrality alteration.

Chapter 3 is dedicated to *Background* and *Methods* illustration. We first review basic concepts related to connectomes statistical comparison, with a particular emphasis on possible scales of investigation (section 3.1). We discuss different methodological strategies for the identification and characterization of altered subnetworks in pathological populations. Next, we review theoretical elements of network attack procedures (section 3.2). Moreover we discuss recent works characterizing brain network elements centrality (individual nodes or edges) by means

of network attack (section 3.2.2). These approaches are conceptually related to our subnetwork characterization strategy.

In section 3.3 we formally define the subnetwork topological centrality measure  $\zeta$ . Intuitively, we expect  $\zeta$  to vary as function of the size  $f$  of the considered subnetwork, and of the percentage  $q$  of high/low centrality nodes included in the subnetwork. Moreover, for a fixed combination of the  $(f, q)$  parameters, we expect  $\zeta$  to reflect some organizational properties of the overall network. We characterize the subnetwork topological centrality measure for a set of benchmark networks, and as function of the parameters  $(f, q)$ . In order to sample subnetworks with predefined  $q$  values, we introduce a new hybrid attack procedure.

Chapter 4 is entirely devoted to the characterization of the structural connectome in pathologies. We first investigate a cohort of chronic schizophrenia patients. Our analyses confirm the disruption of global segregation and integration properties in patients, and identify a spatially distributed set of brain regions, dubbed affected core, driving the loss of global brain network properties. The centrality of the affected core is compromised in patients, as quantified by means of  $\zeta$ . Next, we investigate a group of patients in the early stage of psychosis. We test a staging model for psychopathology, suggesting that brain connectivity alteration might be more abnormal in more severe stages of the pathology. Consistently, we investigate the progressive impairment of the affected core from early psychosis stages to chronic schizophrenia. Finally, we considered a group of patients affected by 22q11 deletion syndrome, a genetic disease considered to be a model for the study of psychosis. Again, we confirm that global network measures are impaired in the disorder, and we identify an affected core partially overlapping our findings on schizophrenia patients.

Taken together these results suggest that the structural alteration and topological decentralization of spatially distributed affected cores might be a major mechanism underlying the psychosis dysconnectivity syndrome.

Elements of the present Part I have been published in (Griffa *et al.*, 2015a, 2014, 2013b, 2015c; Meskaldji *et al.*, 2013; Vasa *et al.*, 2015).

# Topological characterization of brain subnetworks: background and methods

---

# 3

## 3.1 *Background* Scales and statistics for group-comparison of network topologies

The formalism representing the overall brain connectivity as a complex network enables the comparison of connectivity patterns across populations, at different levels of abstraction: from networks of single neurons, to networks of cortical brain areas, brain subsystems, and overall system organization. Strategies for group-comparison of brain networks encompass graph theoretical aspects and fundamentals of statistics (Fornito & Bullmore, 2014; Griffa *et al.*, 2013b; Meskaldji *et al.*, 2013; Varoquaux & Craddock, 2013), and are reviewed in this section with a particular emphasis on different network scales of investigation: global, local and subsystem scales (figure 3.1).

### *System scale*

At a first scale of investigation, different groups can be tested using univariate statistical testing of single measures summarizing overall brain network topological aspects. Typically, independent Student's t-tests (assuming Gaussianity of the network measures distribution), or non-parametric statistics (like the Wilcoxon rank sum test (Wilcoxon, 1945) or permutation tests (Westfall, 1993)) are used. When heterogeneous populations are investigated, it is good practice to correct tested measures for possible confounding factors (such as age, gender, handedness or years of education) that could partially drive the observed group-wise differences. A linear regression of the confounding factors prior of statistical testing, or a Generalized Linear Model (GLM) setting are possible options.

In this framework, one may for instance be interested in assessing group-differences of measures quantifying overall integration, segregation, modular, assortative and hierarchical aspects of the connectome topology. It is worth noting that the majority of such measures is highly dependent on the density (or equivalently, sparsity) of the networks under investigation (Romero-Garcia *et al.*, 2012; van Wijk *et al.*, 2010), and on the overall connections weight in case of weighted networks. In order to disentangle effective topological alterations from cost variations when comparing populations with potentially different network densities and average weight,

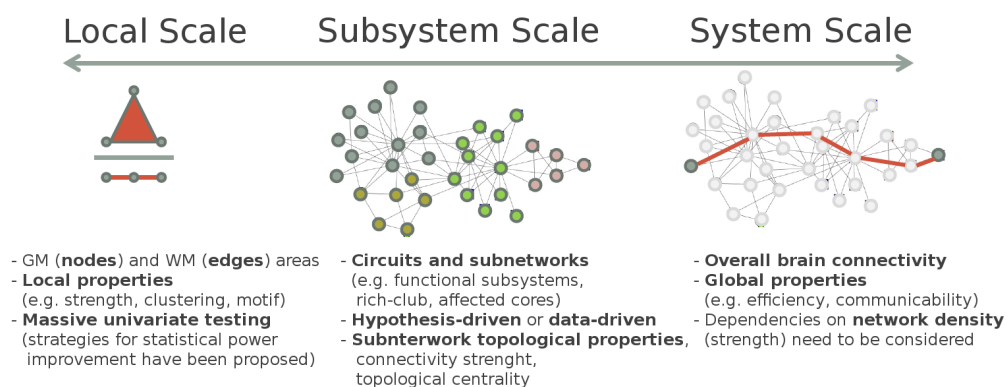


Figure 3.1 – Scales for brain networks investigation and comparison. Figure adapted from <http://www.math.ucr.edu/iamis/bassett.pdf>

these dependencies need to be considered. To address this issue it is possible to threshold the individual connectivity matrices in order to get homogeneous cost. This kind of thresholding eliminates the dependency of the topological features on the wiring cost, but exposes to the risk of significantly altering the effective network topology by discarding important connections, or including noisy ones (de Reus & van den Heuvel, 2013). Possible alternative approaches are testing for between-group cost alterations prior further analyses, or adopting a cost-integration strategy by integrating network measures over a range of thresholds on the network density (Ginestet *et al.*, 2011). In case of weighted networks and weighted graph analysis, another possibility to separate absolute connectivity strength from network topological alterations is to normalize the connectivity weights (for an example of this approach see section 4.1).

### *Local scale*

At a finer level of investigation, researchers may be interested in comparing single brain elements (nodes or edges) to identify specifically affected grey matter areas or white matter tracts. For instance, it is common procedure to compare nodal topological properties such as some centrality or clustering measure, or single-edge connectivity strength, i.e. the values of the single cells of a brain connectivity matrix. The main obstacle when moving from a global network investigation to a nodal or edge-wise scale is the necessity of correction for the massive multiple comparison testing that is performed, while preserving a sufficient statistical power.

A correction for multiplicity has to be considered whenever multiple tests, involving different null hypotheses, are performed on the same dataset. Classical procedures for multiple comparison correction control some expression of the **Type I error** (false positive or false discovery). Possible expressions of the Type I error rate are the family wise error rate (**FWER**) (e.g.: Bonferroni procedure), or the less stringent false discovery rate (**FDR**) (e.g.: Benjamini-Hochberg step-wise procedure (Benjamini & Hochberg, 1995)). The FWER is defined as the probability of having at least one false discovery over the collection of performed tests; the FDR is defined as the expectation of the proportion of false discoveries over the total number of rejections. The Bonferroni and Benjamini-Hochberg step-wise procedures allows to robustly identify sets of nodes or edges (brain subnetworks) altered in a given group of subjects compared to a reference group. However, in the framework of connectomics analysis, these methods might lack of sufficient statistical power considering (i) the high number of performed statistical tests (of the order of  $O(N)$  or  $O(N^2)$ , with  $N$  number of network nodes ranging from set of ten to thousands), (ii) the typically small size of the effect, and (iii) the consistent level of noise affecting the brain

connectivity matrices. We mention here that the statistical power, or sensitivity of a test, is defined as the probability of rejecting the null hypothesis when the null hypothesis is truly false, and is equal to  $(1-\beta)$  with  $\beta$  probability of committing a **Type II error** (false negatives).

In order to address statistical power limitations, different authors have proposed methods tailored to brain connectivity analysis. These methods exploit some kind of dependency in the data structure. The objective is to relax the FWER and FDR control and to increase the overall statistical power of the multiple testing procedure. Among these approaches we find the Network-Based Statistics (NBS) (Zalesky *et al.*, 2010) and the Spatial Pairwise Clustering (SPC) (Zalesky *et al.*, 2012a), that provide a weak FWER control; the Screening-Filtering (SF) (Meskaldji *et al.*, 2015) method, that provides a strong FWER control on edge-wise testing; the Spatial Parametric Network (SPN) analysis (Ginestet & Simmons, 2011).

The **NBS** and the **SPC** procedures exploit possible positive dependencies among the effects on edges belonging to the same brain subnetworks. A set of independent statistical tests is performed at the edge-wise level, providing an uncorrected p-values matrix of the same size of the brain connectivity matrix. Thereafter, subnetworks are identified by thresholding the p-values matrix, and detecting the resultant connected components (NBS). The SPC adds a constraint of spatial proximity on groups of nodes belonging to the same component, with the purpose of denoising the resultant components from presumably spurious, isolated connections. Finally, a permutation testing procedure which considers the size (number of edges) of each component ascribes a single, FWER-corrected p-value to each component.

The **SF** is a multi-step procedure. Once edge-wise (or node-wise) tests have been performed, and a collection of nodes or edges subsets have been defined in an arbitrary way, a first screening phase distinguishes affected from non-affected subsets on the basis of within-subset p-values. In a second filtering phase, relaxation coefficients are computed on the basis of the previous screening phase: p-values belonging to affected subsets can be relaxed (decreased). Finally, the relaxed p-values can be corrected for multiple comparison using the preferred multiple comparison correction procedure (e.g. Bonferroni or Benjamini-Hochberg step-wise procedure). This method guarantees a strict FWER or FDR control at the edge/node-wise level, and globally improves the statistical power of the multiple comparison procedure.

On the whole, these statistical methods allow identifying altered brain circuits and regions when comparing specific cohorts of subjects. One of the main objectives of connectome group-comparison is the identification of biomarkers or quantitative measures that could determine the presence of the disorder. It is therefore of primary importance to identify which local alterations can be associated to a specific disorder, or can constitute a pathological endophenotype. The statistical methods listed above were used to localize affected brain circuits in different diseases (Bai *et al.*, 2012; Li *et al.*; Meskaldji *et al.*, 2011; Verstraete *et al.*, 2011; Zalesky *et al.*, 2011, 2012b).

### ***Subsystem scale***

At an intermediary scale of investigation, it is of interest to characterize brain subsystems and their possible alteration across different conditions. In this section we review approaches for brain subsystems identification ( (i) hypothesis-driven, (ii) multi-modal and (iii) data-driven approaches) and quantitative characterization.

Brain subsystems of interest can be selected according to some **pre-established hypothesis** or previous observation. For example, Alzheimer's disease has been widely associated with DMN impairment (Koch *et al.*, 2012); schizophrenia with prefrontal cortex and fronto-striato-thalamic loops alteration (Fitzsimmons *et al.*, 2013). Based on similar strong hypotheses, one

could investigate specific brain subsystems in order to confirm previous findings on specific cohorts, or to extend previous findings to patients in a premorbid or early phase of the pathology. In this thesis we have used a similar strategy for the investigation of an early psychosis cohort in relation to a group of subjects affected by chronic schizophrenia (see section 4.1).

The **integration of multi-modal information** is also a possible strategy to identify subsystems of interest. For instance, one could identify some relevant functional circuit from fMRI data, and thereafter investigate intra-circuit and inter-circuit anatomical connectivity estimated from DWI acquisitions or cortical thickness correlation. This kind of trans-modal approaches can provide interesting insights into pathological mechanisms and the relationship between the functional dynamics and the anatomical substrate (Douaud *et al.*, 2011; Supekar *et al.*, 2010; Zhang *et al.*, 2011).

Recent literature has driven attention on particular subnetworks of **hubs**, such as the brain backbone (van den Heuvel *et al.*, 2012), k- and s-cores (Hagmann *et al.*, 2008), and particularly the rich-club (van den Heuvel & Sporns, 2011). The rich-club is a set of highly central nodes whose inter-connectivity is higher than expected by their degree or strength alone (Alstott *et al.*, 2014; van den Heuvel & Sporns, 2011). The rich-club subnetwork has been investigated in a variety of brain diseases and conditions (Ball *et al.*, 2014; Collin *et al.*, 2014a; Grayson *et al.*, 2014; Ray *et al.*, 2014; van den Heuvel *et al.*, 2013). The analysis of brain central circuits allowed to conclude that brain hubs are preferentially affected in many pathologies (Crossley *et al.*, 2014). The high sensitivity of hub regions has been associated with their high metabolic cost, sustained activity and long-range projections (Bullmore & Sporns, 2012).

Finally, following **data-driven approaches**, node-wise and edge-wise statistical comparisons allow to identify subsystems of interest for specific pathologies or conditions.

Subnetworks of interest identified through hypothesis-driven or data-driven approaches can be further investigated. Typically, measures summarizing the connectivity properties of the subnetwork, such as its average connectivity strength or the efficiency computed within the subnetwork, can be compared between groups. The alteration of brain structural connectivity within subsystems may involve a reorganization of communication pathways and functional dynamics, and can affect the overall network properties. The characterization of the topological role of brain cores across conditions might help elucidating pathological and developmental mechanisms. In this thesis we propose a measure of subnetwork topological centrality (section 3.3), and we investigate cores centrality and shortest paths layout in schizophrenia and 22q11 deletion syndrome (chapter 4).

## 3.2 *Background*

### **Network attack for resilience and centrality assessment**

#### 3.2.1 **Network resilience**

The study of network resilience to lesion of some of its elements (nodes or edges), is of central interest in many domains of applied network theory (Newman, 2010). Network resilience has been extensively investigated in communication systems, power grids or social networks. For instance, it is important to quantify how a wireless communication system behaves after the breakdown of one or more of its routers, to characterize phenomena such as disease spreading in population networks, or to predict the impact of stroke or traumatic brain injury on the overall brain network connectivity. These questions can be (partially) answered through resilience analysis and simulated network attack.

### *Types of network attack*

Network resilience is traditionally evaluated for two extreme cases: failure (*aka* random attack) and targeted attack. A **random attack** is the damage of a fraction of randomly selected network elements. A **targeted attack** is the damage of a fraction of network elements selected by decreasing order of some element-wise centrality value (*e.g.* degree, betweenness, eigenvector centrality or other measures (Iyer *et al.*, 2013; Newman, 2010)). Moreover, single- and variable-ranking strategies for targeted attack have been investigated (Dall’Asta *et al.*, 2006; Holme *et al.*, 2002). In the first case the elements’ centrality ranking is computed on the original network, and a fraction  $f$  of elements is removed all at once. In the second case the elements are removed one by one, and the centrality ranking is recursively recalculated after each element removal. The variable-ranking attack strategy has been shown to be more harmful than the single-ranking removal (Dall’Asta *et al.*, 2006). The parameters that characterize a network attack are therefore **(i)** the type of removed elements (nodes or edges), **(ii)** the fraction  $f$  of removed network elements, and **(iii)** the strategy adopted for elements removal.

### *Characterization of network resilience*

The network resilience is understood as the ability of the system to maintain its connectivity properties after the deletion of a fraction of its elements. It is typically quantified by computing some topological measure on the lesioned network (Newman, 2010). In a resilience analysis the behaviour of network topological measures is investigated for different attack strategies as a function of the fraction  $f$  of removed elements. Historically, network resilience has been characterized by evaluating the diameter, the characteristic path length, the size of the largest connected component, or the average size of the connected components of the lesioned network (Albert *et al.*, 2000; Callaway *et al.*, 2000) (for further details about listed network measures we refer to (Rubinov & Sporns, 2010)). The use of the network efficiency rather than the characteristic path length is better suited to assess the network resilience when high fractions of elements are removed, resulting in relatively fractionated systems (Crucitti *et al.*, 2003). The use of topological measures of integration such as network communicability (Estrada & Hatano, 2008) have as well been proposed (Andreotti *et al.*, 2014; Estrada *et al.*, 2012). Topological measures of local connectedness (*e.g.* the local efficiency) also proved to be affected by network damaging (Crucitti *et al.*, 2003). Different topological measures can lead to relatively different characterizations of network resilience (Holme *et al.*, 2002).

### *Resilience of benchmark networks*

The resilience of a network to targeted attack and failure depends on subtle features of the dynamics taking place in the modelled system. Nevertheless, at a first level of analysis the resilience depends on static topological characteristics of the network under investigation, and first of all on its **degree distribution** structure. **Random networks** with binomial degree distribution (Erdős–Rényi model) are particularly robust to both targeted and random attack, while **scale-free networks** demonstrate low resilience to targeted attack. A scale-free network is defined such that its degree histogram  $P(k)$  follows a power-law distribution ( $P(k) \sim k^{-\gamma}$ , with  $k$  nodal degree), and counts a small fraction of highly connected hubs. Indeed the presence of hubs introduces into the network weak elements in terms of resilience.

In their seminal paper, Albert and colleagues investigated the resilience to targeted and random attacks of a random network, a scale-free network, the Internet and the World-Wide Web network (Albert *et al.*, 2000). Figure 3.2 illustrates the network diameter behaviour of the exponential ( $E$ ) and scale-free ( $SF$ ) networks for different levels  $f$  of damage. The removal of a small fraction of elements logically increases the network diameter. For the random network, the increase of network diameter is slow and linear for both targeted attack and failure. For the

scale-free network, the increase of diameter after targeted attack is much steeper, doubling its original value when only 5% of the nodes are removed. This low resilience to targeted attack is rooted in the inhomogeneity of the *SF* degree distribution, shared by many real systems.

Studies compared real systems resilience behaviour with different network models, such as highly/poorly clustered scale-free or small-world models. Substantial differences between the generated curves suggest that network topological properties other than the degree distribution or the clustering level, such as redundancy or modularity, may consistently contribute to the network behaviour under attack (Estrada, 2006, 2007; Newman, 2002; Shargel *et al.*, 2003).

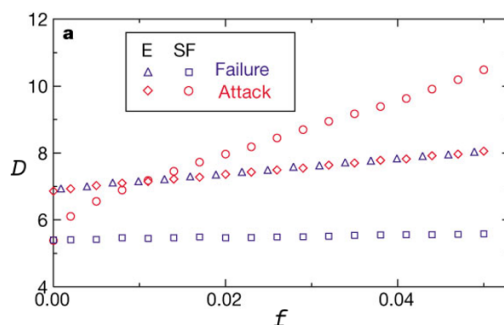


Figure 3.2 – Behaviour of network diameter  $D$  as a function of the fraction  $f$  of removed nodes for the random ( $E$ ) and scale-free ( $SF$ ) network models, in case of failure (blue symbols) and targeted attack (red symbols). Reprinted by permission from Macmillan Publishers Ltd: Nature (Albert *et al.*, 2000), copyright (2000).

### 3.2.2 Brain network attack

#### *Resilience of brain networks*

The resilience of the brain network under targeted or random attack has been characterized for both structural and functional connectomes. Considering their heavy-tailed and heterogeneous degree distributions, brain networks demonstrate a low resilience to attacks targeted towards hub nodes. Conversely, the brain networks are robust to random removal of network elements.

Under targeted lesioning, anatomical brain networks of macaque and cat demonstrate a behaviour similar to scale-free network (Kaiser *et al.*, 2007).

Consistently, the human structural connectivity network is characterized by a poor robustness to targeted attack: the removal of the 25% of the most central nodes entails a reduction of the largest connected component size of the 50% (Alstott *et al.*, 2009).

Similarly, Achard and colleagues investigated the resilience of functional brain networks estimated from resting-state recording (Achard *et al.*, 2006). They showed that the degree distribution of a functional network approximatively follows an exponentially truncated power law, and observed that its resilience to targeted attack is higher than expected for an equivalent scale-free network. Despite the presence of sensitive hubs, peculiar brain topological properties such as its modular structure may confer distinctive benefits in terms of network resilience.

#### *Brain network attack and elements centrality*

In the context of brain networks study, it is of particular interest to understand the impact that the insult of specific brain areas might have on the overall system, and which functional consequences the damage may cause. It is of interest to characterize the impact of WM



or GM focal insults occurring after a stroke, traumatic brain injury, or in multiple sclerosis, for example to predict their implications for a possible recovery. In this sense, the artificial lesioning of a brain network element can characterize its degree of centrality with respect to the overall brain architecture, and its relevance to the overall system functioning. In this section we review approaches to network elements centrality assessment *via* simulated network lesioning.

In their study from 2009, Alstott and colleagues observed that GM lesions of different locations and spatial extensions, differently affect the overall brain network properties and functioning (Alstott *et al.*, 2009). For instance, the insult of network hubs, such as mid-line and parietal regions, has the largest impact on the functional synchronization patterns (Alstott *et al.*, 2009). Moreover, considering the hierarchical, modular structure of the brain system, the deletion of hubs with higher participation coefficient (or inter-module connectors) have a higher impact on (simulated) functional dynamics than the deletion of peripheral hubs (Honey & Sporns, 2008).

Recently, Irimia and colleagues, and Reus and colleagues, have characterized the degree of centrality of different brain areas by repetitively applying targeted attacks towards single network elements.

The work by Irimia and colleagues is centred on the identification of a set of WM edges (a core scaffold) whose lesioning is highly critical to network structure, leading to significant changes of network properties (Irimia & Van Horn, 2014). The core scaffold includes WM tracts interconnecting primary and secondary visual, primary somatosensory, anterior cingulate and middle-inferior temporal cortices.

The study by Reus and colleagues (de Reus & van den Heuvel, 2014) is as well centred on the characterization of edge-wise selective attack with respect to the overall system properties, with a particular attention towards the type of network topological measure used to quantify the impact of a lesioning. The edges with an high impact on the overall system functioning (whose removal cause a consistent reduction of network communicability) are concentrated around (even though do not limit to) the brain network hubs and the brain medial line (figure 3.3). The authors underlie that the entity of the topological impact of single-element network lesioning highly depends on the metrics chosen to quantify such effect. In this sense, the network communicability (Estrada & Hatano, 2008) might be a measure better suited for the characterization of single-element lesioning than the characteristic path length.

Taken together these studies suggest that the centrality of single network elements for the maintenance of brain system integrative properties is related to the interplay of different topological characteristics of the overall network, such as degree distribution and modular structure, and that network attack might be a suitable instrument for the study of these complex interplays. In this thesis we push forward the network lesioning approach to the investigation of brain subnetworks, extending the analysis of single network elements centrality to the characterization of subnetworks topological role within the brain complex system.

### 3.3 *Methods*

#### **Subnetwork topological centrality**

In this section we introduce a new measure of subnetwork topological centrality. The term subnetwork refers to a subset of network nodes and to all the edges linking the nodes of the subset.

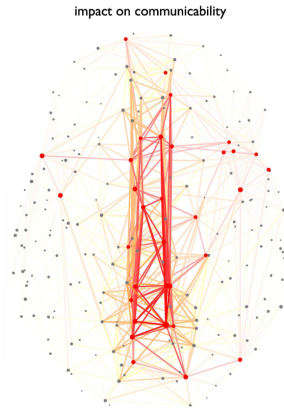


Figure 3.3 – White matter edge centrality from selective network lesioning. This figure represents the importance of individual WM tracts for overall network communicability as quantified by (Estrada & Hatano, 2008). The most important connections are the most opaque and red-colored. Adapted from (de Reus & van den Heuvel, 2014).

We define the **subnetwork topological centrality**  $\zeta$  as the network efficiency loss after a targeted attack towards the subnetwork itself, with respect to a reference distribution. The reference distribution describes the network efficiency loss after random attacks towards (randomly selected) network elements. In our model, the number of elements (nodes and edges) deleted during the random attacks matches the number of elements lesioned during the targeted attack.

We expect  $\zeta$  to vary as function of the size  $f$  and on the mixing rate  $q$  of the investigated subnetwork. The mixing rate expresses the ration of low/high degree nodes included in the subnetwork. Conceptually,  $\zeta$  characterizes the topological importance of a subnetwork of interest within the overall network in terms of maintenance and contribution to overall network integration properties.

In section 3.3.1 we formally define the subnetwork topological centrality for binary and weighted undirected networks. Next, we characterize the measure  $\zeta$  for a set of  $(f, q)$  values, for different benchmark networks: the Erdős–Rényi model, the scale-free model, the structural brain anatomical network, and a randomized version of the brain network. In order to sample subnetworks with given  $(f, q)$  values, we need to introduce an original hybrid attack procedure (section 3.3.2). Finally, and as a proof of concept, we assess the topological centrality of well known brain functional circuits and clubs (section 3.3.3).

### 3.3.1 Definition

Let's consider a binary undirected graph  $G = (V, E)$ , with nodes  $V = \{v_1, \dots, v_n\}$  and edges  $E = \{e_{ij}, \dots, e_{kl}\}$ , specified by an adjacency matrix  $A$  with  $a_{ij} = 1$  if nodes  $v_i$  and  $v_j$  are connected,  $a_{ij} = 0$  otherwise. The distance between each pair of nodes  $(v_i, v_j)$  is the number of edges in a shortest path  $g_{i \leftrightarrow j}$  connecting them:

$$d_{ij} = \sum_{a_{ij} \in g_{i \leftrightarrow j}} a_{ij}.$$

Let's consider now a non-null subgraph  $H = (V', E')$  of  $G$ , with order  $(|V'| = m) < (|V| = n)$ . The vertex set  $V'$  of  $H$  is a subset of the vertex set  $V$  of  $G$ , and the adjacency relation  $A'$  of  $H$  is a subset of that of  $G$  to the subset  $V'$ .

We quantify the resilience of the network  $G$  to a targeted attack towards the subnetwork  $H$  as the efficiency

$$Eff_H = \frac{1}{n-m} \sum_{i \in V_H} \frac{\sum_{j \in V_H, i \neq j} d_{ij}}{n-m-1}$$

of  $G$  after the deletion of the set of nodes  $V'$  and relative edges, with  $V_H = V \setminus V'$  set difference of  $V$  and  $V'$ .

Let  $(m, p)$  be the number of nodes and edges removed from the overall network during the targeted attack toward  $H$ .

To quantify the topological centrality of a subnetwork  $H$  within the overall network, we compare the resilience of  $G$  to an attack towards  $H$ , with a suitable reference distribution. The reference distribution is built by repeating  $n_{iter}$  times a random attack procedure toward an equal number of network resources. Therefore, and consistently with the targeted attack, each random attack entails the deletion of exactly  $m$  nodes and  $p$  edges from the original network.  $n_{iter}$  should be large enough (e.g.  $n_{iter} = O(100)$  or  $n_{iter} = O(1000)$ ) in order to reliably estimate the reference distribution. After each random attack, the efficiency  $Eff_{rand}$  of the lesioned network is computed. The repeated random attack procedure provides an estimate of the statistical distribution  $P(Eff_{rand})$  of network efficiency after the random removal of a fixed amount of network resources ( $m$  nodes and  $p$  edges).

The topological centrality of the subnetwork  $H$  is defined as

$$\zeta_H = \frac{Eff_H - \mu[Eff_{rand}]}{\sigma[Eff_{rand}]},$$

with  $\mu[Eff_{rand}]$ ,  $\sigma[Eff_{rand}]$  expectation and standard deviation of  $P(Eff_{rand})$ .

A value of  $\zeta_H$  significantly lower than zero indicates that the targeted attack towards  $H$  is more deleterious than by chance. Conceptually,  $\zeta_H$  quantifies the topological relevance of a subnetwork  $H$  of  $G$  for the maintenance of the overall network efficiency. We stress that the null model for the random attack is matched with the targeted attack in terms of (i) number of removed nodes, and (ii) number of removed edges. The procedure for the computation of  $\zeta$  is graphically summarized in figure 3.4.

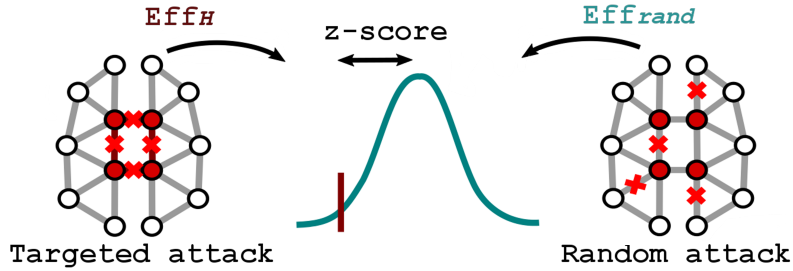


Figure 3.4 – Schematic representation of the subnetwork topological centrality computation. The left and right graphs represent a targeted and a matched random attack. After each attack, the efficiency of the lesioned network is computed. Repeated random attacks allow estimating an efficiency reference distribution. The subnetwork topological centrality  $\zeta$  is computed as the z-score of the efficiency after targeted attack with respect to the reference distribution. Adapted from (Vasa *et al.*, 2015).

We next extend the definition of  $\zeta$  to weighted, undirected networks.

Let's consider a weighted, undirected network  $G^w = (V, E)$ , specified by an adjacency matrix  $A^w$  with  $a_{ij} = w_{ij}$  if nodes  $v_i$  and  $v_j$  are connected,  $a_{ij} = 0$  otherwise.  $w_{ij} \in \text{Re}^+$  represents the

connectivity strength between nodes  $v_i$  and  $v_j$ . Equivalently, a subnetwork  $H^w = (V', E')$  of  $G^w$  is specified by an adjacency matrix  $A'^w$ , subset of  $A^w$ . The weighted distance  $d_{ij}^w$  between each pair of nodes  $(v_i, v_j)$  is the sum of the weights of the edges in a (weighted) shortest path  $g_{i \leftrightarrow j}^w$  connecting them. The weighted efficiency  $Eff^w$  is defined equivalently to the binary efficiency  $Eff$ , by substituting  $d_{ij}$  with the weighted distance  $d_{ij}^w$  (for further details we refer to (Rubinov & Sporns, 2010)).

A targeted attack towards a (weighted) subnetwork of interest  $H^w$  entails the removal of  $m$  nodes and  $p$  edges from the original network, resulting in an overall loss of connectivity strength

$$W_H = \sum_{e_{ij} \in E_m} w_{ij},$$

with  $E_m$  set of edges connected to the nodes  $V'$  of  $H^w$ . Note that the set  $E_m$  includes edges connecting nodes of  $H^w$  between them, and with the rest of the network.

We define a random attack matched to the targeted attack towards the weighted subnetwork  $H^w$  as the deletion of an equal number  $m$  of nodes, and of an overall connectivity strength  $W_H \pm \varepsilon$ . The tolerance level  $\varepsilon$  should be set *a priori*, for example as a percentage of the average nodal strength of the network.

After each network attack, the (weighted) efficiency of the lesioned network is computed, allowing to evaluate the (weighted) subnetwork topological centrality

$$\zeta_{H^w}^w = \frac{Eff_{H^w}^w - \mu[Eff_{rand}^w]}{\sigma[Eff_{rand}^w]}.$$

As a practical consideration, the random attack procedure can be performed in two steps. First,  $m$  randomly selected nodes are deleted from the original network. The deletion entails the removal of a given set of edges  $E_{m,random}$  with overall connectivity strength  $W_{E_{m,random}}$  ( $W_{E_{m,random}}$  corresponds to the number of removed edges for a binary network). As a second step, extra edges are randomly added to, or removed from the lesioned network until the value  $W_H$  is matched up to a given tolerance level  $\varepsilon$  ( $\varepsilon$  can be set to zero for binary networks).

We also mention that the choice of the network efficiency measure for the quantification of the network damage after attack is robust to network fragmentation (Crucitti *et al.*, 2003). As opposed to the characteristic path length, the network efficiency is well-defined also for disconnected graphs. It is therefore possible to compute the topological centrality  $\zeta$  for subnetworks of large size, whose removal can potentially disconnect the original network. Anyway, the topological centrality measure (and the efficiency measure in general) can be unstable for extreme network fragmentation. The average size  $\langle s \rangle$  of the connected components after network attack is a good measure of network fragmentation. In the following we will investigate the topological centrality of subnetworks whose removal doesn't reduce the average size  $\langle s \rangle$  of connected components below the 2% of the original network size.

### 3.3.2 Characterization

In this section we characterize the subnetwork topological centrality measure for four distinct binary undirected networks (benchmark networks), namely a brain structural network  $BN$ , its randomized version  $RN$ , an Erdős–Rényi network  $ER$ , and a scale-free network  $SF$ .

### Benchmark networks

The **structural brain network** was estimated from the diffusion-based anatomical connectivity of 40 healthy subjects. The considered group-representative brain network  $BN$  counts  $n = 82$  nodes, corresponding to 68 cortical and 14 subcortical regions, and according to the Desikan-Killiany atlas (Desikan *et al.*, 2006). An edge was included in the group-wise  $BN$  if present in at least the 80% of the 40 subjects.  $BN$  is an undirected binary graph, with no self-loops and density (i.e. number of edges over the total number of possible edges  $n(n-1)$ )  $\delta \approx 0.2$  (table 3.1). We obtained a **randomized version**  $RN$  of the  $BN$  network by recursive swapping of the brain network edges, as described in (Maslov & Sneppen, 2002). The network  $RN$  has the same degree sequence of the group-wise brain network (see figures 3.5c, 3.6c), but randomized structure.

For a matter of comparison, the **Erdős–Rényi random graph**  $ER$  and the **scale-free random graph**  $SF$  were built in order to have the same number of nodes  $n$  and approximately the same density  $\delta$  as the human brain network.  $ER$  was built according to the model  $G(n, m)$ , i.e. drawn uniformly at random from the collection of all graphs which have  $n$  nodes and  $m$  edges, with  $m = \delta n(n-1)$ . The  $ER$  graph was symmetrized with respect to the main diagonal in order to obtain an undirected binary network, and self-loops were avoided.

For the scale-free model, we generated a network  $SF$  with  $n = 82$  nodes and fixed degree sequence  $P(k) \sim k^{-\alpha}$ , setting  $\alpha = 2.2$ . We should mention here that a variety of real networks, such as the Internet, demonstrate a degree sequence that approximately follows a power-law distribution  $P(k) \sim k^{-\alpha}$ , with  $\alpha$  typically bounded between 2 and 3 (Newman, 2010). Moreover, the brain network has been associated with power-law (Kaiser *et al.*, 2007) or exponentially-truncated power-law degree distributions (Achard *et al.*, 2006).

All the investigated networks are composed of one single connected component.

Figures 3.5, 3.6, 3.7 and 3.8 picture the adjacency matrix and the degree sequence (linear and log-log scale) of the four considered networks: **brain network** ( $BN$ ), **randomized network** ( $RN$ ), **Erdős–Rényi** ( $ER$ ), and **scale-free** ( $SF$ ). Table 3.1 reports the main topological properties of the investigated networks. We observe that the four networks have approximately equivalent density  $\delta$ , and similar global efficiency  $Eff$ . The brain network and the Erdős–Rényi network have a higher clustering level than the randomized and scale-free networks. Compared to the other networks, the brain network is modular (higher  $Q$ ) and small-world ( $sw > 1$ ).

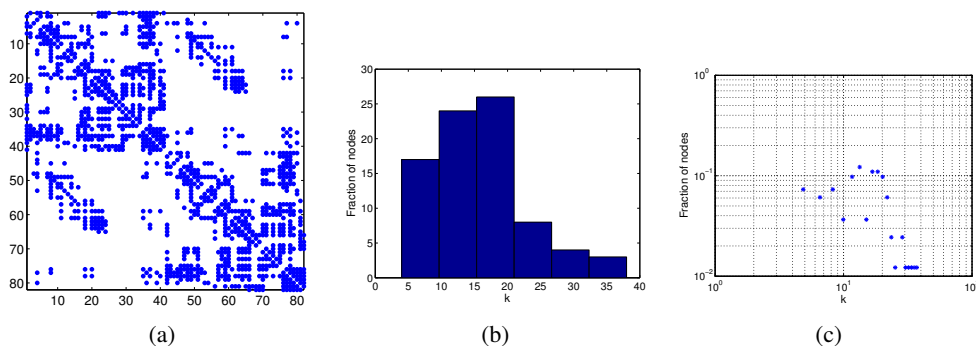


Figure 3.5 – Structural brain network  $BN$ : (a) adjacency matrix; (b) degree sequence; (c) degree sequence in log-log scale.

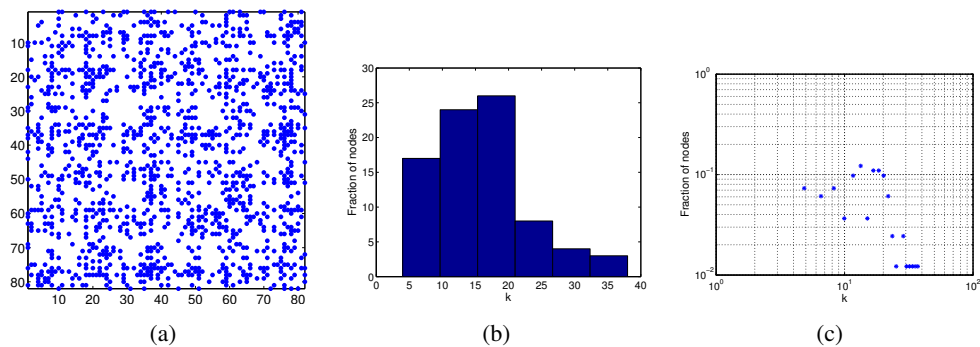


Figure 3.6 – Randomized structural brain network  $RN$ : (a) adjacency matrix; (b) degree sequence; (c) degree sequence in log-log scale. Note that the degree sequence of the  $RN$  network is equal to the degree sequence of the  $BN$  network.

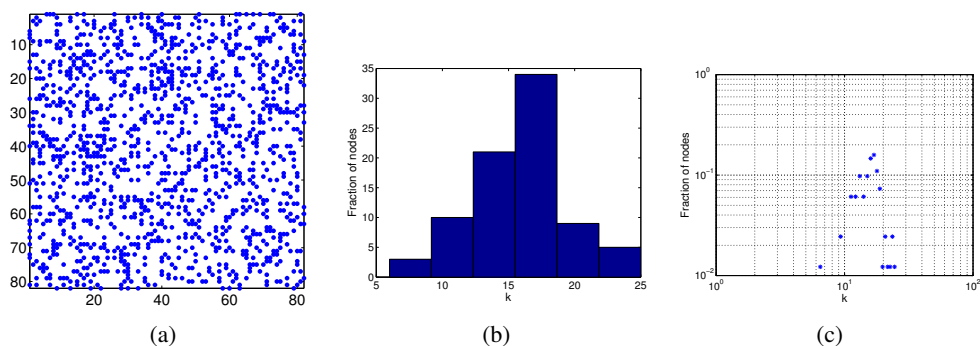


Figure 3.7 – Erdős-Rényi network  $ER$ : (a) adjacency matrix; (b) degree sequence; (c) degree sequence in log-log scale (approximately Poisson-distributed).

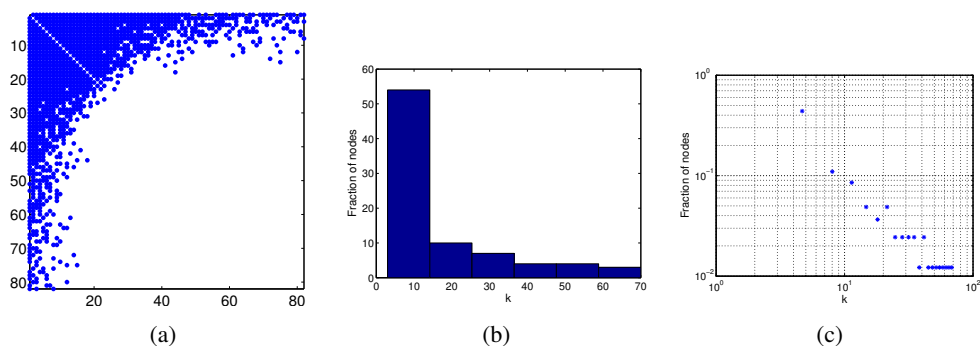


Figure 3.8 – Scale-free network  $SF$ : (a) adjacency matrix; (b) degree sequence; (c) degree sequence in log-log scale (power-law distribution).

Topological measure	$BN$	$RN$	$ER$	$SF$	$BN_{hr}$
$\delta$	0.196	0.196	0.198	0.196	0.076
$C$	0.585	0.199	0.891	0.285	0.524
$Eff$	0.554	0.593	0.596	0.585	0.495
$Q$	0.393	0.195	0.142	0.190	0.509
$sw$	1.923	0.976	1.001	1.011	3.465

Table 3.1 – Topological properties of the brain ( $BN$ ), the randomized brain ( $RN$ ), the Erdős–Rényi ( $ER$ ) and the scale-free ( $SF$ ) networks. The last column reports the topological measures for a binary brain network  $BN_{hr}$  from high-resolution cortical parcellation (1014 nodes), described in section 3.3.  $\delta$ : network density;  $C$ : average clustering coefficient;  $Eff$ : efficiency;  $Q$ : modularity;  $sw$ : small-world index.  $Q$  was evaluated by repeating the Louvain algorithms 100 times and selecting the best solution (higher  $Q$  value).  $sw$  was computed by comparing the average clustering coefficient and the characteristic path length of the benchmark of interest with randomized networks obtained from repeated edge-swapping (Maslov & Sneppen, 2002) and with equivalent degree distributions. For topological measures expression we refer to (Rubinov & Sporns, 2010).

### Hybrid network attack

We characterize the topological centrality of a subnetworks  $H$  for different benchmark networks, and for different sizes and compositions of  $H$ . Particularly, we consider subnetworks of different relative sizes  $f$ , with different degree mixing rates  $q$ .  $f$  is defined as the **relative number of nodes** composing the subnetwork (i.e. fraction  $f$  of nodes deleted during a network attack). The **degree mixing rate**  $q$  quantifies the proportion of higher and lower degree nodes included in the subnetwork, and is specified in relation to an hybrid attack procedure defined hereafter.

In order to sample from a network  $G$  a subnetwork  $H$  with fixed parameters  $(f, q)$ , we define a new strategy for network attack, named **hybrid network attack (HYB)**. In the **HYB** attack procedure nodes are removed one by one. Each time a step of the **Random Node ( $rn$ ) sampling** is performed with probability  $q$ , while a step of the **Targeted Node ( $tn$ ) sampling** is performed with probability  $(1 - q)$ . In the  $tn$  sampling, nodes are selected according to their degree ranking. In the  $rn$  sampling each node has equal probability to be selected. The node degree ranking is computed only at the beginning of the attack procedure, and it is not updated recursively at each step.

One should note that setting  $q = 0$  corresponds to perform a targeted attack towards a fraction  $f$  of network hubs, while setting  $q = 1$  is equivalent to perform a random attack towards a fraction  $f$  of randomly selected nodes. The parameter  $q$  tunes the degree mixing rate of the attacked subnetwork. The hybrid attack strategy allows selecting subnetworks of different compositions, and exploring the behaviour of networks under attack over a range of intermediary conditions between the targeted and the random attack extreme cases.

We assessed the average degree  $\bar{k}$  of sampled subnetworks for different values of  $f$  (fraction of removed nodes) and  $q$  (mixing rate, i.e. switching probability between  $tn$  and  $rn$  node selection) (figure 3.9). The mean degree values in the figure represent the average over  $n_{rep} = 100$  repetitions of the hybrid attack procedure, for each  $(f, q)$  parameters combination.  $q$  values are

encoded by the curve color, with dark red corresponding to  $q = 0$  (targeted attack) and dark blue corresponding to  $q = 1$  (random attack). For the mixing rate, we considered the following values:

$$\underline{q} = [0, 0.1, 0.2 \dots 1].$$

For the number  $m$  of removed nodes we considered the following values:

$$\underline{m} = [1, 2 \dots 66],$$

corresponding to  $0 < f \leq 0.8$ .

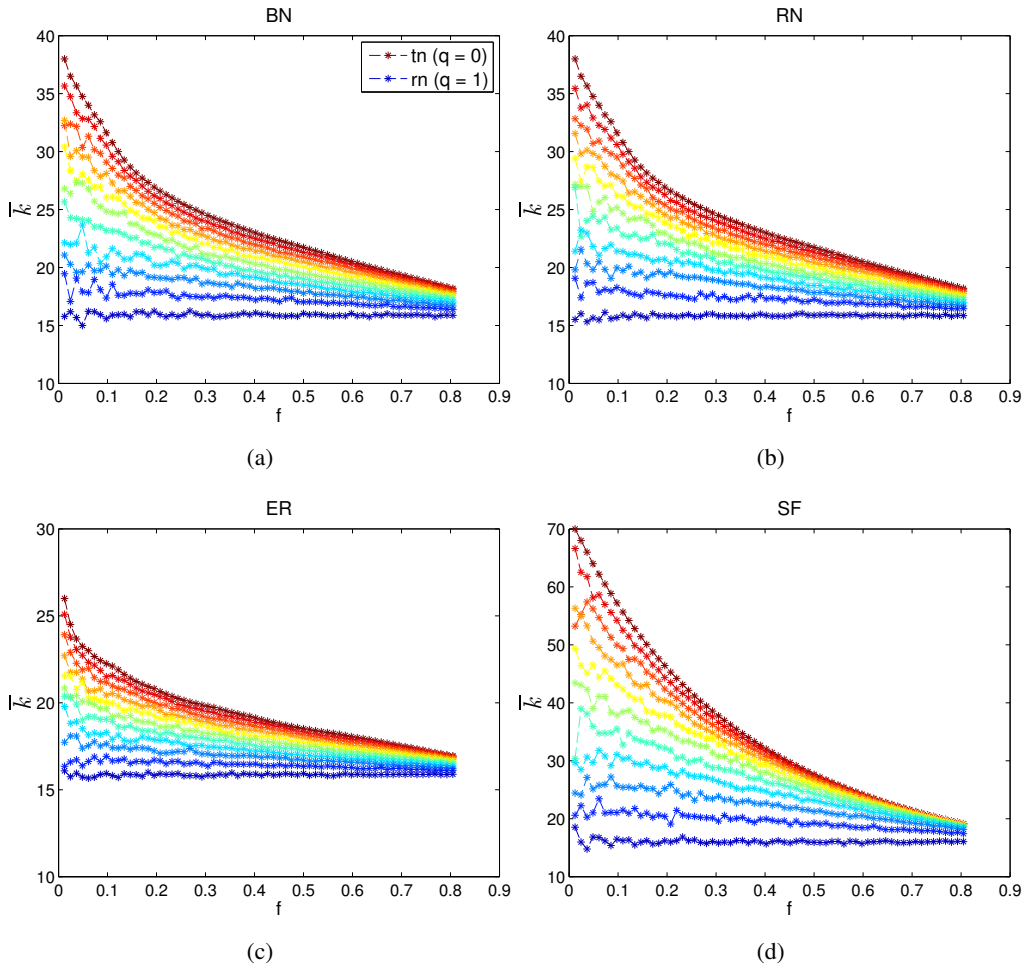


Figure 3.9 – Average degree for hybrid attack. The plots represent the mean degree  $\bar{k}$  of the removed subnetworks during hybrid attacks, for different combinations of the  $(f, q)$  parameters. The subnetwork size  $f$  is represented on the  $x$ -axis; the subnetwork mixing rate  $q$  is encoded in the color scale, with dark red corresponding to targeted attack ( $q = 0$ ) and dark blue corresponding to random attack ( $q = 1$ ). The represented  $\bar{k}$  values are the average over  $n_{rep} = 100$  repetitions of the hybrid sampling *HYB*, for each  $(f, q)$  parameters combination. Hybrid attacks were performed on the brain *BN* (a), the randomized brain *RN* (b), the Erdős–Rényi *ER* (c) and the scale-free *SF* (d) networks.



### *Network resilience under hybrid attack*

Before considering the subnetwork topological centrality measure, and for a matter of completeness, we first characterize the behaviour of the Erdős–Rényi, scale-free, brain and randomized networks under the attack towards a fraction  $f$  of nodes, with different degree mixing rates  $q$ .

Figures 3.10, 3.11 and 3.12 represent the **efficiency**  $Eff$ , the size of **largest connected component**  $S$ , and the **average size of connected components**  $\langle s \rangle$  of the lesioned networks, as a function of the fraction  $f$  of removed nodes ( $x$ -axis), and of the degree mixing rate  $q$  (color scale).  $Eff$ ,  $S$  and  $\langle s \rangle$  are classical measures used to quantify the network damage after an attack (Albert *et al.*, 2000; Crucitti *et al.*, 2003; Newman, 2010).

Considering the two extreme curves ( $q = 1$ ) (random attack) and ( $q = 0$ ) (targeted attack), our results are in line with previous literature. The brain network  $BN$  demonstrates a high resilience to random attack, equivalently to the exponential and scale-free networks, and an intermediate behaviour in response to targeted attack.

When exposed to targeted attack ( $q = 0$ , dark red curve), the network efficiency  $Eff$  is decreased to the 50% of its original value when only the  $\sim 10\%$  of nodes is removed from the  $SF$  network, but it is necessary to remove the  $\sim 75\%$  of nodes to get a similar effect on the  $ER$  network. The efficiency of the brain network  $BN$  is reduced of 50% when the  $\sim 50\%$  of nodes is removed, globally in line with previous observations (Achard *et al.*, 2006; Alstott *et al.*, 2009).

Around  $f = 50\%$ ,  $q = 0$ , the brain network also experiences a drop of  $S$  and  $\langle s \rangle$  values, indicating network fragmentation. The  $SF$  network gets fragmented when very few nodes are removed, with a drop of  $S$  and  $\langle s \rangle$  values for  $f = 4 - 5\%$  ( $q = 0$ ).

For the  $ER$  network, targeted attack,  $S$  and  $\langle s \rangle$  curves diverge from the linear behaviour characterizing the random attack only for  $f \simeq 70\%$ . The resilience to targeted and random attack of the randomized network  $RN$  is similar but not equal to the resilience of the brain network  $BN$  (see in particular figures 3.12a, 3.12b), indicating that the degree distribution is not the only factor influencing the brain network resilience.

The curves included between the ( $q = 0$ ) and ( $q = 1$ ) lines portrait the resilience of the four networks for different degree mixing rates (figures 3.10, 3.11, 3.12). Figure 3.13 highlights the dependency of  $Eff$  on  $q$  for different, fixed  $f$  values.

For small values of  $f$ , the mixing rate  $q$  has little or no influence on the efficiency drop for all the considered networks (figure 3.13a). However, even for small values of  $f$  the scale-free network experiences a linear decrease of  $Eff$  as function of  $q$ . For instance, for  $f = 5\%$  the  $SF$  efficiency drops of approximately the 20% for targeted attack, and of the 10% for a mixed attack with  $q = 0.4$  (figure 3.13a). For higher  $f$  values, the relationship between  $Eff$  and  $q$  for the  $SF$  network becomes exponential, with a rapid efficiency drop when moving from random to targeted attack. The scale-free network is highly sensitive to the degree mixing rate  $q$ .

For growing values of  $f$ , the relationship between  $Eff$  and  $q$  is linear with growing slope for the brain and randomized networks, which show a similar behaviour.

It is interesting to note that, although the Erdős–Rényi network is highly resilient to both random and targeted attacks, it shows as well a linear relationship between  $Eff$  and  $q$ , for growing  $f$  values (figures 3.13b, 3.13c, 3.13d).

### *Subnetwork topological centrality*

In section 3.3.1 we defined the topological centrality measure  $\zeta$  for a subnetwork of interest as the efficiency z-score after targeted attack towards the subnetwork itself, compared to a reference distribution obtained from repeated random attacks. The main idea underlying the definition of  $\zeta$  is to quantify the topological relevance of a subnetwork (with variable size and composition) for the maintenance of the overall efficient network communication. We can expect that  $\zeta$  will

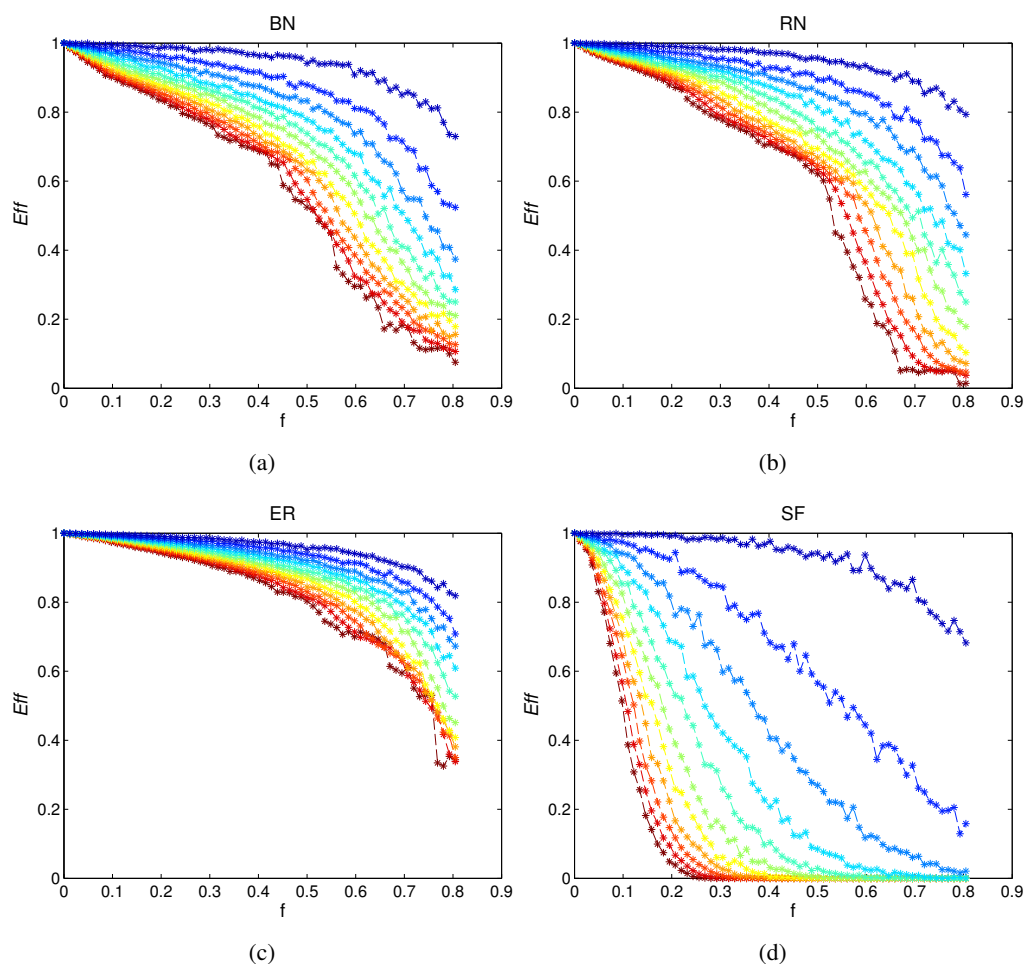


Figure 3.10 – Network resilience to hybrid attack as quantified by means of the efficiency  $Eff$  of the lesioned network. The resilience of the brain  $BN$  (a), the randomized brain  $RN$  (b), the Erdős–Rényi  $ER$  (c) and the scale-free  $SF$  (d) networks is investigated as a function of the removed subnetwork size  $f$  ( $x$ -axis) and degree mixing rate  $q$  (color-coding, with dark red corresponding to  $q = 0$  and dark blue corresponding to  $q = 1$ ). The represented  $Eff$  values are the average over  $n_{rep} = 100$  repetitions of the hybrid attack, for each  $(f, q)$  parameters combination.  $Eff$  values are normalized with respect to the original network efficiencies reported in table 3.1.

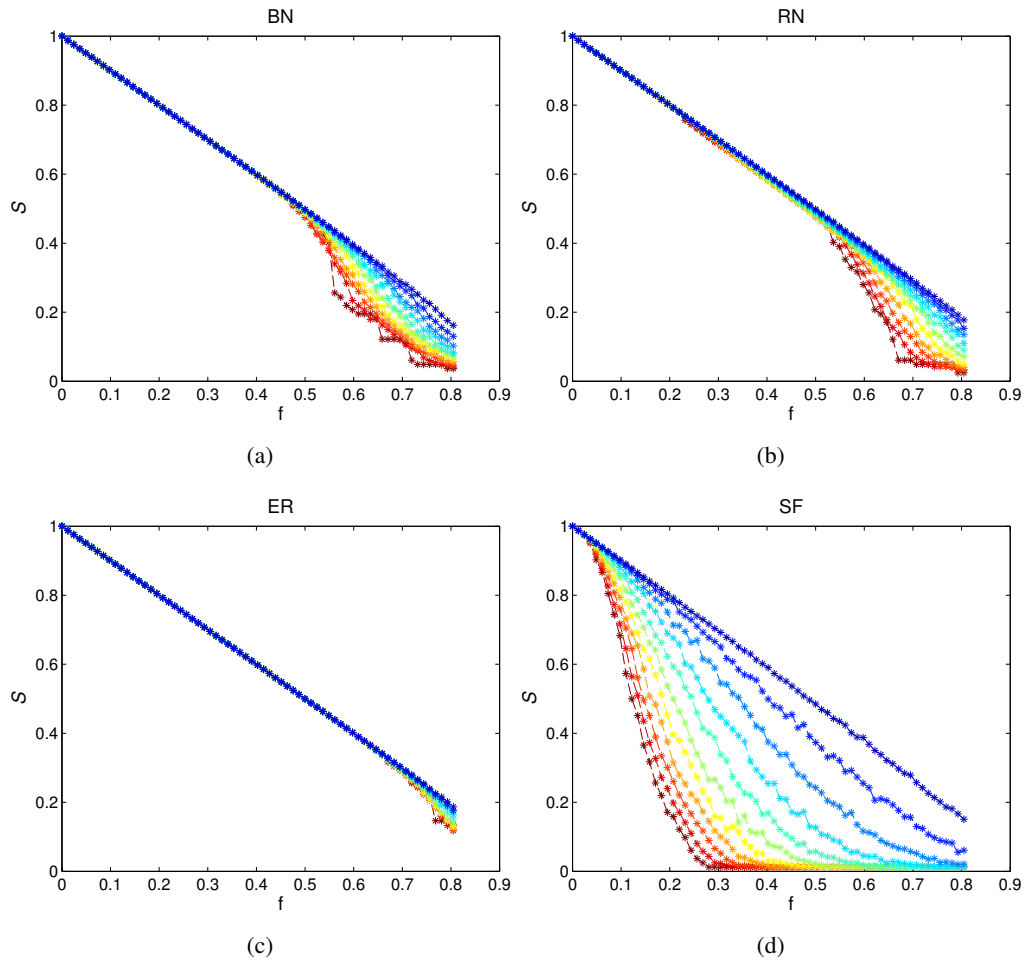


Figure 3.11 – Network resilience to hybrid attack as quantified by means of the size  $S$  of largest connected component in the lesioned network. The resilience of the brain  $BN$  (a), the randomized brain  $RN$  (b), the Erdős-Rényi  $ER$  (c) and the scale-free  $SF$  (d) networks is investigated as a function of the removed subnetwork size  $f$  ( $x$ -axis) and degree mixing rate  $q$  (color-coding, with dark red corresponding to  $q = 0$  and dark blue corresponding to  $q = 1$ ). The represented  $S$  values are the average over  $n_{rep} = 100$  repetitions of the hybrid attack, for each  $(f, q)$  parameters combination.  $S$  values are normalized with respect to  $n$ , number of nodes in the original network.

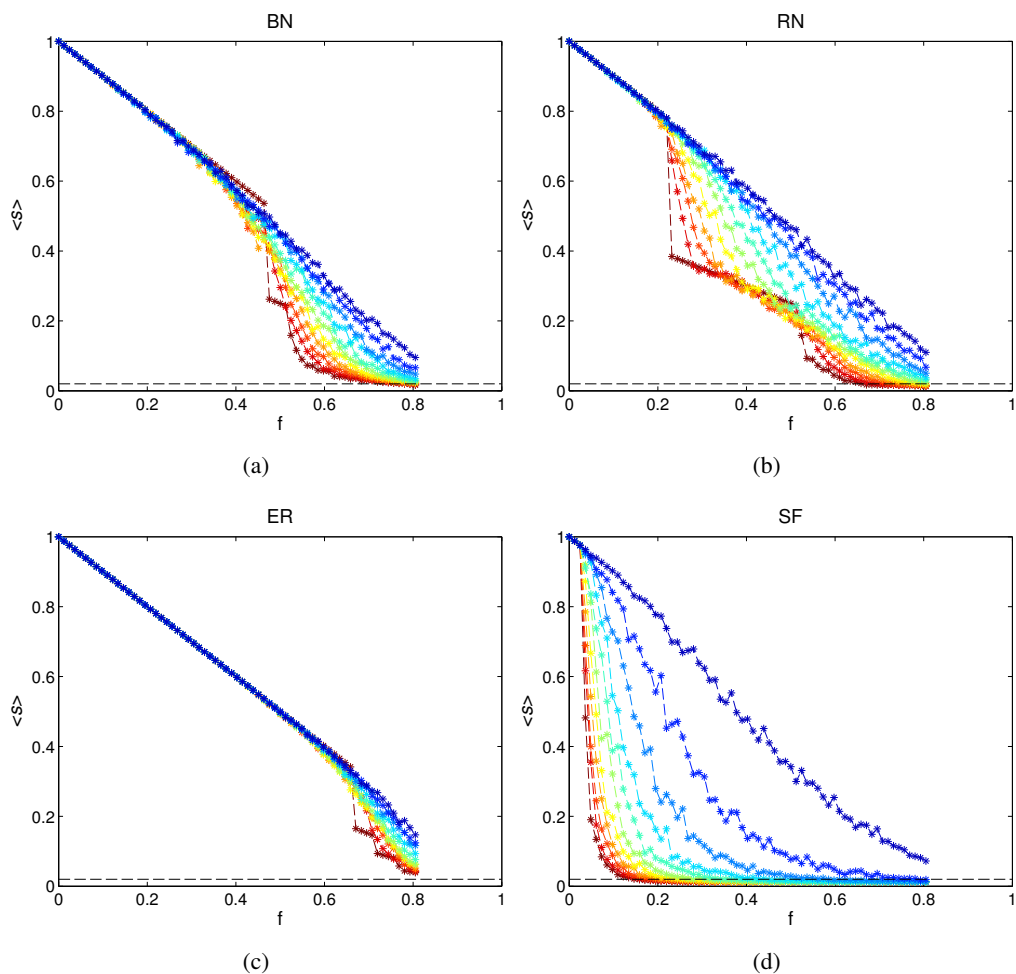


Figure 3.12 – Network resilience to hybrid attack as quantified by means of the average size of connected components  $\langle s \rangle$  in the lesioned network. The resilience of the brain *BN* (a), the randomized brain *RN* (b), the Erdős–Rényi *ER* (c) and the scale-free *SF* (d) networks is investigated as a function of the removed subnetwork size  $f$  ( $x$ -axis) and degree mixing rate  $q$  (color-coding, with dark red corresponding to  $q = 0$  and dark blue corresponding to  $q = 1$ ). The represented *Eff* values are the average over  $n_{rep} = 100$  repetitions of the hybrid attack, for each  $(f, q)$  parameters combination.  $\langle s \rangle$  values are normalized with respect to  $n$ , number of nodes in the original network. Note that the horizontal dotted lines represent an average connected components size  $\langle s \rangle$  equal to 5% of the original network size  $n$ .

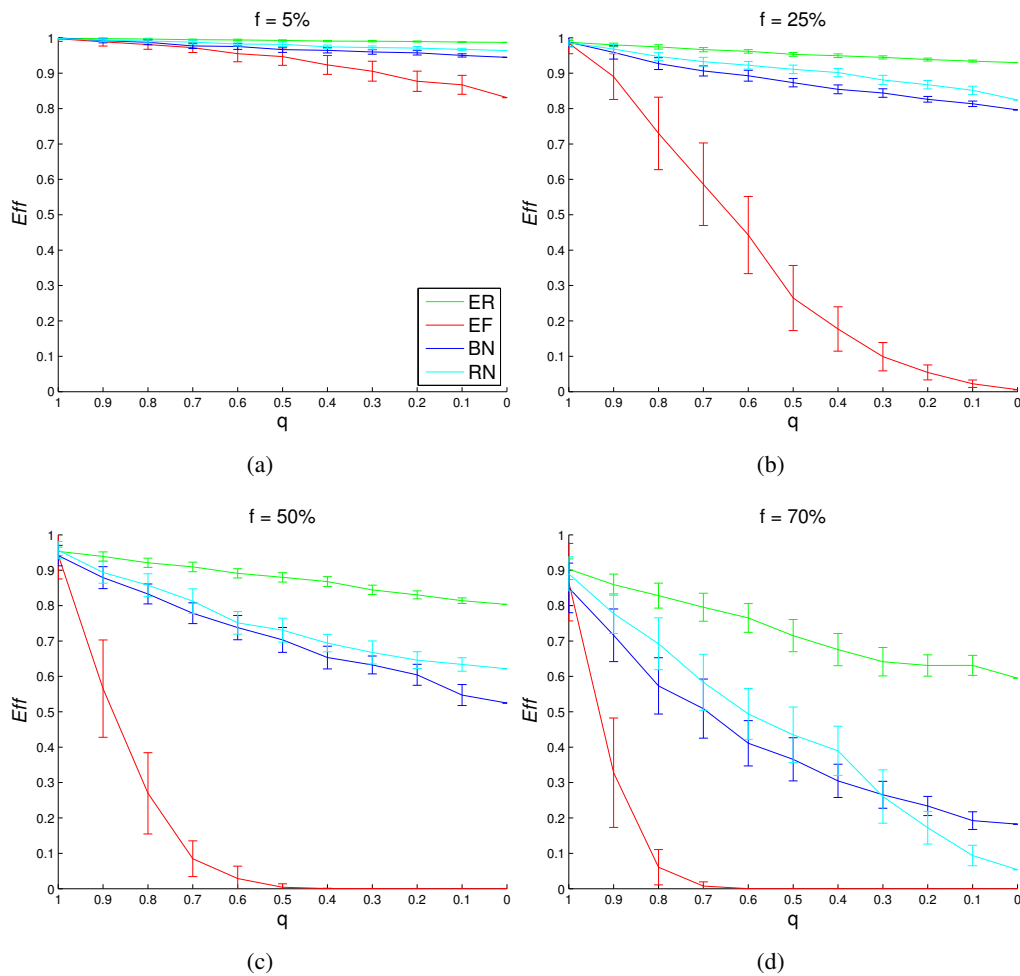


Figure 3.13 – Degree mixing rate - efficiency curves for fixed  $f$  values ( $f = 5\%$ (a),  $25\%$ (b),  $50\%$ (c),  $70\%$ (d)), for the four benchmark networks ( $ER, SF, BN, RN$ ). The plots represent the efficiency  $Eff$  computed on the lesioned networks after hybrid attack, as function of the degree mixing rate  $q$ , with  $q = 1$  corresponding to random attack and  $q = 0$  corresponding to targeted attack. The vertical bars indicate the standard deviation of the efficiency values over  $n_{perm} = 100$  repetitions of the hybrid attack, for each  $(f, q)$  parameters combination.  $Eff$  values are normalized with respect to the original network efficiencies reported in table 3.1.

depend on the composition of the subnetwork under investigation, and in particular on its size and degree mixing rate,

Here, we investigate the dependency of  $\zeta$  on (i) the size  $f$  and (ii) the mixing rate  $q$  of the subnetwork of interest, for the four reference networks  $BN$ ,  $RN$ ,  $ER$  and  $SF$ . We sample subnetworks from the reference networks for each possible combination of the  $(f, q)$  parameters, and we compute their  $\zeta$  values. This operation is repeated  $n_{iter} = 100$  times, and is summarized in the procedure 3.1. Figure 3.14 represent the average  $\zeta_{(m,q)}$  values over the  $n_{iter} = 100$  repetitions of procedure 3.1, and shows the topological centrality  $\zeta$  of subnetworks with different mixing rates  $q$  and sizes  $f$  (with  $f = n \cdot m$ ,  $n$  number of nodes in the original network).

---

**Procedure 3.1: evaluate  $\zeta$  curves for all  $(m, q)$  combinations**

---

**Input:**  $n_{iter} = 100$ ,  $n_{perm} = 100$

$\underline{m} = [1, 2 \dots (0.8 \cdot n)]$ ,  $\underline{q} = [0, 0.1 \dots 1]$

$\underline{G} = (V, E)$  reference network,  $n = |V|$

**for**  $i = 1 \rightarrow n_{iter}$  **do**

**for all**  $(m, q)$  in  $(\underline{m} \times \underline{q})$  **do**

Remove subnetwork  $\mathbf{H}_{(m,q)}^i$  from  $\mathbf{G}$  (*HYB attack*)

Compute efficiency  $Eff(\mathbf{H}_{(m,q)}^i)$  of lesioned network  $\mathbf{G}$

$d_{(m,q)}^i \leftarrow$  number of removed edges during *hybrid attack*

**for**  $j = 1 \rightarrow n_{perm}$  **do**

Randomly remove subnetwork  $\mathbf{H}_{rand(m)}^{(i,j)}$  from  $\mathbf{G}$  (*random attack*)

$d_{rand(m)}^{(i,j)} \leftarrow$  number of removed edges during *random attack*

**while**  $d_{rand(m)}^{(i,j)} < d_{(m,q)}^i$  **do**

Randomly *remove* one edge from  $\mathbf{G}$

**end while**

**while**  $d_{rand(m)}^{(i,j)} > d_{(m,q)}^i$  **do**

Randomly *add* one edge to  $\mathbf{G}$

**end while**

Compute efficiency  $Eff(\mathbf{H}_{rand(m)}^{(i,j)})$  of lesioned network  $\mathbf{G}$

**end for**

$\mu_{(m,q)}^i \leftarrow$  mean( $Eff(H_{rand(m)}^{(i,j)})$ )

$\sigma_{(m,q)}^i \leftarrow$  standard deviation( $Eff(H_{rand(m)}^{(i,j)})$ )

$\zeta_{(m,q)}^i \leftarrow (Eff(H_{(m,q)}^i) - \mu_{(m,q)}^i) / \sigma_{(m,q)}^i$

**end for**

**end for**

---

We observe that both the **Erdős–Rényi network**  $ER$  and the **randomized network**  $RN$  have a random edges distribution, with no particular modular, hierarchical or clusterized network structure (table 3.1). We therefore expect that none of their subnetworks will present a  $\zeta$  higher than expected by their overall amount of resources alone, as no structure is present in the networks.

In this sense, we can test the null hypothesis  $H_0 : \mu^{Eff} = \mu_0^{Eff}$  that the average efficiency  $\mu^{Eff}$  of a set of subnetworks with parameters  $(f, q)$  is equal to the average efficiency  $\mu_0^{Eff}$  of the reference distribution obtained from (matched) random attacks, for the  $ER$  and  $RN$  networks. In fact **z-statistics** can be directly related to quantiles of the standard normal distribution. The critical  $z$ -values for a 95% confidence level (two-sided alternative hypothesis  $H_1 : \mu^{eff} \neq \mu_0^{Eff}$ ) are **-1.96** and **1.96**. Figure 3.14c, 3.14b reports the average  $z$ -scores ( $\zeta$  values) for subnetworks with parameters  $(f, q)$ , extracted from the  $ER$  and  $RN$  networks. We can remark that, as expected, the

$\zeta$  values oscillate around the 0, with no crossing of the  $-1.96$  line, that is, none of the selected subnetworks is topologically more central than what it would be expected by their total resources amount only. It is interesting to note that these considerations are true also for the randomized network  $RN$ , which has a skewed degree distribution (figure 3.6b). Taken together, these observations indicate that the measure  $\zeta$  here introduced correctly characterizes subnetworks topological centrality for networks with random structure.

On the contrary, the **brain network**  $BN$ , which has degree distribution equivalent to  $RN$  (figure 3.5b), demonstrates a different behaviour. For a high subnetwork ratio between low and high degree nodes, the subnetwork topological centrality oscillates close to 0, independently from its size  $f$ . For lower low/high degree ratios ( $q < 0.8$ ), the subnetworks show a topological centrality  $\zeta$  higher than predicted by their resources amount alone ( $\zeta < -1.96$ ). Moreover we remark that:

- even for very small subnetwork sizes ( $f \cong 0$ ), the curves ( $q = 0$ ), ( $q = 0.1$ ), ( $q = 0.2$ ), ( $q = 0.3$ ) and ( $q = 0.4$ ) lie below the  $-1.96$  threshold. Conceptually, subnetworks with low mixing rates  $q$  correspond to sets of brain hubs. Therefore, the measure  $\zeta$  consistently assigns high topological centrality to brain network hubs;
- the curves with  $q < 0.8$  reach a minimum for progressively higher  $f$  values. We can speculate that when the complete set of network hubs are included within the subnetwork of interest, we have a maximal (absolute) subnetwork topological centrality. Thereafter, the topological centrality decreases (in absolute value) as less central nodes are included into the subnetwork

Similar considerations apply to the **scale-free network** (figure 3.14d).

The comparison between the behaviour of the brain network  $BN$  and its randomized version  $RN$  highlights that the topological centrality  $\zeta$  of a subnetwork does not relate only to the network degree distribution, but also encodes information about the topological structure of the network itself.

### 3.3.3 Centrality of brain circuits

As a proof of concept, in this section we investigate the topological centrality  $\zeta$  of well-known brain circuits and clubs, and particularly: (i) the rich-club, and (ii) the hub cores separately composed by connector and peripheral hubs.

To this end, we considered binary structural brain networks derived from  $DSI$  data of 40 healthy subjects. The healthy subjects cohort here investigated is the same as in section 3.3.2. Nevertheless, for the current analyses we used a different grey matter parcellation with a higher resolution, and therefore a different definition of the graph nodes. The higher resolution parcellation was obtained by subdividing the 68 Desikan-Killiany cortical regions (Desikan *et al.*, 2006) into 1000 smaller and approximately equally-sized regions, according to (Cammoun *et al.*, 2012), for a total of 1014 nodes (1000 cortical regions and 14 subcortical regions).

Both subject-wise and group-representative brain networks were analysed. An edge was included in the representative brain network  $BNhr$  if present in at least 10% of the subjects. The network  $BNhr$  had density  $\delta = 0.076$  (table 3.1); its degree distribution is represented in figure 3.15.

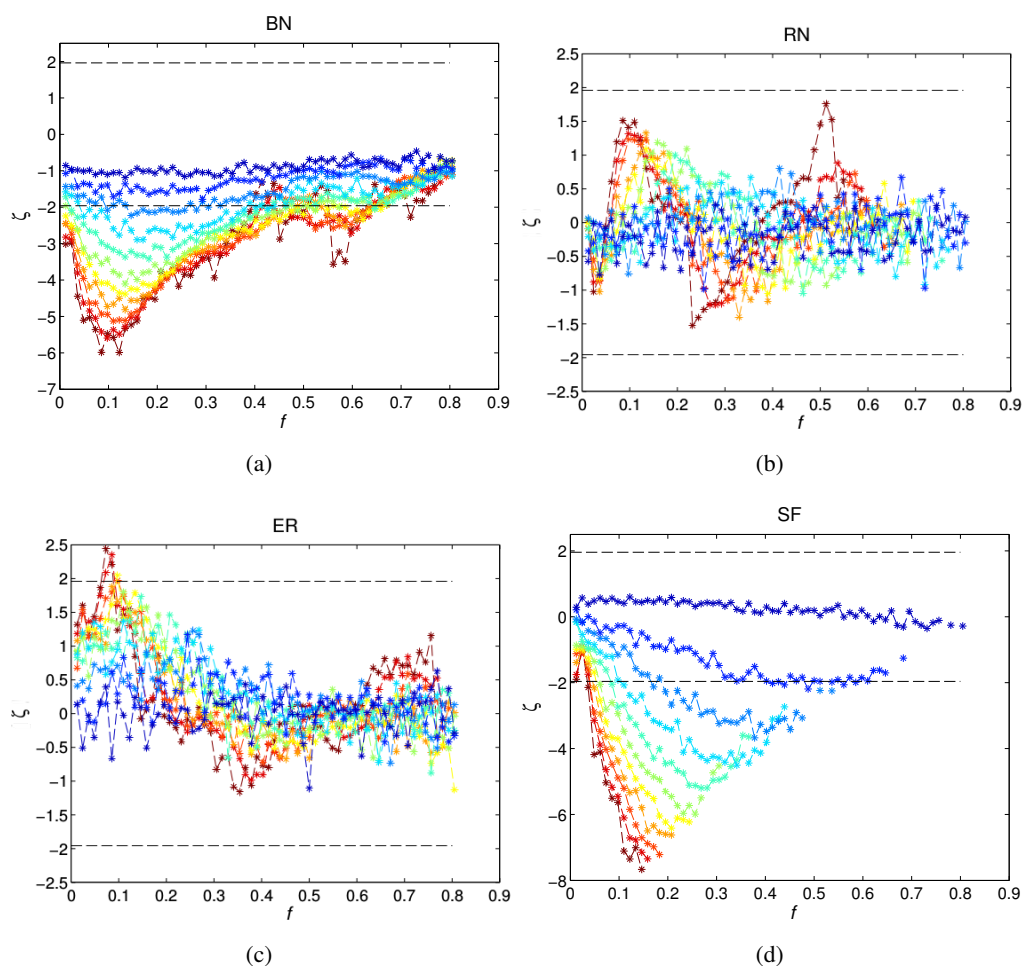


Figure 3.14 – Subnetwork topological centrality for different subnetwork sizes  $f$  ( $x$ -axis) and degree mixing rates  $q$  (color-coding, with dark red corresponding to  $q = 0$  and dark blue corresponding to  $q = 1$ ). The represented  $\zeta$  values are the average over  $n_{rep} = 100$  repetitions of the hybrid attack (subnetwork sampling), for each  $(f, q)$  parameters combination. The horizontal dashed lines indicate critical  $z$ -values at a significance level  $\alpha = 0.05$  (two-sided alternative hypothesis). Only  $(f, q)$  combinations that do not cause network fragmentation (defined as  $\langle s \rangle < 0.02 \cdot n$ ) are represented. The subnetwork topological centrality is evaluated for the four benchmark networks: (a) brain  $BN$ , (b) randomized brain  $BN$ , (c) Erdős-Rényi  $ER$  and (d) scale-free  $SF$  networks.



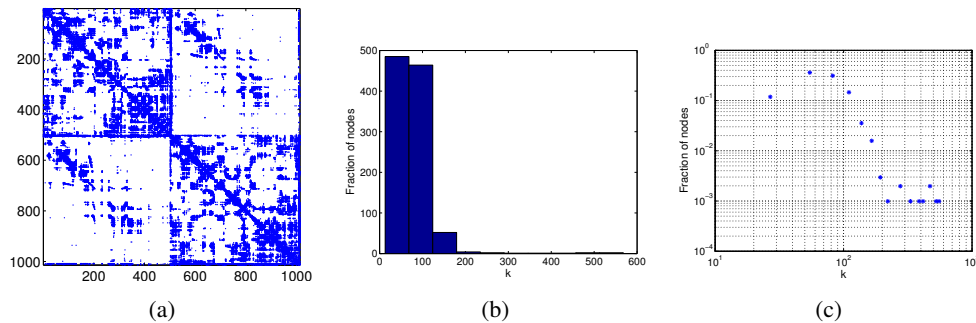


Figure 3.15 – Group-representative structural brain network  $BN_{hr}$ , 1014 nodes: (a) adjacency matrix; (b) degree sequence; (c) degree sequence in log-log scale.

### *Rich-club topological centrality*

We defined the rich-club subnetwork according to (van den Heuvel & Sporns, 2011), therefore including the following anatomical regions: right and left superiorfrontal, superiorparietal, precuneus, thalamus, putamen and hippocampus. All the high-resolution nodes corresponding to the listed anatomical regions were selected. The rich-club subnetwork therefore counted 196 nodes, corresponding to a fraction  $f = 19.3\%$  of the overall 1014  $BN_{hr}$  network nodes.

The rich-club is a set of network hubs whose inter-connectivity is higher than expected by their degree only (Alstott *et al.*, 2014). The rich-club has been shown to play an important role within the overall brain system and to be a central subnetwork as quantified by the relative high number of network shortest paths passing through its nodes and edges (van den Heuvel & Sporns, 2011). Moreover, the rich-club architecture has been shown to increase the number of possible stable configurations of cortical activity, thus promoting a large set of different brain functions (Senden *et al.*, 2014). We therefore expect the topological centrality  $\zeta_{rc}$  of the rich-club to be significantly different from zero ( $\zeta < -1.96$ ).

The topological centrality  $\zeta_{rc}$  of the rich club subnetwork was evaluated by computing the network efficiency  $Eff$  after rich-club nodes lesioning, and comparing it to its reference distribution. The random attack procedure was repeated 100 times. Each random attack entailed the removal of a number of nodes and edges exactly equal to the number of elements removed during the targeted attack towards the rich-club. We found a rich-club topological centrality  $\zeta_{rc} = -7.55$ , indicating that the topological role of the rich club is more prominent than expected by its high connectivity alone.

### *Peripheral and connector hubs topological centrality*

The brain network has been shown to have a modular organization, with high degree nodes acting as shortcuts for communication between segregated communities. Brain hubs can be formally identified as the nodes whose degree exceeds the mean degree value plus one standard deviation (this is of course not an univocal definition) (Sporns *et al.*, 2007). Brain hubs can be classified into peripheral, connector or kinless hubs according to their participation index  $PI$  computed with respect to a network decomposition into non-overlapping modules (Guimerà & Amaral, 2005).  $PI$  quantifies the ratio of inter-modular *vs* intra-modular connections of each node and is bounded between 0 and 1. **Peripheral hubs** ( $PI < 0.30$ ) are central nodes within their topological module, but have few connections with other modules' nodes. **Connector hubs** ( $0.30 < PI < 0.75$ ) share a consistent number of links with other modules' nodes, therefore promoting overall net-

work integration. Brain connector hubs mediate the relatively sparse connections between the different modules (Meunier *et al.*, 2010), and play a role in maintaining long-range synchronized functional activity (He *et al.*, 2009; Honey & Sporns, 2008).

Here we test the topological centrality of subnetworks composed by connector or peripheral hubs only, and matched in terms of size (number of nodes) and average nodal degree. For equivalent subnetworks size and average degree, we expect connector hubs subnetworks to have topological centrality higher than peripheral hubs subnetworks.

As a remark, we mention that the 82-nodes brain network  $BN$  investigated in the previous section 3.3.2 counted relatively few peripheral and connector hubs, with peripheral hubs subnetworks presenting a significantly lower average degree than connector hubs subnetworks. On the contrary, and as described below, for the 1014-nodes brain networks it was possible to identify peripheral and connector hubs subnetworks matched in terms of size and average degree. These considerations motivated our choice of a higher resolution cortical parcellation for the current analyses.

Each subjects-wise binary network (excluding subcortical regions) was decomposed into modules using the Louvain algorithm (Blondel *et al.*, 2008). Specifically, the Louvain algorithm was run 100 times for each subject, and the best network decomposition in terms of modularity value  $Q$  was chosen for each subject. For illustrative purposes, the same procedure was applied to the group-representative network  $BN_{hr}$ , and its modular decomposition is shown in figure 3.16. For each subject-wise brain network, hubs were identified as nodes whose degree  $k$  exceed the average network degree plus one standard deviation. Network hubs were then classified as connector or peripheral according to their participation index  $PI$ . We note that, according to this procedure, different subject-wise networks can present different numbers of connector and peripheral hubs. For each subject, and in order to identify a hubs subnetworks of the same size, we therefore selected  $n_{subnetwork}$  connector hubs and  $n_{subnetwork}$  peripheral hubs, with  $n_{subnetwork} = \min(n_{connector}, n_{peripheral})$ .  $n_{connector}$  is the overall number of connector hubs for the considered subject;  $n_{peripheral}$  is the overall number of peripheral hubs for the considered subject. For each subject,  $n_{subnetwork}$  connector and  $n_{subnetwork}$  peripheral hubs were selected in order to reach the best possible degree matching between the two sets. No overall statistical difference was present in terms of average degree (and therefore number of removed edges during targeted attack) between the two sets.

For each subject, the topological centralities of the connector hubs subnetwork ( $\zeta_{connector}$ ) and of the peripheral hubs subnetwork ( $\zeta_{peripheral}$ ) were computed for the two connector and peripheral cores. The (absolute) topological centrality of connector subnetworks was significantly higher than the topological centrality of peripheral subnetworks (Wilcoxon rank sum test,  $p = 0.00006$ ), as expected.

Moreover, even if composed of network hubs, the peripheral subnetworks showed a topological centrality close to zero (figure 3.17). Peripheral hubs are mainly connected to nodes within their own module, and poorly connected between them. We can therefore speculate that these nodes play an important role within single modules, but have a relatively low impact on the overall network communication efficiency.

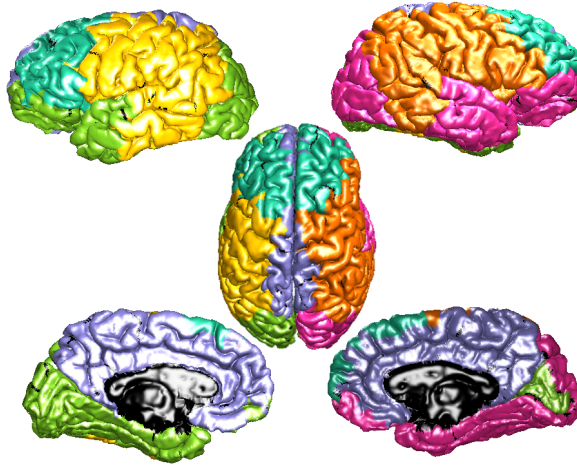


Figure 3.16 – Surface plots representing the modular decomposition of the 1014-nodes brain network  $BN_{hr}$ .

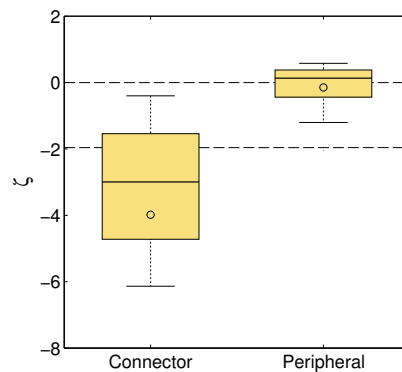


Figure 3.17 – Box plots representing the distributions of subject-wise topological centrality values for subnetworks composed of connector hubs (on the left,  $\zeta_{connector}$ ), and for subnetworks composed of peripheral hubs (on the right,  $\zeta_{peripheral}$ ). Subject-wise connector and peripheral subnetworks were matched in terms of size and average degree.  $\zeta_{connector}$  values were significantly smaller than  $\zeta_{peripheral}$  values (Wilcoxon rank sum test,  $p = 0.00006$ ).

### 3.4 Conclusions

The investigation of brain connectivity networks across multiple spatial scales provides important insights into brain organizational principles and their alteration in diseases. The alteration of global network properties is probably an hallmark for the majority of brain disorders. Anyway, system-scale analyses lack of specificity toward peculiar pathological traits, and global network measures remain of difficult biological interpretation. On the other hand, nodal measures do not capture large and middle-scale interactions potentially important for the understanding of pathological mechanisms. Moreover, local analyses are particularly sensitive to the noise intrinsic to brain connectivity matrices.

Moved by these considerations, in this chapter we focused on the topological characterization of brain sub-systems. Particularly, in clinical studies it is often of interest to quantify how much the disruption of a particular brain circuit can impact the overall brain communication efficiency, and potentially lead to altered functionalities and symptoms. Anyway, network science literature has dedicated limited attention to the characterization of subnetwork topological roles.

Previous works have suggested that the network attack procedure might be a valuable instrument for the characterization of elements (nodes and edges) centrality within the overall brain network. Here, we built on this concept, and we defined a simple measure  $\zeta$  quantifying the topological centrality of a subnetwork within a whole network architecture.

The subnetwork topological centrality  $\zeta$  was defined as the network efficiency loss after targeted attack toward the subnetwork of interest, with respect to an appropriate reference distribution. We expected that subnetworks of different sizes  $f$  and degree mixing rates  $q$  would have distinct topological roles within an overall network. Moreover, we expected that such topological role would vary as a function of the original network architecture.

We therefore characterized  $\zeta$  for a set of  $(f, q)$  parameter values, with  $f$  representing the relative size of the subnetwork of interest, and  $q$  its degree mixing rate. As expected, we observed that for unstructured networks (Erdős–Rényi and randomized brain networks)  $\zeta$  is close to zero for all possible combinations of  $(f, q)$  values. When no structure is present in the network, none of its subnetworks presents a topological centrality higher than expected by the amount of its resources (nodes and edges) alone.

On the contrary, in structured networks (scale-free and brain networks)  $\zeta$  identified sets of subnetworks with distinctive topological centrality. In particular, subnetworks of the brain graph with medium/low mixing rate, i.e. including a large percentage of high degree nodes, showed a high topological centrality, and their damage significantly affected the overall network communication efficiency. For the brain network, maximal (absolute)  $\zeta$  values are reached when sampling low mixing rate subnetworks with size of approximately 10-12 nodes. This subnetwork dimension is consistent with the size of the largely investigated brain rich-club.

As a proof of concept, we computed  $\zeta$  for well-known brain cores, and we characterized the different topological roles of the rich-club, the connector hubs, and the peripheral hubs subnetworks.

Taken together, our analyses suggest that the subnetwork topological centrality measure here introduced can capture complex interplays between network subsystems and overall network topology, and might be a valuable instrument for the characterization of brain subsystems in health and diseases.

In the next chapter we will apply this measure to the investigation of brain dysconnectivity patterns characterizing different brain disorders, namely schizophrenia, early psychosis and 22q11 deletion syndrome.

# Topological characterization of brain subnetworks in diseases

---

# 4

## 4.1 *Applications*

### **Tracking brain connectivity alterations across psychosis stages**

#### 4.1.1 Purposes

Schizophrenia is a major psychiatric disorder characterized by disabling positive, negative, and cognitive symptoms. According to the dysconnectivity hypothesis (Friston & Frith, 1994), distributed alterations of brain connectivity patterns, and abnormal functional integration between distinct brain areas could underlie the symptoms observed in the pathology (Stephan *et al.*, 2009, 2006). Indeed a remarkable number of studies based on magnetic resonance imaging (MRI) highlighted morphological (Glahn *et al.*, 2008; Honea *et al.*, 2005), functional (Calhoun *et al.*, 2009) and structural connectivity (Fitzsimmons *et al.*, 2013; Pettersson-Yeo *et al.*, 2011) disturbances spatially distributed, but particularly involving temporal, parietal, frontal and subcortical structures (Bora *et al.*, 2011; Canu *et al.*, 2015; Ellison-Wright & Bullmore, 2009; Shepherd *et al.*, 2012), in full blown-up syndrome as well as in earlier phases of the disease.

According to the staging model proposed by McGorry and colleagues (McGorry *et al.*, 2006; Wood *et al.*, 2011), progressive clinical stages can be formally defined on the basis of symptomatology and cognitive markers, as summarized in figure 4.1. Consistently, increasing evidence suggests that critical brain structural and functional modifications occur early in the disease process, and follow a progressive evolution with more abnormal brain changes corresponding to more severe psychotic stages. In this regard, McGorry and colleagues have recently reviewed evidences of brain structural changes progression as quantified by magnetic resonance imaging studies (McGorry *et al.*, 2014):

"The brain region most commonly shown to be abnormal in chronic schizophrenia, the lateral ventricles, is less affected in first-episode patients (Steen *et al.*, 2006), and unaffected in ultra-high risk individuals (Borgwardt *et al.*, 2007). A recent study has shown that gray matter decreases, predominantly in the frontal cortex, are far more pronounced in chronic schizophrenia than in first episode psychosis patients (Ellison-Wright *et al.*, 2008), while other work has extended this evidence to ultra-high risk subjects (Sun *et al.*, 2009a). We have found similar patterns in the superior temporal gyri (Takahashi *et al.*, 2009c) and insular cortex (Takahashi *et al.*, 2009a,b), with clear evidence for increasing abnormality across the stages of illness (McIntosh *et al.*, 2011). Similarly, marked reductions in hippocampal volume have been noted in chronic schizophrenia patients, while this is less clear in first-episode patients (Vita *et al.*, 2006), and non-significant in ultra-high risk subjects (Buehlmann *et al.*, 2010; Velakoulis *et al.*, 2006; Wood *et al.*, 2010). ... Taken together, these observations support the view that progressive brain structural changes in schizophrenia clearly involve a linear gradient of change, though a non-linear step function is also possible. ... Such progressive evolution and differentiation of neuroanatomical changes may be paralleled by changes in function, connectivity and neurochemical integrity in these circuits, and will need systematic research."

The characterization of progressive pathological stages by means of neurobiological markers is therefore of central interest. The identification of early psychosis biomarkers through neuroimaging methods would help the quantitative identification of disease stages. It will contribute to the understanding of pathological mechanisms and the assessment of early intervention and personalized treatments. Magnetic resonance imaging, brain connectivity analysis and graph theory are perfectly suited for the investigation and characterization of dysconnectivity syndromes such as schizophrenia. The purposes of the present studies are (i) the identification of connectivity alterations occurring in chronic schizophrenia patients, and (ii) the extension of findings to the earlier stages of the pathology. Characterizing connectomics anomalies in chronic schizophrenia and then moving to earlier stages is an important conceptual framework, as brain changes already present in the early phase of psychosis are subtler and more difficult to measure (McGorry *et al.*, 2014).

Here, we first review current findings from diffusion MRI-based connectome studies on schizophrenia and psychosis neuropathology (section 4.1.2). Thereafter, we propose a sound analysis pipeline based on graph theory elements for the identification of a brain core affected in chronic schizophrenia patients (section 4.1.3). In order to characterize the topological role of such affected core, we use the subnetwork topological centrality measure  $\zeta$  defined in the previous chapter 3. Next, we extend our findings from chronic patients (corresponding to stage IV of figure 4.1) to a cohort of early psychosis patients (corresponding to clinical stages II and III of figure 4.1). Moreover, we use the number of hospitalizations variable to distinguish between less severe (approximately, clinical stage II) and more severe (approximately, clinical stage III) illness stages. We show that, although global network measures are not altered in early psychosis patients, the brain core affected in chronic schizophrenia is precociously impaired in the early stages of psychosis (section 4.1.4). We propose the disruption and topological decentralization of the affected core as central pathological mechanism. We conclude the present section with closing remarks and discussion (section 4.1.5).

## 4.1.2 Introduction

Schizophrenia is a severe psychiatric disorder hypothesized to be the result of brain connectivity impairment (Friston & Frith, 1994). Studies based on graph theoretical approaches report

Clinical Stage	Definition	Example Populations
0	Increased risk of psychotic or severe mood disorder. No symptoms currently.	First-degree teenage relatives of probands.
Ia	Mild or nonspecific symptoms, including neurocognitive deficits, subthreshold psychotic-like experiences associated with only mild functional decline, mood or anxiety symptoms that are distressing and/or have resulting in help-seeking with or without comorbid substance abuse. Mild functional change or decline.	Individuals referred to youth mental health service by primary care physicians or school counselors.
Ib	Ultra high risk: Moderate but subthreshold symptoms, with/without mild to moderate neurocognitive changes, comorbid substance abuse, and with functional decline to caseness.	Individuals who meet CAARMS criteria.
II	Full threshold disorder with moderate-severe symptoms, neurocognitive deficits, and functional decline.	Individuals who meet psychosis criteria as defined by the CAARMS.
III	Incomplete remission or recurrence/relapse.	Individuals with a recurrence of stage II psychosis.
IV	Severe, persistent, and unremitting illness as judged on symptoms and disability criteria.	Patients with established schizophrenia with functional impairment.

Figure 4.1 – Outline of clinical staging in psychotic disorder (Wood *et al.*, 2011). Reprinted from Biological Psychiatry, Volume 70, Issue 7, Wood SJ *et al.*, Neuroimaging and Treatment Evidence for Clinical Staging in Psychotic Disorders: From the At-Risk Mental State to Chronic Schizophrenia, pp. 619-625. Copyright (2011), with permission from Elsevier.

a decrease of brain network efficiency, associated with a reduced capacity of integration of information between brain areas (Fornito *et al.*, 2012; van den Heuvel & Fornito, 2014). Various structural substrates have been proposed to underlie the brain network efficiency loss occurring in schizophrenia. Moving from the analysis of system-level network properties to the role of individual nodes (local scale), different brain subnetworks have been shown to be involved in the pathology. Applying a network based statistics (NBS) approach, Zalesky and colleagues identified a distributed fronto-parietal / occipital network as possible substrate of global network alterations (Zalesky *et al.*, 2011). Default mode network (DMN) regions were also shown to be involved in advanced (Skudlarski *et al.*, 2010; Zhang *et al.*, 2012) and early stages (Zhang *et al.*, 2014) of psychosis.

A common element among reported brain damages in schizophrenia is the presence of brain network hubs. Global network alterations can indeed be associated to a distributed weakening of hub regions, and specially prefrontal, limbic, temporal and parietal areas (van den Heuvel *et al.*, 2010; Zhang *et al.*, 2012). Brain hubs are nodes presenting a high degree of centrality within the brain network, and have therefore been associated to a considerable metabolic cost and a potential higher vulnerability in the context of psychiatric disorders (Bullmore & Sporns, 2012). Brain connections between a specific set of hub regions, the rich-club (van den Heuvel & Sporns, 2011), have recently been shown to be weakened in schizophrenia patients (van den Heuvel *et al.*, 2013). This result is paralleled by resting state functional studies (Yu *et al.*, 2013). Interestingly, rich-club regions have been shown to be affected, but in less severe form, in unaffected siblings of schizophrenia patients (Collin *et al.*, 2014a), and in 22q11 deletion syndrome patients (Ottet *et al.*, 2013b). The 22q11 deletion syndrome is a genetic sub-type of schizophrenia (see as well section 4.2). These findings may reflect a link between familial and genetic bases, and white matter connectivity alterations for schizophrenia vulnerability (Collin *et al.*, 2014a; van den Heuvel & Fornito, 2014).

Even though there is a large amount of evidence pointing towards an alteration of normal hub cores in schizophrenia and to an affection of the related connections disproportionate to other brain tracts, this effect may not necessarily be specific to schizophrenia neuropathology only (Rubinov & Bullmore, 2013b), considering that high degree nodes have been implicated in different brain pathologies (Drzezga *et al.*, 2011; Griffa *et al.*, 2013b; Lo *et al.*, 2010; Zhang *et al.*, 2011) and normal aging (Damoiseaux *et al.*, 2009; Tomasi & Volkow, 2012). In schizophrenia, losses of overall brain network properties have been extensively associated to hubs and rich-club disruption (Rubinov & Bullmore, 2013b; van den Heuvel & Fornito, 2014); to alterations of brain network hierarchical organization (Bassett *et al.*, 2008); to disruption of anatomical connections

among fronto-parietal-occipital areas (Zalesky *et al.*, 2011) and fronto-temporal poles (van den Heuvel *et al.*, 2010), default mode network (Skudlarski *et al.*, 2010), and to long associative fasciculi (Canu *et al.*, 2015). Taken together these findings corroborate the hypothesis that schizophrenia is associated to a widespread rather than localized alteration of brain structural connectivity, implying a modified organization of the brain communication system that involves, but is not limited to high degree cores.

Building on these considerations, we present here an investigation of brain network topology and subnetworks impairment underlying the connectome disruption observed in schizophrenia, and we quantitatively characterize such alterations across psychosis stages. Particularly, we propose the decentralization of a distributed set of brain regions as a possible mechanism underlying the schizophrenia pathology, and characterizing early stages of the pathology and their evolution. Brain connectivity networks were estimated from *DSI* data for 16 chronic schizophrenia patients, 59 early psychosis patients, and an equal number of controls.

*DSI* is characterized by strong diffusion weighting and high angular resolution. As a consequence *DSI* is more sensitive to white matter microstructural organization than classical Diffusion Tensor Imaging (*DTI*). Crossing-fibers can be mapped accurately and tissue alterations affecting the white matter slow diffusion compartment may be captured (Baumann *et al.*, 2012; Mendelsohn *et al.*, 2006; Wedeen *et al.*, 2012).

As a first step, global and nodal integration and segregation network properties were assessed in order to corroborate previous findings (Bassett *et al.*, 2008; van den Heuvel *et al.*, 2010; Zalesky *et al.*, 2011). Thereafter, alterations of nodal properties allowed identifying a distributed brain subnetwork affected in chronic schizophrenia patients, in substantial agreement with previous studies (van den Heuvel & Fornito, 2014). More importantly, the topological role of such affected core within the overall brain system was assessed in a graph theoretical framework, in order to characterize brain organizational principles underlying the pathology. The topological position of the affected core within the overall brain network appears to be precociously compromised in the earlier stages of the disease. We propose affected core network measures as possible markers of illness progression.

### 4.1.3 Methods and Materials

#### 4.1.3.1 Subject cohorts

Patients were recruited from the outpatient clinic of the department of psychiatry (Service for General Psychiatry, PGE), Lausanne University Hospital, Switzerland.

16 patients (10 males and 6 females, aged  $42 \pm 10$  years old) met criteria DSM-IV for schizophrenia or schizo-affective disorder (Association, 2000) and were assigned to the chronic schizophrenia patients group (*SCHZ*).

59 patients (42 males and 26 females, aged  $26 \pm 6$  years old) were recruited from the TIPP Program (Treatment and Early Intervention in Psychosis Program, University Hospital, Lausanne) (Baumann *et al.*, 2013), and met the threshold for psychosis according to the CAARMS (Comprehensive Assessment of the At-Risk Mental State) criteria (Yung *et al.*, 2005). They were assigned to the early psychosis group (*EP*).

For each one of the two investigation groups, healthy controls were recruited and assessed by means of the Diagnostic Interview for Genetic Studies (Preisig *et al.*, 1999). Major mood, psychotic, or substance-use disorder and having a first-degree relative with a psychotic disorder were exclusion criteria for controls. Neurological disorders and severe head trauma were exclusion criteria for all subjects. A total of 68 healthy subjects was considered, and pair-wise matched to the patients according to age, gender and handedness. 6 of the 68 healthy subjects were used as controls for both the *SCHZ* and the *EP* group. The control group *CTRL<sub>SCHZ</sub>* for the *SCHZ* patients was composed of 15 healthy subjects (8 males and 7 females, aged  $41 \pm 10$  years old). The



control group  $CTRL_{EP}$  for the  $EP$  patients was composed of 59 healthy subjects (40 males and 19 females, aged  $26 \pm 6$  years old). No statistical difference in terms of age, gender or handedness was present between the groups  $CTRL_{SCHZ}$  and  $SCHZ$ , nor between the groups  $CTRL_{EP}$  and  $EP$ . Informed written consent in accordance with our institutional guidelines (protocol approved by the Ethic Committee of Clinical Research of the Faculty of Biology and Medicine, University of Lausanne, Switzerland) was obtained for all the subjects.

In order to assess their cognitive profile, all participants performed the MATRICS Consensus Battery (MCCB Matrics Assessment, Inc. (August *et al.*, 2012; Kern *et al.*, 2008; Nuechterlein *et al.*, 2008)). Particularly, the following cognitive domains were assessed: speed of processing (category fluency, TMT and BACS scores), attention and vigilance (CPT score), verbal (LNS score) and non-verbal (WMS) working memory, verbal learning (HVL score), visual learning (BVMT score), reasoning and problem solving (NAC scores). Moreover, all the  $SCHZ$  and  $EP$  patients were assessed with the Positive and Negative Syndrome Scale (PANSS) (Kay *et al.*, 1987).

In order to quantify therapeutic dose equivalence across antipsychotic medications, different medication doses were converted to chlorpromazine equivalent dose ( $CPZ$ ) (Andreasen *et al.*, 2010)  $CPZ$  is defined as the dose of a drug, equivalent to 100 mg of oral dose of chlorpromazine. The drug equivalent to 200-300 mg of chlorpromazine is considered the minimum effective dose, while a drug equivalent exceeding 1000 mg of chlorpromazine is considered high (Taylor *et al.*, 2007). 14 of the 16  $SCHZ$  patients were taking medication at the time of this study, with average medication of  $341 \pm 202$  mg  $CPZ$ . 48 of 59  $EP$  patients were taking medication at the time of this study, with average medication of  $378 \pm 253$  mg  $CPZ$ .

For all patients, the duration of illness was estimated as the temporal lapse between the date the patient passed the psychosis threshold according to the CAARMS, and the date of the MRI scan. Average illness duration for  $SCHZ$  patients was  $16 \pm 9$  years; average illness duration for  $EP$  patients was  $2 \pm 2$  years. For  $EP$  patients, the number of hospitalizations before the MRI scan was also recorded.

#### 4.1.3.2 Diffusion MRI

##### *MRI acquisitions*

All subjects (68  $CTRL$ , 59  $EP$  and 16  $SCHZ$ ) included in this study underwent an MRI session on a 3 Tesla scanner (Magnetom TrioTim, Siemens Medical Solutions), equipped with a 32-channel head coil. Each scanning session included a magnetization-prepared rapid acquisition gradient echo (MPRAGE) sequence with 1 mm in-plane resolution and 1.2 mm slice thickness, covering  $240 \times 257 \times 160$  voxels. The TR, TE and TI were, respectively, 2300, 2.98, and 900 ms. The DSI sequence included 128 diffusion-weighted images with a maximum b-value of  $8000 \text{ s/mm}^2$  and one  $b_0$  reference image. The acquisition volume was made of  $96 \times 96 \times 34$  voxels with  $2.2 \times 2.2 \times 3$  mm resolution. TR and TE were 6100 and 144 ms, respectively.  $DSI$  datasets were visually inspected for signal drop-outs across the scanning time. Signal drop-outs are linked to motion artefacts (Yendiki *et al.*, 2014). None of the investigated subjects presented important signal drop-outs and needed to be excluded from this study.

##### *MRI data processing and connectivity estimation*

MRI datasets were processed in order to estimate the overall brain anatomical connectivity by computing the white matter tracts connecting pairs of cortical and subcortical regions.  $MPRAGE$  volumes were segmented into white matter, grey matter, and cerebrospinal fluid compartments, and linearly registered to the  $b_0$  volume. Thereafter, the grey matter volume was subdivided

into 68 cortical and 14 subcortical anatomical regions, according to the Desikan-Killiany atlas (Desikan *et al.*, 2006), and defining  $N = 82$  brain network nodes. *DSI* data were reconstructed according to (Wedeen *et al.*, 2005), estimating voxel-wise orientation distribution functions (ODFs). From ODFs, generalized fraction anisotropy (gFA) (Tuch, 2004) and apparent diffusion coefficient (ADC) (Sener, 2001) maps were computed. Deterministic streamline tractography (Mori *et al.*, 1999) was performed on *DSI* reconstructed data, initiating 32 streamline propagations per voxel, per diffusion direction. The connectivity between each pair of cortical and subcortical regions was estimated by evaluating the streamlines starting and ending within the two regions.

#### 4.1.3.3 A graph-theory based pipeline for diffusion data analysis

##### *Brain network estimation*

The structural connectivity between each pair of network nodes was quantified as the normalized connection density, (normalized effective number of connecting streamlines per unit surface). The effective number of streamlines  $n_{uv}$  connecting a pair of regions ( $u, v$ ) was defined by normalizing the raw number of streamlines (the number of connecting curves estimated from the tractography algorithm) by their average length. Formally:

$$n_{uv} = \sum_{f \in F_{uv}} \frac{1}{l(f)},$$

with  $f \in F_{uv}$  a streamline belonging to the set of streamlines connecting regions  $u$  and  $v$ , and  $l(f)$  the length of streamline  $f$ . The normalization of the raw number of streamlines is motivated by tractography biases. In this study we used deterministic streamline tractography and we seeded uniformly the WM volume. By taking this approach, there are more streamlines that are initiated in longer bundles than in shorter bundles simply because a long tract passes through more WM voxels. In fact the number of fibers initiated in a tract is directly proportional to its length. In order to correct for this bias we chose the simplest approach of normalizing the number of streamlines in a bundle by the average fiber length of the bundle (Hagmann *et al.*, 2008). We should anyway point out that this approach does not correct for all tractography biases. It is in fact known that tract reconstruction suffers of biases due to error propagation and multiple seeds along the tract path. Anyway it is not yet clear (at least to our knowledge) how to best quantify such bias and compensate for it. In this study, the normalization procedure by the average fiber length restores a plausible and on average inverse relationship (Gigandet *et al.*, 2013; Oh *et al.*, 2014) between the connection length and the connectivity strength (figure 4.2). No between-group difference was present in terms of average streamline length between the groups (*CTRL<sub>SCHZ</sub>* vs *SCHZ*) and (*CTRL<sub>EP</sub>* vs *EP*), table 4.1.

The normalized connection density between each pair of cortical and subcortical regions was formally defined as follows:

$$w_{uv} = \frac{1}{W} d_{uv} = \frac{1}{W} \left( \frac{2}{S_u S_v} n_{uv} \right),$$

with  $w_{uv}$  connectivity strength associated to the edge connecting nodes  $u$  and  $v$ ,  $W$  normalization factor, and  $d_{uv}$  connection density between nodes  $u$  and  $v$  as defined in (Hagmann *et al.*, 2008) (as an example, figure 4.3 represents two connectivity matrices weighted by the absolute connection density between pairs of nodes).  $S_u$  and  $S_v$  indicate the surfaces of the brain regions  $u$  and  $v$ . The normalization factor  $W$  was defined as the sum of the connection density values over all the edges belonging to the subject-wise connectivity matrix:

$$W = \sum_{u \in N} \sum_{v \in N, v \neq u} d_{uv},$$

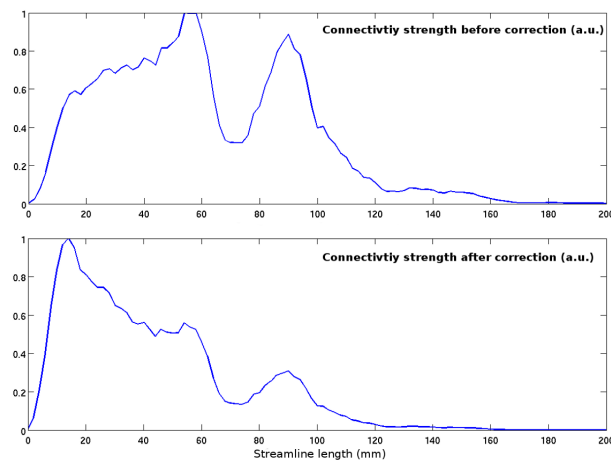


Figure 4.2 – Histograms of connectivity strength as a function of streamline length (in mm), before and after the tractography bias correction. The connectivity strength is quantified as the number of connecting streamlines (first row), or as the number of connecting streamlines normalized by the average streamline length (second row). Both histograms have been normalized by their maximum for comparison. The tractography bias correction normalizes the number of connecting fibers by their length harmonic mean, similarly to (Gigandet *et al.*, 2013; Hagmann *et al.*, 2008). Although this is a simple correction method compared to more sophisticated approaches (see for example (Girard *et al.*, 2014; Morris *et al.*, 2008; Smith *et al.*, 2013)), it reestablishes a more plausible (on average inverse) relationship between connectivity strength and connection length. Indeed, studies based on imaging modalities other than diffusion MRI suggested that connectivity strength is negatively correlated to connection distance in the brain (fMRI-based studies: (Alexander-Bloch *et al.*, 2013; Salvador *et al.*, 2005); tracer injection study in rat: (Oh *et al.*, 2014)).

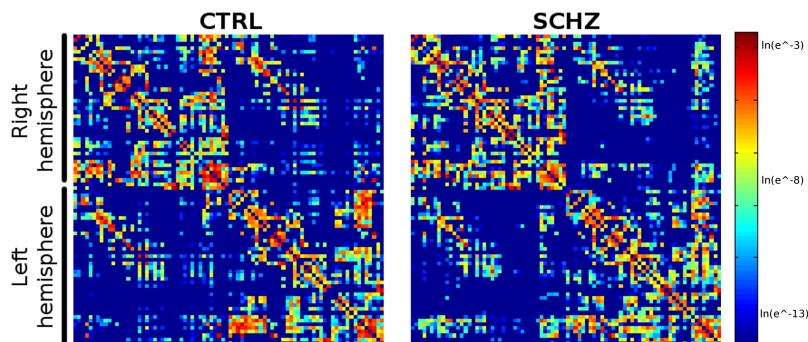


Figure 4.3 – Example of brain connectivity matrices weighted by absolute connection density values, for a control subject and a schizophrenia patient. The connection density values are represented in logarithmic scale. The 82 nodes are ordered according to (Cammoun *et al.*, 2012), from frontal to occipito-temporal and subcortical regions, right hemisphere before, left hemisphere after. Note that connections on the diagonal have been discarded for all the computations throughout this study and have been set to zero in this figure.

Measure	<i>CTRL<sub>SCHZ</sub></i>	<i>SCHZ</i>	p-values	<i>CTRL<sub>EP</sub></i>	<i>EP</i>	p-values
<b>Brain-<i>W</i></b>	3.757 ± 0.305	3.907 ± 0.178	0.09	3.604 ± 0.309	3.523 ± 0.362	0.4
<b>Brain-<math>\delta</math></b>	0.308 ± 0.019	0.320 ± 0.018	0.1	0.305 ± 0.020	0.306 ± 0.024	0.9
<b>Brain- avg length (mm)</b>	77.3 ± 5.8	79.0 ± 6.1	0.5	77.9 ± 6.7	77.1 ± 7.1	0.6
<b>Brain-avg <i>w</i></b>	0.000982 ± 0.00006	0.000943 ± 0.00005	0.1	0.000990 ± 0.000068	0.000990 ± 0.000078	0.9
<b>Brain-<i>wgFA</i></b>	1.98 ± 0.20	1.88 ± 0.20	0.24	2.04 ± 0.23	1.96 ± 0.27	0.05*
<b>Brain-<i>wiADC</i></b>	16534 ± 1598	15698 ± 1658	0.31	16919 ± 2370	16044 ± 2185	0.05*
<b>a-core-avg <i>w</i></b>	0.0014 ± 0.0001	0.0012 ± 0.0001	0.00035*	0.0014 ± 0.0002	0.0014 ± 0.0002	0.06
<b>a-core-<i>wgFA</i></b>	2.55 ± 0.38	2.17 ± 0.26	0.0076*	2.63 ± 0.42	2.40 ± 0.36	0.005*
<b>a-core-<i>wiADC</i></b>	21751 ± 3022	18671 ± 2006	0.0042*	22140 ± 4065	20034 ± 2894	0.003*
<b>Out-core-avg <i>w</i></b>	0.00102 ± 0.00008	0.00109 ± 0.00008	0.017*	0.00103 ± 0.00009	0.00105 ± 0.00010	0.3
<b>Out-core-<i>wgFA</i></b>	1.99 ± 0.15	2.04 ± 0.26	0.68	2.05 ± 0.24	2.00 ± 0.32	0.1
<b>Out-core-<i>wiADC</i></b>	16152 ± 1255	16819 ± 2175	0.4	16778 ± 2405	16182 ± 2596	0.09

Table 4.1 – Quantitative characteristics of the investigated network for the four groups of subjects *CTRL<sub>SCHZ</sub>*, *SCHZ*, *CTRL<sub>EP</sub>* and *EP*. The overall brain network density  $\delta$ , average streamline length and normalization factor *W* are listed. Moreover the average normalized connections density *w*, the average *wgFA* and the average *wiADC* values are reported for the overall brain network, the a-core subnetwork, and the subnetwork complementary to the a-core (‘Out-core’). Reported numerical values refer to group-average values  $\pm$  one standard deviation. The ‘p-values’ columns list the FDR-corrected p-values from *WRS* statistical testing between the group pairs (*CTRL<sub>SCHZ</sub>*, *SCHZ*) and (*CTRL<sub>EP</sub>*, *EP*). \* indicates between-group statistically significant difference, at a significance level  $\alpha = 0.05$  (FDR-corrected).

with *N* set of brain nodes. Consequently, the weight of each edge represents a fraction of the overall brain connectivity strength available for the considered subject, and not an absolute connectivity strength value. This normalization allows focusing on the topological organization of each subject brain network, and disentangles dependencies between measures of network organization and total connectivity weight (van Wijk *et al.*, 2010). We note that other factors may influence the value of network topological measures, and particularly the number of nodes in the network (obviously the same for all the subjects), and the network density  $\delta$ , i.e. the fraction of existing edges over the maximum number of possible edges in the graph. No differences were present in terms of network density  $\delta$  and integrated connection density *W* between the group pairs (*CTRL<sub>SCHZ</sub>* vs *SCHZ*) and (*CTRL<sub>EP</sub>* vs *EP*) (table 4.1).

Besides the normalized connection density  $d_{uv}$ , the average *gFA* and *ADC* values and the effective number of fibers  $f_{uv}$  were computed for each connecting tract (*u*, *v*). The *gFA* and *ADC* measures are known to be markers of tract integrity such as axonal packing and myelination levels (Beaulieu, 2002; Takahashi *et al.*, 2002). In order to capture the relative importance of tracts sizes we took a similar approach as previous works (Fischi-Gómez *et al.*, 2014; Hagmann *et al.*, 2010), and weighted the *gFA* and the (inverse) *ADC* average values along each white matter tract by the effective number of fibers  $n_{uv}$  belonging to the tract (*u*, *v*) itself:

$$wgFA_{uv} = gFA_{uv} \cdot n_{uv},$$

$$wiADC_{uv} = \frac{n_{uv}}{ADC_{uv}},$$

with  $gFA_{uv}$  and  $ADC_{uv}$  average *gFA* and *ADC* values along the streamlines connecting regions *u* and *v*. For each one of the investigated subjects we therefore obtained multiple weighted undirected connectivity matrices, with the following weighting schemes: (i) normalized connection density  $d_{uv}$ , (ii) weighted *gFA*  $wgFA$ , (iii) weighted (inverse) *ADC*  $wiADC$ . For each subject the three weighted matrices had the same binary structure.

### ***System- and local-scale analysis***

For each subject's connectome, global and local weighted network measures describing integration and segregation properties of the brain topology were computed. All the analyses were performed using MATLAB 8.0, The MathWorks Inc., and the Brain Connectivity Toolbox (Rubinov & Sporns, 2010; Sporns). Network integration was quantified through the global efficiency measure  $Eff$  (Latora & Marchiori, 2001) and the nodal closeness centrality  $L_i^{-1}$  (Freeman, 1978). In brief, the global efficiency is inversely proportional to the network characteristic path length, and describes the level of integration of communication between distant parts of the brain network. The nodal closeness centrality is a local measure of centrality, proportional to the inverse average shortest path length between the considered node and all the other brain regions. Segregation properties were quantified through the network transitivity  $T$  (Newman, 2003) and the nodal local efficiency  $Eff_{loc(i)}$  (Latora & Marchiori, 2001). The transitivity measure quantifies the average level of local connectedness in the network (Opsahl & Panzarasa, 2009), and compared to other segregation measures (e.g. clustering coefficient) is robust with respect to low-strength nodes contribution (Rubinov & Sporns, 2010; Watts & Strogatz, 1998). The nodal local efficiency describes the degree of connectedness between the neighbours of the considered node. These different measures were chosen because of their relevance in describing small-world networks (Bassett & Bullmore, 2006; Latora & Marchiori, 2001; Rubinov & Sporns, 2010). We refer to (Rubinov & Sporns, 2010) for formal mathematical expressions of the listed measures.

Taken together, these measures allowed identifying a distributed set of brain nodes affected in schizophrenia patients  $SCHZ$  compared to control subjects  $CTRL_{SCHZ}$ . Specifically, in the framework of the present study, the **affected core** of the schizophrenia brain network was defined as the set of nodes presenting *significantly decreased values of closeness centrality (integration property) or local efficiency (segregation property)* compared to controls. As reported below (section 4.1.4), the affected core included 26 out of 82 brain nodes, corresponding to approximately the 30% of the overall brain network. On the contrary, none of the brain network nodes considered individually presented decreased  $L_i^{-1}$  or  $Eff_{loc(i)}$  when comparing  $EP$  and  $CTRL_{EP}$  subjects.

An investigation of the closeness centrality measures  $L_i^{-1}$  allowed identifying brain hubs, typically defined as the nodes whose centrality measure is significantly higher than on average (Sporns *et al.*, 2007; van den Heuvel & Sporns, 2011). In this study, normal brain hubs were identified in the overall control group composed by 68 subjects as the set of nodes presenting a closeness centrality  $L_i^{-1}$  larger than the mean closeness centrality over the whole 82 brain nodes, plus one standard deviation (figure 4.6). Moreover, the closeness centrality ranking position (i.e. ordering number)  $r_i$  of each node was evaluated for each one of the 149 subjects included in this study.

### ***Subsystem-scale analysis***

Targeted and random attacks have been extensively used in connectome analyses, particularly as a model to understand the relevance of localized brain damages (Alstott *et al.*, 2009; Bullmore & Sporns, 2009; Kaiser *et al.*, 2007). Here we combined targeted and random attacks to assess the degree of centrality of a specific set of nodes within the overall brain network. Specifically, the topological role of the affected core (from now on dubbed a-core) for the maintenance of the overall network efficiency was quantified by means of the topological centrality measure  $\zeta^w$  introduced in chapter 3. The measure  $\zeta^w$  is defined as the standard score of the network efficiency after targeted attack towards the subnetwork of interest (a-core), relative to the efficiency distribution after repeated random attacks. In order to estimate the efficiency reference distribution, the null model for the random attack was matched with the targeted attack in terms of (i) number of removed nodes, and (ii) overall removed connectivity strength up to a tolerance level  $\sigma$ . The weighted topological centrality measure  $\zeta^w$  was applied.

In the random attack procedure, and for each subject, we first removed 26 randomly selected nodes together with their edges. Thereafter, if necessary, additional edges were removed in order to match, up to a tolerance level  $\sigma$ , the overall connectivity strength removed during the targeted attack towards the a-core. In this way the subject-wise amount of damage, quantified in terms of removed number of nodes and total strength, remained identical across conditions. The tolerance level  $\sigma$  was set equal to one standard deviation of the network efficiency values after targeted attack, computed over all the subjects of the two classes ( $CTRL_{EP}, EP$ ) and ( $CTRL_{SCHZ}, SCHZ$ ). During node and edge removal we controlled for network disconnectedness, i.e. none of the 56-nodes surviving network was disconnected. The random attack was repeated  $n_{iter} = 1000$  times per subject. For illustrative purposes, figure 4.7a pictures the overall efficiency reference distribution for the  $CTRL_{SCHZ}$  and  $SCHZ$  groups, and the relative efficiency dispersions after targeted attack towards the affected core.

Furthermore, the affected core was quantitatively characterized by computing the number of shortest paths crossing the a-core. A shortest path is the geodesic path connecting two brain regions and represents a probable pathway of communication (Bullmore & Sporns, 2012; van den Heuvel *et al.*, 2012). All the brain network shortest paths were evaluated. Subgroups of the whole-brain shortest paths layout were then considered: (i) paths connecting nodes not belonging to the a-core and NOT passing through the a-core, and (ii) paths connecting nodes not belonging to the a-core BUT passing through the a-core. A path was defined to pass through the a-core if it involved at least one step within it.

Finally, the affected core was characterized in terms of white matter tracts indicators. Tracts connection a-core regions and regions outside the a-core were considered separately. White matter microstructure within and outside the affected core was indirectly quantified by means of average weighted  $gFA$ , and average weighted inverse  $ADC$ .

### ***Between-group comparison***

Between-group statistical differences of network and connectivity measures defined in the previous paragraphs were evaluated using the non-parametric Wilcoxon rank-sum test ( $WRS$ ) test (Wilcoxon, 1945; Wolfe, 2012), setting the significance level  $\alpha = 0.05$ . When necessary (for instance, when testing node-wise closeness centrality, local efficiency, and centrality ranking) multiple comparison correction was applied by controlling the false discovery rate ( $FDR$ ) at  $\alpha = 0.05$  (Benjamini & Hochberg, 1995; Meskaldji *et al.*, 2013). The null hypothesis that the affected core topological centrality  $\zeta_{a-core}^w$  of each group of subjects came from a distribution with zero-median was tested with the non-parametric Wilcoxon signed-rank ( $WSR$ ) test (Wilcoxon, 1945; Wolfe, 2012). The correlations between the node centrality rankings of the paired groups ( $CTRL_{EP}, EP$ ) and ( $CTRL_{SCHZ}, SCHZ$ ) were evaluated using the Spearman's rank correlation coefficient  $\rho$ . In order to limit the effect of possible confounding factors, the groups of subjects were carefully matched by age, gender and handedness. Accordingly, covarying by these three variables did not change the outcomes of the statistical tests performed in this study. In order to assess statistical dependencies between a-core measures (a-core topological centrality  $\zeta_{a-core}^w$ ,  $wgFA$  averaged within the a-core, or  $wiADC$  averaged within the a-core), and subject type ( $CTRL, EP$  and  $SCHZ$ ) or early psychosis disease severity ( $EP_a$ : low number of hospitalizations corresponding to lower disease severity;  $EP_b$ : high number of hospitalizations corresponding to higher disease severity; see section 4.1.4), generalized linear models ( $GLM$ ) including age and gender as covariates were tested. Finally, previous studies suggested a possible relationship between grey and white matter alterations and medication (Moncrieff & Leo, 2010; Smieskova *et al.*, 2009; Szeszko *et al.*, 2013). The relationship between all the network measures evaluated in this study and the  $CPZ$  dose equivalents were therefore assessed for the schizophrenia and early psychosis groups by means of the Spearman's rank correlation coefficient  $\rho$ .

### 4.1.4 Results

#### *System-level analysis*

First, global integration and segregation properties of the brain connectivity network were investigated in patients and healthy subjects. The global efficiency and the transitivity measures were both decreased in schizophrenia patients compared to controls ( $p=0.0086$ ,  $p=0.0042$ ). In contrast, no difference was present when comparing the  $CTRL_{EP}$  and  $EP$  groups. Transitivity and efficiency value dispersions for the four groups  $CTRL_{EP}$ ,  $EP$ ,  $CTRL_{SCHZ}$  and  $SCHZ$  are shown in figure 4.4.

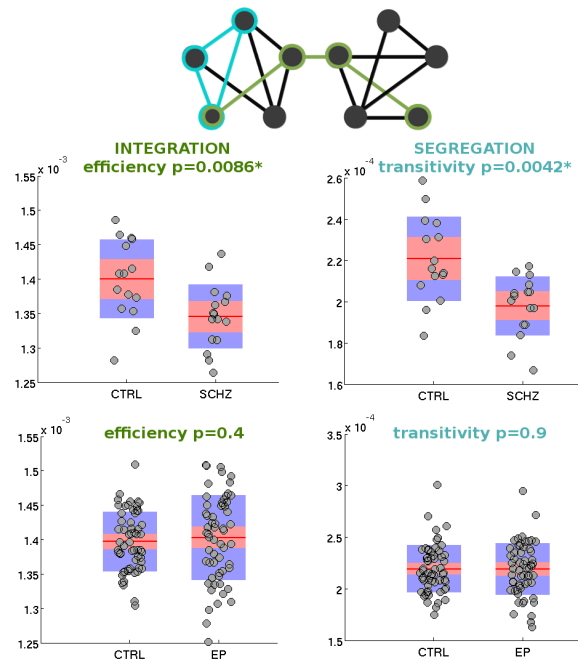


Figure 4.4 – Integration and segregation global network properties in healthy subjects ( $CTRL_{SCHZ}$ ,  $CTRL_{EP}$ ), schizophrenia ( $SCHZ$ ) and early psychosis ( $EP$ ) patients. First row: schematic representation of network integration and segregation properties (adapted from (Bullmore & Sporns, 2009)). The green line highlights the shortest path between two distant nodes; the blue line highlights a local triangles. Box plots: the red line indicates the groups mean; the pink area represents the 95% confidence interval. P-values from two-sided *WRS* tests are reported.

#### *Identification of an affected core in SCHZ patients*

Thereafter, local integration and segregation properties were assessed. In order to identify the brain regions that mostly contribute to the loss of global topological properties in schizophrenia patients, the single nodes were tested for decreased closeness centrality and decreased local efficiency (one-side *WRS* test, comparison between the  $CTRL_{SCHZ}$  and  $SCHZ$  groups). The investigation of the local integration and segregation properties allowed identifying a set of nodes compromised in schizophrenia patients. Such affected core was defined as the set of nodes presenting a significant decrease in nodal closeness centrality  $L_i^{-1}$  or local efficiency  $Eff_{loc(i)}$ , surviv-

ing multiple comparison correction at  $FDR = 0.05$ . The affected core included fronto-basal (bilateral medial orbitofrontal and left lateral orbitofrontal), middle frontal (bilateral caudal middle frontal, right rostral middle frontal) and inferior frontal (right pars triangularis, left pars orbitalis and left pars opercularis) cortices, left precentral cortex, parietal (bilateral postcentral region, right supramarginal and precuneus, left superiorparietal) and left temporal-occipital (lateral occipital, middle temporal, inferior temporal) areas, the basal ganglia (bilateral caudate, pallidum and accumbens areas, right putamen), and the left thalamus. Figure 4.5 shows the FDR-corrected p-values from closeness centrality comparisons ( $CTRL_{SCHZ}$  vs  $SCHZ$ ) for the cortical regions belonging to the affected core. Local efficiency and closeness centrality values for the a-core regions are as well listed in table 4.2, together with their between-group statistics ( $CTRL_{SCHZ}$  vs  $SCHZ$ ). The affected core encompassed 26 regions involving approximately 30% of the whole brain network nodes. There was no evidence for increased nodal closeness centrality or local efficiency in schizophrenia patients compared to matched controls in any of the 82 cortical and subcortical regions.

Nodal integration and segregation measures were computed for each early psychosis patient and healthy control. None of the 82 brain regions' between-group comparison ( $CTRL_{EP}$  vs  $EP$ ) of nodal closeness centrality and local efficiency survived multiple comparison correction.

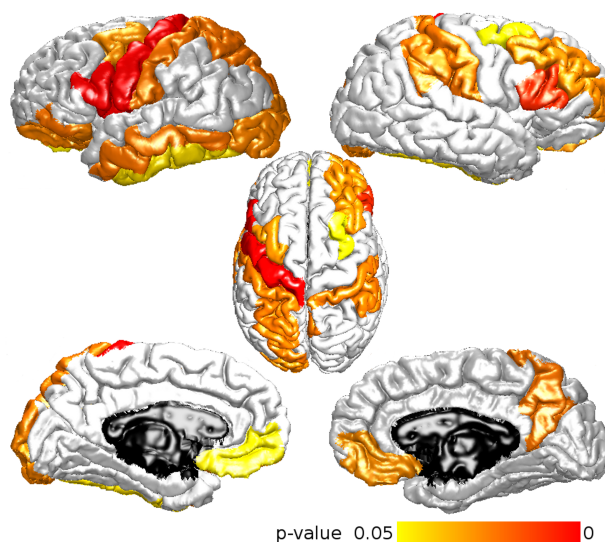


Figure 4.5 – Surface representation of the cortical areas belonging to the affected core (in color), that is, presenting an alteration of segregation and/or integration properties in schizophrenia patients. Colormap: p-values for significantly decreased closeness centrality in  $SCHZ$  compared to  $CTRL_{SCHZ}$  (one-side  $WRS$  test), corrected for multiple comparison ( $FDR$  control procedure (Benjamini & Hochberg, 1995)).

### ***Topological role of the affected core***

In order to further investigate the brain network organization and the role of the identified a-core within the overall brain topology for both schizophrenia and early psychosis patients, we studied the degree of centrality of the different brain regions within the individual brain networks. Particularly, brain nodes were ranked according to their closeness centrality values in order to identify hubs regions (Sporns *et al.*, 2007), and to evaluate the topological position of the a-core regions within the overall brain network, in the different groups. We tested eventual hubs alter-



Affected core brain regions	<i>CTRL</i> <sub>SCHZ</sub>	<i>SCHZ</i>	FDR-corrected
	Closeness centrality	Closeness centrality	p-values
Rh medialorbitofrontal	0.00137 ± 0.00010	0.00126 ± 0.00014	0.0243*
Rh parstriangularis	0.00123 ± 0.00015	0.00107 ± 0.00021	0.0355*
Rh rostralmiddlefrontal	0.00115 ± 0.00010	0.00103 ± 0.00013	0.0251*
Rh caudalmiddlefrontal	0.00118 ± 0.00012	0.00099 ± 0.00010	0.0111*
Rh postcentral	0.00111 ± 0.00010	0.00100 ± 0.00013	0.0268*
Rh supramarginal	0.00088 ± 0.00010	0.00077 ± 0.00008	0.0268*
Rh precuneus	0.00107 ± 0.00011	0.00100 ± 0.00008	0.0268*
Rh caudate	0.00140 ± 0.00011	0.00129 ± 0.00012	0.0268*
Rh putamen	0.00146 ± 0.00012	0.00131 ± 0.00014	0.0215*
Rh pallidum	0.00145 ± 0.00011	0.00128 ± 0.00009	0.0111*
Rh accumbensarea	0.00138 ± 0.00012	0.00126 ± 0.00011	0.0251*
Lh lateralorbitofrontal	0.00113 ± 0.00011	0.00100 ± 0.00012	0.0251*
Lh parsorbitalis	0.00117 ± 0.00019	0.00102 ± 0.00016	0.0268*
Lh medialorbitofrontal	0.00135 ± 0.00010	0.00124 ± 0.00010	0.0132*
Lh parsopercularis	0.00121 ± 0.00019	0.00106 ± 0.00019	0.0403*
Lh caudalmiddlefrontal	0.00116 ± 0.00010	0.00104 ± 0.00010	0.0241*
Lh precentral	0.00141 ± 0.00013	0.00131 ± 0.00012	0.0403*
Lh postcentral	0.00113 ± 0.00012	0.00103 ± 0.00010	0.0268*
Lh superiorparietal	0.00119 ± 0.00014	0.00103 ± 0.00016	0.0268*
Lh lateraloccipital	0.00088 ± 0.00015	0.00074 ± 0.00010	0.0251*
Lh inferiortemporal	0.00093 ± 0.00013	0.00077 ± 0.00011	0.0150*
Lh middletemporal	0.00094 ± 0.00016	0.00079 ± 0.00011	0.0268*
Lh thalamusproper	0.00150 ± 0.00012	0.00136 ± 0.00012	0.0251*
Lh caudate	0.00140 ± 0.00009	0.00128 ± 0.00009	0.0157*
Lh pallidum	0.00144 ± 0.00013	0.00130 ± 0.00010	0.0215*
Lh accumbensarea	0.00133 ± 0.00014	0.00120 ± 0.00011	0.0268*

	<i>CTRL</i> <sub>SCHZ</sub>	<i>SCHZ</i>	FDR-corrected
	Local efficiency	Local efficiency	p-values
Rh medialorbitofrontal	0.00073 ± 0.00023	0.00059 ± 0.00016	0.1289
Rh parstriangularis	0.00050 ± 0.00016	0.00047 ± 0.00016	0.3457
Rh rostralmiddlefrontal	0.00045 ± 0.00011	0.00038 ± 0.00007	0.1180
Rh caudalmiddlefrontal	0.00060 ± 0.00022	0.00054 ± 0.00013	0.4096
Rh postcentral	0.00047 ± 0.00012	0.00044 ± 0.00011	0.3514
Rh supramarginal	0.00058 ± 0.00013	0.00044 ± 0.00008	0.0449*
Rh precuneus	0.00038 ± 0.00006	0.00031 ± 0.00004	0.0914
Rh caudate	0.00069 ± 0.00015	0.00055 ± 0.00013	0.0617
Rh putamen	0.00075 ± 0.00014	0.00065 ± 0.00009	0.0859
Rh pallidum	0.00065 ± 0.00013	0.00058 ± 0.00017	0.1107
Rh accumbensarea	0.00075 ± 0.00024	0.00068 ± 0.00017	0.2953
Lh lateralorbitofrontal	0.00039 ± 0.00006	0.00035 ± 0.00012	0.1798
Lh parsorbitalis	0.00057 ± 0.00032	0.00049 ± 0.00017	0.4043
Lh medialorbitofrontal	0.00061 ± 0.00024	0.00055 ± 0.00015	0.4379
Lh parsopercularis	0.00070 ± 0.00021	0.00055 ± 0.00017	0.0914
Lh caudalmiddlefrontal	0.00061 ± 0.00012	0.00052 ± 0.00011	0.0942
Lh precentral	0.00085 ± 0.00012	0.00072 ± 0.00011	0.0449*
Lh postcentral	0.00045 ± 0.00009	0.00042 ± 0.00010	0.1798
Lh superiorparietal	0.00033 ± 0.00007	0.00032 ± 0.00007	0.2478
Lh lateraloccipital	0.00029 ± 0.00005	0.00024 ± 0.00006	0.1232
Lh inferiortemporal	0.00041 ± 0.00011	0.00030 ± 0.00012	0.0617
Lh middletemporal	0.00042 ± 0.00011	0.00038 ± 0.00008	0.2953
Lh thalamusproper	0.00068 ± 0.00011	0.00062 ± 0.00017	0.1232
Lh caudate	0.00068 ± 0.00021	0.00058 ± 0.00014	0.2184
Lh pallidum	0.00069 ± 0.00011	0.00056 ± 0.00013	0.0617
Lh accumbensarea	0.00076 ± 0.00017	0.00070 ± 0.00026	0.2225

Table 4.2 – Closeness centrality and local efficiency values for brain nodes belonging to the affected core. Group-average values ± one standard deviation are reported for the *CTRL*<sub>SCHZ</sub> and *SCHZ* groups. The region labels have been defined as in FreeSurfer, Desikan- Killiany atlas (Desikan *et al.*, 2006). The last column lists FDR-corrected p-values from between-group comparison (*WRS* one-side statistical test.)

ations in patient groups compared to controls by (i) computing the Spearman's rank correlation coefficient  $\rho$  between the average group-wise nodal closeness centrality ranking, and (ii) by comparing node-wise closeness centrality ranking  $r_i$  within subject-wise networks between groups. No significant difference in terms of nodes ranking  $r_i$  was found between the groups  $CTRL_{SCHZ}$  and  $SCHZ$  (node-wise  $WRS$  test,  $\alpha = 0.05$ ,  $FDR = 0.05$ ), and  $CTRL_{EP}$  and  $EP$  (node-wise  $WRS$  test,  $\alpha = 0.05$ ,  $FDR = 0.05$ ). The Spearman's rank correlation coefficients between the group-wise average ranking of the nodes were  $\rho = 0.94$  ( $CTRL_{SCHZ}$  vs  $SCHZ$ ) and  $\rho = 0.98$  ( $CTRL_{EP}$  vs  $EP$ ). This quantitative analysis suggested no significant alteration of node centrality ranking and hubs position between the investigated groups. Figure 4.6 represents the average nodal closeness centrality for the healthy, early psychosis and schizophrenia subjects. In order to visually compare the nodal ranking position among the three groups, nodes are ordered according to average closeness centrality ranking (descending order) over the complete group of 68 healthy subjects ( $CTRL_{EP} + CTRL_{SCHZ}$ ). Regions belonging to the affected core are represented in darker colors. 10 of the 26 regions belonging to the identified a-core (i.e. approximately 40% of the a-core regions) positioned themselves among the most central brain nodes (hubs), while the other regions of the a-core were more peripheral.

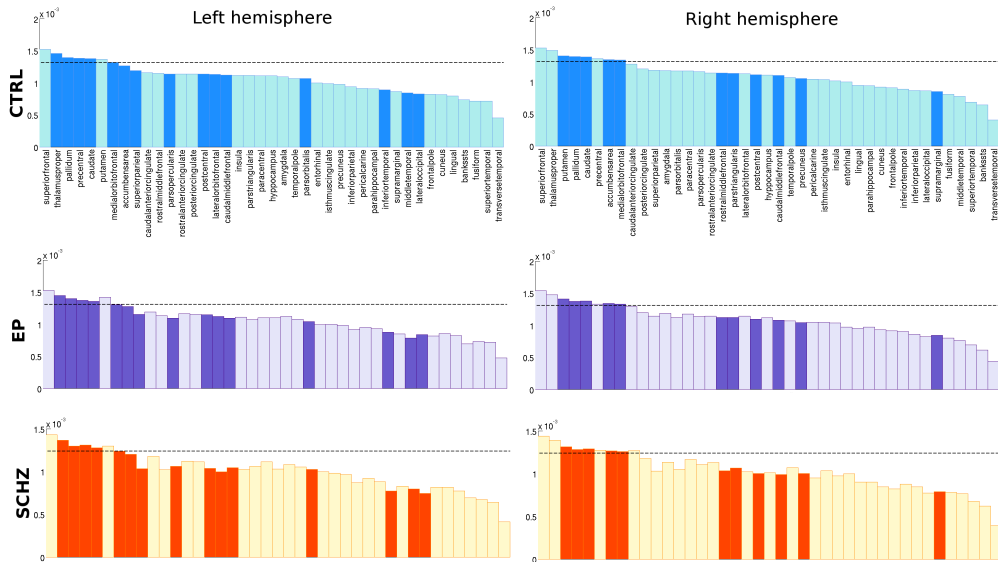


Figure 4.6 – Ranking of the average node-wise closeness centrality values for the three groups,  $CTRL$  (including  $CTRL_{EP}$  and  $CTRL_{SCHZ}$ , first row),  $EP$  (second row) and  $SCHZ$  (third row). Left column: left hemisphere nodes; right column: right hemisphere nodes. Hub nodes are concentrated on the left part of the bar plot, and surpass the dotted line (representing the group average closeness centrality, plus one standard deviation). Darker bars represent nodes belonging to the affected core. In the figure the nodes ordering for the  $EP$  and  $SCHZ$  groups corresponds to the  $CTRL$  node descending ranking.

We next examined the topological centrality of the affected core within the overall brain network by means of the measure  $\zeta^w$ . The a-core topological centrality was significantly lower than zero for all the considered groups ( $WSR$  test,  $p < 0.0002$ ), indicating that a targeted attack towards the affected core nodes had a more severe impact on the overall brain communication capacity than a random attack towards a comparable number of network resources (nodes and edges). Moreover,  $\zeta^w_{a-core}$  was higher (closer to zero) in schizophrenia patients compared to matched controls ( $WRS$  test,  $p = 0.004$ ), indicating a weakening of the a-core topological role

in schizophrenia patients (figure 4.7b). Since in the schizophrenia patients the a-core is already weakened compared to matched controls, the impact of a targeted attack towards the a-core is less harmful in patients than in controls. The average a-core topological centrality of *EP* patients was higher (closer to zero) than matched healthy controls, but the comparison did not reach statistical significance (*WRS* test,  $p = 0.07$ , figure 4.7c).

Finally, the shortest paths layout related to the affected core was compared between the investigated groups of subjects. A shortest path is a favourable path, in terms of network distance, between two brain regions, and represents a probable pathway of communication between two nodes (Bullmore & Sporns, 2012; van den Heuvel *et al.*, 2012). Considering the shortest paths connecting nodes external to the a-core only, the number  $n_{a-core}^{SP}$  of paths passing through the a-core was decreased in schizophrenia patients compared to matched controls ( $p = 0.008$ ). On the contrary, and by consequence, the number of shortest paths  $n_{out-a-core}^{SP}$  not passing through the a-core was increased in schizophrenia patients compared to matched controls ( $p = 0.008$ ) (figure 4.8). These findings are in line with the definition of the a-core (decreased closeness centrality and local efficiency), and highlight an alteration of the communication pathways, as represented by shortest paths, in schizophrenia patients. In contrast, no alteration of the shortest path layout, as quantified through the number of shortest path throughout and outside the a-core, was highlighted in early psychosis patients compared to matched healthy controls.

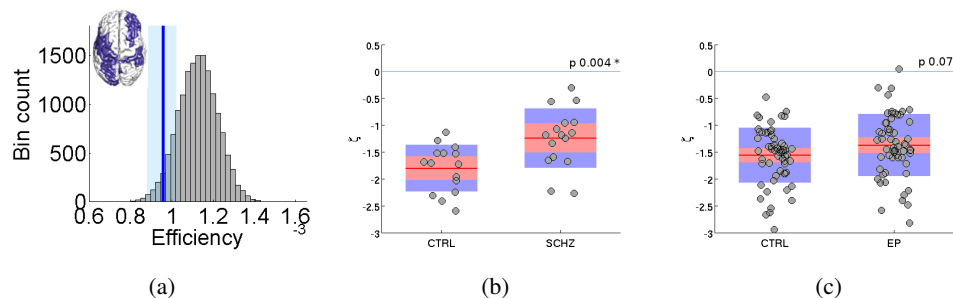


Figure 4.7 – Effect of random and targeted attack on healthy subjects, schizophrenia, and early psychosis patients brain networks. a) Histogram representing the group-wise distribution of the efficiency values after  $n_{rep} = 1000$  repetitions *per* subject of random attacks, for the control group. The blue line and light blue area in (a) represent the mean efficiency values after targeted attack towards the a-core,  $\pm 1$  standard deviation. b,c) Box plots representing the a-core topological centrality values for the groups ( $CTRL_{SCHZ}, SCHZ$ ) (b) and ( $CTRL_{EP}, EP$ ) (c).  $\zeta_{a-core}^w$  values were significantly smaller than zero for all the four groups (*WSR* test,  $\alpha = 0.05$ ). The topological centrality  $\zeta_{a-core}^w$  of *SCHZ* patients was significantly decreased compared to matched controls ( $p = 0.004$ ), while the comparison did not reach statistical significance for the *EP* group ( $p = 0.07$ ).

### Quantitative characterization of the affected core

The affected core of the schizophrenia brain network was identified as the set of regions showing decreased integration or segregation properties. The a-core includes hubs and peripheral regions, and globally plays an important role for the achievement of high global network communication efficiency. The centrality of the affected core was compromised in schizophrenia patients. In the early psychosis patients the (absolute) topological centrality of the affected core was lower than in matched healthy controls, but the comparison did not reach statistical significance (figure 4.7). In order to further characterize the affected core and the white matter tracts connecting a-core regions, white matter indexes averaged within and outside the affected core connections

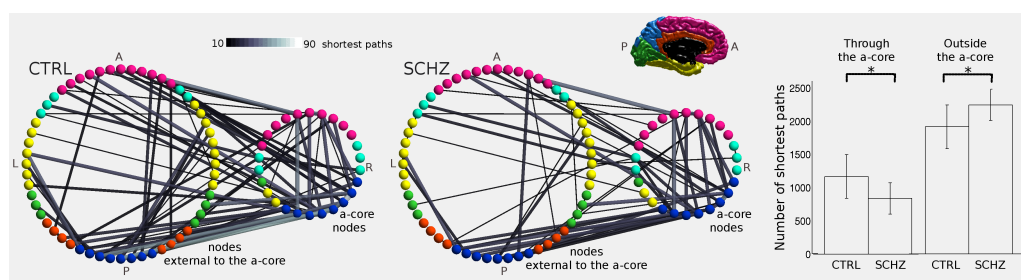


Figure 4.8 – Communication pathways throughout the affected core. The figure represents the average shortest paths layout between nodes not belonging to the affected core, for schizophrenia patients (*SCHZ*) and matched healthy controls (*CTRL<sub>SCHZ</sub>*). Only shortest paths between nodes not belonging to the a-core, but passing through the a-core, are represented. The edge color and thickness represent the number of shortest paths passing through the specific edge, averaged over the two groups of subjects. The nodes are grouped according to their a-core membership, and color-coded according to their lobe membership. It is possible to visually appreciate that the average number of shortest paths passing through the a-core is decreased in patients compared to controls. The bar plots report the number of shortest paths between nodes not belonging to the a-core, and passing or not passing through the a-core (group-wise median values  $\pm 1$  standard deviation), for the *CTRL* and the *SCHZ* groups. \* indicates significant between-group difference. No alteration of number of shortest paths throughout or outside the affected core was detected in early psychosis patients (*EP*) compared to matched healthy controls (*CTRL<sub>EP</sub>*).

were estimated and compared between the groups. The following white matter indicators were considered: (i) generalized fractional anisotropy weighted by the size of the fiber tract (*wgFA*); (ii) inverse apparent diffusion coefficient weighted by the size of the fiber tract (*wiADC*). Indeed, in order to capture the importance of tract size, *gFA* and *ADC* values were weighted by the tract size, expressed as effective number of fibers  $n_{uv}$ . The *wgFA* and *wiADC* measures were averaged over all the connections between a-core regions ('within a-core'), and over all the connections between regions not belonging to the a-core ('outside a-core'). The weighted generalized fractional anisotropy and the weighted inverse apparent diffusion coefficient were altered in both schizophrenia and early psychosis patients compared to matched healthy controls, when averaged within the a-core (*wgFA*: *SCHZ* – *CTRL<sub>SCHZ</sub>*  $p = 0.007$ , *EP* – *CTRL<sub>EP</sub>*  $p = 0.005$ ; *wiADC*: *SCHZ* – *CTRL<sub>SCHZ</sub>*  $p = 0.004$ , *EP* – *CTRL<sub>EP</sub>*  $p = 0.003$ ). No between-group difference was found when considering the average *wgFA* and *wiADC* over the connections external to the a-core (figure 4.9). Average white matter indexes for the overall brain connections, within a-core connections, and outside a-core connections, and relative statistics are reported in table 4.1.

### Affected core across psychosis stages

In order to assess affected core impairment across psychosis stages, we performed two kinds of analyses. First, we built different generalized linear models to assess the relationship between single a-core measures (namely, a-core topological centrality  $\zeta_{a-core}^w$ ; number of shortest paths  $n_{a-core}^{SP}$  between nodes not belonging to the a-core, but passing through the a-core; average *wgFA* over a-core connections; average *wiADC* over a-core connections) and the subject type (*CTRL*, *EP* and *SCHZ*). Moreover, with equivalent GLMs we tested eventual dependencies between the global network efficiency *Eff*, the network transitivity *T*, the average *wgFA* outside the a-core and the average *wiADC* outside the a-core, and the subject type *CTRL/EP/SCHZ*. Given the heterogeneity of the subjects included in the different groups, age and gender were included as covariates in the GLMs. We found a significant relationship between all the tested a-core

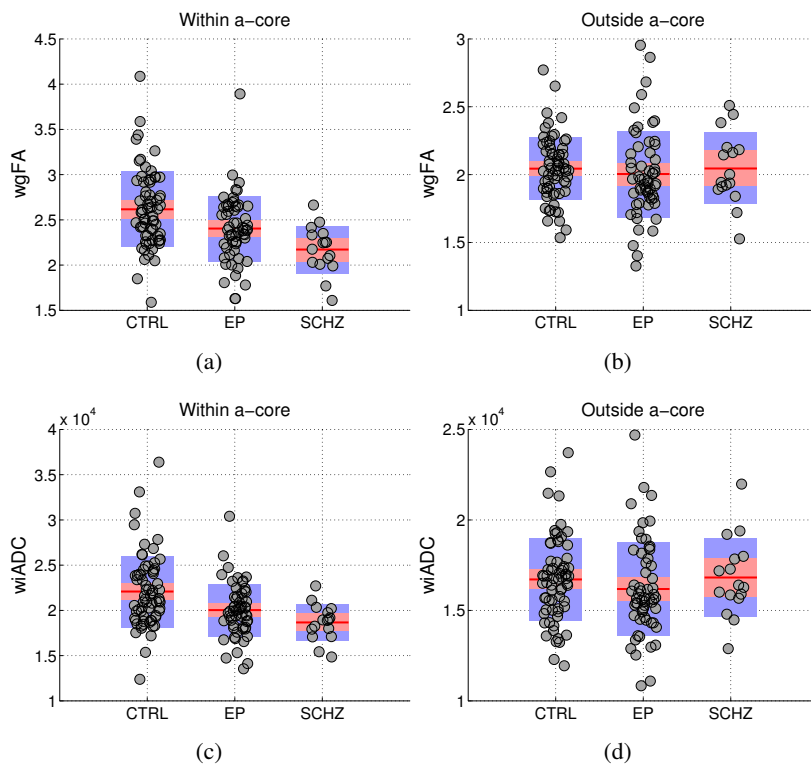


Figure 4.9 – Box plots representing white matter indexes dispersion when averaged within the a-core connections (left column, (a,c)), and over the connections outside the a-core (right column, (b,d)), for the different groups *CTRL* ( $CTRL_{SCHZ}$  and  $CTRL_{EP}$  are pooled together), *EP* and *SCHZ*. The following indexes are reported: average *gFA* values weighted by the size of the tracts (*wgFA*); average inverse *ADC* weighted by the size of the tract (*wiADC*).

measures and the subject type (from separate GLMs,  $\zeta_{a-core}^w$ :  $p = 0.002$ ;  $n_{a-core}^{SP}$ :  $p = 0.03$ ; a-core  $wgFA$ :  $p = 0.00005$ ; a-core  $wiADC$ :  $p = 0.00003$ ). On the contrary, no statistical relationship between network transitivity  $T$ , average  $wgFA$  outside the a-core or average  $wiADC$  outside the a-core from one side, and subject type from the other side was present. The global network efficiency  $Eff$  demonstrated a decreasing trend across groups  $CTRL$  to  $EP$  to  $SCHZ$ , but the relationship did not reach statistical significance ( $p = 0.06$ ).

Second, we subdivided the early psychosis patients into two groups on the basis of the number of hospitalizations occurred before the MRI acquisition. We considered here the number of hospitalizations as possible indicator of illness severity. The first group ( $EP_a$ ) included 27 early psychosis patients with 0 or 1 hospitalization (8 subjects with no hospitalization history and 19 subjects with 1 hospitalization); the second group ( $EP_b$ ) included 32 early psychosis patients with more than 1 hospitalization (mean number of hospitalizations  $3.0 \pm 1.8$ ). Considering the a-core measures topological centrality, average  $wgFA$  and average  $wiADC$ , we performed the following between-group comparisons:  $EP_a$  vs  $CTRL_{EP}$ ,  $EP_b$  vs  $CTRL_{EP}$  and  $EP_a$  vs  $EP_b$ . No significant differences were present between the two early psychosis sub-groups  $EP_a$  and  $EP_b$ . The a-core topological centrality  $\zeta_{a-core}^w$  of  $EP_b$  subjects was closer to zero compared to matched healthy controls, but the comparison did not reach statistical significance ( $p = 0.07$ ) (figure 4.10). The average  $wgFA$  within the a-core, and the average  $wiADC$  within the a-core were both decreased in  $EP_b$  compared to controls (in the order:  $p = 0.07$ ,  $p = 0.007$ ,  $p = 0.008$ ). Moreover,  $wgFA$  and  $wiADC$  were as well decreased in  $EP_a$  compared to controls. Figure 4.10 exemplifies the global trend of progressive worsening of a-core measures (from  $CTRL$  to  $EP_a$  to  $EP_b$  to  $SCHZ$ ), quantified by means of GLMs and between-group comparisons. These results suggest that the identified affected core is precociously and progressively altered across psychosis conditions.

No correlation was found between any connectivity measure considered in this Results section and the CPZ equivalent dose.

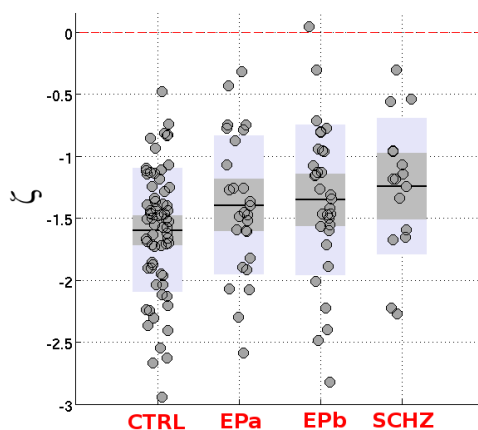


Figure 4.10 – Dispersion of a-core topological centrality values  $\zeta_{a-core}^w$  for the four groups: control  $CTRL$ , early psychosis with 0 or 1 hospitalization history ( $EP_a$ ), early psychosis with a more severe hospitalization history ( $EP_b$ ), chronic schizophrenia  $SCHZ$ . A GLM including subject group, age and gender as independent variables, and the a-core topological centrality  $\zeta_{a-core}^w$  as dependent variable highlighted a significant relationship between the group and the a-core topological centrality ( $p = 0.02$ ).

### 4.1.5 Discussion

The main contribution of the present study was to further characterize the connectome in schizophrenia with (i) the identification of a distributed set of affected regions (the affected core or a-core), main responsible for the loss of global integration and segregation network properties; (ii) the topological characterization of the affected core within the overall brain network architecture; and (iii) the investigation of white matter markers along the affected core tracts. Moreover, we (iv) investigated a-core measures in a group of early psychosis patients who underwent the same MRI protocol as schizophrenia subject. The early psychosis patients did not show any global brain network alteration, but demonstrated an already impaired affected core. Based on this results, we propose affected core measures as possible psychosis biomarkers for early diagnosis and illness progression tracing.

Based on the brain probability map of figure 4.5, we observe that schizophrenia affects connectivity in large parts of prefrontal, pericentral, superior parietal areas and striatum in both hemispheres, as well as left temporo-occipital and thalamic areas, which is in good agreement with previous literature of grey and white matter alterations (see for instance (Canu *et al.*, 2015; Shepherd *et al.*, 2012; van den Heuvel *et al.*, 2010; Zalesky *et al.*, 2011)). By definition the affected core of schizophrenia patients comprises regions presenting decreased local integration and segregation properties (surviving FDR correction), with a preponderance of integration deficit (table 4.2). These nodes exhibit the strongest altered connectivity patterns, and accordingly play a major role with respect to the decline of the global topological properties observed in schizophrenia patients.

At the global level the schizophrenia connectome exhibited decrease network efficiency, indicating an overall deficit of functional integration in the network, and in agreement with previous studies (van den Heuvel & Fornito, 2014). The transitivity measure was as well decreased in schizophrenia patients compared to controls, indicating an overall altered level of local connectedness. Anyway, no alteration of global network efficiency or transitivity was detectable in early psychosis patients. Various diffusion-based studies have reported a less integrated and more segregated network in schizophrenia neuropathology (van den Heuvel & Fornito, 2014). A tendency towards increased, or unchanged overall clustering coefficient has also been reported (Zalesky *et al.*, 2011). In the present study no brain region showed any increased level of segregation in patients compared to controls. Discrepancies between studies might be attributed to the use of different imaging sequences, different edge weights or different network binarization strategies.

The affected core identified in this study includes parts of the default mode network (Greicius *et al.*, 2009) (medial prefrontal regions), of the rich-club (van den Heuvel *et al.*, 2012) (right precuneus, left superior parietal cortex), and of high degree cores of the human connectome (Hagmann *et al.*, 2008; van den Heuvel & Sporns, 2011), particularly subcortical and medial orbitofrontal structures (table 4.2, figure 4.5). The rich-club nodes have recently been the center of growing attention, and have been shown to be disproportionately affected in pathological conditions compared to less central brain regions (Crossley *et al.*, 2014; Rubinov & Bullmore, 2013b; van den Heuvel & Fornito, 2014). The rich-club has been shown to be altered in schizophrenia patients (van den Heuvel *et al.*, 2013), and in unaffected siblings of schizophrenia patients (Collin *et al.*, 2014a). Consistently, the affected core partially overlap rich-club regions.

Despite the weakening of highly central regions (part of the affected core), the overall nodes centrality hierarchy was not altered in schizophrenia, nor in early psychosis patients compared to healthy controls. Node hubness was related to the node-wise closeness centrality ranking. Hubs can be identified as those nodes whose centrality measure exceeds the average value of at least one standard deviation (Sporns *et al.*, 2007; van den Heuvel & Sporns, 2011). Figure 4.6 illus-

trates the position of the a-core regions within the centrality ranking of the brain network nodes for the three investigated groups (controls, early psychosis and schizophrenia subjects), with dot lines indicating group-wise mean closeness centrality value plus one standard deviation. Considering the node centrality ranking of the reference control group, the affected core includes 10 of the 15 brain hubs (approximately 65% of the whole network hubs), and 16 of the 67 non-hub regions (approximately 25% of the whole network non-hub nodes). Hence our results confirm that hub regions are disproportionately affected compared to more peripheral regions. Anyway, schizophrenia neuropathology would not selectively affect hubs regions only. It is noteworthy to observe that a-core nodes do concentrate over the left part of the closeness centrality histograms (higher centrality nodes), but span as well towards the lower-centrality area, therefore including more peripheral nodes (figure 4.6). As such, these findings corroborate the hypothesis that schizophrenia is characterized by the breakdown of distributed brain circuits including central and peripheral brain regions, all contributing to the overall decrease of network communication efficiency (figure 4.7). Significant pathophysiological hypotheses link schizophrenia with the high vulnerability of brain network hubs to metabolic insults (Bullmore & Sporns, 2012; Do *et al.*, 2009; Rubinov & Bullmore, 2013b). Additional complex, yet unknown, mechanisms might explain the involvement of non-hub regions. Our findings suggest that schizophrenia might be not solely, or not specifically a hub disease.

The characterization of the affected core and related shortest paths allowed highlighting different aspects of the brain network topological organization in schizophrenia and early psychosis patients compared to healthy controls (figures 4.7, 4.8). The topological centrality values  $\zeta_{a-core}^w$  significantly lower than zero for all the investigated groups (figure 4.7), suggest that the a-core subnetwork plays a distinct role in the maintenance of the brain network communication capacity, since its removal impacts the overall network communication efficiency more than expected by chance. Moreover, the topological centrality of the a-core subnetwork is weakened in schizophrenia patients compared to matched controls. In fact, removing from the overall brain network nodes that already suffer dysconnectivity has a smaller impact than removing nodes with normal connectivity. The between-group alteration of the  $\zeta_{a-core}^w$  values in schizophrenia patients suggests a topological decentralization of the a-core regions, associated to a modification of the brain network shortest paths layout and to a redistribution of the relative connection weights. The number of shortest paths passing through the affected core was reduced in schizophrenia patients compared to controls (figure 4.8). Globally, these findings indicate a weakening of the functional role of the identified affected core with respect to the global brain network architecture. This topological configuration leads to a less efficient global network topology.

The decentralization of the affected core subnetwork may be related to white matter alterations concentrated over the a-core connections. The decrease of  $wgFA$  and  $wiADC$  values along the affected core tracts may in fact suggest a disruption of the WM microstructure possibly specific to the affected core circuits. Indeed, no alteration of  $wgFA$  or  $wiADC$  was found when considering fiber tracts external to the a-core. These results suggest an intrinsic white matter alteration of a-core regions, that could be related to the topological decentralization of the a-core subnetwork, and may already be present in the earlier stages of the pathology.

Although no system-level or node-wise alterations of integration and segregation properties were detected in early psychosis patients compared to healthy controls, white matter impairment of the a-core circuit was evident when investigating within a-core  $wgFA$  and  $wiADC$  values (figure 4.9). Moreover, GLMs including a-core measures across different pathological stages (from early psychosis to chronic schizophrenia) suggest that the impairment of the a-core brain subnetwork is progressive and worsen in time, eventually leading to a global brain network efficiency loss that it is not yet traceable in the earlier stages of the disease. The progressive decentralization of the a-core subnetwork (figure 4.10) linked to white matter alterations (figure 4.9) may be



important factors for the identification of early disease biomarkers, and for the characterization of pathological stages. In support of this hypothesis, the affected core turned to be more impaired in early psychosis patients with a more severe history of hospitalization, and possibly corresponding to a more severe stage of the disease (figure 4.10). Staging in psychotic disorders is clinically relevant for tailoring particular care to the severity of the disease. Importantly, the analysis pipeline and the topological centrality measure proposed in this thesis may help identifying biomarkers of illness progression, or characterizing specific stages of illness.

This study has several limitations. Firstly, for most aspects of this report, the connection strength characterization relies on a normalized version of the connectivity density between region pairs. Although the proposed normalization allows focusing on network topology rather than on absolute connectivity strength alterations, and allows reducing the inter-subjects variability, it does not directly take into account white matter microstructural properties. Hence we cannot distinguish whether the observed topological alterations observed in the schizophrenia connectome are related to an intrinsic pathology of the white matter, to an imbalance and redistribution of white matter tracts, and/or to compensatory effects. However, we quantitatively studied the connectivity strength of the a-core with diffusion-based white matter markers (*gFA*, *ADC*), which were clearly diminished in patients. This result suggests the presence of intrinsic white matter microstructural alterations of the a-core connections. However, the use of more specific, possibly multimodal white matter markers and sensitive MR sequences such as magnetization transfer ratio or T2\* relaxation (Laule *et al.*, 2007), or new diffusion-based quantitative techniques (Alexander, 2008; Assaf *et al.*, 2013), could potentially address this issue in a more complete way. Secondly, the restricted size of the sample limits the statistical power and the expected robustness of the findings. This may have as a consequence the under-estimation of the size of the affected network. The replication of the presented findings on larger, possibly independent datasets would definitively be desirable. Thirdly, this study offers a partial vision of schizophrenia pathoconnectomics (Rubinov & Bullmore, 2013a), focusing on relative network organizational principles, and shortest paths framework. Alternative visions of brain communication mechanisms such as random walk processes (Goñi *et al.*, 2013) could offer new interpretations of pathological configurations.

In conclusion, we characterized the network topology underlying the disruption of global network communication capacity observed in schizophrenia. The previously reported loss of global structural network integration is confirmed. A set of distributed nodes, which drive this global efficiency loss in schizophrenia patients, is identified as the affected core of schizophrenia. Through the failure of these core nodes the topology of the schizophrenia connectome is modified in a way that the shortest path layout is redistributed, yielding a more decentralized network. The affected core of patients is characterized by microstructural changes of its connections as measured with *gFA* and *ADC*, leading to the above described topological changes. Moreover, this study investigates the evolution of brain network alteration across different phases of the pathology, from early psychosis to chronic schizophrenia. An hypothesis-driven investigation of the early psychosis cohort targeted to the a-core regions allowed identifying early, subtle connectivity alterations confined to the a-core subnetwork. We propose a-core network measures as possible markers of illness progression, while loss of global network efficiency and transitivity might characterize the advanced stages of the disease.

## 4.2 Applications

### Identifying the affected core of 22q11 deletion syndrome

#### 4.2.1 Purposes

The 22q11.2 deletion syndrome (*22q11DS*) is considered an endophenotype of schizophrenia. A high percentage of patients suffering from this syndrome develop schizophrenia or other psychotic disorders later in life. In line with our study on early psychosis and schizophrenia patients (section 4.1), in this section we investigate a cohort of *22q11DS* patients. We adopt the very same analysis pipeline developed for schizophrenia patients (section 4.1.3.3), identifying an affected core for *22q11DS* patients. Again, we quantify alterations of the affected core topological role with respect to the overall *22q11DS* brain network architecture by means of the subnetwork centrality measure  $\zeta$  defined in chapter 3.

#### 4.2.2 Introduction

Chromosome 22q11.2 deletion syndrome (*22q11DS*) is a genetic disease generally caused by a 1.5-3 megabase deletion on the long arm of chromosome 22 (Lindsay *et al.*, 1995). It has become an established genetic model for schizophrenia, which approximately 30% of *22q11DS* patients develop (Schneider *et al.*, 2014). Moreover, numerous non-schizophrenic *22q11DS* patients suffer from other psychotic, schizoaffective and delusional disorders (Schneider *et al.*, 2014) and present further schizotypal traits (Baker & Skuse, 2005; Monks *et al.*, 2014), which refer to an endophenotype of schizophrenia (Fanous *et al.*, 2007; Grant *et al.*, 2013). An endophenotype is a class that includes a candidate gene or gene region, heritability aspects, and disease association parameters, and can be usefully investigated as probabilistic prognosticator of disease (Gottesman & Gould, 2003).

Patients with *22q11DS* exhibit overall reductions in brain volume, morphological abnormalities of white and grey matter, and white matter alterations as deduced from diffusion weighted imaging. Impairments are consistently localized in parietal, temporal and frontal lobes (Barnea-Goraly *et al.*, 2003; Campbell *et al.*, 2006; Jalbrzikowski *et al.*, 2013; Kates *et al.*, 2001; Kikinis *et al.*, 2012; Sundram *et al.*, 2010), but involve as well the corpus callosum and midline structures (Simon *et al.*, 2005), and tracts within and between limbic structures and fronto-temporal regions (Ottet *et al.*, 2013a). These findings indicate diffuse and extensive WM alterations in *22q11DS*, following a similar pattern of WM abnormalities observed in schizophrenia patients (Bora *et al.*, 2011; Shepherd *et al.*, 2012).

Ottet and colleagues investigated *22q11DS* brain connectivity maps derived from *DTI* data within a graph-theoretical framework (Meskaldji *et al.*, 2011; Ottet *et al.*, 2013a,b). Comparing binary structural connectivity matrices, they found reduced network density  $\delta$  and increased characteristic path length  $L$  in patients compared to controls, with degree  $k$  loss concentrated in hub regions, and connectivity deficit localized within and between limbic structure, and between left fronto-temporal regions. Moreover, the authors demonstrated a negative correlation between hallucination scores and the local efficiency  $Eff_{loc}$  of a frontal subnetwork, hypothesized to be involved in hallucinations causing (Allen *et al.*, 2008; Ottet *et al.*, 2013b). Functional connectivity alterations have also been shown, with a prevalent involvement of frontal and right temporal areas (Scariati *et al.*, 2014).

The first aim of this analysis was to confirm previous global findings using weighted networks. Additionally, we studied the spatial distribution of regions causing integration deficits, referred to as the affected core, and described its role in disrupting communication efficiency in the *22q11DS* connectome.

### 4.2.3 Methods and Materials

#### *DTI imaging and brain network estimation*

44 participants with *22q11DS* aged  $19.1 \pm 4.7$  years (23 female and 21 males), and 44 healthy controls *CTRL* aged  $18.4 \pm 4.8$  years (23 female and 21 males) participated in the study. The chromosome 22q11.2 deletion was confirmed by analysis of a blood sample with the Quantitative Fluorescent Polymerase Chain Reaction. None of the control subjects had a history of psychiatric or neurological disorders. No age or gender difference was present between the two groups (*WRS* test, see section 4.1.3). Written informed consent was obtained from all participants or their parents. The institutional review board of Geneva University School of Medicine approved the study protocol. The participant sample presents overlap with a recent study by Ottet and colleagues (Ottet *et al.*, 2013b). Specifically, 28 / 44 patients with *22q11DS* (15 / 23 females and 13 / 21 males) and 27 / 44 healthy participants (12 / 23 females and 15 / 21 males) are common to both studies.

All the 88 subjects included in this study underwent an MRI session on a 3 Tesla scanner (Magnetom TrioTim, Siemens Medical Solutions), including an *MPRAGE* acquisition (TR = 2500 ms, TE = 3 ms, acquisition matrix size = 256 x 256 voxels, FOV = 22 cm, slice thickness = 1.1 mm, 192 slices) and a *DTI* sequence (TR = 8300-8800 ms, TE = 82 ms, acquisition matrix size = 128 x 128 voxels, FOV = 25.6 cm, slice thickness = 2 mm, 64 slices) with 30 diffusion-weighted directions, one  $b_0$  volume and maximum b-value  $1000s/mm^2$ .

MRI datasets were processed in order to estimate the overall brain anatomical connectivity. The structural connectivity between each pair  $(u, v)$  of network nodes was quantified by the effective number of streamlines  $n_{u,v}$  connecting the two regions (a correction for the fiber length bias was applied as described in section 4.1.3.3).

#### *Connectivity analysis pipeline*

In order to investigate structural connectivity alterations in *22q11DS* patients, system-, subsystem- and local-scale analyses were performed, similarly to the schizophrenia study reported in section 4.1. Briefly, global integration and segregation properties were quantified by global network efficiency  $Eff$  and transitivity  $T$  measures, and compared between-group with non-parametric *WRS* statistical testing. Next, each brain network node  $i$  was characterized by its closeness centrality  $L_i^{-1}$  and local efficiency  $Eff_{loc(i)}$  values, indicators of nodal integration and segregation within the overall brain network. The between-group comparison of nodal properties allowed identifying a set of cortical and subcortical regions impaired in *22q11DS* subjects. Taken together, regions presenting decreased closeness centrality (two-sided *WRS* test, *FDR* correction at significance level  $\alpha = 0.05$  (Benjamini & Hochberg, 1995; Wilcoxon, 1945)) and their reciprocal connections form a subnetwork affected in *22q11DS* patients. Such affected core (or a-core) included 31 of the 82 brain nodes, corresponding approximatively to the 38% of the overall brain network.

In order to assess the topological position of the affected core within the overall brain network, and its eventual alteration in *22q11DS* patients, the a-core weighted topological centrality  $\zeta_{a-core}^w$  was assessed for each subject. Briefly, the network efficiency after targeted attack towards the a-core was compared to an efficiency reference distribution estimated from  $n_{rep} = 1000$  repetitions of random attacks towards a matched number of network resources (removed nodes and connections strength). Between-group differences of  $\zeta_{a-core}^w$  score distributions were assessed using one-sided *WRS* test. Considering that a-core regions are by definition affected in *22q11DS*, we expected attacks on a-core edges to have a lesser impact on global efficiency (higher absolute  $\zeta_{a-core}^w$ ) of *22q11DS* patients than controls.

#### 4.2.4 Results

Connectomes of *22q11DS* patients presented significantly decreased global integration (decreased  $Eff$ ,  $p = 0.019$ ) and segregation (decreased  $T$ ,  $p = 0.032$ ) properties (figure 4.11). Importantly, these topological differences could not be explained by a potential difference in the total number of reconstructed streamlines ( $WRS$ ,  $p = 0.32$ ) or in edge density  $\delta$  ( $WRS$ ,  $p = 0.95$ ).

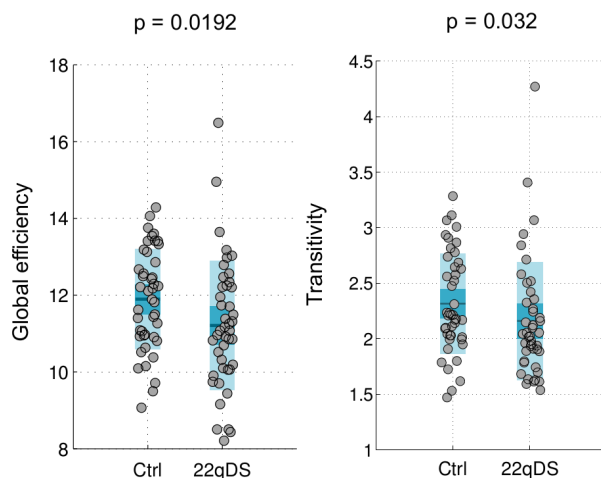


Figure 4.11 – Integration and segregation global network properties in healthy subjects (*CTRL*) and *22q11DS* patients. Adapted from (Vasa *et al.*, 2015).

Based on the robust integration deficit results, we investigated the spatial distribution of regions driving the global group difference using the closeness centrality measure. A total of 31 regions presented decreased closeness centrality in *22q11DS* patients compared to controls (FDR-corrected  $p < 0.05$ ), which were defined as the affected core, or a-core (figure 4.12). No region with increased closeness centrality in *22q11DS* was found. Affected regions were broadly symmetric bilaterally. Regions with bilaterally decreased closeness centrality included superior frontal and orbitofrontal cortex, precentral gyrus, superior and inferior parietal lobules, precuneus and entorhinal cortex as well as caudate nucleus, putamen, thalamus and hippocampus. On the left side, the cingulate cortex, parahippocampal gyrus, cuneus and amygdala were also affected, whereas on the right side the pericalcarine cortex and pallidum were involved. For all patients and controls, a-core nodes formed a single connected component, which justified considering them as an affected subnetwork.

a-core nodes were largely hubs of the healthy network, featuring among highest-ranked nodes for node closeness centrality evaluated on control connectomes. 13 of the 20 highest closeness centrality nodes evaluated on the *CTRL* group were a-core members, and the a-core was composed for the 40% of network hubs.

When comparing the topological centrality of the a-core,  $\zeta_{a-core}^w$  absolute values were lower in patients compared to controls ( $p = 0.0007$ ). Notably, lesions of deficient edges seemed less harmful to network integrity than lesions of healthy edges.  $\zeta_{a-core}^w$  values were significantly negative in both healthy controls ( $p = 1.8e - 39$ ) and *22q11DS* patients ( $p = 3.5e - 34$ ), figure 4.13.

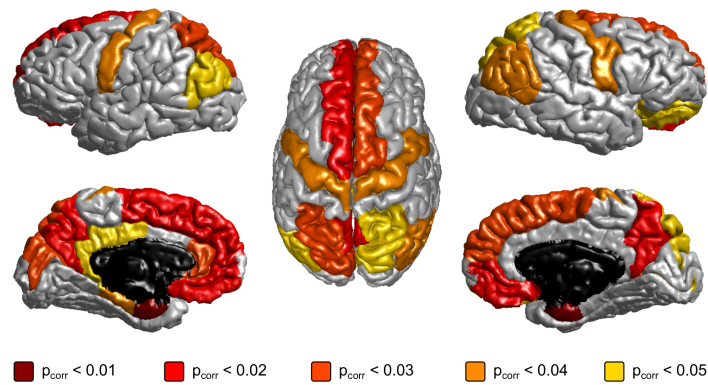


Figure 4.12 – The affected core, or a-core, of cortical regions with reduced closeness centrality in *22q11DS*. Regions are color-coded according to p-values, corrected for multiple comparisons using the FDR. Reproduced from (Vasa *et al.*, 2015).

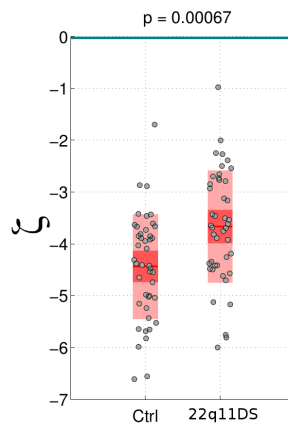


Figure 4.13 – Box plots representing the a-core topological centrality values for the two groups CTRL and *22q11DS*.  $\zeta_{a-core}^2$  values were significantly lower than zero for both groups. The a-core topological centrality (absolute  $\zeta_{a-core}^2$  values) was significantly decreased in patients compared to controls. Adapted from (Vasa *et al.*, 2015).

### 4.2.5 Discussion

Present results confirm previously reported integration deficits in *22q11DS* (Ottet *et al.*, 2013b), and identify the spatial distribution of affected regions driving global effects – the a-core, which consists chiefly of densely interconnected hubs, critical for efficient network integration, and topologically decentralized in patients.

While global graph theoretical measures can be sensitive to differences between patients and healthy controls, they are not sufficiently specific to characterize individual diseases, which can impact global brain topology in similar ways (Griffa *et al.*, 2013b; Rubinov & Bullmore, 2013b). The present approach reaches beyond global integration differences, to identify a subnetwork specifically affected in *22q11DS*. The a-core identified here exhibits significant overlap with regions previously identified as affected in *22q11DS*. Reports of deficits in corpus callosum as well as other midline structures (Bearden *et al.*, 2009; Machado *et al.*, 2007; Simon *et al.*, 2005) could explain the largely bilateral integration reductions reported here. Furthermore, previous voxel-based studies reported decreases in radial diffusivity in bilateral parietal and frontal regions (Simon *et al.*, 2008), in fractional anisotropy and axial diffusivity in the left parietal lobe (Kikinis *et al.*, 2012) and in axial and radial diffusivity in multiple WM tracts (Jalbrzikowski *et al.*, 2013).

Our results confirm an involvement of brain hubs in *22q11DS*, shown by (Ottet *et al.*, 2013a,b). Indeed, many a-core regions are highly connected and central nodes. Furthermore, our a-core exhibits substantial overlap with known structural cores of the brain (Hagmann *et al.*, 2008; van den Heuvel & Sporns, 2011). Nonetheless, it is worth noting that the a-core nodes are spatially highly distributed, and includes as well topologically peripheral (low closeness centrality) nodes such as the pericalcarine, entorhinal and rostral anterior cingulate cortices (figure 4.12). Taken together, a-core nodes and edges interconnecting them play an important role in maintaining and efficient network communication, as emphasized by the strong impact of a-core-targeted attack. Moreover, the intuitive fact that attacks on deficient edges have a lesser impact on network efficiency than attacks on healthy edges, is quantified by the alteration of the a-core topological centrality values  $\zeta^w$  in patients compared to controls.

*22q11DS* is considered an endophenotype and high-risk model for schizophrenia. 30% of individuals with *22q11DS* develop schizophrenia or affective psychosis, and *22q11DS* account for up to 1% to 2% of schizophrenia cases (Jonas *et al.*, 2014). The emergence of psychotic symptoms in *22q11DS* patients during adolescence is hypothetically linked to neuronal volume reduction and connectivity deficit, and *22q11DS* neurocognitive features partially overlap with those observed in schizophrenia (Chow *et al.*, 2011; Jonas *et al.*, 2014). In line with these considerations, our results exhibit similarities with the dysconnectivity findings in schizophrenia. In section 4.1 we reported a decrease of global network efficiency in a small cohort of 16 chronic schizophrenia patients. Deficit of integration properties is a consistent finding in schizophrenia literature (Zalesky *et al.*, 2011; Zhang *et al.*, 2012), and has been associated with distributed white matter alterations, concentrated in fronto-parieto-occipital (Zalesky *et al.*, 2011), fronto-limbic (Campbell *et al.*, 2006) circuits and rich-club connections (Collin *et al.*, 2014a; van den Heuvel *et al.*, 2013). In the previous section we identified an affected core for schizophrenia involving fronto-basal, middle and inferior frontal cortices, parietal and left precentral areas, the basal ganglia and the left thalamus, including 26 out of 82 brain nodes. We showed that although no global integration deficit was present in patients in earlier phases of the disease, the affected core (as defined in chronic schizophrenia) was precociously impaired in early psychosis. In parallel, individuals affected by *22q11DS* included in the present study show an overall deficit of global network integration properties, mainly driven by the decentralization of an affected core involving superior and inferior frontal cortices, precentral gyrus, parietal, precuneus

and entorhinal cortices, basal ganglia and thalamus, including 31 out of 82 brain nodes. The *22q11DS* affected core is spatially more spread than the *SCHZ* one. The overlap between the two cores mainly involves orbitofrontal-subcortical circuitry and left parietal areas. Table 4.3 lists the brain regions belonging to both *SCHZ* and *22q11DS* a-cores. Alterations of inferior frontal pole, together with fronto-occipital and uncinate fasciculus WM disruption, have previously been identified as an hallmark for schizophrenia in a group of individuals affected by *22q11DS* (da Silva Alves *et al.*, 2011). Moreover, severity of schizophrenia-like symptoms in *22q11DS* subjects were associated with FA reduction in the same areas (da Silva Alves *et al.*, 2011).

In conclusion, the present study confirms the disruption of global integration properties in *22q11DS* patients. The impairment of a distributed set of cortical and subcortical regions, mainly hubs but including as well peripheral nodes, was identified as main substrate for the loss of global integration capacity. The topological role of the affected core, and its alteration (decentralization) in *22q11DS* patients were quantified by means of the subnetwork topological centrality measure introduced in chapter 3. The *22q11DS* a-core partially overlaps the schizophrenia affected core identified in section 4.1 and (Griffa *et al.*, 2015c): further investigations may help identifying schizophrenia risk-factor within *22q11DS* cohort and elucidating pathological mechanisms of brain connectivity organization.

List of brain regions involved in *SCHZ* AND *22q11DS* affected cores

Left medialorbitofrontal	Right medialorbitofrontal
Left precentral	Right precuneus
Left superiorparietal	Right putamen
Left caudate	Right caudate
Left thalamusproper	Right pallidum

Table 4.3 – List of brain regions included in both schizophrenia and 22q11 deletion syndrome affected cores, as defined in sections 4.1 and 4.2. Regions labelling corresponds to the Desikan-Killiany atlas notation (Desikan *et al.*, 2006).

## 4.3 Conclusions

In this chapter we investigated brain structural network alterations occurring across different stages of psychosis disorder, and in the 22q11 deletion syndrome.

Brain alterations characterizing the early phase of psychosis may be very subtle and of difficult detection. For this reason, we first investigated a cohort of chronic schizophrenia patients. Next, we questioned whether connectivity alterations highlighted in the chronic phase of the pathology were already present in the earlier stages of the disease.

System-scale connectivity analyses of chronic schizophrenia connectomes highlighted a disruption of global integration and segregation properties. The alteration of the global network properties was mainly driven by the impairment of a brain subnetwork, named affected core, composed of both hubs and peripheral areas. The affected core subnetwork was topological decentralized within the overall brain network, as quantified by means of the topological centrality measure  $\zeta$ .

Early psychosis patients did not demonstrate any global network property alteration. Anyway, the affected core was precociously impaired. Moreover, network measures characterizing the affected core distinguished early psychosis patients with different degrees of illness severity.

The consistency of the findings related to the affected core across the chronic schizophrenia patients and different early psychosis stages is highly encouraging, and supports a-core measures as possible biomarkers of psychosis progression.

Using a similar analysis pipeline, we investigated brain connectivity alterations occurring in 22q11 deletion syndrome. This genetic disease is considered a model for the investigation of schizophrenia pathology.

Subjects affected by 22q11 deletion syndrome demonstrated an overall decrease of network efficiency, mainly driven by the disruption of a brain subnetwork partially overlapping the schizophrenia affected core.

The characterization of common connectivity alterations between schizophrenia and early psychosis patients on the one side, and 22q11 deletion syndrome subjects on the other side, certainly deserve further future investigations.

In general, the analysis pipeline proposed in this chapter 4 can be extended to other diseases affecting network connectivity, as well as to functional connectomes, with the aim of identifying specific sub-system abnormalities driving global topological deficits.



Part II

---

**Insights into  
brain structural modularity**



# Overview

---

The human brain has been characterized as a modular network (Chen *et al.*, 2008; Hagmann *et al.*, 2008; Meunier *et al.*, 2009b). From an anatomical point of view, the structural connectome can be decomposed into compartments highly intra-connected, but sparsely connected with the rest of the network. Structural modules derived from diffusion data and cortical thickness correlation extensively overlap known functional and anatomical domains such as the visual area, the frontal cortex and the posteromedial parietal area (Chen *et al.*, 2008; Hagmann *et al.*, 2008). In parallel, the functional connectome shows consistent and reproducible spatial communities of co-activation, correlated with developmental (Fair *et al.*, 2009; Tymofiyeva *et al.*, 2013) and task-based (Crossley *et al.*, 2013; Stevens *et al.*, 2012) profiles, and highly consistent with structural modules (Alexander-Bloch *et al.*, 2012; Meunier *et al.*, 2010). It is in fact hypothesized that the modular architecture of the brain structural network supports functional segregation and time-scale separation (Meunier *et al.*, 2010), promoting a reach panorama of brain dynamics (Kaiser & Hilgetag, 2010; Russo *et al.*, 2014), and responds to brain system robustness and evolvability demands.

Importantly, the brain modular architecture has been shown to evolve across development and aging (Chen *et al.*, 2011; Fair *et al.*, 2009; Meunier *et al.*, 2009a), and to be altered in different pathologies (Alexander-Bloch *et al.*, 2010; Baggio *et al.*, 2014; van den Heuvel *et al.*, 2013). As highlighted by (Alexander-Bloch *et al.*, 2012), alterations of brain modular structure may concern mainly intra-module connectivity, or may imply perturbations of the community structure by itself, with different nodal clusterings across populations. The modularity measure  $Q$  is widely used in clinical studies to quantify the degree of decomposability of a network, and is defined as the relative number of intra-module links. Anyway, modularity does not provide explicit information about the spatial topology of the communities. The use of alternative metrics, such as the variation of information or the mutual information between partitions, is therefore advisable if one wish to unravel spatial modular topology alterations across populations. These measures borrowed from information theory directly quantify the distance and level of agreement between partitions.

A second related point of interest is the identification of characteristic modular topologies within homogeneous groups of subjects. It is clearly of interest to compare characteristic partitions between different populations. Moreover, it can be insightful to investigate specific community properties across individuals belonging to the same group. In order to answer to these needs, it is necessary to robustly identify partitions representative of a whole group of individuals. The problem has been addressed in literature by considering the community decomposition of an average group-wise connectivity matrix (Fair *et al.*, 2009), or by choosing the decomposition of the most representative subject in terms of partition agreement with the other members of the groups (Meunier *et al.*, 2009b). Alternatively, one might consider methods explicitly tailored to the estimation of a consensus between multiple clustering results, such as the consensus clustering procedure proposed by (Monti *et al.*, 2003).

The quantitative and qualitative evaluation of topological alterations of brain community structure may be of special interest in the early phases of brain development, when substan-

tial modifications of white matter connectivity occur, and the modules architecture can change rapidly and significantly. If newborn babies already demonstrate brain modular decomposability, during development brain communities substantially evolve, moving from highly local subnetworks to more spatially distributed circuits (Fair *et al.*, 2009). Considering these elements, it is therefore important to carefully characterize, compare and represent potentially different modular spatial topologies, specially for the investigation of sensitive phases of brain changes.

Part II of this thesis is organized as follows. In section 5.1.1 we briefly review methods for community detection. Our review is not meant to be exhaustive, but focuses on algorithms extensively applied to brain network investigation and clinical studies, and highlights related open questions. We also review information theoretical metrics of clustering distance and agreement used for pair-wise comparison of partitions (section 5.1.2), and following (Alexander-Bloch *et al.*, 2012; Rubinov & Sporns, 2011). Next, we focus on the comparison of brain network topologies by means of the normalized variation of information and normalized mutual information measures, and on the evaluation of different representative partition estimations. In section 5.2 we consider a group of 47 healthy subjects and quantify the intra-subject and inter-subject variability of modularity-maximization network decomposition. Differently from the majority of reports, investigating brain functional communities, in the following chapter we focus exclusively on brain structural modules. We quantitatively evaluate the representativeness of three different group-wise partitions: the modular decomposition of the group-average connectivity matrix ( $C^{avg}$ ), the modular decomposition of the most central subject in the clustering space ( $C^{central}$ ), and the consensus clustering partition ( $C^{cons}$ ). Finally, we apply information theoretic measures and consensus clustering to investigate the brain modular fingerprints within sensitive populations of high-risk preterm born children (section 5.3).

Elements of the present Part II have been published in (Fischi-Gomez *et al.*, 2015; Griffa *et al.*, 2013a).

# Group-comparison of brain network community structure

# 5

## 5.1 *Background*

### Estimation and comparison of clustering structures

#### 5.1.1 Algorithms for community detection

Community detection algorithms have gain increasing interest in different domains of applied science, from social networks to biological systems. Since it has become clearer that complex systems share non-random topological properties, a variety of approaches such as divisive or agglomerative algorithms, optimization strategies or methods based on graph dynamical processes have been proposed to disentangle network community structures (Fortunato, 2010; Newman, 2010). It is out f the scope of this thesis to provide here an extensive review of community detection algorithms. Instead, we will focus on approaches that have been typically used in brain network analysis, with particular attention on the multi-scale and hierarchical nature of the brain network organization.

Let's consider a network module as a set of nodes highly interconnected between them, but sparsely connected with the rest of the network. In such scenario, the modularity quantity  $Q$  is a popular and effective measure of network decomposability and quality of the partitions. Modularity was originally defined by (Newman & Girvan, 2004) as the number of edges connecting nodes belonging to the same community, minus the expected value of interconnecting edges in absence of any community structure, i.e. in an equivalent random graph. Formally,  $Q$  can be expressed as (Newman, 2006):

$$Q = \frac{1}{2m} \sum_{ij} (A_{ij} - P_{ij}) \delta(C_i, C_j),$$

with  $A$  the binary or weighted adjacency matrix of network  $G$  ( $A_{ij}$  being an element of  $A$ ),  $m$  the total number of edges in the graph, and the  $\delta$  function expressing the co-occurrence of two nodes  $(i, j)$  in the same cluster, i.e.  $\delta(C_i, C_j) = 1$  iff  $C_i \equiv C_j$ .  $P_{ij}$  expresses the expected number of edges between nodes  $i$  and  $j$  in an equivalent random network<sup>1</sup>. The probability of connection between two nodes an equivalent random network is proportional to the product of the nodal degrees  $k$ :

$$P_{ij} = \frac{k_i k_j}{2m}.$$

---

<sup>1</sup>A random equivalent network is a random network equal to our non random graph  $G$  in degree sequence.

Thus, the modularity can be written as:

$$Q = \frac{1}{2m} \sum_{ij} (A_{ij} - \frac{k_i k_j}{2m}) \delta(C_i, C_j).$$

The modularity has been used to compare the quality of different graph partitioning algorithms, or as an objective function by itself. However, the modularity optimization is a computationally hard problem, and different strategies have been proposed such as greedy techniques or simulated annealing. Here we review a greedy approach to the modularity optimization problem proposed by (Blondel *et al.*, 2008) and known as Louvain algorithm. The Louvain algorithm has been often used for brain community detection (Meunier *et al.*, 2009b; Rubinov & Sporns, 2011), and is included in brain graph analysis toolboxes (Rubinov & Sporns, 2010). Besides its computation efficiency, the Louvain algorithm does incorporate a notion of modular hierarchical structure that is well suited to brain analysis questions. The algorithm is composed of two steps which are iteratively repeated until convergence to a modularity maximum. First, each node is placed in a separate module, and all possible node moves between modules are evaluated in terms of modularity gain (step 1). When no individual move can further improve the  $Q$  value, nodes belonging to the same community are agglomerated (step 2) in order to form new 'super-nodes'. Step one (moves evaluation) is repeated on the new 'super-nodes' network. The two steps are repeated until convergence. The procedure is sketched in figure 5.1.

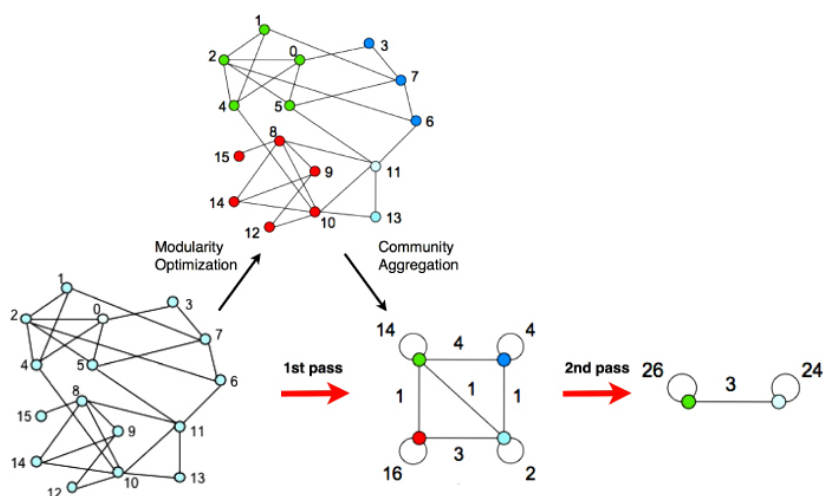


Figure 5.1 – Schematic representation of Louvain algorithm procedure. First, all possible nodal moves between communities are performed if increasing the modularity  $Q$ . Second, nodes belonging to the same community are agglomerated into new 'super-nodes': edges between the community nodes and the rest of the network are summed-up, while intra-community edges are transformed into self-loops. The two-steps procedure is repeated iteratively until convergence. From (Blondel *et al.*, 2008), ©SISSA Medialab Srl. Reproduced by permission of IOP Publishing. All rights reserved.

As mentioned above, brain topology can be modelled as a hierarchical modular network. In fact, hierarchical scales span various orders of magnitude, from nervous column level, to long distance communication (Leergaard *et al.*, 2012). At the macroscopic scale, the brain network is composed of brain regions linked in segregated functional circuits, connected in order to form integrated large-scale subsystems corresponding to higher level functions (Sporns, 2013). It is therefore of interest to uncover multi-scale relationships between brain network elements. Even

though the Louvain algorithm can provide a hierarchical partition of the brain network, it does not explicitly address multi-scale aspects of the brain network modular architecture. Different hierarchical and multi-scale graph partitioning methods have been proposed (Fortunato, 2010). We mention here the works by (Betzel *et al.*, 2013; Lambiotte, 2010; Schaub *et al.*, 2012). The approach described by (Betzel *et al.*, 2013) is a multi-resolution technique delivering modules at different scales and according to a tunable parameter  $t$ . Instead of optimizing the classic modularity function, the following quantity is optimized:

$$Q'(\mathcal{P}, t) = \frac{1}{2m} \sum_{ij} (A'_{ij} - \frac{k_i k_j}{2m}) \delta(C_i, C_j),$$

with  $A'_{ij}$  the flow graph adjacency matrix with elements

$$A'_{ij} = (e^{-tL} k_j),$$

where  $L$  is the normalized graph Laplacian matrix. The flow graph  $A'$  expresses the probability that a random walker will cross a given edge  $(i, j)$  at time  $t$  of a continuous-time random walk. The intuition underlying this approach is that random walkers on the original graph  $G$  will be 'trapped' within progressively larger communities as the diffusion time  $t$  increases. This method has been successfully used to highlight high resolution (small  $t$ ) and lower resolution (larger  $t$ ) structural brain network communities consistent with functional synchronization patterns (Betzel *et al.*, 2013).

At this point, it is worth noting that dynamical aspects of the brain network modular architecture deserve further investigation in the future. Considering brain functional activity, patterns of synchronization among regions or functional modules may exhibit non stationary dynamics and be transient in time. Moreover, single nodes may participate to different functional patterns, resulting in spatially overlapping functional modules (Hutchison *et al.*, 2013). From a structural connectivity point of view, hubs linking segregated circuits may in fact be considered regions of overlap between communities (Wu *et al.*, 2011). The detection of dynamic and/or overlapping communities is therefore a topic of central interest, and will be partially tackled in Part III of this thesis.

### 5.1.2 Information theory metrics for clustering comparison

A large variety of conceptually different and competing methods for community detection in graphs has been proposed in recent years. In order to evaluate the output of different algorithms and to compare the modular structure of different networks, measures quantifying similarities and differences between graph partitions are needed. In this section we review the mutual information  $MI$  and variation of information  $VI$  theoretical measures described by (Meilă, 2007). Similarly to (Alexander-Bloch *et al.*, 2012; Betzel *et al.*, 2013; Rubinov & Sporns, 2011), we will use these measure to establish the similarity between pairs of brain network partitions, and to quantify how well an estimated group-wise anatomical partition represents whole sets of subjects (section 5.2).

Let's consider a network  $G$  with  $n$  nodes, and two clusterings  $C$  and  $C'$  of  $G$ , with  $K$  and  $K'$  number of non-overlapping modules in  $C$  and  $C'$  respectively. The mutual information  $MI$  quantifies how much information is shared by the two (different) partitions  $(C, C')$  of network  $G$ , and is defined by (Meilă, 2007) as

$$MI_{C,C'} = \sum_{k=1}^K \sum_{k'=1}^{K'} P(k, k') \log \frac{P(k, k')}{P(k)P(k')}.$$

The value  $P(k)$  represents the probability of assigning a given network node  $i$  to the cluster  $k$  and is equal to

$$P(k) = \frac{n_k}{n},$$

with  $n_k$  number of nodes in cluster  $k$ . The quantity  $P(k, k')$  expresses the probability that a given node  $i$  belongs to cluster  $k$  in partition  $C$  and to cluster  $k'$  in partition  $C'$ , and is formally the joint probability

$$P(k, k') = \frac{n_{k,k'}}{n},$$

with  $n_{k,k'}$  number of nodes in cluster  $k$  for  $C$  and in  $k'$  for  $C'$ .

The mutual information and variation of information measures are based on the concept of entropy. In an information theory framework, the Shannon entropy  $H(C)$  of a network with clustering  $C$  represents the uncertainty intrinsic to  $C$  or, equivalently, its information content:

$$H(C) = - \sum_{k=1}^K P(k) \log P(k) = - \sum_{k=1}^K \frac{n_k}{n} \log \frac{n_k}{n}.$$

Intuitively,  $H(C)$  expresses the uncertainty that a node  $i$  is assigned to a given cluster in  $C$ . The conditional entropy of two clusterings is defined as

$$H(C | C') = \sum_{k=1}^K \sum_{k'=1}^{K'} P(k, k') \log \frac{P(k')}{P(k, k')} = \frac{n_{k,k'}}{n} \log \frac{n_{k'}}{n_{k,k'}}.$$

The mutual information  $MI(C, C')$  is always non-negative and inferior or equal to the entropy of the two clusters ( $MI(C, C') \leq \min(H(C), H(C'))$ ).

The variation of information  $VI$  is defined as

$$VI(C, C') = H(C) + H(C') - 2MI(C, C'),$$

and expresses the quantity of information intrinsic to the two partitions, corrected by the information shared by the two partitions (figure 5.2). Particularly,  $VI(C, C') = 0$  iff  $C \equiv C'$ . Moreover  $VI$  is always non-negative, symmetric and respects the triangle inequality, therefore representing a measure of distance in the data clustering space.  $VI$  is up-bounded by the logarithm of the number  $n$  of nodes ( $\log n$ ), and can therefore be normalized by this value, giving a rescaled value of  $VI$  to the range  $[0, 1]$ . This value is known as the "normalized variation of information" and is formally defined as:

$$VIn(C, C') = VI(C, C') / \log n.$$

In the same line, the mutual information measure can as well be rescaled to the  $[0, 1]$  range, giving the "normalized mutual information" index as (Danon *et al.*, 2005):

$$MIn = \frac{2MIn(C, C')}{H(C) + H(C')}.$$

## 5.2 Methods

### Strategies for group-comparison and representative partitions

The human brain network proved to be small-world and organized according to a hierarchical modular architecture, composed by communities of nodes highly interconnected between them, but sparsely connected with other modules (Bullmore & Sporns, 2009; Meunier *et al.*, 2010, 2009b). Particularly, modularity is thought to be a crucial characteristic in terms of brain evolution and development (Meunier *et al.*, 2009b). The study of modular topology and decomposability of brain networks in health and disease is therefore raising new interest but also new challenges.



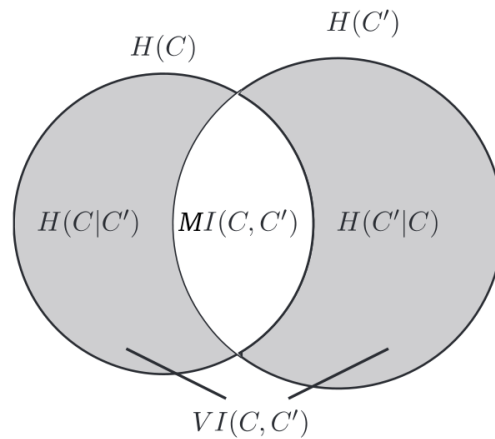


Figure 5.2 – Logical representation of  $MI$  and  $VI$  measure in function of clusterings entropy and conditional entropy. Reprinted from Journal of Multivariate Analysis, Volume 98, Issue 5, M. Meilă, Comparing clusterings - an information based distance, pp. 873-895. Copyright (2007), with permission from Elsevier.

One first concern is how to better compare brain modular topologies between different populations. A common approach in clinical studies is to compare modularity values  $Q$  between different groups. However, although the modularity  $Q$  indirectly quantifies the degree of decomposability of a network, it does not provide explicit information about the spatial topology of its communities. For this reason, and as suggested by (Alexander-Bloch *et al.*, 2012), we advocate the use of clusterings distance metrics such as the variation of information or the mutual information (reviewed in section 5.1.2) to unravel topological differences of modular structure between clinical groups.

Going one step backwards, the model used to define anatomical human brain networks is based on DWI data which is intrinsically noisy, and includes both false positive and false negatives edges (de Reus & van den Heuvel, 2013). This fact can have a high impact on the resulting optimal modular decomposition. The intrinsic noisiness of structural brain connectivity matrices accounts for part of the variability across individuals belonging to homogeneous populations. Indeed, by definition, communities are parts of graph with few ties with the rest of the system and thus, it may be of interest to evaluate them independently from the graph as a whole. Or, for instance, it can be of interest to investigate specific community characteristics across subject belonging to a same group. The estimation of a partition representative of a whole group of subjects may help overcoming decomposition biases due to graphs (non systematic) noise, and offer a qualitatively smooth description of the community fingerprint of different populations (for an example, see section 5.3).

Motivated by these considerations, in this chapter we describe a framework for group-comparison of brain communities topology, and group-wise representative partitions estimation. First, we evaluated partitions distance measures and group-wise representative partitions on a group of 47 healthy subjects (sections 5.2.1, 5.2.2). Second, we investigated the brain modular fingerprint of high-risk preterm born children (section 5.3). In general, the described framework can be applied to clinical studies, when it is of interest to investigate the graph modular architecture of different populations (Alexander-Bloch *et al.*, 2012).

### 5.2.1 Methods and Materials

In order to formulate a robust framework for group-wise comparison in terms of brain modular structure, one should first evaluate the intra- and inter- subject variability of brain modular architecture. To this end, we considered a set of healthy individuals, and (i) established subject-wise optimal partitions using a modularity-optimization algorithm; (ii) evaluated and compare group-representative partitions considering subjects centrality in clustering space, average partition, and consensus clustering; (iii) used the normalized variation of information ( $VIn$ ) and the normalized mutual information ( $MIn$ ) measures. The main assumption of this analysis is that a group-wise partition well represents the set of subjects if the average distance in the clustering space between subject-wise partitions and group-representative partition is small. Under this assumption, the results prove that the consensus clustering and the representative partition estimated from the average connectivity matrix are appropriate for group-representation.

#### *MRI acquisitions and connectivity estimation*

47 healthy subjects aged  $25 \pm 4$  years underwent an MRI imaging session (3T Siemens TrioTim, 32-channel head coil), composed of a diffusion spectrum imaging (DSI) and a high resolution MPRAGE morphological acquisition as anatomical reference. Whole brain structural connectivity was determined by tissues segmentation and streamline tractography. This processing yielded 47 weighted structural networks  $G^i$ , each one composed of  $n = 448$  nodes (each node being a cortical region, according to the parcellation described in (Cammoun *et al.*, 2012)), and with edge weights  $w_{(u,v)}$  representing the streamlines connectivity density (Hagmann *et al.*, 2008) between regions  $u, v$ . 7 out of 47 subjects were excluded from this study because the corresponding brain networks presented disconnected nodes. For this reason, only 40 subjects were considered.

#### *Community detection in brain graphs*

For each brain network, the optimal decomposition in terms of modularity value  $Q$  was determined by means of the modularity-optimization algorithm proposed by (Blondel *et al.*, 2008) (Louvain algorithm), and reviewed in section 5.1.1. Given the dependency of the algorithm output on the initial ordering of the considered nodes, the algorithm was run  $n_{iter} = 100$  times for each subject, and the highest modularity partition was selected. Next, a fine-tuning procedure (Sun *et al.*, 2009b) was run on each optimal Louvain solution. This optimization step consists in finding the optimal solution by moving each node of the network to all other existing communities or to a new community of its own, if the move improve the overall modularity value  $Q$ . This fine-tuning procedure has been shown to deliver final higher modularity partitions, and to partially circumvent the resolution limit intrinsic to many community detection algorithms (Sun *et al.*, 2009b). This procedure delivers a single partition  $C^i$  for each subject  $i$  of the considered set.

#### *Group-representative partitions*

In order to determine a representative partition for the considered group of 40 healthy subjects, we tested three distinct strategies. First, we estimated the optimal partition  $C^{avg}$  (best solution over 100 runs of the Louvain algorithm and fine-tuning procedure, as described above) for the group-wise average connectivity matrix  $G^{avg}$ , similarly to (Fair *et al.*, 2009).  $G^{avg}$  was built merging the 40 individual connectivity matrices  $G^i$ . An edge was maintained in  $G^{avg}$  if present in at least the 66% of the 40 subjects. This percentage ensures that the resulting  $G^{avg}$  is a connected graph (higher consistency percentages returned disconnected graphs). A weight corresponding to the average over the 40 subjects non-zero density values was assigned to each existing edge in  $G^{avg}$ .

Second, the partition  $C^{central}$  of the most central subject in the clustering space was considered as possible representative for the group. The distance between subjects in the clustering space was quantified by means of the normalized variation of information  $VIn$ . The subject-wise partition with the minimum sum of distances with all the other 39 subject-wise partitions was selected as group-wise representative partition, similarly to (Meunier *et al.*, 2009b).

Third, and similarly to (Betzler *et al.*, 2013), we evaluated the consensus clustering partition  $C^{cons}$  from the 40 subject-wise partitions. The consensus clustering is an approach proposed by (Monti *et al.*, 2003) that delivers an agreement partition across multiple outputs of a given clustering algorithm. The basic element of the consensus clustering approach is the construction of a consensus matrix  $M$  which stores the normalized number of co-occurrence of two elements (i.e. of two nodes)  $(i, j)$  in the same cluster, considering the overall set of subject-wise partitions  $C^i$ , with  $i = 1, \dots, n$ . The consensus matrix  $M$  has dimensions equal to the brain graph adjacency matrices  $G^i$ . Its entries (denoted consensus indexes  $m_{(u,v)}$ ) are bounded to the range  $[0, 1]$ . A consensus index  $m_{(u,v)}$  equal to 0 indicates that the two nodes  $u, v$  are never assigned to the same community, while  $m_{(u,v)} = 1$  indicates that nodes  $u, v$  are assigned to the same community for all the considered subjects. Ideally, a perfectly stable and recurrent partition over the 40 samples would correspond to a consensus matrix exclusively composed by 0s and 1s, as the node affiliation would not change across samples. The consensus indexes can be used as similarity measure in place of the connection density  $w_{(u,v)}$ , and feed to the Louvain algorithm. In practice, the consensus matrix  $M$  obtained from the 40 samples was thresholded at  $\tau = 0.3$  (i.e. all the consensus indexes smaller than 0.3 were considered as noise and set to zero), and the Louvain algorithm was run  $n_{iter} = 100$  times, delivering a new consensus matrix. This iterative procedure was repeated until the final consensus matrix  $M$  presented a perfectly binomial distribution of 0s and 1s values only, delivering the consensus clustering partition  $C^{cons}$ .

### ***Distance measures***

The normalized variation of information  $VIn$  (Meilă, 2007) was used as a metric of distance between partitions  $C^i$  in the clustering space. The normalized mutual information  $MIn$  (Danon *et al.*, 2005) was used to measure the amount of information shared by different partitions  $C^i$ .  $VIn = 0$  and  $MIn = 1$  express perfect agreement between partitions.  $VIn$  and  $MIn$  quantified the intra-subject and inter-subject variability of the modular decomposition obtained with the Louvain algorithm, and the representativeness of the considered group-wise partitions  $C^{avg}$ ,  $C^{central}$  and  $C^{cons}$ . The Brain Connectivity Toolbox (Rubinov & Sporns, 2010) was used for Louvain community detection and partitions distance computation.

## **5.2.2 Results and Discussion**

### ***Modular architecture variability***

Each one of the 40 brain networks was composed of a single connected component. Figure 5.3 pictures the connectivity matrix of a single example subject. The intra-subject variability in terms of Louvain algorithm runs was quantified by means of  $VIn$  and  $MIn$  values. For each subject, the mean  $VIn$  and  $MIn$  values between each pair of community detection runs (Louvain algorithm and fine-tuning procedure) were computed, and group-wise statistics are reported in table 5.1.  $VIn$  values close to zero, and  $MIn$  values close to one suggest that the network clustering procedure outputs consistent and robust decompositions.

The 40 brain networks were decomposed on average into  $k = 14$  modules ( $k_{min} = 10$ ,  $k_{max} = 16$ ), each one comprising on average 32 nodes (minimum number of nodes=1, maximum number of nodes=76). Inter-subject variability of modular decomposition is reported in

table 5.1. Normalized mutual information values are comparable to what reported by (Meunier *et al.*, 2009b) for functional brain networks, indicating a fair degree of similarity between partitions of an homogeneous group of healthy individuals.

### ***Representative partitions***

Three distinct group-representative partitions were estimated.  $C^{avg}$  is the optimal partition from  $n_{iter} = 100$  runs of the Louvain algorithm and fine-tuning procedure on the group-wise connectivity matrix  $G^{avg}$ , and counts 11 modules.  $C^{central}$  is the partition of the subject with the overall smaller distance  $VIn$  to all the other individuals of the group, and counts 13 modules.  $C^{cons}$  (8 modules) was obtained by computing the consensus matrix (figure 5.4) over all the 40 individual partitions, and iteratively re-cluster it till convergence. Both the average partition  $C^{avg}$  and the consensus clustering  $C^{cons}$  showed smaller distance ( $VIn$ ) to the single subject-wise partitions than the  $C^{central}$  partition (rank sum test,  $p \sim 10^{-7}$ ,  $p \sim 10^{-5}$ ) (table 5.3). The  $MIn$  values between the representative partitions and the subject-wise partitions was significantly higher for  $C^{avg}$  compared to  $C^{central}$  and  $C^{cons}$  ( $p = 0.007$ ,  $p = 0.006$ ). The three representative partitions are pictured in figure 5.5. The representative modules cover well-known anatomical areas as the occipital and temporal lobules, the medial frontal cortex and the precuneus area. Medial modules are highly symmetrical across the two hemispheres.

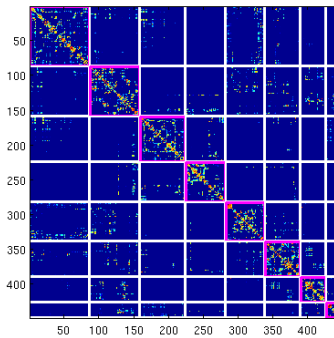


Figure 5.3 – Single subject structural connectivity matrix representing a 448 nodes brain network. Color-coding corresponds to  $t \log w_{(u,v)}$ . Nodes have been ordered such to group consensus clustering modules along the diagonal.

### ***Discussion***

The modular architecture of the brain structural network was characterized for 40 healthy subjects. The relatively high inter-subject  $MIn$  and low  $VIn$  values indicated a good degree of consistency between individual partitions, and is consistent with previous findings (Alexander-Bloch *et al.*, 2012; Meunier *et al.*, 2009b). Group-representative partitions were identified using three different approaches. We can assume that a partition effectively represents a group if the distance in the clustering space between each subject and the group-wise partition is small. We quantified the distance between partitions with the  $VIn$  measure, while the  $MIn$  expresses the degree of agreement between different partitions. The  $VIn$  distributions between subject-wise modular decompositions and representative partitions suggest that both the consensus clustering  $C^{cons}$  and the average partition  $C^{avg}$  effectively represent the modular topology of the group, while the central subject partition  $C^{central}$  is less representative of the group. Both the consensus clustering

Groups	$VIn$ (mean $\pm$ std)	$MIn$ (mean $\pm$ std)
<i>intra-subject</i>	$0.091 \pm 0.022$	$0.891 \pm 0.026$
<i>inter-subject</i>	$0.325 \pm 0.023$	$0.607 \pm 0.028$
$C^{avg}$	$0.265 \pm 0.033$	$0.662 \pm 0.033$
$C^{center}$	$0.295 \pm 0.021$	$0.640 \pm 0.026$
$C^{cons}$	$0.267 \pm 0.027$	$0.641 \pm 0.034$

Table 5.1 –  $VIn$  and  $MIn$  values between  $n_{iter} = 100$  runs of the Louvain algorithm for each subject (*intra-subject variability*), optimal modular decomposition of different subjects (*inter-subject variability*), and between single subject modular decomposition and representative partitions ( $C^{avg}$ ,  $C^{center}$  and  $C^{cons}$ ).

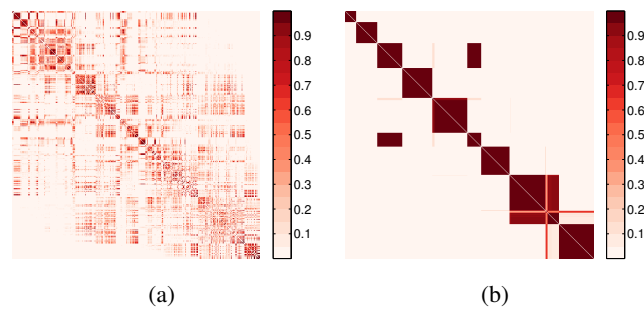


Figure 5.4 – Consensus matrix from 40 subject-wise brain network modular decomposition (a). The matrix (b) represent the consensus matrix after iterative procedure for consensus clustering estimation (Monti *et al.*, 2003). The node have been re-ordered according to the sparse reverse Cuthill-McKee ordering (Gilbert *et al.*, 1992) in order to promote a block-diagonal structure (modules forming blocks along the main diagonal).

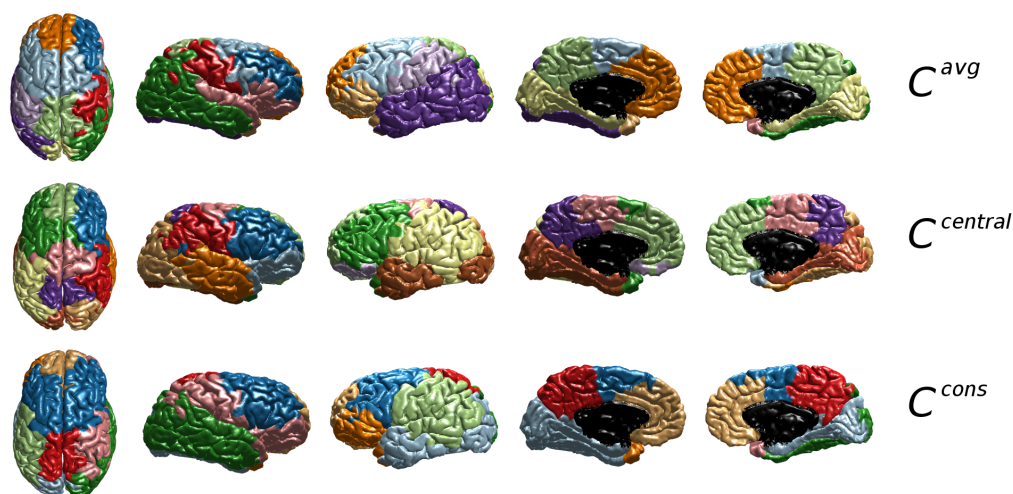


Figure 5.5 – Surface plots of representative partitions: modular decomposition of the average group-wise connectivity matrix ( $C^{avg}$ ); modular decomposition of the most central subject in clustering space ( $C^{central}$ ); consensus clustering partition ( $C^{cons}$ ).

and the average partition count a number of modules smaller than the single subjects partitions, suggesting that these representative partitions introduce a smoothing and denoising factor with respect to individual partitions. The identification of effective clustering distance measures and agreement partitions from sets of subjects is central for the characterization of the brain modular organization, and in view of groups comparison.

### 5.3 Applications

#### Brain network modular fingerprint of high-risk preterm born children

##### 5.3.1 Introduction

The modular structure of brain networks is thought to be a crucial characteristic in terms of brain evolution and development (Meunier *et al.*, 2010, 2009b). Newborns demonstrate already a brain network modular architecture, even though such structure is subject to substantial changes across development. Particularly, during development brain communities topology would move from local subnetworks partially overlapping with brain lobes, to more spatially distributed circuits (Fair *et al.*, 2009). A decrease of modularity and an increase of the number of modules during development from birth to pre-adolescence age have as well been highlighted (Huang *et al.*, 2013). These processes might be associated with pruning of short-range (intra-modular) connections, and strengthening of long-range associative tracts (inter-modular links) during development (Hagmann *et al.*, 2012). Characterizing brain communities fingerprint in normal brain development, and finding alterations due to risk factors such as extreme prematurity and/or intrauterine growth restriction, can offer insight into the developmental origin of childhood and adult brain disorders.

Extreme prematurity (*EP*) and intrauterine growth restriction (*IUGR*) have both been associated with alterations of brain structure (Dubois *et al.*, 2014; Padilla *et al.*, 2011; Thompson *et al.*, 2014), and are considered major risk factors for long term cognitive and behavioural impair-

ments (Feldman & Eidelman, 2006; Morsing *et al.*, 2011). For instance, frontal lobe white matter abnormalities have been associated with impaired neurocognitive functions in children born preterm (Duerden *et al.*, 2013). Considering related network-based studies, decreased global efficiency and nodal strength in *IUGR* and *EP* children have been associated with abnormal scores in neurodevelopmental and socio-cognitive performances (Batalle *et al.*, 2012; Fischi-Gómez *et al.*, 2014).

Here, we use the above mention framework to describe the modular topology of structural brain networks of children born extreme premature and/or with additional intrauterine growth restrictions, and we quantify the similarity of their brain communities structure using information theory metrics reviewed in section 5.2.1. Next, we qualitatively evaluate the group-wise modular topologies from group-representative brain network partitions, obtained by means of the consensus clustering algorithm (described in section 5.2.2).

### 5.3.2 Methods and Materials

52 premature born children aged 6 years old underwent an MRI imaging session on a 3T Siemens TrioTim system, equipped with a 32-channels head coil. The scanning protocol included and *MPRAGE* acquisition with TR 2500 ms, TE 2.91 ms and TI 1100 ms, in-plane resolution 1.8 mm and slice thickness 2 mm, covering a field of view of 160x256x208 voxels, and a diffusion tensor imaging (*DTI*) sequence with 30 directions, maximum b-values 100  $s/mm^2$ , one  $b_0$  reference image, TR and TE respectively of 1020 and 107 ms, 1.82 mm in-plane resolution and 2 mm slice thickness, covering a field of view of 230x230x256 voxels.

The gestational age (GA) at birth ranged from 24 to 33 weeks, and birth weight ranged from 510 g to 1150 g. All subjects were free from prematurity-associated brain lesions and ventriculomegaly at term equivalent age, and the 6 years-old scans were read as normal by experienced neuroradiologists. For further details on the children cohorts we refer to (Fischi-Gomez, 2015; Fischi-Gomez *et al.*, 2015).

Infants were distributed in 4 groups: 23 were born at  $GA < 28$  weeks and classified as extreme premature (*EP*); 11 were born moderately preterm ( $GA > 28$  weeks) with intrauterine growth restriction (*IUGR*) after placental insufficiency (*IO*, i.e. *IUGR-Only*); 11 were born at  $GA < 28$  weeks of gestation age with additional *IUGR* (*IE*, for *IUGR + EP*). The control group (*CTRL*) comprised 8 children moderately preterm ( $GA > 28$  weeks) with normal birth weight.

For each subject a brain structural connectivity matrix was computed by combining *MPRAGE* and *DTI* data. Particularly, the *MPRAGE* volumes were segmented into WM, GM and CSF tissue compartments. The GM was parcellated into 83 cortical and subcortical regions according to the Desikan-Killiany atlas (Desikan *et al.*, 2006). *DTI* data were reconstructed, and streamline tractography was performed as described in (Daducci *et al.*, 2012).

The subject-wise structural brain connectivity was modelled as an undirected, weighted graph counting 83 nodes corresponding to the Desikan-Killiany cortical and subcortical regions of interest. An edge  $e_{u,v}$  was added to the graph if at least one streamline of the tractogram had start and end extremes within brain regions  $u$  and  $v$ . A weight was associated to each edge, equal to the product of the fractional anisotropy (*FA*) value averaged along the connecting streamlines by the group-wise average connection density (Hagmann *et al.*, 2008), as proposed by (Fischi-Gómez *et al.*, 2014).

Each subject-wise weighted brain network was decomposed into modules using the Louvain algorithm (Blondel *et al.*, 2008). Specifically, for each child brain network the Louvain algorithm was run  $n_{iter} = 100$  times, and the best decomposition  $C_i$  in terms of modularity value  $Q$  was selected. In order to compare the intra-group and inter-group distance between subject-wise modular decompositions, we used the normalized variation of information index (*VIn*) and the normalized mutual information index (*MIn*) measures (section 5.2.1). *MIn* and *VIn* values were computed between each pair  $(C_i, C_j)$  of subject optimal modular decompositions.  $Q$ , *MIn* and

$V_{in}$  values were statistically compared using the non-parametric Wilcoxon rank sum test. Finally, a representative brain network partition was estimated for each group by means of the consensus clustering algorithm (Lancichinetti & Fortunato, 2012), as described in section 5.2.2, obtaining four representative partitions  $CC_{EP}$ ,  $CC_{IO}$ ,  $CC_{IE}$  and  $CC_{CTRL}$ .

### 5.3.3 Results

The four groups showed modular brain network architecture, with overall comparable modularity values  $Q$  and number of modules (see table 5.2). Nevertheless, modularity  $Q$  was higher in  $EP$  children compared to  $CTRL$  and  $IO$  subjects (respectively  $p = 0.002$  and  $p = 0.009$ ).  $EP$  children also showed the smallest average number of brain network modules (table 5.2).

The  $M_{in}$  and  $V_{in}$  values between the partitions of each pair of subjects are reported in figure 5.6. In order to assess the variability of intra-group modular decompositions, we considered the  $M_{in}$  and  $V_{in}$  distributions for pairs of subjects belonging to the same group ( $CTRL$ ,  $IO$ ,  $IE$ ,  $EP$ ). Distributions' mean and standard deviation are reported in table 5.3. No statistical difference was found between intra-group  $M_{in}$  and  $V_{in}$  distributions when comparing the four different groups (repeated 2-sample Wilcoxon rank sum test), indicating similar levels of intra-group variability in terms of modular topology.

Next, we evaluated the  $M_{in}$  and  $V_{in}$  distributions for pairs of subjects belonging to different groups ( $CTRL - IO$ ,  $CTRL - IE$ ,  $CTRL - EP$ ,  $IO - IE$ ,  $IO - EP$  and  $IE - EP$ ). Distributions' mean and standard deviation are reported in table 5.3. These inter-group  $M_{in}$  and  $V_{in}$  values quantify the distance between different groups in terms of modular topology. Taken together, the intra-group (diagonal blocks in figure 5.6) vs inter-group (off-diagonal blocks in figure 5.6)  $M_{in}$  and  $V_{in}$  values were statistically different ( $M_{in}, p \sim 10^{-63}$ ;  $V_{in}, p \sim 10^{-64}$ ), indicating different group-specific modular brain network structures. Significant statistical differences ( $p < 0.05$ ) held as well when comparing specific inter-group  $M_{in}$  and  $V_{in}$  values (e.g. the  $CTRL - IO$   $M_{in}$  and  $V_{in}$  distributions), and the relative intra-group  $M_{in}$  and  $V_{in}$  values (e.g.  $CTRL$  and  $IO$   $M_{in}$  and  $V_{in}$  values). We also observed that the  $IE$  and  $EP$  groups showed on average the highest inter-group similarity (maximum average  $M_{in}$ , minimum average  $V_{in}$ , table 5.3), while the highest dissimilarities (smallest average  $M_{in}$ , largest average  $V_{in}$ , table 5.3) were related to the  $IO$  group.

Group-wise representative partitions are shown in figure 5.7. The four consensus clustering partitions  $CC_{CTRL}$ ,  $CC_{IO}$ ,  $CC_{IE}$  and  $CC_{EP}$  counted respectively 10, 11, 10 and 9 modules. The visual inspection of the consensus clustering configurations corroborates the numerical results, and allows us to hypothesize that  $IE$  subjects are closer in modular brain structure to  $EP$  subjects, while  $IO$  subjects appear to have the most different structure with on average a higher number of modules (table 5.2).

Groups	Number of modules	$Q$
	mean $\pm$ std	mean $\pm$ std
$CTRL$	10.125 $\pm$ 0.64087	0.68796 $\pm$ 0.0098426
$IO$	10.8182 $\pm$ 0.75076	0.69886 $\pm$ 0.022563
$IE$	9.7 $\pm$ 0.67495	0.69751 $\pm$ 0.006496
$EP$	9.3478 $\pm$ 0.71406	0.70501 $\pm$ 0.010022

Table 5.2 – Average and standard deviation number of clusters and modularity values  $Q$  from subject-wise brain network modular decompositions, for the four groups  $CTRL$ ,  $IO$ ,  $IE$ ,  $EP$ .



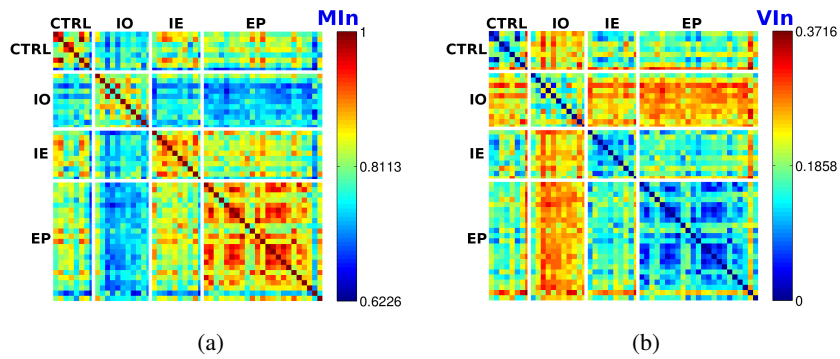


Figure 5.6 – Matrices representing the  $MIn$  (a) and  $VIn$  (b) values between optimal modular decompositions of each pair of subjects. The white lines highlight the different intra-group (diagonal) and inter-group (off diagonal) blocks.

Groups	$MIn$	$VIn$
	mean $\pm$ std	mean $\pm$ std
<i>CTRL</i>	$0.81613 \pm 0.081501$	$0.18418 \pm 0.081337$
<i>IO</i>	$0.82578 \pm 0.050917$	$0.1818 \pm 0.052754$
<i>IE</i>	$0.85195 \pm 0.049577$	$0.14386 \pm 0.047798$
<i>EP</i>	$0.86198 \pm 0.056419$	$0.13186 \pm 0.054544$
<i>CTRL – IO</i>	$0.76813 \pm 0.04112$	$0.23726 \pm 0.042292$
<i>CTRL – IE</i>	$0.81224 \pm 0.061895$	$0.1955 \pm 0.055527$
<i>CTRL – EP</i>	$0.79988 \pm 0.056778$	$0.1955 \pm 0.055527$
<i>IO – IE</i>	$0.76368 \pm 0.04176$	$0.23821 \pm 0.040862$
<i>IO – EP</i>	$0.74954 \pm 0.038688$	$0.2502 \pm 0.038781$
<i>IE – EP</i>	$0.81904 \pm 0.048115$	$0.17442 \pm 0.047043$

Table 5.3 – Average and standard deviation intra-group and inter-group  $MIn$  and  $VIn$  values.

### 5.3.4 Discussion

The goal of this analysis was to investigate the modular brain network structure in preterm born infants (with or without additional intrauterine growth restriction) at school age, and explore their brain network communities' fingerprint. All the four groups demonstrated non-random community structure, with modules partially overlapping brain lobes (figure 5.7). The extreme premature children showed higher modularity values and a smaller number of modules compared to the other three groups. Huang and colleagues highlighted a similar trend in diffusion-derived brain connectivity networks of new-born babies with respect to toddlers and pre-adolescents (Huang *et al.*, 2013). This similarity might suggest a delayed modular structure development of *EP* children compared to the *CTRL* and *IO* groups.

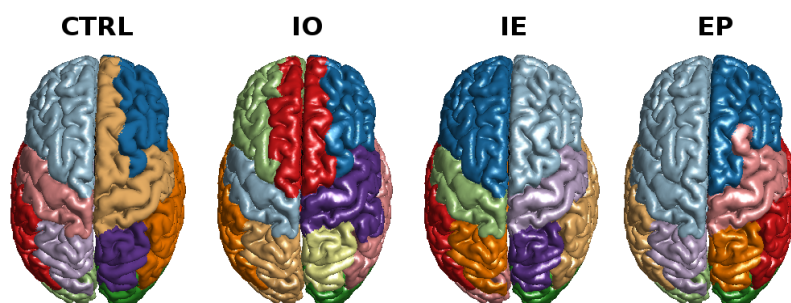


Figure 5.7 – Surface plots representing the group-wise representative modular decomposition estimated by means of the consensus clustering algorithm, for the four groups *CTRL*, *IO*, *IE*, *EP*.

The decomposition of each individual brain network into consistent modules enabled between-group comparisons using information theory measures of clustering similarity. As we can assume that one subject's partition is similar to another if the distance (in terms of  $MIn$  and  $VIn$  values) between the two partitions is small and *vice versa*, the significant  $MIn$  and  $VIn$  intra- vs inter-group differences suggest a group-specific different modular brain network structure. The visual inspection of the group representative partitions of figure 5.7 corroborates the analytical results, and allows to hypothesize that subjects born extreme premature and with intrauterine growth restriction (*IE*) are closer to the extreme premature infants (*EP*) than the other two groups. It may therefore be hypothesized that the *EP + IUGR* brain modular architecture is mainly affected by the effect of the extreme prematurity rather than prenatal growth restriction. Qualitatively, the most striking difference among group modular topologies is located within the frontal lobe (figure 5.7), in concordance with a recent study where disruptions of frontostriatal white matter pathways were found in school-aged children born preterm, and negatively correlated with measures of cognitive functioning (Duerden *et al.*, 2013).

This preliminary investigation of children born extreme premature and/or with additional intrauterine growth restriction proves the applicability of clustering similarity metrics and consensus clustering representation to clinical studies. Taken together, the listed results suggest that each cohort can be described by an own brain network modular architecture, paving the way to characterizing brain communities fingerprint to detect brain alterations.

## 5.4 Conclusions

In this chapter we reviewed different strategies for the brain network decomposition into communities, for the comparison of community structures across different populations, and for the identification of group-representative brain partitions.

Similarly to (Alexander-Bloch *et al.*, 2012) we recognized the importance of considering measures of partition distance in the clusters space (such as the variation of information  $VI$ ) when comparing community topologies across different groups, and complementary to the more traditional modularity measure  $Q$ .

This precaution is particularly important when comparing populations with potentially highly different community structures, such as babies in different developmental stage. We applied the variation of information and the mutual information measures to the investigation of the brain community structure in sensitive populations of high-risk preterm born children.

Finally, in this chapter we quantitatively compared the representativeness of different group-average partitions. Our analyses indicate that the consensus clustering algorithm may be a preferential choice for the estimation of group-wise representative partitions.

Part III

---

**A spatio-temporal network model  
for the joint investigation of  
brain structure and dynamics**



# Overview

---

Diffusion MRI allows mapping the wiring diagram of white matter bundles interconnecting brain cortical and subcortical areas. This complex information can be represented in the form of a network where nodes represent brain regions, and edges express their anatomical links.

Functional MRI maps in time activation events taking place in the brain cortex, during the execution of tasks or in the resting state.

By conceptually combining the structural and functional information measured by means of *dMRI* and *fMRI*, on the top of the brain anatomical network each node can be associated with a time-evolving functional signal.

During resting-state condition, local functional activities have been shown to organize into spatially distributed patterns of synchronization. These resting-state networks overlap well-known functional systems such as the primary motor cortex, the visual area or the frontal cortex. The resting state networks are typically estimated over the whole duration of an *fMRI* scanning session, and therefore constitute a time-average representation of functional synchronization patterns. Overall, RSNs are reproducible across individuals, but regional pair-wise functional signal correlations demonstrate a high level of variability even among different MRI scans of the same subject.

In this relation, recent works have shown that a time-average analysis of resting-state activity might be over simplistic, and that resting-state functional signals are intrinsically non-stationary (Hutchison *et al.*, 2013). Investigations of resting-state dynamics have highlighted short and temporally-localized events of spatial synchronization patterns (Zalesky *et al.*, 2014), topologically different and more complex than the traditional resting state networks (Allen *et al.*, 2012; Liu & Duyn, 2013; Smith *et al.*, 2012).

Stepping back to the combination of the brain structural and functional information, we can picture active cortical nodes communicating through the underlying anatomical network, and forming transient patterns of synchronization expressed by temporarily correlated nodal signals. Studies investigating the brain structure-function relationship have mainly focus on time-average characteristics of the fMRI data. Multilinear regression analyses have shown that different features of the anatomical network are partially predictive of functional correlations (Deligianni *et al.*, 2011; Goñi *et al.*, 2014; Honey *et al.*, 2009). Moreover, large-scale neural computational models (informed by the anatomical connectivity information), have highlighted the presence of different functional interactions at different temporal scales of investigation (Deco *et al.*, 2011). If resting state networks appear when summarizing the models behaviour over tens of seconds, more complex dynamics take place at a finer temporal scale.

Integrating these different inputs, in Part III of this thesis we propose an original theoretical framework for the integration and joint representation of both functional and structural brain connectivity information, as measured by means of diffusion and resting-state MRI. Particularly, we introduce a new network model, namely the spatio-temporal connectome, that

allows mapping reproducible spatio-temporal patterns of brain activation. The spatio-temporal connectome representation handles the locality or proximity of data points both in space and time. Proximity in space is given by the anatomical brain network; proximity in time is determined by the temporal co-activation of cortical regions.

Each activation pattern detected on the spatio-temporal graph is by itself a multi-layers (sub)graph, that can be further characterized in terms of inter-nodal interactions.

Part III of this thesis is organized into two parts.

After a brief review of literature dedicated to the structure-function relationship and resting-state dynamics topics (sections 6.1, 6.2), in chapter 6 we formally define our spatio-temporal connectome model. We clearly state the hypotheses that underlie the framework structure, and we describe in details the procedure for the construction of the spatio-temporal graph(section 6.3). Moreover we discuss the detection of activation components on the spatio-temporal graph, and their clustering into representative dynamical patterns of resting-state activity(section 6.4).

Next, in chapter 7 we investigate brain resting-state spatio-temporal patterns in a group of healthy subjects (section 7.1). The clustering of time-resolved activation patterns allowed identifying reproducible spatial configuration of synchronous activation. In section 7.2 we describe the detected activation patterns both in terms of spatial morphology and of temporal evolution, we discuss their overlap with task-based activation maps derived from large meta-analyses, and we represent inter-regional causality relationships in the form of a transition probability matrix. Moreover, we thoroughly investigate the role that the anatomical network plays in shaping the activation components detected on the spatio-temporal graph.

The majority of the work presented in this Part III is unpublished. Preliminary results can be found in (Griffa *et al.*, 2015b).

This research was conducted in collaboration with the Signal Processing Laboratory LTS4 of the École polytechnique fédérale de Lausanne<sup>2</sup>, and particularly Dr. Benjamin Ricaud, Kirell Benzi and Dr. Xavier Bresson.

---

<sup>2</sup><http://lts4.epfl.ch/>

# Mapping resting-state dynamics on spatio-temporal connectomes

---

# 6

## 6.1 *Background*

### Relationship between brain structure and function

In the past decade diffusion and resting-state functional MRI have gained increasing interest among the scientific community as two complementary techniques for the study of brain organization. As already reviewed in chapter 2, dMRI allows estimating the structural connectivity between cortical and subcortical areas *via* white matter tracts, while fMRI records neural-related brain activity signals. dMRI and fMRI map brain structural and functional connectivity networks. It is commonly accepted that functional brain connectivity reflects, at least at some extent, the underlying structural connectivity. Anyway, the investigation of their complex interplay is not trivial.

$$M_{A_i B_j} = \frac{A_i \cap B_j}{A_i \cup B_j}$$

The first study that directly compared anatomical and functional connectivity was published in 2002 (Koch *et al.*, 2002). Despite some limitations of this pioneering work (first of all the investigation of a single brain slice instead of the whole brain volume), the authors already pointed out some fundamental results. Particularly, they observed that strong anatomical connectivity can be consistently associated with strong functional correlation. In contrast, strong functional correlation can be observed also between weakly or not (structurally) connected regions. They interpreted this finding as an indication that BOLD signal correlations may be mediated by trigger areas and indirect anatomical paths. Consistently, investigations of the structure-function relationship within resting state networks reported similar observations (Damoiseaux & Greicius, 2009; van den Heuvel *et al.*, 2009). For example, medial temporal and frontal areas of the default mode network are temporally related even though they are not directly anatomically connected (Greicius *et al.*, 2009).

From a network-science perspective, the spatial distribution of functional patterns of co-activation has been related to various aspects of the underlying anatomical architecture. The investigation of different multilinear regression models has shown that the functional connectivity between brain regions is partially predicted by direct anatomical connections strength (Hagmann *et al.*, 2008), indirect connections (Deligianni *et al.*, 2011; Honey *et al.*, 2009), Euclidean

distance between considered regions (Hermundstad *et al.*, 2013; Honey *et al.*, 2009), and measures of shortest path embedding within the anatomical network (Goñi *et al.*, 2013). Figure 6.1 illustrates the prediction of functional coupling *via* structural search information, an information theory metric quantifying the accessibility of a shortest path within the overall structural network. System-level structural properties, such as rich-club topology and weak modular organization, have been shown to be central for the appearance of resting state networks and of plausible patterns of functional synchronization (Betzel *et al.*, 2013; Russo *et al.*, 2014; Senden *et al.*, 2014). Finer-grain investigations at nodal level highlighted that brain regions with different topological roles within the structural brain graph, may differentially participate to resting state dynamics. Particularly, structural hub nodes position themselves at the edge between different RSNs, show high interaction with topologically distant brain regions and demonstrate, on average, particularly variable inter-regional coupling (Collin *et al.*, 2014b; Kolchinsky *et al.*, 2014; van den Heuvel & Sporns, 2013).

Taken together, these evidences suggest that (i) the structural graph and its topological properties play a fundamental role in shaping resting state functional synchronization patterns; (ii) the relationship between structural and functional connectivity is complex and spans different spatial scales (Euclidean space scales and structural graph scales); (iii) structural hub nodes may have a pivotal role in linking different local patterns of functional synchronization.

A different approach to the investigation of the structure-function relationship come from the computational modelling field. The main *rationale* behind the development of computational models of large-scale neural dynamics is the investigation of brain activity principles and communication mechanisms (Sporns, 2014). A large-scale computational model includes a set of nodes representing neural populations (usually macroscopic anatomical regions), whose local dynamics can be modelled through more or less complex oscillators (Deco *et al.*, 2009; Honey *et al.*, 2009, 2007), or realistic biophysical neural models (Deco & Jirsa, 2012). Spatially distant oscillators are coupled through anatomical connectivity maps. The investigation of different dynamical models allowed gaining insights into the role that distinct factors, such as transmission delay and noise, play in shaping whole-brain resting-state dynamics (Cabral *et al.*, 2014; Deco *et al.*, 2011). Importantly, substantially different whole-brain computational models, informed by structural connectivity matrices, proved to be able to reproduce empirical patterns of time-average functional coordination and resting state networks.

At shorter temporal scales, simulated neural activities give rise to transient patterns of synchronization, suggesting that the brain system may dynamically explore a metastable space of distinct spatio-temporal states (Deco *et al.*, 2011). This observation highlights the fact that functional connectivity depends on the temporal scale at which it is characterized, and that considering multiple temporal scales and functional dynamics may help clarifying interdependencies between structural and functional brain connectivity.

## 6.2 *Background*

### **Dynamic resting-state connectivity**

Resting state fMRI data has been typically investigated by means of time-average statistics. Regional pair-wise correlation (functional connectivity) and spatial ICA allowed to highlight the modular structure of brain functional networks, and decompose them into a set of reproducible resting state networks (RSNs) that partially overlap known functional circuits (van den Heuvel & Hulshoff Pol, 2010). These approaches implicitly assume the stationarity of the investigated dynamics, and provide an information that is representative of the whole period of fMRI acquisition.

Anyway, brain functional activity is intrinsically dynamic and condition-dependent, with activation patterns variable for instance in function of task-demand or sleep. Moreover and as



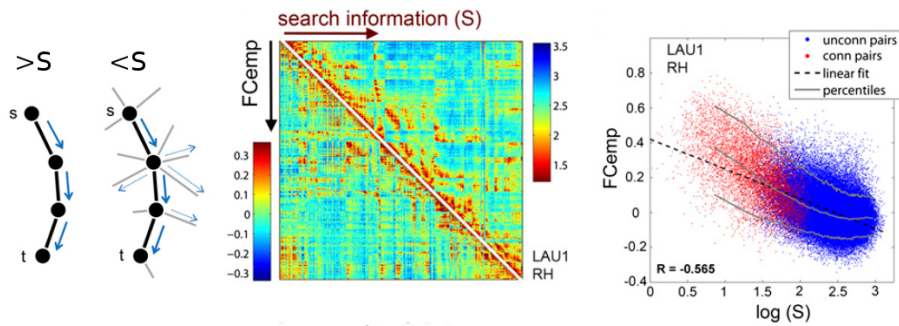


Figure 6.1 – Prediction of functional connectivity by means of measures of shortest path embedding measures. Left: schematic illustration of the search information measure  $S$ , characterizing the topological embedding of a shortest path within the overall brain anatomical network. High  $S$  values indicate high paths 'hiddenness'. Center: empirical functional connectivity (lower triangular part of the matrix) and search information (upper triangular part) values. Right: functional connectivity prediction with search information measure. Adapted from (Goñi *et al.*, 2014).

above discussed, large scale computational models suggest that, in absence of precise external stimuli or driven forces, the brain system would explore a set of transient, multistable states of spatio-temporal synchronization (Deco *et al.*, 2011). Very recent experimental works on rs-fMRI have started to address dynamical aspects of the resting state activity (Hutchison *et al.*, 2013).

Time-frequency investigations showed in fact that resting-state signals are not static, and that resting-state connectivity has dynamic properties that may be overlooked by stationary analyses (Chang & Glover, 2010). Particularly, the traditional resting state networks might be a smooth representation of more complex and variable interactions. Smith and colleagues proposed to use temporal ICA to decompose the resting state into a set of patterns represented by mutually independent time courses (Smith *et al.*, 2012). Although not directly addressing dynamical aspects of functional connectivity, this approach highlighted the presence of spatial synchronization patterns other than classical RSNs, and broke down RSNs, and particularly the DMN, into subcomponents. Similarly, sliding window approaches combined with clustering techniques were able to resolve in time spatial synchronization patterns distinct from time-average RSNs, and partially corresponding to areas associated with tasks execution (Allen *et al.*, 2012). Representatively, the DMN could be decomposed into subcomponents as precuneus area, posterior cingulate and parietal cortex showing non-constant inter-synchronization, and variable patterns of synchronization with sensorimotor, language and visual areas.

Importantly, time-average correlation patterns (RSNs) may reflect a summation of transient synchronization motifs, highlighting that the characterization of functional connectivity largely depends on the temporal scale of investigation. Liu and colleagues have for instance identified time-varying CoActivation patterns (CAPs) by means of point process analysis (Tagliazucchi *et al.*, 2012) and single-volume correlation (Liu & Duyn, 2013), and showed that summation of CAPs leads back to time-average RSNs.

The CAP approach and sliding-window investigations have also pointed out that resting state dynamics may be better described by short and temporally-localized events of spatial synchronization, rather than continuous and sustained activity. Zalesky and colleagues applied a sliding window approach to high temporal resolution data in order to track functional networks evolution in time (Zalesky *et al.*, 2014). They could isolate temporally well-defined switches among different connectivity configurations, at which multiple connections transit together to a different pattern of synchronization. These findings would support the idea that the resting brain would transiently visit a finite set of synchronization states in a multistable framework. Anyway, it

is not clear yet if functional dynamics are better represented by localized and sequential states, global highly-efficient configuration involving the overall brain network, or linear combination of multiple *FC* patterns (Hutchison *et al.*, 2013; Leonardi *et al.*, 2014; Zalesky *et al.*, 2014).

Under the multi-stability and state-space hypothesis, an interesting perspective is also the investigation of states sequence. Functional states have been shown to have different probabilities of recurrence over the acquisition period and across subjects (Allen *et al.*, 2012; Calhoun *et al.*, 2014). Interestingly, states transitions may be informative of complex interaction between different patterns of synchronization. Moreover, the temporal profiles of states recurrence may help associating individual functional configurations with different mental states. For example, a spatial pattern including posterior cingulate and parietal areas has been associated to light sleep condition because of its increasing occurrence over fMRI acquisition periods (Allen *et al.*, 2012). Not only the states sequence, but also finer-grain intra-state local activation dynamics may be informative of brain functioning mechanisms. For example, spatial waves of local activations, possibly representing propagation of intensity from focal points, have been qualitatively observed in human data (Majeed *et al.*, 2011). Finally, and importantly, early studies have identified alterations of resting state dynamics in brain disorders such as schizophrenia (Ma *et al.*, 2014) and multiple sclerosis (Leonardi *et al.*, 2013), underlying the importance of considering dynamical aspects of the BOLD signals in the study of the brain functional connectivity.

## 6.3 Methods

### Definition of a spatio-temporal framework

Building on the above-discussed notions on the brain structure-function relationship and resting-state dynamics, in this thesis we propose a new network model for the robust extraction of dynamic activation patterns between anatomically linked brain regions.

This section specifies our network model. In brief, we build a new spatio-temporal connectome. A spatio-temporal connectome is a multi-layer graph where edges connect nodes that are close in both the temporal AND structural spaces, where the structural space refers to the brain anatomical graph. We begin by stating the conceptual assumptions underlying the model. Next, we describe the reduction of the fMRI data to point processes, a step necessary for the construction of the spatio-temporal graph. In section 6.3.3 we formally define our spatio-temporal connectome network model.

#### 6.3.1 Underlying hypotheses

The formulation of a spatio-temporal framework for the joint representation of structural and functional data relies on few assumptions, discussed below.

General assumptions:

- *during rest, local spontaneous brain activity configure into spatial patterns of synchronization.* This is a very general statement, supported by large amount of literature that attributes spatially distributed maps of co-activation to neural sources (Fox & Raichle, 2007). Time-average resting state networks detected with PCA, ICA or other techniques are consistent across scanning sessions and subjects (van den Heuvel & Hulshoff Pol, 2010).
- *spatial patterns of resting state synchronous brain activity are transient in time.* In fact, recent works reviewed in section 6.2 suggests that a static description of functional connectivity might be over simplistic, and similar transient functional states have been reported by different authors (Allen *et al.*, 2012; Liu & Duyn, 2013; Smith *et al.*, 2012).

Assumptions related to the fMRI signals:

- *rs-fMRI dynamics are well represented by sparse sequences of time-localized events.* This hypothesis is supported by recent evidences identifying brief phases of global functional synchronization, alternated by longer periods of low-synchrony configurations (Zalesky *et al.*, 2014). In turn, rs-fMRI signals can be highly compressed without dramatic loss of information. In particular, we assume that a fMRI time series can be effectively reduced to a point process (or binary sequence of events), as suggested by (Tagliazucchi *et al.*, 2012). The point process analysis has successfully been used to investigate non-stationarities of functional signal (Tagliazucchi *et al.*, 2012), extract resting state networks from reduced set of data points (Liu & Duyn, 2013; Tagliazucchi *et al.*, 2012), and investigate functional dynamics alterations across populations (Li *et al.*, 2014; Tagliazucchi *et al.*, 2014).

Hypotheses specific to the spatio-temporal graph framework:

- *the dynamic synchronization between distant brain regions takes place through communication via anatomical connections.* This hypothesis, although pretty logical, is in fact a strong assumption. We should mention that time-average resting-state analyses have shown strong functional correlation between weakly anatomically coupled regions (Greicius *et al.*, 2009; Honey *et al.*, 2009). Nevertheless, this observation may result from (i) the practice of averaging an intrinsically dynamic information over relatively long acquisition periods, and (ii) not considering indirect anatomical paths of communication between functionally coupled areas, two aspects that will be overcome by our model. Moreover, a collection of recent experimental and computational works have largely proved the essential role played by the brain anatomical network in shaping the observed functional dynamics (Deco *et al.*, 2011; Goñi *et al.*, 2013; Honey *et al.*, 2009).

### 6.3.2 fMRI data reduction

#### *Node definition*

In order to build a spatio-temporal connectome, it was necessary to define the graph nodes. Each node in the spatio-temporal graph corresponds to a particular cortical region (spatial localization), and to a particular time point over the acquisition period (temporal localization), as better explained in section 6.3.3. The definition of the graph nodes therefore requires (i) the subdivision of the cortical volume into well-defined ROIs, and (ii) the extraction of ROI-wise time series (from fMRI recordings).

#### *Point process*

Each ROI-wise functional signal was reduced to a binary point process representing active and inactive time points. Consider a rs-fMRI recording of  $T$  volumes. For each ROI  $i$ , the average time series  $F_i(t)$  was computed, and normalized to unitary mean and standard deviation

$$F_i^z = \frac{F_i(t) - \mu(F_i(t))}{\sigma(F_i(t))},$$

with  $\mu(F_i(t))$  and  $\sigma(F_i(t))$  the time-average and standard deviation of the ROI-wise signal  $F_i(t)$ . This normalization allows defining a unique threshold for time series derived from different brain regions and subjects. The point process  $PP_i(t)$  of  $F_i^z(t)$  was defined as

$$PP_i(t) = \begin{cases} 1, & \text{if } F_i^z(t) > \tau, \\ 0, & \text{otherwise,} \end{cases} \quad (6.1)$$

with  $\tau$  *a priori* defined arbitrary threshold. This definition slightly differs from (Tagliazucchi *et al.*, 2012, 2014), where a localized activation is detected at time  $t$  ( $PP_i(t) = 1$ ) if  $F_i^z(t) > \tau$  and  $F_i^z(t-1) < \tau$ . In this setting, a localized activation  $PP_i(t) = 1$  would represent a short-lived event triggering the slow (up to 20 s) BOLD response (Tagliazucchi *et al.*, 2012). However, supra-threshold peaks of the normalized fMRI signal  $F_i^z(t)$  last few time points (up to 8-10 s), and the exact temporal localization of a neural event is not possible. In our framework we rather want to determine the time points for which a brain region is active or inactive, and this justify our definition 6.1. We should mention that for a given sampling frequency, the duration of a supra-threshold peak clearly depends on the choice of the threshold value  $\tau$ , which is arbitrary. Anyway, different values  $\tau$  were tested in our analyses, with consistent results across thresholds (see chapter 7). Figure 6.2 picture the reduction to point process of a ROI-wise functional time series.

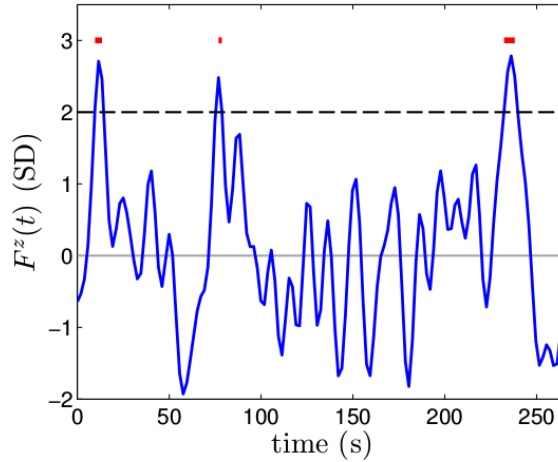


Figure 6.2 – Detection of local activation time points by means of point process analysis. The plot represents the normalized average time series  $F_i^z(t)$  from a single cortical node. The red marks indicate periods of activation of the considered cortical region  $i$ .

### 6.3.3 The spatio-temporal connectome model

Let's consider a static structural connectivity network  $G = (V, E)$ , composed by a set  $V$  of nodes  $v_i$ , connected by a set  $E$  of edges  $e_{ij}$ .  $G$  can for example be estimated by means of diffusion MRI data. We note that the term 'static' refers to the fact that we can consider the graph  $G$  not subject to variations over the observation period encoded in the spatio-temporal graph. The brain structural graph  $G$  counts  $N$  nodes, corresponding to  $N$  cortical regions. Let's consider a set of  $N$  point processes  $PP_i(t)$  of length  $T$  ( $T$  time points), each one representing the sequence of active and non-active states of a node  $i$ . The point process can be derived from rs-fMRI recordings as described in section 6.3.2. A spatio-temporal graph  $\tilde{G} = (\tilde{V}, \tilde{E})$  is composed of  $T$  layers of nodes, each one counting  $N$  nodes, for a total set of nodes  $\tilde{V}$  counting  $N \times T$  elements, and connected by a set of edges  $\tilde{E}$ . Formally, each node  $\tilde{v}_{i,a}$  in  $\tilde{V}$  is identified by two indexes: the first index  $i$  indicates the node position within a layer, and ensures its straightforward association with a specific brain area; the second index  $a$  indicates the node position in time, that is, across layers. Two nodes  $\tilde{v}_{i,a}$  and  $\tilde{v}_{j,b}$  are connected by an edge  $\tilde{e}_{(i,a)(j,b)}$  in  $\tilde{G}$  if the two following conditions are jointly satisfied:

- (i)  $\exists e_{ij}$  in  $G$  or  $i = j$ ,
- (ii)  $PP_i(t = a) = PP_j(t = b) = 1 \quad \& \quad (a = b \oplus a = b \pm 1)$ .

Therefore, two nodes  $\tilde{v}_{i,a}, \tilde{v}_{j,b}$  are connected in  $\tilde{G}$  if (i) they are anatomically connected according to  $G$ , and (ii) they are both active at the same or one-step forward time point, that is they are causal neighbours. Figure 6.3 schematizes the construction of a spatio-temporal graph  $\tilde{G}$ . The first two rows refer to the functional information only. The first  $N \times T$  matrix represents the temporal evolution of the  $N$  time series  $\{F_i^z(t)\}_{i \in [1, \dots, N]}$ . The corresponding point processes  $\{PP_i(t)\}_{i \in [1, \dots, N]}$  are computed by applying an arbitrary threshold  $\tau$  (second row). The point process information and the anatomical information contained in the graph  $G$  are jointly exploited in order to build the spatio-temporal graph  $\tilde{G}$  (last row). This framework is original and formally different from other models representing networks evolving in time. For instance, the multiplex network model, which has been used to characterize brain functional dynamics during learning (Bassett *et al.*, 2011; Mucha *et al.*, 2010), only allows links across layers between the same cortical regions, and does not track possible causal relationship between nodes activation.

We observe that the spatio-temporal graph  $\tilde{G}$  is highly sparse. This is a direct consequence of combining sparse information from the point processes and the brain structural network. The point process analysis can reduce a functional signal of the 80 – 90% (see (Tagliazucchi *et al.*, 2012) and chapter 7). This means that, depending on the chosen threshold  $\tau$ , a node is active only for the 10 – 20% of the recorded time points. Moreover, typical density values for DWI-based structural networks range between 10 – 20%, depending on the adopted parcellation scheme, DWI-reconstruction method and tractography algorithm. The high sparsity of the spatio-temporal graph is especially convenient because  $\tilde{G}$  turns to be composed of a certain number  $M$  of individual connected subgraphs or components  $CC$ . The connected components of the graph  $\tilde{G}$  typically span few cortical ROIs and time points (see chapter 7 for a thoughtful analysis of connected component in DSI and rs-fMRI human brain data).

We can therefore assert that each connected component  $CC$  of  $\tilde{G}$  represents an individual spatio-temporal pattern of activation. This representation not only allows investigating the spatial configuration of temporarily synchronized brain regions (figure 6.4b), but also resolves the temporal sequence and causality relationships between local brain activations (figure 6.4a).

Figure 6.4 pictures a single connected component of a human brain spatio-temporal graph, and constitutes a zoom of figure 6.3c. Conveniently, nodes are represented in anatomical order, from frontal to parietal, occipital and temporal regions, starting from a central ideal line representing the brain midline. Bilateral regions across the two hemispheres are therefore symmetric with respect to the central line. A connected component  $CC$  can as well be represented in a compressed form as a color-coding of the brain surface (figure 6.4). The color-scale represents the temporal occurrence of a node over the  $CC$ .

Recent studies have identified recurrent and reproducible patterns of whole-brain  $FC$  transient configurations (Allen *et al.*, 2012; Calhoun *et al.*, 2014; Smith *et al.*, 2012; Zalesky *et al.*, 2014). Though, a central question is if resting-state dynamic can be "*better conceptualized as a multistable state space where multiple discrete patterns recur, akin to fixed points of a dynamic system, or whether it simply varies along a continuous state space*" (Hutchison *et al.*, 2013). The spatio-temporal framework proposed in this thesis allows exploring brain dynamics both at the level of very local interactions between brain regions, and of possible reproducible synchronization states. For this reason, in the next section 6.4 we discuss the investigation of recurrent synchronization networks. Representative spatio-temporal patterns of resting-state activity can be determined by clustering the connected components  $CC$  of the graph  $\tilde{G}$  in an appropriate feature space.

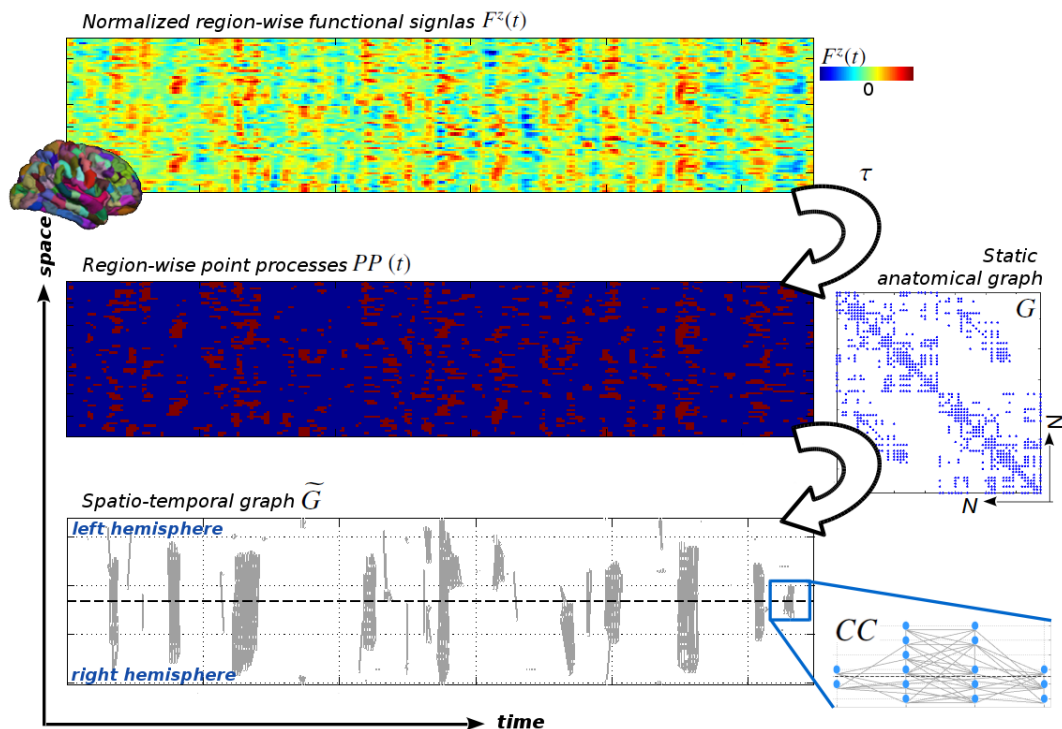


Figure 6.3 – Schematic representation of a spatio-temporal graph construction. First row: normalized functional time series  $F^z(t)$  for a set of cortical brain regions; second row: point processes  $PP(t)$  for a set of cortical brain regions, obtained by thresholding the corresponding normalized functional time series (threshold value:  $\tau$ ); third row: spatio-temporal graph  $\tilde{G}$  obtained by applying locality constraints in both the temporal and the spatial domain, where the spatial domain is represented by the static anatomical graph  $G$ . Bottom right corner: zoom into a single activation component  $CC$  of the spatio-temporal connectome.

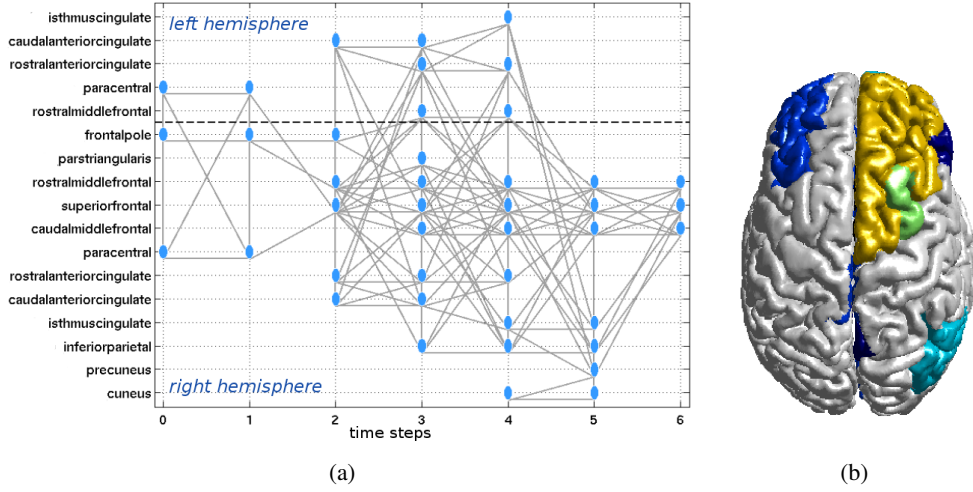


Figure 6.4 – Activation component  $CC_l$  of a spatio-temporal graph. (a) Temporal sequence of nodes activation. (b) Surface representation of brain areas activation persistence within a single activation component, equivalent to the component feature vector  $cc_l$ .

## 6.4 Methods

### Identification of representative spatio-temporal patterns of brain activity

Let's make the assumption that the set of the connected components of a spatio-temporal graph  $\tilde{G}$  expresses a finite number of reproducible activation patterns that repeat in time. In this setting, it must be possible to retrieve the representative activation patterns by clustering the individual components in an appropriate feature space.

#### Feature space

Let's consider a spatio-temporal graph  $\tilde{G}$  composed of  $M$  connected subgraph  $CC_l$ ,  $l \in [1, M]$ . A single activation pattern  $CC_l$  spans  $k_l$  layers of  $\tilde{G}$  or, equivalently, lasts  $k_l$  time points. Let  $K = \max_l k_l$  be the maximal duration of a component, expressed in number of time steps. The subgraph  $CC_l = (\tilde{V}_l, \tilde{E}_l)$  has a set  $\tilde{V}_l$  of nodes  $\tilde{v}_{i,a}$  and a set  $\tilde{E}_l$  of edges  $\tilde{e}_{(i,a)(j,b)}$ , with  $i, j \in [1, N]$  and  $a, b \in [1, K]$  ( $N$  number of cortical regions). Each connected components  $CC_l$  can therefore be vectorized in the form  $d_l \in \mathbb{N}^{(N \times K)}$ , where each element  $d_l(s)$  of  $d_l$  indicates the activation or non-activation of a brain region  $i$  at a certain time point  $a$  within the component:

$$d_l(s) = \begin{cases} 1, & \text{if } s = i \times a \text{ and } \tilde{v}_{i,a} \in \tilde{V}_l, \\ 0, & \text{otherwise.} \end{cases} \quad (6.2)$$

Each connected component  $CC_l$  of  $\tilde{G}$  can be reduced to a feature vector  $cc_l \in \mathbb{N}^N$ , where each element  $cc_l(i)$  of  $cc_l$  quantifies the normalized number of temporal occurrences of the brain regions  $i$  within the component  $CC_l$ . Formally:

$$cc_l(i) = \frac{cc_l^{raw}(i)}{\|cc_l\|_2}.$$

The raw count  $cc_l^{raw}(i)$  of activation time points of the brain region  $i$  within the component  $CC_l$  can be expressed in terms of the vectorized form  $d_l$  of the component  $CC_l$ :

$$cc_l^{raw}(i) = \sum_{k=1}^K d_l(i \times k).$$

The normalization of the feature vectors  $cc$  by the l2-norm of the raw count of regional activations allows to compare and cluster connected components with different durations  $k$ , but possibly with similar spatio-temporal appearance. Figure 6.5 schematizes the construction of the feature vectors. The form chosen here for the representation of connected components is convenient because it drastically reduces the dimensionality of the feature space to  $N$ . Moreover, averaging the activation information over time allows compensating for the noise present in the detected components. In fact, the extraction of the connected components relies on the functional signals reduction to point processes. Considering the high level of noise intrinsic the fMRI data, and the simplicity of the thresholding procedure, we can expect a significant level of noise in the resulting connected components. Anyway, the anatomical constraint introduced by the structural network  $G$  significantly increases the robustness of the detected components  $CC$  (for a detailed discussion of the topic we refer to section 7.2).

Considering the reduction of the connected components  $CC$  to feature vectors  $cc$ , we can notice the temporal sequentiality information is in fact lost. Anyway the feature vectors  $cc \in \mathbb{N}^N$  do not contain only a spatial information. The temporal information about regional activation persistence is encoded in the values of the vector. A connected component can for instance be represented by a brain surface plot of its feature vector entries (figure 6.4b).

The feature vectors of all the  $M$  connected subgraphs in  $\tilde{G}$  can be arranged in a feature matrix  $X \in \mathbb{R}_+^{(M \times N)}$  that can be used as an input to a clustering algorithm.

### **Connected components clustering**

Representative spatio-temporal patterns of graph  $\tilde{G}$  can be estimated by clustering the feature vectors  $cc$ . For a matter of simplicity, we propose here to use a simple clustering technique such as  $k$ -means. The  $k$ -means algorithm partitions the dataset  $X$  into  $k$  sets ( $k < M$ )  $C = \{C_1, C_2, \dots, C_k\}$  so as to minimize the within-cluster sum of squares

$$\operatorname{argmin}_C \sum_{l=1}^k \sum_{cc_i \in C_l} \|cc_i - \mu_l\|_2^2,$$

where  $\mu_l$  is the centroid of  $C_l$ . We remark that in this case the number  $k$  of clusters has to be set *a priori*. One may estimate the number  $k$  of clusters by considering the length of the specific resting-state acquisition, the number of connected components in the relative spatio-temporal graph  $\tilde{G}$ , and reference literature (Allen *et al.*, 2012; Smith *et al.*, 2012). Anyway, more sophisticated clustering algorithms that estimate an optimal number of clusters should be used in the future.



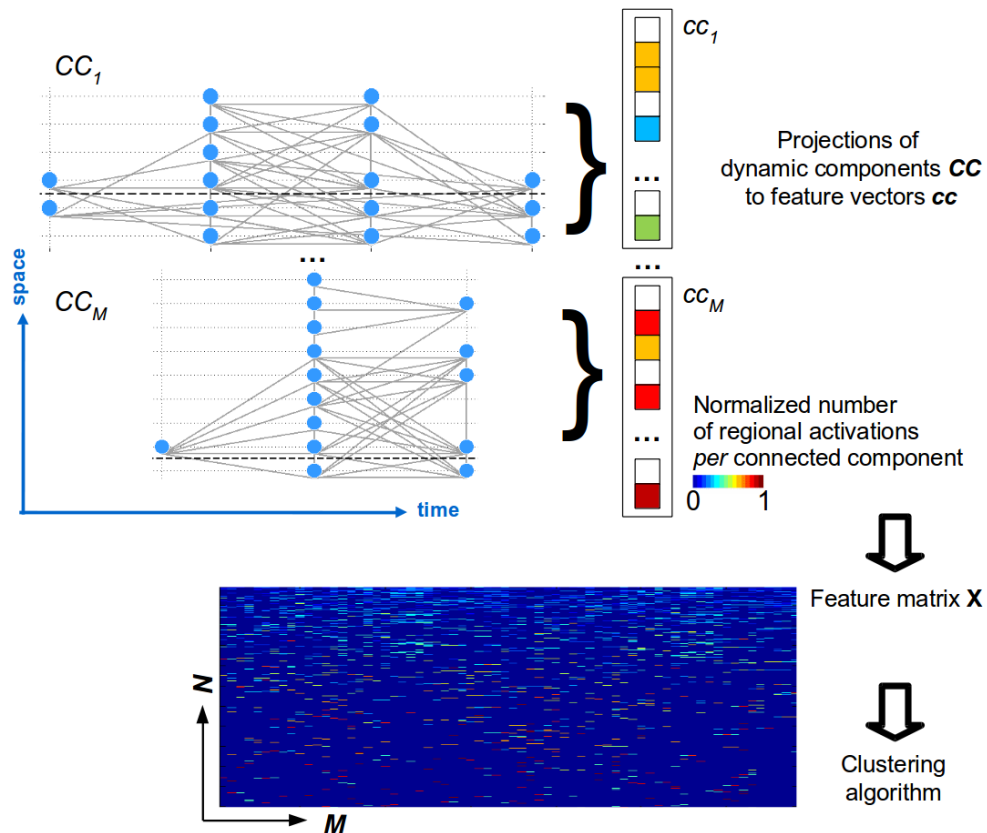


Figure 6.5 – Schematic representation of a feature matrix construction. Individual connected components  $CC$  are projected along the temporal dimension onto feature vectors  $cc \in \mathbb{R}^N$ . Feature vector entries  $cc(i)$  indicate the normalized number of occurrences of a brain region  $i$  within the connected component  $cc$ , that is the relative number of time points for which a region  $i$  is active in  $CC$ . The ensemble of the feature vectors of a spatio-temporal graph  $\tilde{G}$  constitutes a feature matrix  $X$  that can directly be used as input to a clustering algorithm.

## 6.5 Conclusions

In this chapter we formally defined an original network model, named spatio-temporal connectome, suitable for the joint representation of brain functional dynamics and structural connectivity.

The construction of a spatio-temporal graph  $\tilde{G}$  from MRI data is methodologically simple and straightforward. It relies on the point process analysis of the functional data, and on the replication of a static anatomical graph across multiple layers. Each node of  $\tilde{G}$  represents a specific brain areas  $i$  (for example, a region defined by a brain atlas), at a certain time point  $a$  within the acquisition period. Two nodes are connected in  $\tilde{G}$  if they are close in both the spatial and the temporal domains. The closeness in the spatial domain is given by the presence of an anatomical link between the two regions. The closeness in the temporal domain is expressed by the co-activation of the two regions at the same or one-step forward time point. Regional activation is detected by thresholding the functional time series (point process analysis). This approach, although straightforward and relatively robust (Liu & Duyn, 2013; Tagliazucchi *et al.*, 2014), is certainly sensitive to noise. A careful preprocessing of the fMRI volumes can certainly help in this sense. In addition, more sensitive and robust techniques for local activation detection, such as signal deconvolution (Karahanoğlu *et al.*, 2015), should be used in the future. Concerning the construction of the spatio-temporal graph, we should mention that in the current setting graph edges are binary and that, although potentially informative, no notion of connectivity strength is integrated in the model. Future work should address this limitation.

The spatio-temporal connectome combines sparse structural and functional information, and is therefore, and conveniently, highly sparse. The graph proves in fact to be composed of a set of smaller connected subgraphs, each one representing a dynamic spatio-temporal pattern of activation. Each activation component maps in fact a new kind of information, that is transient patterns of joint anatomical and functional connectivity. In the current framework, activation components are detected with no constraint on their temporal duration or spatial extension. In fact, our time-step-resolved analysis does not require the definition of any investigation window. This fact represents a clear advantage compared to sliding-window approaches, where the window size can influence the robustness of correlation statistics (Leonardi & Van De Ville, 2015), and determines the temporal scale of traceable dynamics. Moreover, the spatio-temporal framework can spatially resolve anatomically distinct, but temporally simultaneous, activation patterns. In this connection, in the next chapter 7 we will discuss the impact of the anatomical graph on the structure of the detected activation patterns.

The activation components of a spatio-temporal graph  $\tilde{G}$  can be clustered in order to extract representative and recursive patterns of activation. Each activation component is conveniently reduced to a low-dimensional feature vector before clustering. After classification, the temporal profiles of the representative spatio-temporal patterns of activation can be investigated (see following chapter 7). Moreover, the framework is well-suited for a brain dynamics investigation at multiple scales, from very local interactions between single nodes, to information propagation across the overall brain network. These aspects will be partially discussed in the following chapter 7.

## *Applications*

# Functional dynamics and anatomical substrate in the human brain

---

# 7

In this chapter we investigate the topological and dynamical features of spatio-temporal patterns of activation in human rs-fMRI and dMRI data. The functional and structural informations are jointly investigated within a spatio-temporal framework as defined in the previous chapter 6. Dynamical patterns are composed by regional activations correlated in time, and localized in the underlying structural graph.

At a first level of investigation, we characterize detected dynamical components in terms of temporal and spatial extension, temporal frequency, and spatio-temporal topology (section 7.2.1). Next, we cluster individual activations into representative patterns (for simplicity centroids), recurrent across subjects. The estimated centroids resolve the temporal persistence of individual regional activity within single activation patterns limited in time, and are spatially comparable to task-based intrinsic connectivity networks derived from large meta-analyses (section 7.2.2).

Section 7.2.3 is dedicated to the investigation of the structure-function relationship. Particularly, also using network null-models, we analyse the role that the brain structural network plays in shaping the activation components detected on the spatio-temporal connectome. Previous resting-state studies have reported strong time-average correlations between brain regions weakly anatomically connected. This apparent inconsistency between structural and functional connectivity has been ascribed to indirect paths of communication, and/or to the activity of third trigger regions. Here, we directly test this hypothesis by tracking correlation patterns at the fMRI temporal resolution. Moreover we ask if, at this fine-grain scale of investigation, reproducible functional interactions are actually more likely to happen between anatomically connected or non connected cortical regions.

Finally, we present preliminary analyses on inter-nodal dynamics, and we propose an indirect mapping of the functional usage of the anatomical network infrastructure.

We start this chapter with methods and materials describing the investigated cohort of subjects, MRI data, and the construction of the spatio-temporal graph.

## 7.1 Methods and materials

### 7.1.1 Human brain datasets and MRI data processing

#### *Healthy subjects dataset*

We considered a group of 71 healthy individuals (43 males and 28 females, aged  $29.1 \pm 9.3$  years old). Each subject underwent an MRI session on a 3 Tesla scanner (Magnetom Trio-Tim, Siemens Medical Solutions), equipped with a 32-channel head coil. Each MRI session included an *MPRAGE* sequence, a diffusion spectrum imaging (*DSI*) sequence, and a  $T2^*$ -weighted sequence (*fMRI*) of the duration of 9 minutes (voxel size  $3.3 \times 3.3 \times 3.3$  mm covering a VoI of  $64 \times 58 \times 32$  voxels; TR 1920 ms, TE 30 ms, 280 volumes). During the *fMRI* recording, subjects were lying in the scanner with eyes open, and without focusing on any specific external task (resting state condition).

#### *Structural networks estimation*

*MPRAGE* and *DSI* datasets were processed in order to estimate subject-wise structural connectivity matrices. More specifically, *MPRAGE* volumes were segmented into tissue compartments, and the cortical volume was subdivided into 448 regions, according to (Cammoun *et al.*, 2012). Subcortical structures were not considered in this analysis. Whole-brain connectivity (or tractogram) was estimated from reconstructed *DSI* data by means of deterministic streamline tractography. For each subject, a structural connectivity network was estimated, with 448 nodes corresponding to the segmented cortical regions. In the network, an edge connected two nodes if at least one streamline of the tractogram started and ended within the two corresponding regions. Thereafter, a group-representative structural graph  $G$  was estimated. Two nodes were connected in  $G$  if a corresponding edge was present in at least the 50% of the 71 subjects included in this analysis.

Moreover, two additional null-model networks were constructed. First, we generated a randomized version of  $G$  by recursive swapping of the brain network edges, as described in (Maslov & Sneppen, 2002). The randomized network  $G_r$  has density and degree sequence equal to  $G$ , but random structure. Second, we generated a neighbours network  $G_n$ . Two nodes were connected in  $G_n$  if the corresponding anatomical ROIs were neighbours in the Euclidean space. ROIs neighbourhood was evaluated in the space of the GM-WM surface as estimated by means of FreeSurfer segmentation.

$G_r$  and  $G_n$  will be used in section 7.2.3 for the investigation of the brain structure-function relationship.

#### *rs-fMRI data processing*

*fMRI* datasets were preprocessed in order to reduce noise and correct for motion and physiological artefacts, and according to state-of-the-art pipelines (Murphy *et al.*, 2009; Power *et al.*, 2012). Processing steps included slice timing correction, volumes rigid coregistration, nuisance signals regression (average WM, average CSF and 6 motion signals), and linear regression. The FSL software<sup>1</sup> and the Connectome Mapping Toolkit<sup>2</sup> (Daducci *et al.*, 2012) were used. The first 4 volumes of each subject were excluded in order to allow signal stabilization. Thereafter, each volume was spatially denoised by means of total variation denoising in three dimensions in order

<sup>1</sup>Software available at [www.fmrib.ox.ac.uk/fsl/](http://www.fmrib.ox.ac.uk/fsl/)

<sup>2</sup>Python code available at <http://www.cmtk.org/>

to enforce sharp boundaries between active and non active regions, and as suggested in (Abraham *et al.*, 2013). In addition, voxel-wise time series were band-pass filtered to the range  $[0.01 - 0.1]$  Hz. Data filtering was performed using the UNLOCBOX Matlab toolbox<sup>3</sup>. Node-wise representative *fMRI* time series were obtained by averaging the voxel-wise signals over all the voxels belonging to individual regions. Finally, each time series was normalized to unitary standard deviation and zero mean, and converted to a ROI-wise point process as described in the previous chapter, section 6.3.2. The threshold for point processes estimation was set to  $\tau = 2$  standard deviations.

### *Additional details on the cortical parcellation*

The cortical volume of each subject was subdivided into 448 regions according to (Cammoun *et al.*, 2012). This parcellation resolution was empirically chosen in order to achieve a good trade-off among ROI-wise representativeness of the average functional signals, consistent anatomical localization of regions across subjects, and limited noise in the structural graph  $G$ .

Moreover, each anatomical regions was associated to one of the 20 intrinsic component networks (ICNs) individuated by (Laird *et al.*, 2011). The work by Laird and colleagues, part of the Brain-Map project<sup>4</sup>, is a large meta-analysis of functional brain imaging experiments, and determines a set of spatial activation maps (the ICNs) consistent across experiments, and associated to specific behavioural domains such as action, vision, executive functions or emotion. Each one of the 448 ROIs considered in this study was associated to a particular ICN if at least the 25% of its voxels were overlapping the ICN map. For cortical ROIs associated to more than one ICN, the ICN with the largest overlap was considered.

## 7.1.2 Spatio-temporal graph construction and components clustering

### *Spatio-temporal graph*

The point processes of the individual subjects were concatenated in time, in order to estimate a single spatio-temporal graph  $\tilde{G}$  for the whole dataset. The main *rationale* behind this choice is to obtain more robust statistics for the description of inter-nodal interactions, connected components of  $\tilde{G}$ , and representative patterns of activation across subjects.

$\tilde{G}$  was constructed as described in chapter 6, by combining the group-wise structural network  $G$  and the concatenated ROI-wise point processes.

On the whole,  $\tilde{G}$  integrated 448 anatomical ROIs and  $71 \times 276 = 19'596$  time points (with 71 number of subjects, and 276 number of *fMRI* time points per subject), comprising a total of **8'779'008 nodes**. Each node of  $\tilde{G}$  represented a specific anatomical ROI and a specific time point over the total acquisition period. Moreover, each node could be associated with a binary variable indicating the active or inactive status of the node, according to its point process value. Directed edges were traced between each pair of nodes anatomically linked and temporally co-active (at the same or one-step forward time point), for a total of **1'063'946 edges**. No edge was allowed between nodes belonging to different subjects.

The spatio-temporal graph is an high dimensional object. From an implementation point of view,  $\tilde{G}$  was generated within a *Python* environment. Conveniently, we relied on *NetworkX*<sup>5</sup> (Schult, 2008) data structures and on *gpickle* file format for an efficient graph storing. Practically, the structural graph  $G$  was first duplicated  $T = 71 \times 276$  times in order to construct the skeleton

<sup>3</sup>Matlab toolbox available at <http://unlockbox.sourceforge.net/>

<sup>4</sup>ICN maps and brain templates available at <http://brainmap.org/>

<sup>5</sup>Python library available at <https://networkx.github.io/>

of  $\tilde{G}$ . Each node was associated with a list of attributes in order to simplify further analyses, and particularly to its activation status (on/off). Intra-layer edges were duplicated across layers. Finally, edges were pruned so that only anatomically linked and co-active nodes were connected in the final  $\tilde{G}$  (figure 7.1).

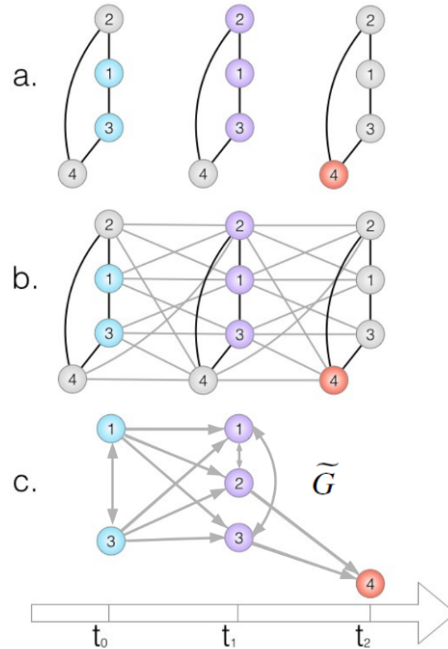


Figure 7.1 – Practical implementation of  $\tilde{G}$  construction. (a) The structural network is duplicated  $T$  times in order to build the initial skeleton of  $\tilde{G}$ . Each node is associated to a binary variable representing its active or inactive status. (b) Next, within-layer structural links are duplicated across layers. (c) Finally, initial links are pruned so that only nodes anatomically linked and co-active are connected in  $\tilde{G}$ . The edges of  $\tilde{G}$  are directed: intra-layer edges are bidirectional, while inter-layer edges follow the temporal sequentiality. Image credits to Kirell Benzi ([kirell.benzi@epfl.ch](mailto:kirell.benzi@epfl.ch)).

### Connected components and k-means clustering

The spatio-temporal graph  $\tilde{G}$  derived in this study was extremely sparse, with a number of edges one order of magnitude smaller of the number of nodes. Weakly connected components of  $\tilde{G}$  were detected using the *NetworkX* library. We call **width** of a component the number of time steps over which the component is active. Similarly, the **height** of a component is the number of distinct anatomical ROIs contained in it.

$\tilde{G}$  counted a total of 18'676 weakly connected components (CC). Anyway the majority of the CC was very small, counting one or few nodes only. Only components with a minimal duration of two time points, and a minimal spatial extension of 6 anatomical ROIs were retained for further analyses, for a total of **2'786 components**. We mention that, in the 448-regions cortical parcellation used in this study, 6 ROIs correspond on average to a single anatomical unit as defined by the Desikan-Killiany atlas (Desikan *et al.*, 2006).

Each one of the 2'786 connected components was reduced to a low-dimensional feature vector as described in chapter 6. Thereafter, the feature vectors were clustered into  $k = 12$  clusters by means of the  $k$ -means algorithm and using *Matlab*<sup>6</sup>. The number of clusters was chosen empirically, and considering previous literature (Calhoun *et al.*, 2014; Smith *et al.*, 2009, 2012). The cluster centroids can be interpreted as representative patterns of spatio-temporal activation. Each centroid was a vector  $\mu$  of length 448. Each element of  $\mu$  corresponded to a specific cortical region. For each cluster, the elements of  $\mu$  quantified the average duration of activation of the different brain regions, over the components classified in the cluster (see section 6.4).

## 7.2 Results and Discussion

### 7.2.1 Individual spatio-temporal activation components

The spatio-temporal graph was composed of 2'796. Components had average width of  $5.8 \pm 3.3$  time points (corresponding to  $11 \pm 6$  s), and average height of  $29 \pm 39$  ROIs. The distributions of components width and height were highly heavy-tailed, with majority of components including less than 50 ROIs, and lasting between 5 and 20 s. The total activation time (corresponding to the presence of appreciable activation components) was equal to 5'779 time points, corresponding to the 30% of the overall observation time  $T = 71 \times 276$  time points. The number of activation components *per* subject was  $39.2 \pm 6.7$ , and its histogram was approximately normally distributed.

A careful visual inspection of the connected components (CCs) allowed to identify some recurrent spatio-temporal patterns:

- the CCs can spatially extend across one single hemisphere, or across both hemispheres;
- some CCs are characterized by a massive activation of a set of ROIs which persists for all the component duration; other CCs can be better described by a propagation of activation between different ROIs, similarly to a wave;
- there are topologically different activation waves, that we could describe as radial or linear. In the radial pattern, the activity starts within an initial activation core, propagates to include a larger cortical area, and eventually reduces back to the starting core. In the linear pattern, the activation starts within a first set of ROIs and propagates to a second, different set of ROIs.

Figure 7.2 exemplifies some propagation patterns. Figures 7.2a and 7.2b represent a single component corresponding to the visual areas and covering the two hemispheres. The activation starts from later-occipital bilateral regions, to progressively include medial regions (lingual and pericalcarine cortices). These regions are associated with primary visual processes, processing of vision and encoding of visual memory. Figures 7.2c, 7.2d, 7.2e and 7.2f show two fronto-parietal patterns involving the left hemisphere only. In the first case we observe a massive activation of frontal regions, which temporally involves inferior parietal and supramarginal areas. In the second case the activation starts within the temporo-parietal cortex and propagates towards the frontal lobe.

### 7.2.2 Representative dynamical patterns of resting state activity

The components of the spatio-temporal graph were classified into 12 clusters using the  $k$ -means algorithm.

<sup>6</sup>MATLAB 8.0, *The MathWorks, Inc.*, Natick, Massachusetts, United States.

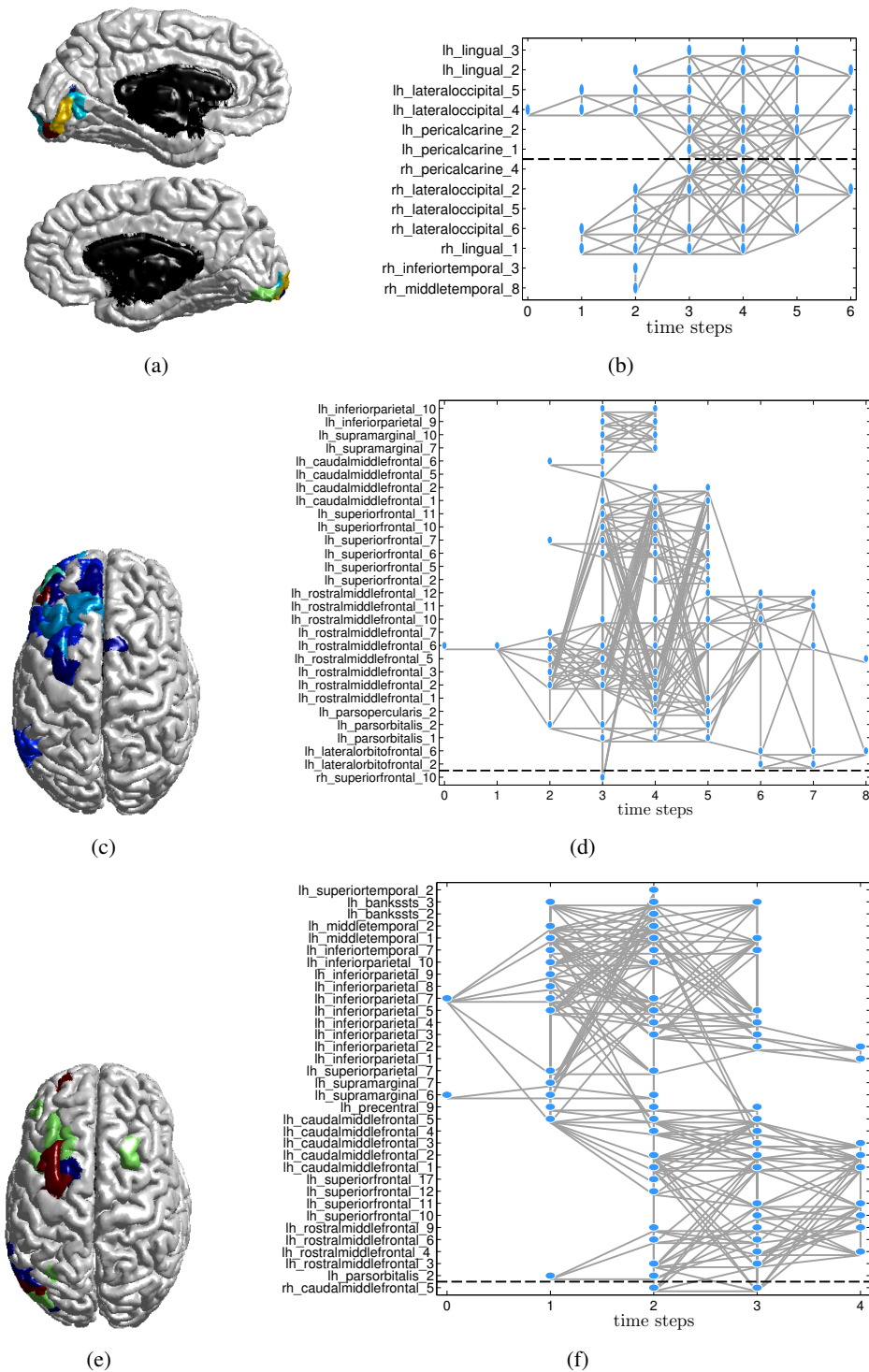


Figure 7.2 – Three examples of individual connected components. (a,b) *CC* covering part of the visual area, across the two hemispheres. (c,d,e,f) Single hemisphere *CC*s extending across fronto-parietal areas. Left column: brain surface plots. The color-coding represents the relative duration of activation of single ROIs (with dark red corresponding to long and dark blue corresponding to short activation). Right-column: spatio-temporal graph representation of the three components. Vertically, nodes are arranged in anatomical order from frontal to parietal-occipital-temporal areas, and starting from an horizontal line representing the brain midline.



The centroids of each cluster are shown in figure 7.3, where the color-coding represents the average temporal persistence of each cortical region within single components. Otherwise said, the surface plots represent the coordinates of the cluster centroids in the component features space.

Each centroid can be interpreted as a representative dynamical pattern of resting state activity. Morphologically, each centroid was composed of a core of persistent activation (dark red anatomical regions), surrounded by a periphery of short activation (yellow-green areas).

The representative patterns of activation were consistent with the task-based intrinsic connectivity networks identified by (Laird *et al.*, 2011). As shown in figure 7.4, each centroid mainly overlapped one or two ICN. Particularly, the cluster centroids identified the following functional circuits: 7.3a medial frontal area, 7.3b sensorimotor cortex, 7.3c primary and secondary visual area, 7.3d precuneus, 7.3e left somatosensory association cortex (supramarginal gyrus), 7.3f left fronto-parietal circuit, 7.3g left superior temporal area, 7.3h caudal limbic cortex, 7.3i right superior temporal area, 7.3j right fronto-parietal circuit, 7.3k right somatosensory association cortex (supramarginal gyrus), 7.3l left inferior temporal area.

The centroids were consistently recurrent across subjects (table 7.1). The most recurrent clusters were the fronto-parietal circuit (bilaterally), the frontal area and the visual system. In terms of temporal duration, the visual and sensorimotor activations demonstrated the longest activations.

<b>Centroid</b>	<i>Total number</i>	<i>Subject-wise number</i>	<i>Width (time points)</i>	<i>Height (ROIs)</i>
1 (a)	325	4.6 ± 1.7	5.8 ± 3.4	25.2 ± 32.1
2 (b)	201	2.8 ± 1.5	6.2 ± 3.2	38.8 ± 45.1
3 (c)	341	4.8 ± 1.5	7.5 ± 4.4	58.4 ± 57.3
4 (d)	245	3.5 ± 1.6	5.9 ± 3.5	34.1 ± 43.0
5 (e)	142	2.0 ± 1.2	5.0 ± 2.4	21.3 ± 28.1
6 (f)	291	4.1 ± 1.9	5.4 ± 3.1	19.7 ± 25.4
7 (g)	128	1.8 ± 1.7	5.1 ± 3.6	20.1 ± 27.4
8 (h)	184	2.6 ± 1.3	6.2 ± 3.2	30.4 ± 33.3
9 (i)	146	2.1 ± 1.5	4.8 ± 1.9	15.7 ± 13.7
10 (j)	453	6.4 ± 2.5	5.4 ± 3.1	18.9 ± 28.3
11 (k)	174	2.5 ± 1.3	5.5 ± 3.3	27.8 ± 38.6
12 (l)	156	2.2 ± 1.3	5.4 ± 3.0	20.9 ± 32.1

Table 7.1 – Statistics for representative resting-state patterns. First column: centroid ID (the letters correspond to the legend in figure 7.3). Second column: total number of *CCs* classified in clusters 1-12. Third column: average and standard deviation number of *CCs* classified in clusters 1-12 *per* subject. Fourth and fifth column: average and standard deviation width and height of *CCs* classified in clusters 1-12.

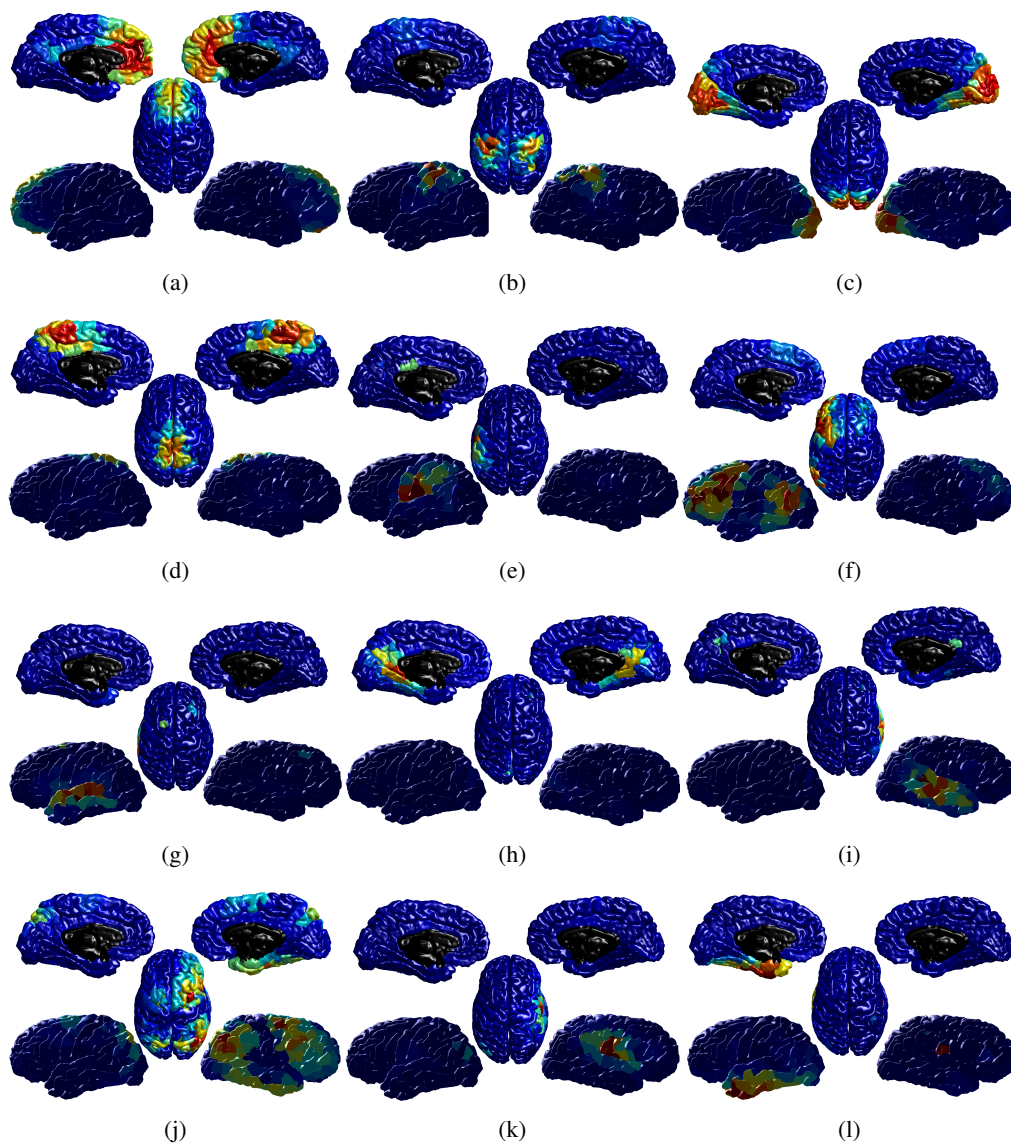


Figure 7.3 – Representative dynamical patterns of resting state activity: cluster centroids in the activation component features space. The color-coding represents the average temporal persistence of individual cortical regions, with dark red corresponding to long duration, and dark blues corresponding to short duration.

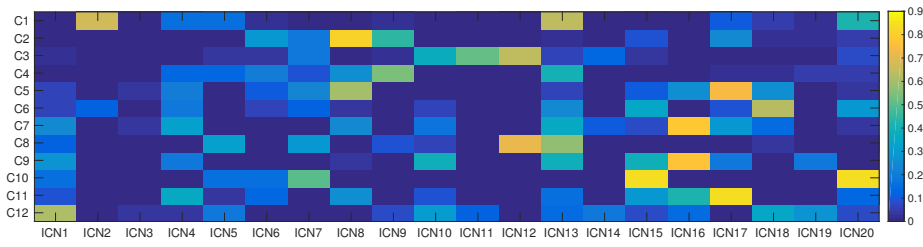


Figure 7.4 – Overlap between resting-state dynamical patterns and ICNs as identified by (Laird *et al.*, 2011). The overlap matrix is highly sparse, indicating a good correspondence between the spatio-temporal graph recurrent patterns and the intrinsic connectivity networks. The color coding represents the percentage spatial overlap between the centroids and the ICNs.

### 7.2.3 Structure-function relationship

In order to investigate the role that the anatomical network  $\tilde{G}$  plays in shaping the activation components topology, we compared the spatio-temporal graph  $\tilde{G}$  to alternative reference graphs  $\tilde{G}_n$ ,  $\tilde{G}_r$  and  $\tilde{G}_c$ .

The three reference graphs were constructed according to the procedure described in section 7.1.2, but using different static skeletons. The static skeleton of  $\tilde{G}$  was for instance the brain structural network  $G$ . For the three reference spatio-temporal graphs, the following static skeletons were used: the neighbourhood network  $G_n$  for  $\tilde{G}_n$ ; the brain randomized network  $G_r$  for  $\tilde{G}_r$ ; a complete network of 448 nodes  $G_c$  for  $\tilde{G}_c$ . We remark that using a complete network as static skeleton is equivalent to build the spatio-temporal graph on the basis of the functional information only. Therefore,  $\tilde{G}_c$  is based on *fMRI* data only, and does not encode any structural information.

For each one of the reference spatio-temporal graphs, the connected components were detected and classified into 12 clusters using the  $k$ -means algorithm, and similarly to  $\tilde{G}$ . Figure 7.5 represents some of the centroids obtained from the clustering of  $\tilde{G}_n$ ,  $\tilde{G}_r$ ,  $\tilde{G}$  and  $\tilde{G}_c$ . We can observe that it was possible to recover anatomically-meaningful centroids for all the three reference graphs. It was therefore possible to qualitatively match centroids across different spatio-temporal graph. For example, and similarly to  $\tilde{G}$ , we could identify a frontal and a sensorimotor cluster for all the three graphs  $\tilde{G}_n$ ,  $\tilde{G}_r$  and  $\tilde{G}_c$  (first and second rows of figure 7.5). Anyway, the centroids of  $G_r$  and  $G_c$  were much more noisy than the centroids of  $\tilde{G}$ . Particularly, without using the structural brain network as static skeleton, it was not possible to recover more complex and spatially-distributed centroids, such as the fronto-parietal pattern. On the other hand, the neighbourhood graph  $G_n$  constrained the activation patterns to localized anatomical areas, and did not allow to recover resting-state activities spanning the two hemispheres.

Next, we compared more specifically the spatio-temporal graph  $\tilde{G}$  with the reference graph  $\tilde{G}_c$ , which does not encode any structural prior.

Let  $\tilde{E}$  be the set of edges of graph  $\tilde{G}$ , and  $\tilde{E}_c$  the set of edges of  $\tilde{G}_c$ . Furthermore, let  $CC_s$  be the connected components of  $\tilde{G}$ , and  $CC_c$ s the connected components of  $\tilde{G}_c$ .

By construction,  $\tilde{E}$  is a subset of  $\tilde{E}_c$ . Moreover, each connected component  $CC_c$  in  $\tilde{G}_c$  contains one or more component  $CC_s$  of  $\tilde{G}$ . This fact is graphically represented in figure 7.6a, where the blue oval represents a component of  $\tilde{G}_c$ , while the violet ovals represent components of  $\tilde{G}$ .

In order to investigate the role of  $G$  on the spatio-temporal network structure, we considered two classes of edges: (i) the set  $\tilde{E}$ , and (ii) the set  $\tilde{E}_{diff} = \tilde{E}_c - \tilde{E}$ . The set  $\tilde{E}_{diff}$  includes the edges that link functionally co-active, but anatomically disconnected nodes. This concept is schematized in figure 7.6a, where edges of  $\tilde{E}$  are represented in blue, and edges of  $\tilde{E}_{diff}$  are represented in red.

We assessed the reproducibility of the edges in  $\tilde{E}$  and in  $\tilde{E}_{diff}$  by counting their relative num-

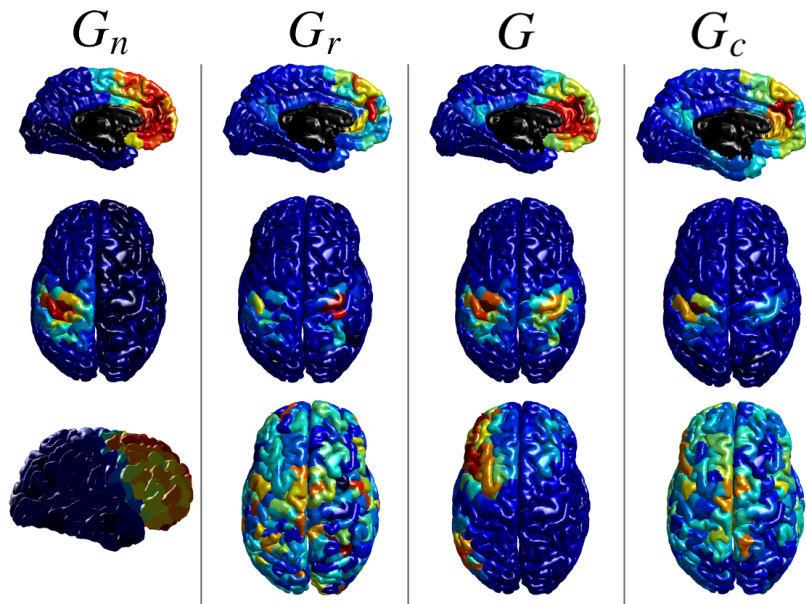


Figure 7.5 – Examples of cluster centroids from the reference spatio-temporal graphs  $\tilde{G}_n$ ,  $\tilde{G}_r$  and  $\tilde{G}_c$ , and from the original graph  $\tilde{G}$ . The color-coding represents the average duration of activation of the single anatomical regions within the connected components classified in the different clusters.

ber of occurrences across subjects. We remark that each edge is identified by the two anatomical ROIs that it connects. For each pair of anatomical ROIs, we therefore evaluated the reproducibility of the corresponding edge (if existing in  $\tilde{G}$  or  $\tilde{G}_c$ ), at the same time distinguishing between edges belonging to  $\tilde{E}$  or to  $\tilde{E}_{diff}$ .

Figure 7.6b represents the histograms of edges occurrence over the total observation period and across subjects. The edges in  $\tilde{E}$  were consistently reproducible across subjects (mean occurrence:  $144 \pm 102$ ). On the contrary, the edges in  $\tilde{E}_{diff}$  were poorly reproducible (mean occurrence:  $8 \pm 7$ ).

Taken together these results elucidate the role of the structural brain network in shaping dynamic spatio-temporal patterns of resting state activity, as detected *via* the spatio-temporal graph framework.

Practically, the anatomical constraint imposed by  $G$  substantially denoised the patterns of resting-state activity, as it was shown both by the qualitative comparison of the centroids across different reference graphs, and by the edges reproducibility analysis.

In more detail, the usage of the anatomical network  $G$  allowed to:

- spatially separate co-occurrent patterns of functional activity;
- temporally resolve patterns of functional activity which were sequential in time, but were not anatomically linked;
- denoise detected patterns of functional activity.

These effects are qualitatively illustrated in figure 7.7, that depicts two extracts from the spatio-temporal graphs  $\tilde{G}$  (first row) and  $\tilde{G}_c$  (second row). The two extracts correspond to the very same acquisition window. The figure exemplifies the role of the anatomical information in separating

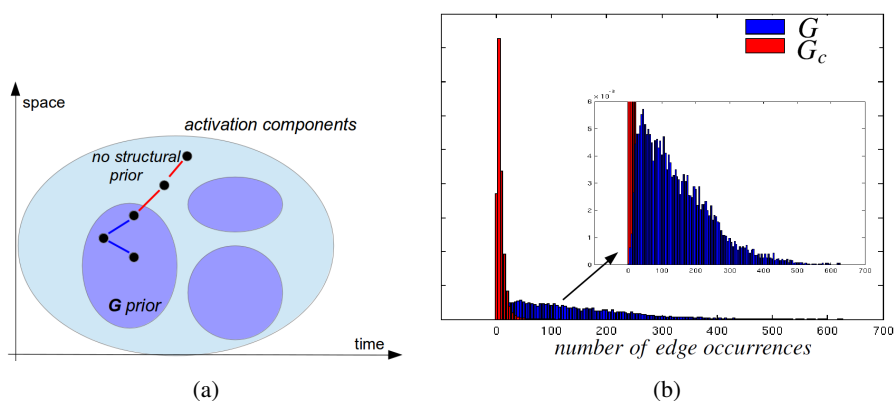


Figure 7.6 – Edge reproducibility analysis on spatio-temporal graphs. (a) Schematic representation of connected components detected by considering (violet ovals) and without considering (blue oval) the anatomical prior  $G$ . A small group of five nodes is represented in the scheme, with blue edges belonging to the set  $\tilde{E}$  and red edges belonging to the set  $\tilde{E}_{diff}$ . (b) Normalized histograms of edge reproducibility for the two sets  $\tilde{E}$  and  $\tilde{E}_{diff}$ .

distinct co-occurrent or sequential functional patterns (green and red circles), and in removing presumably spurious components (blue circles).

Finally, the edges reproducibility analysis pointed out that, at the fine-grain temporal scale of investigation defined by the spatio-temporal framework, functional interactions are in fact more likely to happen between cortical regions which are directly anatomically connected, rather than between regions connected *via* indirect paths.

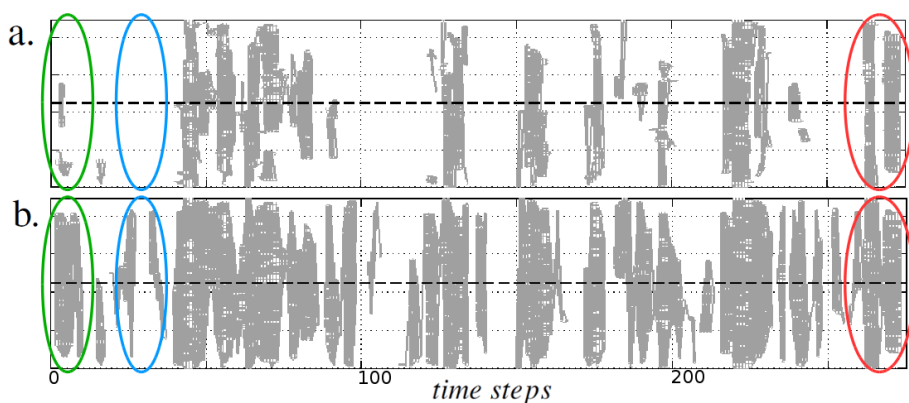


Figure 7.7 – Comparison of spatio-temporal graphs referring to the same acquisition period, and considering (first row) or not considering (second row) the anatomical prior. (a) Extract from  $\tilde{G}$ ; (b) extract from  $\tilde{G}_d$ .

## 7.2.4 Mapping the functional usage of anatomical networks

The spatio-temporal framework allows to characterize functional dynamics at multiple temporal scales.

In order to investigate inter-regional dynamics (between anatomically connected cortical regions), we built a **transition probability matrix TPM**. The transition probability matrix is derived from the spatio-temporal graph  $\tilde{G}$ , and has size  $448 \times 448$  elements.

The transition probability  $p_{ab}$  between each pair  $(a, b)$  of cortical ROIs expresses the probability under which a node  $a$  activates a node  $b$ , and was formally defined as

$$p_{a,b} = \frac{n_{a,b}}{n_{a,0} + \sum_{i=1, i \neq a}^N n_{a,i}},$$

with  $N = 448$  number of cortical regions, and  $n_{a,i}$  number of (directed) edges connecting region  $a$  to region  $b$  in  $\tilde{G}$ .  $n_{a,0}$  quantifies the number of time that an active node  $a$  does not activate any further node. Figure 7.8 represents the transition probability matrix computed from  $\tilde{G}$ .

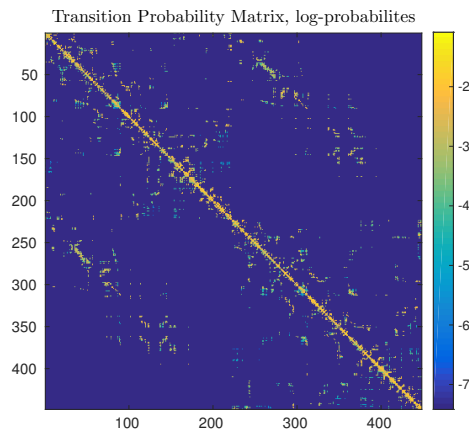


Figure 7.8 – Transition probability matrix (log-probability) estimated from the brain spatio-temporal graphs of 71 healthy subjects.

We compared  $TPM$  with the time-average functional connectivity matrix  $FC$ , and with structural connectivity indicators.

Considering the fact that the  $TPM$  integrates both the binary structural information and the functional information of the brain network, we split the 71-subjects dataset into two groups, and we computed the  $TPM$  from the first group datasets, and the structural and functional connectivity information from the second group datasets.

The first group included 51 subjects. A single spatio-temporal graph was computed by concatenating the 51 subjects in time and using their group-wise binary anatomical network, as described in section 7.1.2. A transition probability matrix was then estimated from the spatio-temporal graph.

The second group included 20 subjects and was used to compute (i) a time-average functional connectivity matrix  $FC$ , (ii) a group-representative structural connectivity matrix, weighted by the normalized connection density (Hagmann *et al.*, 2008) ( $SC_{density}$ ), and (iii) a group-representative structural connectivity matrix, weighted by the average streamline length ( $SC_{length}$ ).

In more detail, a functional connectivity matrix was computed for each subject by computing the Pearson's correlation coefficient between each pair of cortical regions' time series.  $FC$  was then computed as the average matrix over the individual ones. Group-wise  $SC_{density}$  and  $SC_{length}$  were computed by averaging the corresponding subject-wise structural connectivity matrices.

Figure 7.9 represents the group-wise  $SC_{density}$  and  $FC$  matrices.

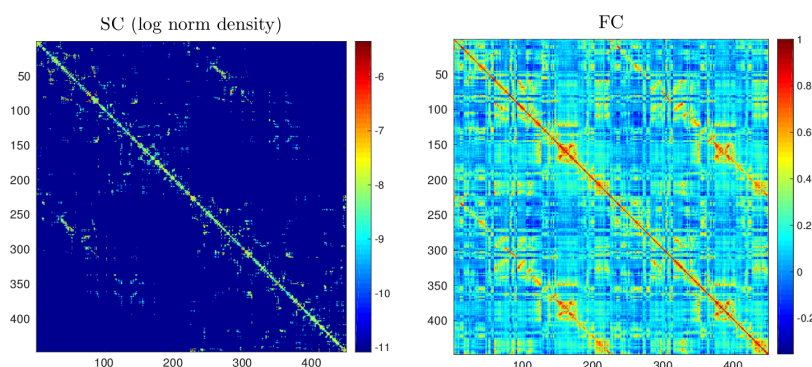


Figure 7.9 – Structural and functional connectivity matrices estimated from 20 healthy subjects’ dMRI and fMRI data. Structural connectivity is quantified by the normalized (Gaussian-resampled) connectivity density as defined in (Hagmann *et al.*, 2008). Functional connectivity is quantified by the Pearson’s correlation coefficient between pairs of ROI-wise functional signals.

In order to investigate the transition probability matrix, we computed the Spearman’s rank correlation coefficient  $\rho$  between the following quantities: (i)  $TPM$  and  $FC$ , (ii)  $SC$  and  $FC$ , (iii)  $TPM$  and  $SC_{density}$ , (iv)  $TPM$  and  $SC_{length}$ . Given the high dimensionality of the data, all the correlation values were statistically significant.

Figure 7.10 displays the four scatter plots corresponding to the above-listed correlations. We can observe that the structure-function correlation (figure 7.10a) was similar to previously reported findings ( $\rho = 0.36$ ) (Hagmann *et al.*, 2008; Honey *et al.*, 2009).

The transition probabilities were highly correlated with the time-average functional connectivity values (7.10b,  $\rho = 0.789$ ). This result is partially not surprising because  $TPM$  was computed from a spatio-temporal graph that encodes both structural and functional information. Nevertheless, we should remember that the  $TPM$  and the  $FC$  were estimated from two independent datasets.

Finally, the transition probabilities were highly (inversely) related to the average length of the corresponding WM tracts (7.10c,  $\rho = -0.59$ ), but poorly correlated with the normalized streamline density (7.10d,  $\rho = 0.31$ ).

The  $TPM$  expresses the probability of communication between pairs of cortical regions; it is an asymmetric matrix, and possesses the same binary structure as the corresponding anatomical graph.

The results reported in this section show that the transition probabilities relate to the anatomical connections length, suggesting a more probable functional communication between cortical regions linked by shorter WM bundles. Furthermore,  $TPM$  does strongly correlate with time-average functional connectivity values, at a level that exceed functional prediction from connectivity density, streamline length, Euclidean distance, indirect anatomical paths and more complex predictors (Goñi *et al.*, 2013; Honey *et al.*, 2009, 2010).

Conceptually, the transition probability matrix maps the usage of the underlying structural infrastructure. Certainly this quantity, that integrates multiple and non directly accessible informations, deserves further investigation. In this direction, future work relating transition probabilities, large-scale neural computational models, and diffusion processes and Markov dynamics, may help improving our understanding of communication principles across the brain network.

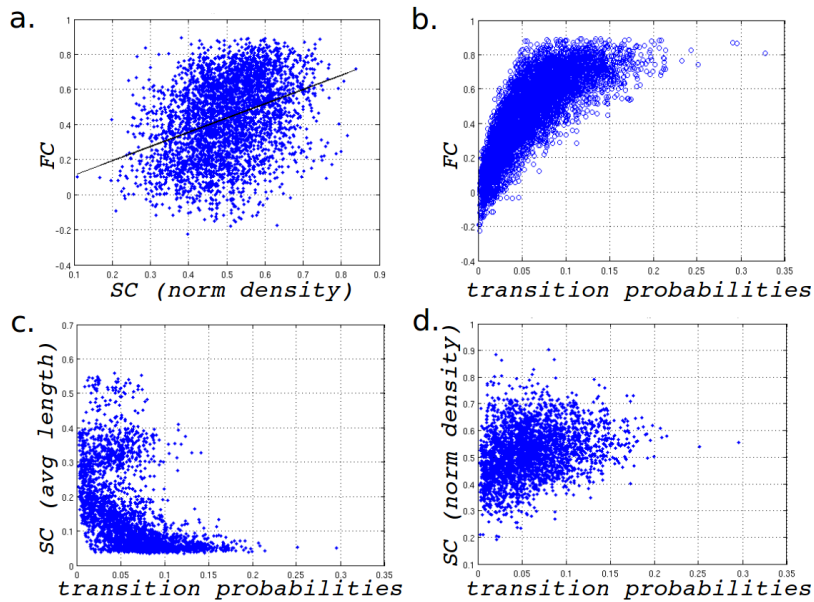


Figure 7.10 – Relationships between structural connectivity, functional connectivity and transition probabilities. Scatter plots representing (a)  $SC_{density}$  vs  $FC$  (the black line renders the least square linear fitting), (b)  $TPM$  vs  $FC$ , (c)  $TPM$  vs  $SC_{length}$ , and (d)  $TPM$  vs  $SC_{density}$ .

### 7.3 Conclusions

The relationship between structural and functional brain connectivity is a topic of current central interest. Moreover, recent works have highlighted important aspects of resting-state functional dynamics, pointing out that a stationary interpretation of the functional correlations might be over-simplistic.

In this chapter we applied a new spatio-temporal network model to the investigation of brain dynamics, enriching our comprehension of the interdependencies between functional activity and anatomical substrate.

First, we could isolate both individual patterns of brain activation (the connected components of the spatio-temporal graph), and transient but reproducible configurations of brain synchronization (the centroids of the connected components clusters). The representative patterns of brain activation were highly consistent with functional circuits estimated from task-based *fMRI* experiments.

Importantly, the spatio-temporal framework allowed highlighting dynamical aspects of isolated cortical co-activations. The connected components demonstrated different spatio-temporal behaviours, with activation starting within a localized area and propagating toward a periphery, or moving from a source region towards a second distinct cortical area. These observations recall the travelling brain waves measured by means of electroencephalography at different temporal and spatial resolutions, and deserve further investigations. Particularly, each activation component represents by itself a peculiar graph object, expanding across multiple layers and encoding two distinct dimensions, the space and the time. Methods for the characterization and comparison of these components should be assessed in the future.

Under a different perspective of investigation, the transition probability matrix summarizes



the average dynamical interactions between individual brain regions. Its high correlation with time-average functional connectivity information, and with anatomical connections' lengths, suggests that the transition probabilities may be interpreted as a mapping of the anatomical infrastructure usage during resting-state activity.

Furthermore, the transition probability matrix can be interpreted as the adjacency matrix of a brain connectivity graph, encoding a new form of integrated structure-function information. The study of such directed, weighted network may highlight causality relationships between brain nodes, and in the future should be related to brain network structures hypothesized to play an important role in functional processes, such as the rich-club and the network motif.

Finally, we investigated the role of the structural connectivity network in shaping spatial functional dynamics. We observed that, at the time scale of seconds, functional co-activations are more likely to happen between directly anatomically connected regions. Importantly, the integration of an anatomical prior to the investigation of the resting-state signals allowed to resolve temporally sequential or spatially co-occurrent functional patterns, and to denoise their detection.

This study certainly presents various limitations, and leaves margin for further improvement. First of all, different methodological issues need to be considered.

The detection of the activation events relies on a thresholding procedure, intrinsically sensitive to noise. More robust approaches such as signal deconvolution should be considered in the future. The number of clusters for the detection of the representative patterns of activation is currently set *a priori*, and is a sensitive parameter. The use of smarter clustering techniques should be investigated.

More importantly, a complementary analysis on surrogate data would offer a more complete perspective for results interpretation, and would confer stronger robustness to the reported findings.



# Discussion and Conclusions

---

# 8

## 8.1 Summary and contributions

This thesis arises from a tight interaction among magnetic resonance neuroimaging techniques, graph analysis mathematical methods and medical science, as a collaborative effort to elucidate fundamental clinical and biological questions.

A primary question faced in this work was the investigation of possible brain connectivity alterations characterizing a sensitive population of early psychosis patients.

Schizophrenia is a psychiatric disorder known to be potentially related to brain dysconnectivity patterns. Nevertheless, it is not clear if structural connectivity alterations are already present, and in which measure, in the earlier stages of the disease. Early impairments of white matter connectivity are likely to be extremely subtle and of difficult detection. Their characterization is of central importance for the identification of neuroimaging biomarkers for early diagnosis, monitoring of pathology progression and assessment of therapeutic approaches.

We have faced the investigation of brain connectivity in early psychosis under a staging perspective, first studying a population of chronic schizophrenia patients and, second, assessing if similar but milder alterations were already present in the earlier phases of the disorder.

A thoughtful and methodologically sound analysis pipeline, centered on graph theoretical methods, allowed us to identify a spatially distributed brain subnetwork, the affected core, impaired in chronic schizophrenia patients.

We expect that the disruption of a sub-system within an overall complex network alters the topology of the communication pathways between the different network elements, and modifies the overall network characteristics as quantified by means of graph measures. Translating this reflection in biological terms, the disruption of a brain subnetwork may alter the way different nervous areas interact, and may ultimately lead to less efficient information processing, cognitive deficits and symptoms. In order to elucidate the relationship between structural connectivity alterations and clinical evidences, it is therefore of interest to characterize the role that a potentially affected subnetwork plays within the overall brain communication infrastructure.

Motivated by these considerations we developed a new, simple network measure  $\zeta$  for the characterization of subnetworks topological centrality within overall networks. We used this measure to characterize the topological role of the affected core within the brain network, both in schizophrenia patients and in healthy controls. We found that the topological centrality of the affected core was compromised in patients, leading to a less efficient brain architecture.

From the analysis of chronic schizophrenia patients, we next moved to the investigation of early psychosis subjects, questioning if the affected core was already compromised in earlier stages of the disorder. Even though global network features were not impaired in the early psychosis group, we could highlight a precocious involvement of the affected core.

Taken together our findings suggested that the decentralization of the affected core as quantified by means of the topological centrality measure may be a valuable biomarker for the characterization of psychosis progression.

In this thesis, a second axis of research was the investigation of brain resting-state functional activity, and its relationship with the anatomical connectivity substrate.

A deeper understanding of the brain structure-function interdependences may help clarifying fundamental brain communication principles, both in health and pathological conditions.

We have proposed a new framework for the joint representation of the brain structural and functional information, named spatio-temporal connectome. Importantly, the spatio-temporal graph integrates dynamical and transient aspects of the resting-state activity. Recent works have shown that brain resting-state signals are in fact not stationary, and therefore their time-average representation may discard valuable information. Moreover, resting-state dynamics have been shown to be altered in diseases, and particularly in schizophrenia.

The spatio-temporal connectome is a particular multi-layer graph extending over both the temporal and the spatial dimensions, and encoding the notions of locality on the brain structural network, and of temporal co-activation of distinct brain regions.

Investigating the spatio-temporal graph of a group of healthy subjects, we identified spatio-temporal patterns of coherent functional activity between anatomically connected brain regions. Importantly, we characterized the temporal evolution of the activation patterns, and we investigated inter-nodal causality relationships in the form of a transition probability matrix.

Finally, we questioned the role that the anatomical connectivity network plays in shaping spatially distributed and temporally localized functional synchronizations. We showed that, at the temporal scale of tens of seconds, brain regions which are directly, rather than indirectly, anatomically connected *via* white matter bundles are more likely to interact.

## 8.2 Perspectives

In this dissertation we have shown that the investigation of brain connectivity networks and of functional interactions across multiple spatial and temporal scales provides important insights into brain organization and information transmission principles.

Graph theoretical measures allow characterizing the brain anatomical network at global and local scales of analysis, and quantifying different aspects of the brain architecture such as its small-worldness, assortativity and modular decomposability.

In our work we have mainly focused on the analysis of brain sub-systems, first by formally defining a measure of subnetwork topological centrality, and then by applying this measure to the investigation of brain dysconnectivity across different psychosis stages, and in the 22q11 deletion syndrome, a genetic disease considered to be a model for the study of psychosis.

The perspective of brain sub-systems analysis for the characterization of brain connectivity alterations in psychosis is of particular interest. Differently from other brain diseases, psychiatric disorders are not associated with localized cortical or white matter insults, but are rather characterized by diffuse dysconnectivity patterns whose clear description is still elusive. Moreover,

early psychosis and schizophrenia patients are extremely heterogeneous in terms of clinical profiles, and present a wide range of different symptoms.

Further investigations of the brain connectivity networks in health and psychosis patients, combined with a clever adaptation of statistical and graph theoretical methods, may allow to associate specific subnetworks alteration with diagnostic subgroups, symptom classes or cognitive deficits.

More broadly, it is tempting to assume that specific cognitive, executive and behavioural functions may be encoded within specific brain subnetworks or, equivalently, functional circuits. Even though this vision might be too simplistic, the understanding of the relationship between (i) the brain network architecture, (ii) the functional processes taking place on the top of the anatomical substrate, and (iii) the sensorimotor, behavioural or cognitive effects resulting from this interaction, is a fundamental interrogative.

In this direction, the investigation of resting-state dynamics *via* functional MRI may provide interesting insights into the relationship between brain functioning (neural activations and communication of information) on the one side, and mental functions (perception, movement, cognition, *etc.*) on the other side.

Recent studies have suggested that the resting-state activity can be decomposed into sparse sequences of temporally-localized activation events, building up transient and spatially-distributed synchronization patterns. These transient activations may potentially be associated with internal or external mental stimuli, information processing or cognitive functions. For example, resting-state synchronization patterns between parieto-occipital areas, and temporally recurring with increasing frequency over single fMRI scanning sessions, have been associated with state of drowsiness or light sleep. Moreover, alterations of resting-state dynamics have been associated with brain diseases, and particularly with schizophrenia.

In this thesis we have proposed an original multi-layer network model for the investigation of the brain functional dynamics taking place on the top of the anatomical connectivity substrate. The spatio-temporal graph offers a convenient formal framework for the investigation of temporally- and spatially-localized functional activation patterns.

Investigating the spatio-temporal connectome built from healthy subjects dMRI and rs-fMRI data, we could identify reproducible patterns of functional activity closely resembling task-based functional networks, as identified by a large meta-analysis of fMRI experiments. This evidence supports the association of the transient functional activations with cognitive and behavioural states. This perspective is clearly of future interest for clinical studies, where the alteration of the temporal occurrence of specific, spatial configurations of synchronization, may be related to peculiar pathological traits.

The proposed spatio-temporal network model allows representing dynamical interactions between individual brain regions occurring at the scale of seconds.

A closer analysis of the single functional components highlighted the presence of different patterns of activation propagation across the brain cortex. If some functional components were radiating from a core activation area toward a periphery, other were travelling from a source to a destination brain area. The characterization of these patterns of activation propagation may help assessing their possible relationship with mental processes.

These early results encourage further methodological development of the proposed spatio-temporal framework. Future related work should focus on the robust detection of isolated activation events in functional time series, on better approaches for the clustering of the activation components, and on the evaluation of appropriate spatio-temporal graph null-models. Moreover, graph theoretical methods should be specifically developed or adapted to the investigation and comparison

of spatio-temporal connectomes.

# Bibliography

---

- Abraham A, Dohmatob E, Thirion B, Samaras D and Varoquaux G. Extracting brain regions from rest fMRI with total-variation constrained dictionary learning. In *Medical Image Computing and Computer-Assisted Intervention – MICCAI 2013*, 607–615. Springer Berlin Heidelberg. (2013).
- Achard S, Salvador R, Whitcher B, Suckling J and Bullmore E. (2006). A resilient, low-frequency, small-world human brain functional network with highly connected association cortical hubs. *The Journal of Neuroscience*, **26**(1), 63–72.
- Albert R, Jeong H and Barabási AL. (2000). Error and attack tolerance of complex networks. *Nature*, **406**(6794), 378–382.
- Alexander DC. (2008). A general framework for experiment design in diffusion MRI and its application in measuring direct tissue-microstructure features. *Magnetic Resonance in Medicine*, **60**(2), 439–448.
- Alexander-Bloch A, Lambiotte R, Roberts B, Giedd J, Gogtay N and Bullmore E. (2012). The discovery of population differences in network community structure: New methods and applications to brain functional networks in schizophrenia. *NeuroImage*, **59**(4), 3889–3900.
- Alexander-Bloch AF, Gogtay N, Meunier D, Birn R, Clasen L, Lalonde F, Lenroot R, Giedd J and Bullmore ET. (2010). Disrupted modularity and local connectivity of brain functional networks in childhood-onset schizophrenia. *Frontiers in Systems Neuroscience*, **4**.
- Alexander-Bloch AF, Vértes PE, Stidd R, Lalonde F, Clasen L, Rapoport J, Giedd J, Bullmore ET and Gogtay N. (2013). The anatomical distance of functional connections predicts brain network topology in health and schizophrenia. *Cerebral Cortex*, **23**(1), 127–138.
- Allen EA, Damaraju E, Plis SM, Erhardt EB, Eichele T and Calhoun VD. (2012). Tracking whole-brain connectivity dynamics in the resting state. *Cerebral Cortex*, **24**, 663–676.
- Allen P, Larøi F, McGuire PK and Aleman A. (2008). The hallucinating brain: A review of structural and functional neuroimaging studies of hallucinations. *Neuroscience & Biobehavioral Reviews*, **32**(1), 175–191.
- Alstott J, Panzarasa P, Rubinov M, Bullmore ET and Vértes PE. (2014). A unifying framework for measuring weighted rich clubs. *Scientific Reports*, **4**.
- Alstott J, Breakspear M, Hagmann P, Cammoun L and Sporns O. (2009). Modeling the impact of lesions in the human brain. *PLoS Computational Biology*, **5**(6), e1000408.
- Andreasen NC, Pressler M, Nopoulos P, Miller D and Ho BC. (2010). Antipsychotic dose equivalents and dose-years: A standardized method for comparing exposure to different drugs. *Biological Psychiatry*, **67**(3), 255–262.

- Andreotti J, Jann K, Melie-Garcia L, Giezendanner S, Abela E, Wiest R, Dierks T and Federspiel A. (2014). Validation of network communicability metrics for the analysis of brain structural networks. *PLoS ONE*, **9**(12), e115503.
- Assaf Y, Alexander DC, Jones DK, Bizzi A, Behrens TE, Clark CA, Cohen Y, Dyrby TB, Huppi PS, Knoesche TR, LeBihan D, Parker GJ and Poupon C. (2013). The CONNNECT project: Combining macro- and micro-structure. *NeuroImage*, **80**, 273–282.
- Association AP. (2000). *Diagnostic and Statistical Manual of Mental Disorders, Fourth Edition: DSM-IV-TR*®. American Psychiatric Pub. ISBN 9780890426654.
- August SM, Kiwanuka JN, McMahon RP and Gold JM. (2012). The MATRICS consensus cognitive battery (MCCB): Clinical and cognitive correlates. *Schizophrenia Research*, **134**(1), 76–82.
- Baggio HC, Sala-Llonch R, Segura B, Marti MJ, Valldeoriola F, Compta Y, Tolosa E and Junqué C. (2014). Functional brain networks and cognitive deficits in parkinson's disease. *Human Brain Mapping*, **35**(9), 4620–4634.
- Bai F, Shu N, Yuan Y, Shi Y, Yu H, Wu D, Wang J, Xia M, He Y and Zhang Z. (2012). Topologically convergent and divergent structural connectivity patterns between patients with remitted geriatric depression and amnesic mild cognitive impairment. *The Journal of Neuroscience*, **32**(12), 4307–4318.
- Baker KD and Skuse DH. (2005). Adolescents and young adults with 22q11 deletion syndrome: psychopathology in an at-risk group. *The British Journal of Psychiatry*, **186**(2), 115–120.
- Ball G, Aljabar P, Zebari S, Tusor N, Arichi T, Merchant N, Robinson EC, Ogundipe E, Rueckert D, Edwards AD and Counsell SJ. (2014). Rich-club organization of the newborn human brain. *PNAS*, **111**(20), 7456–7461.
- Barnea-Goraly N, Menon V, Krasnow B, Ko A, Reiss A and Eliez S. (2003). Investigation of white matter structure in velocardiofacial syndrome: A diffusion tensor imaging study. *The American Journal of Psychiatry*, **160**(10), 1863–1869.
- Bassett DS, Bullmore E, Verchinski BA, Mattay VS, Weinberger DR and Meyer-Lindenberg A. (2008). Hierarchical organization of human cortical networks in health and schizophrenia. *The Journal of Neuroscience*, **28**(37), 9239–9248.
- Bassett DS, Wymbs NF, Porter MA, Mucha PJ, Carlson JM and Grafton ST. (2011). Dynamic reconfiguration of human brain networks during learning. *PNAS*, **108**(18), 7641–7646.
- Bassett DS and Bullmore E. (2006). Small-world brain networks. *Neuroscientist*, **12**(6), 512–523.
- Batalle D, Eixarch E, Figueras F, Muñoz-Moreno E, Bargallo N, Illa M, Acosta-Rojas R, Amat-Roldan I and Gratacos E. (2012). Altered small-world topology of structural brain networks in infants with intrauterine growth restriction and its association with later neurodevelopmental outcome. *NeuroImage*, **60**(2), 1352–1366.
- Baumann PS, Cammoun L, Conus P, Do KQ, Marquet P, Meskaldji D, Meuli R, Thiran JP and Hagmann P. (2012). High b-value diffusion-weighted imaging: A sensitive method to reveal white matter differences in schizophrenia. *Psychiatry Research: Neuroimaging*, **201**(2), 144–151.



- Baumann PS, Crespi S, Marion-Veyron R, Solida A, Thonney J, Favrod J, Bonsack C, Do KQ and Conus P. (2013). Treatment and early intervention in psychosis program (TIPP-lausanne): implementation of an early intervention programme for psychosis in switzerland. *Early Intervention in Psychiatry*, **7**(3), 322–328.
- Bearden CE, Erp TGMv, Dutton RA, Lee AD, Simon TJ, Cannon TD, Emanuel BS, McDonald-McGinn D, Zackai EH and Thompson PM. (2009). Alterations in midline cortical thickness and gyrification patterns mapped in children with 22q11.2 deletions. *Cerebral Cortex*, **19**(1), 115–126.
- Beaulieu C. (2002). The basis of anisotropic water diffusion in the nervous system – a technical review. *NMR in Biomedicine*, **15**(7-8), 435–455.
- Benjamini Y and Hochberg Y. (1995). Controlling the false discovery rate: A practical and powerful approach to multiple testing. *Journal of the Royal Statistical Society: Series B (Statistical Methodology)*, **57**(1), 289–300.
- Betzal RF, Griffa A, Avena-Koenigsberger A, Goñi J, Thiran JP, Hagmann P and Sporns O. (2013). Multi-scale community organization of the human structural connectome and its relationship with resting-state functional connectivity. *Network Science*, **1**(03), 353–373.
- Blondel VD, Guillaume JL, Lambiotte R and Lefebvre E. (2008). Fast unfolding of communities in large networks. *Journal of Statistical Mechanics: Theory and Experiment*, **2008**(10), P10008.
- Bora E, Fornito A, Radua J, Walterfang M, Seal M, Wood SJ, Yücel M, Velakoulis D and Pantelis C. (2011). Neuroanatomical abnormalities in schizophrenia: A multimodal voxelwise meta-analysis and meta-regression analysis. *Schizophrenia Research*, **127**(1–3), 46–57.
- Borgwardt SJ, McGuire PK, Aston J, Berger G, Dazzan P, Gschwandtner U, Pflueger M, D’Souza M, Radue EW and Riecher-Roessler A. (2007). Structural brain abnormalities in individuals with an at-risk mental state who later develop psychosis. *The British Journal of Psychiatry*, **191**, 69–75.
- Buehlmann E, Berger GE, Aston J, Gschwandtner U, Pflueger MO, Borgwardt SJ, Radue EW and Riecher-Rössler A. (2010). Hippocampus abnormalities in at risk mental states for psychosis? a cross-sectional high resolution region of interest magnetic resonance imaging study. *Journal of Psychiatric Research*, **44**(7), 447–453.
- Bullmore E and Sporns O. (2009). Complex brain networks: graph theoretical analysis of structural and functional systems. *Nature Reviews Neuroscience*, **10**(3), 186–198.
- Bullmore E and Sporns O. (2012). The economy of brain network organization. *Nature Reviews Neuroscience*, **13**(5), 336–349.
- Cabral J, Kringelbach ML and Deco G. (2014). Exploring the network dynamics underlying brain activity during rest. *Progress in Neurobiology*, **114**, 102–131.
- Calhoun VD, Eichele T and Pearlson G. (2009). Functional brain networks in schizophrenia: A review. *Frontiers in Human Neuroscience*, **3**.
- Calhoun VD, Miller R, Pearlson G and Adalı T. (2014). The chronnectome: Time-varying connectivity networks as the next frontier in fMRI data discovery. *Neuron*, **84**(2), 262–274.
- Callaway DS, Newman MEJ, Strogatz SH and Watts DJ. (2000). Network robustness and fragility: Percolation on random graphs. *Physical Review Letters*, **85**(25), 5468–5471.

- Cammoun L, Gigandet X, Meskaldji D, Thiran JP, Sporns O, Do KQ, Maeder P, Meuli R and Hagmann P. (2012). Mapping the human connectome at multiple scales with diffusion spectrum MRI. *Journal of Neuroscience Methods*, **203**(2), 386–397.
- Campbell LE, Daly E, Toal F, Stevens A, Azuma R, Catani M, Ng V, Amelvoort Tv, Chitnis X, Cutter W, Murphy DGM and Murphy KC. (2006). Brain and behaviour in children with 22q11.2 deletion syndrome: a volumetric and voxel-based morphometry MRI study. *Brain*, **129**(5), 1218–1228.
- Canu E, Agosta F and Filippi M. (2015). A selective review of structural connectivity abnormalities of schizophrenic patients at different stages of the disease. *Schizophrenia Research*, **161**(1), 19–28.
- Castellanos FX, Di Martino A, Craddock RC, Mehta AD and Milham MP. (2013). Clinical applications of the functional connectome. *NeuroImage*, **80**, 527–540.
- Chang C and Glover GH. (2010). Time-frequency dynamics of resting-state brain connectivity measured with fMRI. *NeuroImage*, **50**(1), 81–98.
- Chen ZJ, He Y, Rosa-Neto P, Germann J and Evans AC. (2008). Revealing modular architecture of human brain structural networks by using cortical thickness from MRI. *Cerebral Cortex*, **18**(10), 2374–2381.
- Chen ZJ, He Y, Rosa-Neto P, Gong G and Evans AC. (2011). Age-related alterations in the modular organization of structural cortical network by using cortical thickness from MRI. *NeuroImage*, **56**(1), 235–245.
- Chow EW, Ho A, Wei C, Voormolen EH, Crawley AP and Bassett AS. (2011). Association of schizophrenia in 22q11.2 deletion syndrome and gray matter volumetric deficits in the superior temporal gyrus. *The American Journal of Psychiatry*, **168**(5), 522–529.
- Collin G, Kahn RS, Reus MAd, Cahn W and van den Heuvel MP. (2014a). Impaired rich club connectivity in unaffected siblings of schizophrenia patients. *Schizophrenia Bulletin*, **40**(2), 438–448.
- Collin G, Sporns O, Mandl RCW and Heuvel MPvd. (2014b). Structural and functional aspects relating to cost and benefit of rich club organization in the human. *Cerebral Cortex*, **24**(9), 2258–2267.
- Crossley NA, Mechelli A, Scott J, Carletti F, Fox PT, McGuire P and Bullmore ET. (2014). The hubs of the human connectome are generally implicated in the anatomy of brain disorders. *Brain*, **137**(8), 2382–2395.
- Crossley NA, Mechelli A, Vértes PE, Winton-Brown TT, Patel AX, Ginestet CE, McGuire P and Bullmore ET. (2013). Cognitive relevance of the community structure of the human brain functional coactivation network. *PNAS*, **110**(28), 11583–11588.
- Crucitti P, Latora V, Marchiori M and Rapisarda A. (2003). Efficiency of scale-free networks: error and attack tolerance. *Physica A: Statistical Mechanics and its Applications*, **320**, 622–642.
- da Silva Alves F, Schmitz N, Bloemen O, van der Meer J, Meijer J, Boot E, Nederveen A, de Haan L, Linszen D and van Amelvoort T. (2011). White matter abnormalities in adults with 22q11 deletion syndrome with and without schizophrenia. *Schizophrenia Research*, **132**(1), 75–83.

- Daducci A, Gerhard S, Griffa A, Lemkaddem A, Cammoun L, Gigandet X, Meuli R, Hagmann P and Thiran JP. (2012). The connectome mapper: An open-source processing pipeline to map connectomes with MRI. *PLoS ONE*, **7**(12), e48121.
- Dall'Asta L, Barrat A, Barthélemy M and Vespignani A. (2006). Vulnerability of weighted networks. *Journal of Statistical Mechanics: Theory and Experiment*, **2006**(4), P04006.
- Damoiseaux JS, Smith SM, Witter MP, Sanz-Arigita EJ, Barkhof F, Scheltens P, Stam CJ, Zarei M and Rombouts SA. (2009). White matter tract integrity in aging and alzheimer's disease. *Human Brain Mapping*, **30**(4), 1051–1059.
- Damoiseaux J and Greicius M. (2009). Greater than the sum of its parts: a review of studies combining structural connectivity and resting-state functional connectivity. *Brain Structure and Function*, **213**(6), 525–533.
- Danon L, Díaz-Guilera A, Duch J and Arenas A. (2005). Comparing community structure identification. *Journal of Statistical Mechanics: Theory and Experiment*, **2005**(9), P09008.
- de Reus MA and van den Heuvel MP. (2013). Estimating false positives and negatives in brain networks. *NeuroImage*, **70**, 402–409.
- de Reus MA and van den Heuvel MP. (2014). Simulated rich club lesioning in brain networks: a scaffold for communication and integration? *Frontiers in Human Neuroscience*, **8**.
- Deco G, Jirsa V and McIntosh A. (2011). Emerging concepts for the dynamical organization of resting-state activity in the brain. *Nature Reviews Neuroscience*, **12**(1), 43–56.
- Deco G, Jirsa V, McIntosh AR, Sporns O and Kötter R. (2009). Key role of coupling, delay, and noise in resting brain fluctuations. *PNAS*, **106**(25), 10302–10307.
- Deco G and Jirsa VK. (2012). Ongoing cortical activity at rest: Criticality, multistability, and ghost attractors. *The Journal of Neuroscience*, **32**(10), 3366–3375.
- Deligianni F, Robinson E, Beckmann C, Sharp D, Edwards A and Rueckert D. (2011). Inference of functional connectivity from direct and indirect structural brain connections. In *2011 IEEE International Symposium on Biomedical Imaging: from Nano to Macro*, 849–852.
- Desikan RS, Ségonne F, Fischl B, Quinn BT, Dickerson BC, Blacker D, Buckner RL, Dale AM, Maguire RP, Hyman BT, Albert MS and Killiany RJ. (2006). An automated labeling system for subdividing the human cerebral cortex on MRI scans into gyral based regions of interest. *NeuroImage*, **31**(3), 968–980.
- Do K, Cabungcal J, Frank A, Steullet P and Cuenod M. (2009). Redox dysregulation, neurodevelopment, and schizophrenia. *Current Opinion in Neurobiology*, **19**(2), 220–230.
- Douaud G, Filippini N, Knight S, Talbot K and Turner M. (2011). Integration of structural and functional magnetic resonance imaging in amyotrophic lateral sclerosis. *Brain*, **134**(12), 3470–3479.
- Drzezga A, Becker JA, Dijk KRAV, Sreenivasan A, Talukdar T, Sullivan C, Schultz AP, Sepulcre J, Putcha D, Greve D, Johnson KA and Sperling RA. (2011). Neuronal dysfunction and disconnection of cortical hubs in non-demented subjects with elevated amyloid burden. *Brain*, **134**(6), 1635–1646.
- Dubois J, Dehaene-Lambertz G, Kulikova S, Poupon C, Hüppi PS and Hertz-Pannier L. (2014). The early development of brain white matter: A review of imaging studies in fetuses, newborns and infants. *Neuroscience*, **276**, 48–71.

- Duerden EG, Card D, Lax ID, Donner EJ and Taylor MJ. (2013). Alterations in frontostriatal pathways in children born very preterm. *Developmental Medicine & Child Neurology*, **55**(10), 952–958.
- Ellison-Wright I and Bullmore E. (2009). Meta-analysis of diffusion tensor imaging studies in schizophrenia. *Schizophrenia Research*, **108**(1), 3–10.
- Ellison-Wright I, Glahn DC, Laird AR, Thelen SM and Bullmore E. (2008). The anatomy of first-episode and chronic schizophrenia: an anatomical likelihood estimation meta-analysis. *The American Journal of Psychiatry*, **165**(8), 1015–1023.
- Estrada E. (2006). Network robustness to targeted attacks. the interplay of expansibility and degree distribution. *The European Physical Journal B*, **52**(4), 563–574.
- Estrada E. (2007). Food webs robustness to biodiversity loss: The roles of connectance, expansibility and degree distribution. *Journal of Theoretical Biology*, **244**(2), 296–307.
- Estrada E and Hatano N. (2008). Communicability in complex networks. *Physical Review E*, **77**(3), 036111.
- Estrada E, Hatano N and Benzi M. (2012). The physics of communicability in complex networks. *Physics Reports*, **514**(3), 89–119.
- Fair DA, Cohen AL, Power JD, Dosenbach NUF, Church JA, Miezin FM, Schlaggar BL and Petersen SE. (2009). Functional brain networks develop from a “local to distributed” organization. *PLoS Computational Biology*, **5**(5), e1000381.
- Fanous AH, Neale MC, Gardner CO, Webb BT, Straub RE, O’Neill FA, Walsh D, Riley BP and Kendler KS. (2007). Significant correlation in linkage signals from genome-wide scans of schizophrenia and schizotypy. *Molecular Psychiatry*, **12**(10), 958–965.
- Feldman R and Eidelman AI. (2006). Neonatal state organization, neuromaturation, mother-infant interaction, and cognitive development in small-for-gestational-age premature infants. *Pediatrics*, **118**(3), 869–878.
- Fischi-Gomez E. (2015). Graph network measures of brain connectivity in high-risk preterm-born 6 years-old children and its relation with behavior and cognitive performance. *Submitted*.
- Fischi-Gomez E, Griffa A, Munoz-Moreno E, Vasung L, Borradori-Tolsa C, Lazeyras F, Thiran JP and Hüppi PS. (2015). Brain network modular fingerprint of premature born children. In *23rd International Symposium on Magnetic Resonance in Medicine (ISMRM)*.
- Fischi-Gómez E, Vasung L, Meskaldji DE, Lazeyras F, Borradori-Tolsa C, Hagmann P, Barisnikov K, Thiran JP and Hüppi PS. (2014). Structural brain connectivity in school-age preterm infants provides evidence for impaired networks relevant for higher order cognitive skills and social cognition. *Cerebral Cortex*, doi:10.1093/cercor/bhu073.
- Fitzsimmons J, Kubicki M and Shenton ME. (2013). Review of functional and anatomical brain connectivity findings in schizophrenia. *Current Opinion in Psychiatry*, **26**(2), 172–187.
- Fornito A and Bullmore ET. (2014). Connectomics: A new paradigm for understanding brain disease. *European Neuropsychopharmacology*.
- Fornito A, Zalesky A, Pantelis C and Bullmore ET. (2012). Schizophrenia, neuroimaging and connectomics. *NeuroImage*, **62**(4), 2296–2314.
- Fortunato S. (2010). Community detection in graphs. *Physics Reports*, **486**(3), 75–174.

- Fox MD and Raichle ME. (2007). Spontaneous fluctuations in brain activity observed with functional magnetic resonance imaging. *Nature Reviews Neuroscience*, **8**(9), 700–711.
- Freeman LC. (1978). Centrality in social networks conceptual clarification. *Social Networks*, **1**(3), 215–239.
- Friston K and Frith C. (1994). Schizophrenia: a disconnection syndrome? *Journal of Clinical Neuroscience*, **3**(2), 89–97.
- Gigandet X, Griffa A, Kober T, Daducci A, Gilbert G, Connelly A, Hagmann P, Meuli R, Thiran JP and Krueger G. (2013). A connectome-based comparison of diffusion MRI schemes. *PLoS ONE*, **8**(9), e75061.
- Gilbert J, Moler C and Schreiber R. (1992). Sparse matrices in MATLAB: Design and implementation. *SIAM Journal on Matrix Analysis and Applications*, **13**(1), 333–356.
- Ginestet CE, Nichols TE, Bullmore ET and Simmons A. (2011). Brain network analysis: Separating cost from topology using cost-integration. *PLoS ONE*, **6**(7), e21570.
- Ginestet CE and Simmons A. (2011). Statistical parametric network analysis of functional connectivity dynamics during a working memory task. *NeuroImage*, **55**(2), 688–704.
- Girard G, Whittingstall K, Deriche R and Descoteaux M. (2014). Towards quantitative connectivity analysis: reducing tractography biases. *NeuroImage*, **98**, 266–278.
- Glahn DC, Laird AR, Ellison-Wright I, Thelen SM, Robinson JL, Lancaster JL, Bullmore E and Fox PT. (2008). Meta-analysis of gray matter anomalies in schizophrenia: Application of anatomic likelihood estimation and network analysis. *Biological Psychiatry*, **64**(9), 774–781.
- Gottesman II and Gould TD. (2003). The endophenotype concept in psychiatry: etymology and strategic intentions. *The American Journal of Psychiatry*, **160**(4), 636–645.
- Goñi J, Avena-Koenigsberger A, Velez de Mendizabal N, van den Heuvel MP, Betzel RF and Sporns O. (2013). Exploring the morphospace of communication efficiency in complex networks. *PLoS ONE*, **8**(3), e58070.
- Goñi J, van den Heuvel MP, Avena-Koenigsberger A, Mendizabal NVd, Betzel RF, Griffa A, Hagmann P, Corominas-Murtra B, Thiran JP and Sporns O. (2014). Resting-brain functional connectivity predicted by analytic measures of network communication. *PNAS*, **111**(2), 833–838.
- Grant P, Kuepper Y, Mueller EA, Wielpuetz C, Mason O and Hennig J. (2013). Dopaminergic foundations of schizotypy as measured by the german version of the oxford-liverpool inventory of feelings and experiences (o-LIFE)—a suitable endophenotype of schizophrenia. *Frontiers in Human Neuroscience*, **7**.
- Grayson DS, Ray S, Carpenter S, Iyer S, Dias TGC, Stevens C, Nigg JT and Fair DA. (2014). Structural and functional rich club organization of the brain in children and adults. *PLoS ONE*, **9**(2), e88297.
- Greicius M, Supekar K, Menon V and Dougherty R. (2009). Resting-state functional connectivity reflects structural connectivity in the default mode network. *Cerebral Cortex*, **19**(1), 72–78.
- Griffa A, Baumann P, Ferrari C, Eric T, Conus P and DoK, Thiran JP and Hagmann P. (2015a). Diffusion spectrum imaging connectomics: a biomarker for staging in psychotic disorders. In *23rd International Symposium on Magnetic Resonance in Medicine (ISMRM)*.

- Griffa A, Benzi K, Ricaud B, Bresson X, Vandergheynst P, Hagmann P and Thiran JP. (2015b). Mapping resting-state dynamics on spatio-temporal graphs: a combined functional and diffusion mri approach. In *23rd International Symposium on Magnetic Resonance in Medicine (ISMRM)*.
- Griffa A, Betzel R, Do K, Conus P, Hagmann P and Thiran JP. (2013a). Group-representative partitions of human brain structural networks. In *21st International Symposium on Magnetic Resonance in Medicine (ISMRM)*.
- Griffa A, Baumann PS, Ferrari C, Conus P, Do KQ, Thiran JP and Hagmann P. (2014). MR connectomics identifies a distributed subnetwork lesioned in schizophrenia. In *22nd International Symposium on Magnetic Resonance in Medicine (ISMRM)*.
- Griffa A, Baumann PS, Thiran JP and Hagmann P. (2013b). Structural connectomics in brain diseases. *NeuroImage*, **80**, 515–526.
- Griffa A, Baumann PS, Ferrari C, Do KQ, Conus P, Thiran JP and Hagmann P. (2015c). Characterizing the connectome in schizophrenia with diffusion spectrum imaging. *Human Brain Mapping*, **36**(1), 354–366.
- Guimerà R and Amaral LAN. (2005). Cartography of complex networks: modules and universal roles. *Journal of Statistical Mechanics: Theory and Experiment*, **2005**(2), P02001.
- Hagmann P, Cammoun L, Gigandet X, Meuli R, Honey C, Wedeen V and Sporns O. (2008). Mapping the structural core of human cerebral cortex. *PLoS Biology*, **6**(7), e159.
- Hagmann P, Sporns O, Madan N, Cammoun L, Pienaar R, Wedeen VJ, Meuli R, Thiran JP and Grant PE. (2010). White matter maturation reshapes structural connectivity in the late developing human brain. *PNAS*, **107**(44), 19067–19072.
- Hagmann P, Grant PE and Fair DA. (2012). MR connectomics: a conceptual framework for studying the developing brain. *Frontiers in Systems Neuroscience*, **6**.
- He Y, Wang J, Wang L, Chen ZJ, Yan C, Yang H, Tang H, Zhu C, Gong Q, Zang Y and Evans AC. (2009). Uncovering intrinsic modular organization of spontaneous brain activity in humans. *PLoS ONE*, **4**(4), e5226.
- Hermundstad AM, Bassett DS, Brown KS, Aminoff EM, Clewett D, Freeman S, Frithsen A, Johnson A, Tipper CM, Miller MB, Grafton ST and Carlson JM. (2013). Structural foundations of resting-state and task-based functional connectivity in the human brain. *PNAS*, **110** (15), 6169–6174.
- Holme P, Kim BJ, Yoon CN and Han SK. (2002). Attack vulnerability of complex networks. *Physical Review E*, **65**(5), 056109.
- Honea R, Crow TJ, Passingham D and Mackay CE. (2005). Regional deficits in brain volume in schizophrenia: A meta-analysis of voxel-based morphometry studies. *The American Journal of Psychiatry*, **162**(12), 2233–2245.
- Honey CJ, Sporns O, Cammoun L, Gigandet X, Thiran JP, Meuli R and Hagmann P. (2009). Predicting human resting-state functional connectivity from structural connectivity. *PNAS*, **106**(6), 2035–2040.
- Honey CJ, Kötter R, Breakspear M and Sporns O. (2007). Network structure of cerebral cortex shapes functional connectivity on multiple time scales. *PNAS*, **104**(24), 10240–10245.

- Honey CJ and Sporns O. (2008). Dynamical consequences of lesions in cortical networks. *Human Brain Mapping*, **29**(7), 802–809.
- Honey C, Thivierge J and Sporns O. (2010). Can structure predict function in the human brain? *NeuroImage*, **52**(3), 766–776.
- Huang H, Shu N, Mishra V, Jeon T, Chalak L, Wang ZJ, Rollins N, Gong G, Cheng H, Peng Y, Dong Q and He Y. (2013). Development of human brain structural networks through infancy and childhood. *Cerebral Cortex*, doi:10.1093/cercor/bht335.
- Hutchison RM, Womelsdorf T, Allen EA, Bandettini PA, Calhoun VD, Corbetta M, Della Penna S, Duyn JH, Glover GH, Gonzalez-Castillo J, Handwerker DA, Keilholz S, Kiviniemi V, Leopold DA, de Pasquale F, Sporns O, Walter M and Chang C. (2013). Dynamic functional connectivity: Promise, issues, and interpretations. *NeuroImage*, **80**, 360–378.
- Irimia A and Van Horn JD. (2014). Systematic network lesioning reveals the core white matter scaffold of the human brain. *Frontiers in Human Neuroscience*, **8**.
- Iyer S, Killingback T, Sundaram B and Wang Z. (2013). Attack robustness and centrality of complex networks. *PLoS ONE*, **8**(4), e59613.
- Jalbrzikowski M, Jonas R, Senturk D, Patel A, Chow C, Green MF and Bearden CE. (2013). Structural abnormalities in cortical volume, thickness, and surface area in 22q11.2 microdeletion syndrome: Relationship with psychotic symptoms. *NeuroImage: Clinical*, **3**, 405–415.
- Jonas RK, Montojo CA and Bearden CE. (2014). The 22q11.2 deletion syndrome as a window into complex neuropsychiatric disorders over the lifespan. *Biological Psychiatry*, **75**(5), 351–360.
- Kaiser M and Hilgetag CC. (2010). Optimal hierarchical modular topologies for producing limited sustained activation of neural networks. *Frontiers in Neuroinformatics*, **4**.
- Kaiser M, Martin R, Andras P and Young MP. (2007). Simulation of robustness against lesions of cortical networks. *European Journal of Neuroscience*, **25**(10), 3185–3192.
- Karahanoğlu FI, Caballero-Gaudes C, Lazeyras F and Van De Ville D. (2015). Total activation: fMRI deconvolution through spatio-temporal regularization. *NeuroImage*, **73**, 121–134.
- Kates WR, Burnette CP, Jabs EW, Rutberg J, Murphy AM, Grados M, Geraghty M, Kaufmann WE and Pearlson GD. (2001). Regional cortical white matter reductions in velocardiofacial syndrome: a volumetric MRI analysis. *Biological Psychiatry*, **49**(8), 677–684.
- Kay SR, Flszbein A and Opfer LA. (1987). The positive and negative syndrome scale (PANSS) for schizophrenia. *Schizophrenia Bulletin*, **13**(2), 261–276.
- Kern RS, Nuechterlein KH, Green MF, Baade LE, Fenton WS, Gold JM, Keefe RS, Mesholam-Gately R, Mintz J, Seidman LJ, Stover E and Marder SR. (2008). The MATRICS consensus cognitive battery, part 2: Co-norming and standardization. *The American Journal of Psychiatry*, **165**(2), 214–220.
- Kikinis Z, Asami T, Bouix S, Finn CT, Ballinger T, Tworog-Dube E, Kucherlapati R, Kikinis R, Shenton ME and Kubicki M. (2012). Reduced fractional anisotropy and axial diffusivity in white matter in 22q11.2 deletion syndrome: A pilot study. *Schizophrenia Research*, **141**(1), 35–39.
- Koch M, Norris D and Hund-Georgiadis M. (2002). An investigation of functional and anatomical connectivity using magnetic resonance imaging. *NeuroImage*, **16**(1), 241–250.

- Koch W, Teipel S, Mueller S, Benninghoff J, Wagner M, Bokde ALW, Hampel H, Coates U, Reiser M and Meindl T. (2012). Diagnostic power of default mode network resting state fMRI in the detection of alzheimer's disease. *Neurobiology of Aging*, **33**(3), 466–478.
- Kolchinsky A, van den Heuvel MP, Griffa A, Hagmann P, Rocha LM, Sporns O and Goñi J. (2014). Multi-scale integration and predictability in resting state brain activity. *Frontiers in Neuroinformatics*, **8**.
- Laird AR, Fox PM, Eickhoff SB, Turner JA, Ray KL, McKay DR, Glahn DC, Beckmann CF, Smith SM and Fox PT. (2011). Behavioral interpretations of intrinsic connectivity networks. *Journal of Cognitive Neuroscience*, **23**(12), 4022–4037.
- Lambiotte R. (2010). Multi-scale modularity in complex networks. In *2010 Proceedings of the 8th International Symposium on Modeling and Optimization in Mobile, Ad Hoc and Wireless Networks (WiOpt)*, 546–553.
- Lancichinetti A and Fortunato S. (2012). Consensus clustering in complex networks. *Scientific Reports*, **2**.
- Latora V and Marchiori M. (2001). Efficient behavior of small-world networks. *Physical Review Letters*, **87**(19), 198701.
- Laule C, Vavasour IM, Kolind SH, Li DK, Traboulsee TL, Moore GW and MacKay AL. (2007). Magnetic resonance imaging of myelin. *Neurotherapeutics*, **4**(3), 460–484.
- Leergaard TB, Hilgetag CC and Sporns O. (2012). Mapping the connectome: Multi-level analysis of brain connectivity. *Frontiers in Neuroinformatics*, **6**.
- Leonardi N, Richiardi J, Gschwind M, Simioni S, Annoni JM, Schlupe M, Vuilleumier P and Van De Ville D. (2013). Principal components of functional connectivity: A new approach to study dynamic brain connectivity during rest. *NeuroImage*, **83**, 937–950.
- Leonardi N, Shirer WR, Greicius MD and Van De Ville D. (2014). Disentangling dynamic networks: Separated and joint expressions of functional connectivity patterns in time: Disentangling dynamic networks. *Human Brain Mapping*, **35**(12), 5984–5995.
- Leonardi N and Van De Ville D. (2015). On spurious and real fluctuations of dynamic functional connectivity during rest. *NeuroImage*, **104**, 430–436.
- Li H, Xue Z, Ellmore TM, Frye RE and Wong ST. Network-based analysis reveals stronger local diffusion-based connectivity and different correlations with oral language skills in brains of children with high functioning autism spectrum disorders. *Human Brain Mapping*, **35**(2), 396–413.
- Li W, Li Y, Hu C, Chen X and Dai H. (2014). Point process analysis in brain networks of patients with diabetes. *Neurocomputing*, **145**, 182–189.
- Lindsay EA, Goldberg R, Jurecic V, Morrow B, Carlson C, Kucherlapati RS, Shprintzen RJ and Baldini A. (1995). Velo-cardio-facial syndrome: Frequency and extent of 22q11 deletions. *American Journal of Medical Genetics*, **57**(3), 514–522.
- Liu X and Duyn JH. (2013). Time-varying functional network information extracted from brief instances of spontaneous brain activity. *PNAS*, **110**(11), 4392–4397.
- Lo CY, Wang PN, Chou KH, Wang J, He Y and Lin CP. (2010). Diffusion tensor tractography reveals abnormal topological organization in structural cortical networks in alzheimer's disease. *The Journal of Neuroscience*, **30**(50), 16876–16885.



- Ma S, Calhoun VD, Phlypo R and Adalı T. (2014). Dynamic changes of spatial functional network connectivity in healthy individuals and schizophrenia patients using independent vector analysis. *NeuroImage*, **90**, 196–206.
- Machado AMC, Simon TJ, Nguyen V, McDonald-McGinn DM, Zackai EH and Gee JC. (2007). Corpus callosum morphology and ventricular size in chromosome 22q11.2 deletion syndrome. *Brain Research*, **1131**, 197–210.
- Majeed W, Magnuson M, Hasenkamp W, Schwarb H, Schumacher EH, Barsalou L and Keilholz SD. (2011). Spatiotemporal dynamics of low frequency BOLD fluctuations in rats and humans. *NeuroImage*, **54**(2), 1140–1150.
- Maslov S and Sneppen K. (2002). Specificity and stability in topology of protein networks. *Science*, **296**(5569), 910–913.
- McGorry P, Keshavan M, Goldstone S, Amminger P, Allott K, Berk M, Lavoie S, Pantelis C, Yung A, Wood S and Hickie I. (2014). Biomarkers and clinical staging in psychiatry. *World Psychiatry*, **13**(3), 211–223.
- McGorry PD, Hickie IB, Yung AR, Pantelis C and Jackson HJ. (2006). Clinical staging of psychiatric disorders: a heuristic framework for choosing earlier, safer and more effective interventions. *Australian and New Zealand Journal of Psychiatry*, **40**(8), 616–622.
- McIntosh AM, Owens DC, Moorhead WJ, Whalley HC, Stanfield AC, Hall J, Johnstone EC and Lawrie SM. (2011). Longitudinal volume reductions in people at high genetic risk of schizophrenia as they develop psychosis. *Biological Psychiatry*, **69**(10), 953–958.
- Meilă M. (2007). Comparing clusterings—an information based distance. *Journal of Multivariate Analysis*, **98**(5), 873–895.
- Mendelsohn A, Strous R, Bleich M, Assaf Y and Hendler T. (2006). Regional axonal abnormalities in first episode schizophrenia: Preliminary evidence based on high b-value diffusion-weighted imaging. *Psychiatry Research: Neuroimaging*, **146**(3), 223–229.
- Meskaldji D, Ottet M, Cammoun L, Hagmann P, Meuli R, Eliez S, Thiran J and Morgenthaler S. (2011). Adaptive strategy for the statistical analysis of connectomes. *PloS ONE*, **6**(8), e23009.
- Meskaldji DE, Fischi-Gomez E, Griffa A, Hagmann P, Morgenthaler S and Thiran JP. (2013). Comparing connectomes across subjects and populations at different scales. *NeuroImage*, **80**, 416–425.
- Meskaldji DE, Vasung L, Romascano D, Thiran JP, Hagmann P, Morgenthaler S and Van De Ville D. (2015). Improved statistical evaluation of group differences in connectomes by screening–filtering strategy with application to study maturation of brain connections between childhood and adolescence. *NeuroImage*, **108**, 251–264.
- Meunier D, Achard S, Morcom A and Bullmore E. (2009a). Age-related changes in modular organization of human brain functional networks. *NeuroImage*, **44**(3), 715–723.
- Meunier D, Lambiotte R and Bullmore ET. (2010). Modular and hierarchically modular organization of brain networks. *Frontiers in Neuroscience*, **4**.
- Meunier D, Lambiotte R, Fornito A, Ersche KD and Bullmore ET. (2009b). Hierarchical modularity in human brain functional networks. *Frontiers in Neuroinformatics*, **3**.
- Moncrieff J and Leo J. (2010). A systematic review of the effects of antipsychotic drugs on brain volume. *Psychological Medicine*, **40**(09), 1409–1422.

- Monks S, Niarchou M, Davies AR, Walters JTR, Williams N, Owen MJ, van den Bree MBM and Murphy KC. (2014). Further evidence for high rates of schizophrenia in 22q11.2 deletion syndrome. *Schizophrenia Research*, **153**(1), 231–236.
- Monti S, Tamayo P, Mesirov J and Golub T. (2003). Consensus clustering: A resampling-based method for class discovery and visualization of gene expression microarray data. *Journal of Machine Learning Research*, **52**(1-2), 91–118.
- Mori S, Crain BJ, Chacko VP and Van Zijl PCM. (1999). Three-dimensional tracking of axonal projections in the brain by magnetic resonance imaging. *Annals of Neurology*, **45**(2), 265–269.
- Morris DM, Embleton KV and Parker GJM. (2008). Probabilistic fibre tracking: Differentiation of connections from chance events. *NeuroImage*, **42**(4), 1329–1339.
- Morsing E, Åsard M, Ley D, Stjernqvist K and Maršál K. (2011). Cognitive function after intrauterine growth restriction and very preterm birth. *Pediatrics*, **127**(4), e874–e882.
- Mucha PJ, Richardson T, Macon K, Porter MA and Onnela JP. (2010). Community structure in time-dependent, multiscale, and multiplex networks. *Science*, **328**(5980), 876–878.
- Murphy K, Birn RM, Handwerker DA, Jones TB and Bandettini PA. (2009). The impact of global signal regression on resting state correlations: Are anti-correlated networks introduced? *NeuroImage*, **44**(3), 893–905.
- Newman MEJ. (2002). Assortative mixing in networks. *Physical Review Letters*, **89**(20), doi:10.1103/PhysRevLett.89.208701.
- Newman MEJ. (2003). The structure and function of complex networks. *SIAM Review*, **45**(2), 167–256.
- Newman MEJ and Girvan M. (2004). Finding and evaluating community structure in networks. *Physical Review E*, **69**(2), 026113.
- Newman M. (2010). *Networks: An Introduction*. Oxford University Press. ISBN 9780191500701.
- Newman M. (2006). Modularity and community structure in networks. *PNAS*, **103**(23), 8577.
- Nuechterlein KH, Green MF, Kern RS, Baade LE, Barch DM, Cohen JD, Essock S, Fenton WS, Frese FJ, Gold JM, Goldberg T, Heaton RK, Keefe RSE, Kraemer H, Mesholam-Gately R, Seidman LJ, Stover E, Weinberger DR, Young AS, Zalcman S and Marder SR. (2008). The MATRICS consensus cognitive battery, part 1: test selection, reliability, and validity. *The American Journal of Psychiatry*, **165**(2), 203–213.
- Oh SW, Harris JA, Ng L, Winslow B, Cain N, Mihalas S, Wang Q, Lau C, Kuan L, Henry AM, Mortrud MT, Ouellette B, Nguyen TN, Sorensen SA, Slaughterbeck CR, Wakeman W, Li Y, Feng D, Ho A, Nicholas E, Hirokawa KE, Bohn P, Joines KM, Peng H, Hawrylycz MJ, Phillips JW, Hohmann JG, Wohnoutka P, Gerfen CR, Koch C, Bernard A, Dang C, Jones AR and Zeng H. (2014). A mesoscale connectome of the mouse brain. *Nature*, **508**(7495), 207–214.
- Opsahl T and Panzarasa P. (2009). Clustering in weighted networks. *Social Networks*, **31**(2), 155–163.
- Ottet MC, Schaer M, Cammoun L, Schneider M, Debbané M, Thiran JP and Eliez S. (2013a). Reduced fronto-temporal and limbic connectivity in the 22q11.2 deletion syndrome: Vulnerability markers for developing schizophrenia? *PLoS ONE*, **8**(3), e58429.

- Ottet MC, Schaer M, Debbane M, Cammoun L, Thiran JP and Eliez S. (2013b). Graph theory reveals disconnected hubs in 22q11ds and altered nodal efficiency in patients with hallucinations. *Frontiers in Human Neuroscience*, **7**.
- Padilla N, Falcón C, Sanz-Cortés M, Figueras F, Bargallo N, Crispí F, Eixarch E, Arranz A, Botet F and Gratacós E. (2011). Differential effects of intrauterine growth restriction on brain structure and development in preterm infants: A magnetic resonance imaging study. *Brain Research*, **1382**, 98–108.
- Pettersson-Yeo W, Allen P, Benetti S, McGuire P and Mechelli A. (2011). Dysconnectivity in schizophrenia: Where are we now? *Neuroscience & Biobehavioral Reviews*, **35**(5), 1110–1124.
- Power JD, Barnes KA, Snyder AZ, Schlaggar BL and Petersen SE. (2012). Spurious but systematic correlations in functional connectivity MRI networks arise from subject motion. *NeuroImage*, **59**(3), 2142–2154.
- Preisig M, Fenton BT, Matthey ML, Berney A and Ferrero F. (1999). Diagnostic interview for genetic studies (DIGS): inter-rater and test-retest reliability of the french version. *European Archives of Psychiatry and Clinical Neurosciences*, **249**(4), 174–179.
- Purves D, Augustine GJ, Fitzpatrick D, Hall WC, LaMantia AS, McNamara JO and Williams SM. (2004). *Neuroscience*. Sinauer Associates, 3rd edition. ISBN 0-87893-725-0.
- Ray S, Miller M, Karalunas S, Robertson C, Grayson DS, Cary RP, Hawkey E, Painter JG, Kriz D, Fombonne E, Nigg JT and Fair DA. (2014). Structural and functional connectivity of the human brain in autism spectrum disorders and attention-deficit/hyperactivity disorder: A rich club-organization study. *Human Brain Mapping*, **35**(12), 6032–6048.
- Romero-Garcia R, Aienza M, Clemmensen LH and Cantero JL. (2012). Effects of network resolution on topological properties of human neocortex. *NeuroImage*, **59**(4), 3522–3532.
- Rubinov M and Sporns O. (2010). Complex network measures of brain connectivity: uses and interpretations. *NeuroImage*, **52**(3), 1059–1069.
- Rubinov M and Sporns O. (2011). Weight-conserving characterization of complex functional brain networks. *NeuroImage*, **56**, 2068–2079.
- Rubinov M and Bullmore E. (2013a). Fledgling pathoconnectomics of psychiatric disorders. *Trends in Cognitive Sciences*, **17**(12), 641–647.
- Rubinov M and Bullmore E. (2013b). Schizophrenia and abnormal brain network hubs. *Dialogues in Clinical NeuroSciences*, **15**(3), 339–349.
- Russo R, Herrmann HJ and de Arcangelis L. (2014). Brain modularity controls the critical behavior of spontaneous activity. *Scientific Reports*, **4**.
- Salvador R, Suckling J, Coleman MR, Pickard JD, Menon D and Bullmore E. (2005). Neurophysiological architecture of functional magnetic resonance images of human brain. *Cerebral Cortex*, **15**(9), 1332–1342.
- Scariati E, Schaer M, Richiardi J, Schneider M, Debbané M, Ville DVD and Eliez S. (2014). Identifying 22q11.2 deletion syndrome and psychosis using resting-state connectivity patterns. *Brain Topography*, **27**(6), 808–821.

- Schaub MT, Delvenne JC, Yaliraki SN and Barahona M. (2012). Markov dynamics as a zooming lens for multiscale community detection: Non clique-like communities and the field-of-view limit. *PLoS ONE*, **7**(2), e32210.
- Schneider M, Debbané M, Bassett AS, Chow EW, Fung WLA, van den Bree MB, Owen M, Murphy KC, Niarchou M, Kates WR, Antshel KM, Fremont W, McDonald-McGinn DM, Gur RE, Zackai EH, Vorstman J, Duijff SN, Klaassen PW, Swillen A, Gothelf D, Green T, Weizman A, Van Amelsvoort T, Evers L, Boot E, Shashi V, Hooper SR, Bearden CE, Jalbrzikowski M, Armando M, Vicari S, Murphy DG, Ousley O, Campbell LE, Simon TJ, Eliez S and for the International Consortium on Brain and Behavior in 22q11.2 Deletion Syndrome . (2014). Psychiatric disorders from childhood to adulthood in 22q11.2 deletion syndrome: Results from the international consortium on brain and behavior in 22q11.2 deletion syndrome. *The American Journal of Psychiatry*, **171**(6), 627–639.
- Schult DA. (2008). Exploring network structure, dynamics, and function using NetworkX. In *Proceedings of the 7th Python in Science Conference (SciPy2008)*, 11–15.
- Senden M, Deco G, de Reus MA, Goebel R and van den Heuvel MP. (2014). Rich club organization supports a diverse set of functional network configurations. *NeuroImage*, **96**, 174–182.
- Sener RN. (2001). Diffusion MRI: apparent diffusion coefficient (ADC) values in the normal brain and a classification of brain disorders based on ADC values. *Computerized Medical Imaging and Graphics*, **25**(4), 299–326.
- Shargel B, Sayama H, Epstein IR and Bar-Yam Y. (2003). Optimization of robustness and connectivity in complex networks. *Physical Review Letters*, **90**(6), 068701.
- Shepherd AM, Laurens KR, Matheson SL, Carr VJ and Green MJ. (2012). Systematic meta-review and quality assessment of the structural brain alterations in schizophrenia. *Neuroscience & Biobehavioral Reviews*, **36**(4), 1342–1356.
- Simon TJ, Ding L, Bish JP, McDonald-McGinn DM, Zackai EH and Gee J. (2005). Volumetric, connective, and morphologic changes in the brains of children with chromosome 22q11.2 deletion syndrome: an integrative study. *NeuroImage*, **25**(1), 169–180.
- Simon TJ, Wu Z, Avants B, Zhang H, Gee JC and Stebbins GT. (2008). Atypical cortical connectivity and visuospatial cognitive impairments are related in children with chromosome 22q11.2 deletion syndrome. *Behavioral and Brain Functions*, **4**(1), 25.
- Skudlarski P, Jagannathan K, Anderson K, Stevens MC, Calhoun VD, Skudlarska BA and Pearlson G. (2010). Brain connectivity is not only lower but different in schizophrenia: A combined anatomical and functional approach. *Biological Psychiatry*, **68**(1), 61–69.
- Smieskova R, Fusar-Poli P, Allen P, Bendfeldt K, Stieglitz RD, Drewe J, Radue EW, McGuire PK, Riecher-Rossler A and Borgwardt SJ. (2009). The effects of antipsychotics on the brain: What have we learnt from structural imaging of schizophrenia? a systematic review. *Current Pharmaceutical Design*, **15**(22), 2535–2549.
- Smith RE, Tournier JD, Calamante F and Connelly A. (2013). SIFT: Spherical-deconvolution informed filtering of tractograms. *NeuroImage*, **67**, 298–312.
- Smith SM, Fox PT, Miller KL, Glahn DC, Fox PM, Mackay CE, Filippini N, Watkins KE, Toro R, Laird AR and Beckmann CF. (2009). Correspondence of the brain's functional architecture during activation and rest. *PNAS*, **106**(31), 13040–13045.

- Smith SM, Miller KL, Moeller S, Xu J, Auerbach EJ, Woolrich MW, Beckmann CF, Jenkinson M, Andersson J, Glasser MF, Essen DCV, Feinberg DA, Yacoub ES and Ugurbil K. (2012). Temporally-independent functional modes of spontaneous brain activity. *PNAS*, **109**(8), 3131–3136.
- Sporns O. *Networks of the Brain*. MIT Press, Cambridge, MA 02142-1209 USA. ISBN 9780262288927.
- Sporns O. (2013). Network attributes for segregation and integration in the human brain. *Current Opinion in Neurobiology*, **23**(2), 162–171.
- Sporns O. (2014). Contributions and challenges for network models in cognitive neuroscience. *Nature Neuroscience*, **17**(5), 652–660.
- Sporns O, Honey CJ and Kötter R. (2007). Identification and classification of hubs in brain networks. *PLoS ONE*, **2**(10), e1049.
- Steen RG, Mull C, McClure R, Hamer RM and Lieberman JA. (2006). Brain volume in first-episode schizophrenia: systematic review and meta-analysis of magnetic resonance imaging studies. *The British Journal of Psychiatry*, **188**, 510–518.
- Stephan K, Friston K and Frith C. (2009). Dysconnection in schizophrenia: from abnormal synaptic plasticity to failures of self-monitoring. *Schizophrenia Bulletin*, **35**(3), 509–527.
- Stephan KE, Baldeweg T and Friston KJ. (2006). Synaptic plasticity and dysconnection in schizophrenia. *Biological Psychiatry*, **59**(10), 929–939.
- Stevens AA, Tappon SC, Garg A and Fair DA. (2012). Functional brain network modularity captures inter- and intra-individual variation in working memory capacity. *PLoS ONE*, **7**(1), e30468.
- Sun D, Phillips L, Velakoulis D, Yung A, McGorry PD, Wood SJ, van Erp TGM, Thompson PM, Toga AW, Cannon TD and Pantelis C. (2009a). Progressive brain structural changes mapped as psychosis develops in 'at risk' individuals. *Schizophrenia Research*, **108**(1), 85–92.
- Sun Y, Danila B, Josić K and Bassler KE. (2009b). Improved community structure detection using a modified fine-tuning strategy. *EPL (Europhysics Letters)*, **86**(2), doi:10.1209/0295–5075/86/28004.
- Sundram F, Campbell LE, Azuma R, Daly E, Bloemen OJN, Barker GJ, Chitnis X, Jones DK, Amelvoort Tv, Murphy KC and Murphy DGM. (2010). White matter microstructure in 22q11 deletion syndrome: a pilot diffusion tensor imaging and voxel-based morphometry study of children and adolescents. *Journal of Neurodevelopmental Disorders*, **2**(2), 77–92.
- Supekar K, Uddin L, Prater K, Amin H, Greicius M and Menon V. (2010). Development of functional and structural connectivity within the default mode network in young children. *NeuroImage*, **52**(1), 290–301.
- Szeszko PR, Robinson DG, Ikuta T, Peters BD, Gallego JA, Kane J and Malhotra AK. (2013). White matter changes associated with antipsychotic treatment in first-episode psychosis. *Neuropsychopharmacology*, **39**, 1324–1331.
- Tagliazucchi E, Balenzuela P, Fraiman D and Chialvo DR. (2012). Criticality in large-scale brain fMRI dynamics unveiled by a novel point process analysis. *Frontiers in Physiology*, **3**, 15.

- Tagliazucchi E, Laufs H and Chialvo DR. (2014). A few points suffice: Efficient large-scale computation of brain voxel-wise functional connectomes from a sparse spatio-temporal point-process. *arXiv:1409.6378 [q-bio.NC]*.
- Takahashi M, Hackney DB, Zhang G, Wehrli SL, Wright AC, O'Brien WT, Uematsu H, Wehrli FW and Selzer ME. (2002). Magnetic resonance microimaging of intraaxonal water diffusion in live excised lamprey spinal cord. *PNAS*, **99**(25), 16192–16196.
- Takahashi T, Wood SJ, Soulsby B, McGorry PD, Tanino R, Suzuki M, Velakoulis D and Pantelis C. (2009a). Follow-up MRI study of the insular cortex in first-episode psychosis and chronic schizophrenia. *Schizophrenia Research*, **108**(1), 49–56.
- Takahashi T, Wood SJ, Yung AR, Phillips LJ, Soulsby B, McGorry PD, Tanino R, Zhou SY, Suzuki M, Velakoulis D and Pantelis C. (2009b). Insular cortex gray matter changes in individuals at ultra-high-risk of developing psychosis. *Schizophrenia Research*, **111**(1), 94–102.
- Takahashi T, Wood SJ, Yung AR, Soulsby B, McGorry PD, Suzuki M, Kawasaki Y, Phillips LJ, Velakoulis D and Pantelis C. (2009c). Progressive gray matter reduction of the superior temporal gyrus during transition to psychosis. *Archives of General Psychiatry*, **66**(4), 366–376.
- Taylor D, Paton C and Kerwin R. (2007). *The Maudsley Prescribing Guidelines*. CRC Press. ISBN 9780415424165.
- Thompson DK, Lee KJ, Egan GF, Warfield SK, Doyle LW, Anderson PJ and Inder TE. (2014). Regional white matter microstructure in very preterm infants: Predictors and 7 year outcomes. *Cortex*, **52**, 60–74.
- Tomasi D and Volkow ND. (2012). Aging and functional brain networks. *Molecular Psychiatry*, **17**(5), 549–558.
- Tuch D. (2004). Q-ball imaging. *Magnetic Resonance in Medicine*, **52**(6), 1358–1372.
- Tymofiyeva O, Hess CP, Ziv E, Lee PN, Glass HC, Ferriero DM, Barkovich AJ and Xu D. (2013). A DTI-based template-free cortical connectome study of brain maturation. *PLoS ONE*, **8**(5), e63310.
- van den Heuvel MP and Fornito A. (2014). Brain networks in schizophrenia. *Neuropsychology Review*, **24**(1), 32–48.
- van den Heuvel MP and Hulshoff Pol HE. (2010). Exploring the brain network: A review on resting-state fMRI functional connectivity. *European Neuropsychopharmacology*, **20**(8), 519–534.
- van den Heuvel MP, Kahn RS, Goñi J and Sporns O. (2012). High-cost, high-capacity backbone for global brain communication. *PNAS*, **109**(28), 11372–11377.
- van den Heuvel MP, Mandl RC, Kahn RS and Hulshoff Pol HE. (2009). Functionally linked resting-state networks reflect the underlying structural connectivity architecture of the human brain. *Human Brain Mapping*, **30**(10), 3127–3141.
- van den Heuvel MP and Sporns O. (2011). Rich-club organization of the human connectome. *The Journal of Neuroscience*, **31**(44), 15775–15786.
- van den Heuvel MPvd and Sporns O. (2013). An anatomical substrate for integration among functional networks in human cortex. *The Journal of Neuroscience*, **33**(36), 14489–14500.

- van den Heuvel M, Mandl R, Stam C, Kahn R and Pol H. (2010). Aberrant frontal and temporal complex network structure in schizophrenia: a graph theoretical analysis. *The Journal of Neuroscience*, **30**(47), 15915–15926.
- van den Heuvel M, Sporns O, Collin G, Scheewe T, Mandl R, Cahn W, Goñi J, Hulshoff Pol H and Kahn R. (2013). Abnormal rich club organization and functional brain dynamics in schizophrenia. *JAMA Psychiatry*, **70**(8), 783–792.
- van Wijk BCM, Stam CJ and Daffertshofer A. (2010). Comparing brain networks of different size and connectivity density using graph theory. *PLoS ONE*, **5**(10), e13701.
- Varoquaux G and Craddock RC. (2013). Learning and comparing functional connectomes across subjects. *NeuroImage*, **80**, 405–415.
- Vasa F, Griffa A, Scariati E, Schaer M, Urben S, Eliez S and P H. (2015). Characterizing the connectome in 22q11.2 deletion syndrome with diffusion mri. *submitted to NeuroImage*.
- Velakoulis D, Wood SJ, Wong MTH, McGorry PD, Yung A, Phillips L, Smith D, Brewer W, Proffitt T, Desmond P and Pantelis C. (2006). Hippocampal and amygdala volumes according to psychosis stage and diagnosis: a magnetic resonance imaging study of chronic schizophrenia, first-episode psychosis, and ultra-high-risk individuals. *Archives of General Psychiatry*, **63**(2), 139–149.
- Verstraete E, Veldink JH, Mandl RCW, van den Berg LH and van den Heuvel MP. (2011). Impaired structural motor connectome in amyotrophic lateral sclerosis. *PLoS ONE*, **6**(9), e24239.
- Vita A, De Peri L, Silenzi C and Dieci M. (2006). Brain morphology in first-episode schizophrenia: a meta-analysis of quantitative magnetic resonance imaging studies. *Schizophrenia Research*, **82**(1), 75–88.
- Watts DJ and Strogatz SH. (1998). Collective dynamics of "small-world" networks. *Nature*, **393** (6684), 440–442.
- Wedeen VJ, Hagmann P, Tseng WYI, Reese TG and Weisskoff RM. (2005). Mapping complex tissue architecture with diffusion spectrum magnetic resonance imaging. *Magnetic Resonance in Medicine*, **54**(6), 1377–1386.
- Wedeen VJ, Rosene DL, Wang R, Dai G, Mortazavi F, Hagmann P, Kaas JH and Tseng WYI. (2012). The geometric structure of the brain fiber pathways. *Science*, **335**(6076), 1628–1634.
- Westfall PH. (1993). *Resampling-Based Multiple Testing: Examples and Methods for P-Value Adjustment*. John Wiley & Sons. ISBN 9780471557616.
- Wilcoxon F. (1945). Individual comparisons by ranking methods. *Biometrics Bulletin*, **1**(6), 80–83.
- Wolfe DA. Nonparametrics: Statistical methods based on ranks and its impact on the field of nonparametric statistics. In Rojo J, editor, *Selected Works of E. L. Lehmann*, Selected Works in Probability and Statistics, 1101–1110. Springer US. (2012). ISBN 978-1-4614-1411-7, 978-1-4614-1412-4.
- Wood SJ, Kennedy D, Phillips LJ, Seal ML, Yücel M, Nelson B, Yung AR, Jackson G, McGorry PD, Velakoulis D and Pantelis C. (2010). Hippocampal pathology in individuals at ultra-high risk for psychosis: a multi-modal magnetic resonance study. *NeuroImage*, **52**(1), 62–68.

- Wood SJ, Yung AR, McGorry PD and Pantelis C. (2011). Neuroimaging and treatment evidence for clinical staging in psychotic disorders: From the at-risk mental state to chronic schizophrenia. *Biological Psychiatry*, **70**(7), 619–625.
- Wu K, Taki Y, Sato K, Sassa Y, Inoue K, Goto R, Okada K, Kawashima R, He Y, Evans AC and Fukuda H. (2011). The overlapping community structure of structural brain network in young healthy individuals. *PLoS ONE*, **6**(5), e19608.
- Yendiki A, Koldewyn K, Kakunoori S, Kanwisher N and Fischl B. (2014). Spurious group differences due to head motion in a diffusion MRI study. *NeuroImage*, **88**, 79–90.
- Yu Q, Sui J, Liu J, Plis SM, Kiehl KA, Pearlson G and Calhoun VD. (2013). Disrupted correlation between low frequency power and connectivity strength of resting state brain networks in schizophrenia. *Schizophrenia Research*, **143**(1), 165–171.
- Yung AR, Yuen HP, McGorry PD, Phillips LJ, Kelly D, Dell’Olio M, Francey SM, Cosgrave EM, Killackey E, Stanford C, Godfrey K and Buckby J. (2005). Mapping the onset of psychosis: the comprehensive assessment of at-risk mental states. *Australian and New Zealand Journal of Psychiatry*, **39**(11-12), 964–971.
- Zalesky A, Fornito A, Seal M, Cocchi L, Westin C, Bullmore E, Egan G and Pantelis C. (2011). Disrupted axonal fiber connectivity in schizophrenia. *Biological Psychiatry*, **69**(1), 80–89.
- Zalesky A, Cocchi L, Fornito A, Murray MM and Bullmore E. (2012a). Connectivity differences in brain networks. *NeuroImage*, **60**(2), 1055–1062.
- Zalesky A, Fornito A and Bullmore ET. (2010). Network-based statistic: Identifying differences in brain networks. *NeuroImage*, **53**(4), 1197–1207.
- Zalesky A, Fornito A, Cocchi L, Gollo LL and Breakspear M. (2014). Time-resolved resting-state brain networks. *PNAS*, **111**(28), 10341–10346.
- Zalesky A, Solowij N, Yücel M, Lubman DI, Takagi M, Harding IH, Lorenzetti V, Wang R, Searle K, Pantelis C and Seal M. (2012b). Effect of long-term cannabis use on axonal fibre connectivity. *Brain*, **135**(7), 2245–2255.
- Zhang F, Qiu L, Yuan L, Ma H, Ye R, Yu F, Hu P, Dong Y and Wang K. (2014). Evidence for progressive brain abnormalities in early schizophrenia: A cross-sectional structural and functional connectivity study. *Schizophrenia Research*, **159**(1), 31–35.
- Zhang Y, Lin L, Lin CP, Zhou Y, Chou KH, Lo CY, Su TP and Jiang T. (2012). Abnormal topological organization of structural brain networks in schizophrenia. *Schizophrenia Research*, **141**(2–3), 109–118.
- Zhang Z, Liao W, Chen H, Mantini D, Ding J, Xu Q, Wang Z, Yuan C, Chen G, Jiao Q and others. (2011). Altered functional–structural coupling of large-scale brain networks in idiopathic generalized epilepsy. *Brain*, **134**(10), 2912–2928.



# Curriculum Vitae - Alessandra Griffa

## Personal Information

---

Address Ch. Eugène-Grasset 2, 1006 Lausanne (VD), Switzerland  
Telephone +41 76 778 71 58  
E-mail alessandra.griffa@gmail.com  
Date of birth 29 March 1983 in Torino, Italy  
Nationality Italian

## Working Experience

---

- Jan 2011-May 2015 **PhD Candidate**  
**École polytechnique fédérale de Lausanne (EPFL)** and  
**Centre Hospitalier Universitaire Vaudois (CHUV)**  
Research focus: diffusion and functional MRI, brain connectivity, spatio-temporal connectomics, graph theory, schizophrenia, psychotic disorders.
- Nov 2007-Sept 2010 **Engineer**  
**Bioluming and Optics Platform**  
**- École polytechnique fédérale de Lausanne (EPFL)**  
Train users to image processing and analysis techniques; discuss projects strategy; develop personalized image analysis tools; teaching (doctoral schools and master level); management of platform's software.
- Sept 2005-Feb 2006 **Part-time collaborator**  
**Politecnico di Torino, Italy**  
Support didactic activities for Medical Imaging courses.
- April 2005-June 2005 **Intern**  
**Sorin Group, Saluggia (Vc), Italy**  
Internship related to cardiac valves manufacturing.

## Education

---

- March 2007-Sept 2007 **Master Thesis**  
École polytechnique fédérale de Lausanne (EPFL)
- March 2007-Sept 2007 **MSc in Biomedical Engineering**  
Politecnico di Torino
- March 2007-Sept 2007 **MBC in Biomedical Engineering**  
Politecnico di Torino

## Additional Information

---

- Languages: Italian native speaker  
English C1 good oral and written  
French B2 good oral, discrete written  
Spanish A2 discrete oral and written
- IT Competence: - Programming languages: Matlab, Python, C, PHP, shell scripting  
- OS: Unix, MS Windows
- Personal Information: B driving license  
Swiss C permit



# Publications

---

## Journal Papers

A. Griffa, P. S. Baumann, C. Ferrari, K. Q. Do, P. Conus, J.-P. Thiran and P. Hagmann, "Characterizing the connectome in schizophrenia with diffusion spectrum imaging", *Human Brain Mapping*, vol. 36, num. 1, pp. 354–366, 2015

M. Adhikari, A. R. Beharelle, A. Griffa, P. Hagmann, A. Solodkin, A. McIntosh, S. Small and G. Deco, "Computational Modeling of Resting State Activity demonstrates Markers of Normalcy in Children with Pre- or Perinatal Stroke", *The Journal of Neuroscience*, accepted, 2015

L. Cammoun, J.-P. Thiran, A. Griffa, R. Meuli, P. Hagmann and S. Clarke, "Intrahemispheric cortico-cortical connections of the human auditory cortex", *Brain Structure and Function*, pp. 1–17, 2014

A. Avena-Koenigsberger, J. Goñi, R. F. Betzel, M. P. van den Heuvel, A. Griffa, P. Hagmann, J.-P. Thiran and O. Sporns, "Using Pareto optimality to explore the topology and dynamics of the human connectome", *Philosophical Transactions B*, vol. 369, num. 1653, 2014

A. Monin, P. Baumann, A. Griffa, L. Xin, R. Mekle, M. Fournier, C. Buttica, M. Klaey, J. H. Cabungcal, P. Steullet, C. Ferrari, M. Cuenod, R. Gruetter, J.-P. Thiran, P. Hagmann, P. Conus and K. Q. Do, "Glutathione deficit impairs myelin maturation: relevance for white matter integrity in schizophrenia patients", *Molecular Psychiatry*, pp. 1–12, 2014

A. Kolchinsky, M. P. van den Heuvel, A. Griffa, P. Hagmann, L. M. Rocha, O. Sporns and J. Goñi, "Multi-scale Integration and Predictability in Resting State Brain Activity", *Frontiers in Neuroinformatics*, vol. 8, num. 66, 2014

J. Goñi, M. P. van den Heuvel, A. Avena-Koenigsberger, N. V. de Mendizabal, R. F. Betzel, A. Griffa, P. Hagmann, B. Corominas-Murtra, J.-P. Thiran and O. Sporns, "Resting-brain functional connectivity predicted by analytic measures of network communication", *Proceedings Of The National Academy Of Sciences Of The United States Of America*, vol. 111, num. 2, pp. 833–838, 2014

D. E. Meskaldji, E. Fischi-Gomez, A. Griffa, P. Hagmann, S. Morgenthaler and J.-P. Thiran, "Comparing connectomes across subjects and populations at different scales", *NeuroImage*, vol. 80, pp. 416–425, 2013

A. Griffa, P. Baumann, J.-P. Thiran and P. Hagmann, "Structural connectomics in brain diseases", *Neuroimage*, vol. 80, pp. 515–526, 2013

R. F. Betzel, A. Griffa, A. Avena-Koenigsberger, J. Goñi, P. Hagmann and O. Sporns, "Multi-scale community organization of the human structural connectome and its relationship with resting-state functional connectivity", *Network Science*, vol. 1, num. 03, pp. 353–373, 2013

X. Gigandet, A. Griffa, T. Kober, A. Daducci, G. Gilbert, A. Connelly, P. Hagmann, R. Meuli, J.-P. Thiran and G. Krueger, "A Connectome-Based Comparison of Diffusion MRI Schemes", *Plos One*, vol. 8, num. 9: e75061, 2013

R. Rezakhaniha, A. Agianniotis, J. T. C. Schrauwen, A. Griffa, D. Sage, C. V. C. Bouten, F. N. van de Vosse, M. Unser and N. Stergiopoulos, "Experimental investigation of collagen waviness and orientation in the arterial adventitia using confocal laser scanning microscopy", *Biomechanics and Modeling in Mechanobiology*, vol. 11, num. 3-4, pp. 461–73, 2012

A. Daducci, S. Gerhard, A. Griffa, A. Lemkaddem, L. Cammoun, X. Gigandet, R. Meuli, P. Hagmann and J.-P. Thiran, "The Connectome Mapper: an open-source processing pipeline to map connectomes with MRI", *PLoS ONE*, vol. 7, num. 12: e48121, 2012

S. A. Kobel, O. Burri, A. Griffa, M. Girotra, A. Seitz and M. P. Lutolf, "Automated analysis of single stem cells in microfluidic traps", *Lab On A Chip*, vol. 12, pp. 2843–2849, 2012

N. Vannini, A. Roch, O. Naveiras, A. Griffa, S. Kobel and M. P. Lutolf, "Identification of in vitro HSC fate regulators by differential lipid raft clustering" *Cell cycle*, vol. 11, num. 8, pp. 1535–43, 2012

A. Griffa, N. Garin and D. Sage, "Comparison of Deconvolution Software: A User Point of View—Parts 1 & 2", *G.I.T. Imaging & Microscopy*, vol. 12, num. 3, pp. 41–43, 2010

M. Emmenlauer, O. Ronneberger, A. Ponti, P. Schwarb, A. Griffa, A. Filippi, R. Nitschke, W. Driever and H. Burkhardt, "XuvTools: free, fast and reliable stitching of large 3D datasets", *Journal Of Microscopy-Oxford*, vol. 233, num. 1, pp. 42-60, 2009

## Conference Abstracts

A. Griffa, K. Benzi, B. Ricaud, X. Bresson, P. Vandergheynst, P. Hagmann and J.-P. Thiran, "Mapping resting-state dynamics on spatio-temporal graphs: a combined functional and diffusion MRI approach", *23rd International Symposium on Magnetic Resonance in Medicine (ISMRM)*, Toronto, Canada, 2015

A. Griffa, P. S. Baumann, C. Ferrari, T. Eric, P. Conus, K. Q. Do, J.-P. Thiran and P. Hagmann, "Diffusion spectrum imaging connectomics: a biomarker for staging in psychotic disorders", *23rd International Symposium on Magnetic Resonance in Medicine (ISMRM)*, Toronto, Canada, 2015

E. Fisch-Gomez, A. Griffa, E. Munoz-Moreno, L. Vasung, C. Borradori-Tolsa, F. Lazeyras, J.-P. Thiran and P. S. Huppi, "Brain network modular fingerprint of premature born children",

---

23rd International Symposium on Magnetic Resonance in Medicine (ISMRM), Toronto, Canada, 2015

A. Monin, P. S. Baumann, A. Griffa, L. Xin, R. Mekle, M. Fournier, J.-H. Cabungcal, P. Steullet, C. Buttica, C. Ferrari, P. Hagmann, P. Conus and K. Q. Do, "Glutathione Deficit Affects White Matter Integrity in Prefrontal Cortex and Impairs Brain Connectivity in Schizophrenia", *Society of Biological Psychiatry (SOBP) 69th Annual Scientific Meeting*, New York, NY, 2014

P. S. Baumann, A. Griffa, C. Ferrari, L. Alameda, M. Cuenod, J.-P. Thiran, K. Q. Do, P. Hagmann and P. Conus, "Integrity of the fornix.hippocampus circuit and relationship with peripheral oxidative stress markers in early phase of psychosis", *Society of Biological Psychiatry (SOBP) 69th Annual Scientific Meeting*, New York, NY, USA, 2014

F. Vasa, A. Griffa, M. Schaer, E. Scariati Jaussi, S. Eliez and P. Hagmann, "Characterizing the Connectome in the 22q11.2 Deletion Syndrome", *Organization for Human Brain Mapping (OHBM)*, Hamburg, Germany, 2014

A. Griffa, P. S. Baumann, C. Ferrari, P. Conus, K. Q. Do, J.-P. Thiran and P. Hagmann, "MR connectomics identifies a distributed subnetwork lesioned in schizophrenia", *22nd International Symposium on Magnetic Resonance in Medicine (ISMRM)*, Milan, Italy, 2014

M. H. Adhikari, A. Griffa, P. Hagmann, M. Corbetta and G. Deco, "Mathematical modeling for resting state functional connectivity of cortical and sub-cortical networks", *CNS - 22nd Annual Computational Neuroscience meeting*, Paris, France, 2013

A. Griffa, R. Betzel, K. Q. Do, P. Conus, P. Hagmann and J.-P. Thiran, "Group-representative partitions of human brain structural networks", *21th International Symposium on Magnetic Resonance in Medicine (ISMRM)*, Salt Lake City, UT, USA, 2013

A. Ponce-Alvarez, M. Lechón, A. Griffa, P. Hagmann and G. Deco, "Spatial and temporal patterns of ongoing cortical activity at rest", *Third Biennial Conference on Resting State Brain Connectivity*, Magdeburg, Germany, 2013

A. Griffa, A. Lemkaddem, A. Daducci and J.-P. Thiran, "Local vs global tractography to study brain connectivity", *International biomedical and astronomical signal processing (BASP) Frontiers workshop*, Villars-sur-Ollons, Switzerland, 2013

A. Pauli, J. Schneider, M. Bach Cuadra, A. Griffa, E. Fisch-Gomez, R. Meuli, J.-P. Thiran, A. Truttman and P. Hagmann, "Towards a connectome mapping pipeline for neonates using high-resolution MP2RAGE and DTI", *21st Annual Meeting International Society for Magnetic Resonance in Medicine*, Salt Lake City, UT, USA, 2013

A. Lemkaddem, S. Vulliemoz, A. Griffa, A. Daducci, D. E. Meskaldji, F. Lazeyras, M. Seeck and J.-P. Thiran, "Brain network analysis of patients with Temporal Lobe Epilepsy", *2013 IEEE International Symposium on Biomedical Imaging: From Nano to Macro*, San Francisco, CA, USA, 2013

J. Goñi, A. Kolchinsky, M. P. van den Heuvel, A. Griffa, L. Rocha and O. Sporns, "Information, space and structure in the human brain resting state", *12th GRANADA SEMINAR, on Physics, Computation and the Mind*, Granada, Spain, 2012

A. Griffa, P. S. Baumann, L. Xin, S. Crespi, C. Ferrari, R. Gruetter, J.-P. Thiran, K. Q. Do, P. Conus and P. Hagmann, "The influence of frontal glutathione levels on white matter connectivity in healthy and early psychosis subjects: a preliminary study" *ESMRMB - European Society for Magnetic Resonance in Medicine and Biology*, Lisbon, Portugal, 2012

S. Vulliemoz, A. Lemkaddem, A. Griffa, A. Daducci, F. Lazeyras, M. Seeck and J.-P. Thiran, "Whole-brain structural connectivity in temporal lobe epilepsy: a Diffusion Spectrum Imaging study", *8th Annual Meeting of the Organization for Human Brain Mapping*, Beijing, China, 2012

P. S. Baumann, A. Griffa, L. Xin, S. Crespi, C. Ferrari, J.-P. Thiran, R. Gruetter, P. Hagmann, K. Q. Do and P. Conus, "MRS Frontal Glutathione Levels Correlate with DSI White Matter Integrity Measure in Control Subjects but Not in Early Psychosis Patients", *67th Annual Scientific Convention and Meeting of the Society of Biological Psychiatry*, Philadelphia, PA, USA, 2012

A. Griffa, P. S. Baumann, L. Xin, S. Crespi, C. Ferrari, J.-P. Thiran, R. Gruetter, K. Q. Do, P. Conus and P. Hagmann, "Investigation of Network Metrics Correlation with Frontal Glutathione Levels in Control and First Episode Psychosis Subjects", *67th Annual Scientific Convention and Meeting of the Society of Biological Psychiatry*, Philadelphia, PA, USA, 2012

E. Fischi-Gomez, A. Griffa, A. Daducci, F. Lazeyras, J.-P. Thiran and P. Huppi, "Graph theory to analyse developmental plasticity in connectivity of preterm children", *20th International Society for Magnetic Resonance in Medicine (ISMRM) conference*, Melbourne, Australia, 2012

A. Lemkaddem, S. Vulliemoz, A. Griffa, A. Daducci, M. Seeck and J.-P. Thiran, "Altered structural connectivity in patients with medial temporal lobe epilepsy: A Diffusion Spectrum Imaging and Graph Analysis study", *20th International Society for Magnetic Resonance in Medicine (ISMRM) conference*, Melbourne, Australia, 2012